

Search for Particles with Anomalous Charge in the IceCube Detector

Ward Van Driessche



Search for Particles with Anomalous Charge in the IceCube Detector

Ward Van Driessche

Auteur DATUM

Goedgekeurd door

prof. dr. D. Ryckbosch
Thesis Promotor

Aanvaard door

???
Hoofd Examenjury

Promotor: prof. dr. D. Ryckbosch
Proefschrift ingediend tot het verkrijgen van de academische graad van
Doctor in de Wetenschappen: Fysica en Sterrenkunde

Vakgroep Fysica en Sterrenkunde
Faculteit Wetenschappen
Universiteit Gent
Academiejaar 2018-2019



- To bla bla bla

*If you can keep your head when all about you
Are losing theirs and blaming it on you,
If you can trust yourself when all men doubt you,
But make allowance for their doubting too;
If you can wait and not be tired by waiting,
Or being lied about, don't deal in lies,
Or being hated, don't give way to hating,
And yet don't look too good, nor talk too wise:*

*If you can dream—and not make dreams your master;
If you can think—and not make thoughts your aim;
If you can meet with Triumph and Disaster
And treat those two impostors just the same;
If you can bear to hear the truth you've spoken
Twisted by knaves to make a trap for fools,
Or watch the things you gave your life to, broken,
And stoop and build 'em up with worn-out tools:*

*If you can make one heap of all your winnings
And risk it on one turn of pitch-and-toss,
And lose, and start again at your beginnings
And never breathe a word about your loss;
If you can force your heart and nerve and sinew
To serve your turn long after they are gone,
And so hold on when there is nothing in you
Except the Will which says to them: 'Hold on!'*

*If you can talk with crowds and keep your virtue,
Or walk with Kings - nor lose the common touch,
If neither foes nor loving friends can hurt you,
If all men count with you, but none too much;
If you can fill the unforgiving minute
With sixty seconds' worth of distance run,
Yours is the Earth and everything that's in it,
And - which is more - you'll be a Man, my son!*

~ Rudyard Kipling

Abstract

Bla bla bla

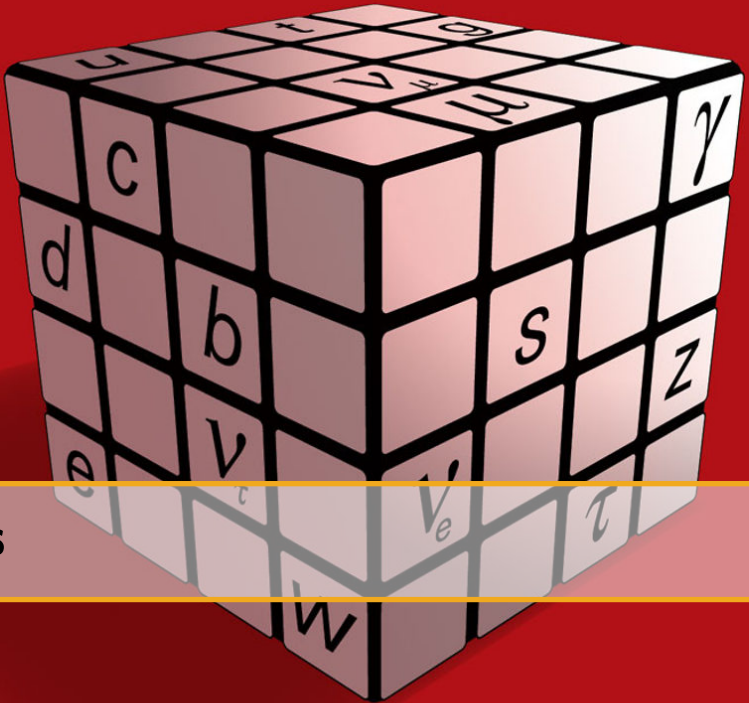


Table of Contents

Nederlandstalige samenvatting 7

Introduction 9

I

Theory and Experiment

1	The Standard Model of Particle Physics	13
1.1	What we call matter: fermions	13
1.1.1	Leptons	14
1.1.2	Quarks	15
1.2	How particles communicate: interactions	15
1.2.1	Gravity	15
1.2.2	Electromagnetism	16
1.2.3	Weak force	17
1.2.4	Strong force	17
1.2.5	A note about bosons	17
1.3	The Standard Model in theory	18
1.3.1	SU(3): quantum chromodynamics	18
1.3.2	SU(2) \times U(1): electroweak	19
1.3.3	Brout-Englert-Higgs mechanism	20
1.3.4	Particle mixing	24
1.4	A success story	25
1.4.1	Wave-particle duality	26
1.4.2	Predictions	26
1.4.3	Precision tests	27
1.5	The need for physics beyond the Standard Model	27
1.5.1	Running of the coupling constants	31
1.5.2	Unifying theories	32
1.5.3	How to look for new physics	32

2	Theoretical Motivation of the Analysis	35
2.1	Introduction	35
2.2	Theory	35
2.3	Properties of the signal	36
2.4	Previous searches	36
2.4.1	Searches with accelerators and fixed targets	36
2.4.2	Colliders	37
2.4.3	Searches for particles with telescopes	38
3	Cosmic Rays and Neutrinos	41
3.1	Cosmic rays	41
3.1.1	Discovery of cosmic rays	41
3.1.2	What are cosmic rays?	42
3.1.3	Acceleration mechanism	46
3.1.4	Sources	47
3.1.5	Propagation	53
3.2	Neutrinos	53
3.2.1	Conventional	54
3.2.2	Prompt	54
3.2.3	Astrophysical	55
3.2.4	Other neutrino sources	56
3.3	Air showers	56
3.3.1	Hadronic component	57
3.3.2	Muonic component	58
3.3.3	Electromagnetic component	58
3.4	Cosmic ray and neutrino detectors	58
4	Relativistic Particles in Matter	59
4.1	Neutrino interactions	59
4.2	Cherenkov effect	59
4.3	Propagation	62
4.3.1	Cascades	62
4.3.2	Muon tracks	63
4.4	Energy loss formulae	64
4.4.1	Ionization	65
4.4.2	Bremsstrahlung	65
4.4.3	Inelastic component	66
4.4.4	Photonuclear	66
4.4.5	Pair production	67
5	The IceCube Experiment	69
5.1	Geometry	69
5.1.1	In-ice array	71
5.1.2	DeepCore	72
5.1.3	IceTop	72
5.1.4	IceCube laboratory	72
5.2	Antarctic ice	72
5.2.1	Ice simulation	73
5.2.2	Systematic uncertainties	74

5.3	Hardware components	74
5.3.1	Digital optical modules	74
5.3.2	Calibration devices	76
5.3.3	Cable systems	76
5.4	Deployment	78
5.5	Data taking	78
5.5.1	Triggers	79
5.5.2	Filters	80
5.5.3	Data handling	81
5.6	Search strategies	81
5.6.1	Multimessenger astronomy and astrophysical neutrinos	81
5.6.2	Oscillations	82
5.6.3	Galactic supernovae	82
5.6.4	Beyond the Standard Model searches	82
5.7	Future upgrades	84
5.7.1	Scintillators	85
5.7.2	IceAct	85
5.7.3	IceCube Upgrade	86
5.7.4	IceCube Gen2	87
5.8	Discussion	88

II

Simulation, Processing and Analysis

6	Simulation: Event Generation and Propagation	91
6.1	Generation	93
6.1.1	Background simulation	93
6.1.2	Signal simulation	95
6.2	Propagation	97
6.2.1	PROPOSAL	97
6.2.2	Photoelectron generators	98
6.3	Detector simulation	99
6.4	Processing	100
6.5	Burn sample	100
6.6	Event viewer	101
7	Reconstruction, Cleaning and Analysis Techniques	103
7.1	Reconstruction	103
7.1.1	Likelihood	103
7.1.2	Line-Fit	104
7.1.3	SPE and MPE	105
7.1.4	Millipede	106
7.1.5	FiniteReco	108
7.1.6	Paraboloid	108
7.2	Pulse cleaning	108
7.3	IceHive	109
7.3.1	HiveSplitter	110
7.3.2	HiveCleaning	111
7.3.3	Remark	111

7.4	CoincSuite	112
7.5	Analysis techniques	112
7.6	Boosted Decision Tree classifiers	112
7.6.1	Structure	113
7.6.2	Training	113
7.6.3	Boosting	114
7.6.4	Overtraining	115
7.7	Minimal-Redundancy-Maximum-Relevance	116
7.8	IceCube coordinate system	116
8	The SPACE Analysis	119
8.1	Filter selection	119
8.1.1	VEF	119
8.1.2	LowUp	119
8.1.3	Online Muon L2	121
8.1.4	DeepCore	121
8.1.5	Burnsample checks	121
8.2	Level 3	121
8.2.1	Zenith angle cut	122
8.2.2	RlogL cut	122
8.2.3	NPE cut	123
8.2.4	Starting rlogL cut	123
8.2.5	Stopping rlogL cut	123
8.3	Level 4	123
8.3.1	Cleaning and quality cuts	124
8.3.2	Variable construction	125
8.3.3	Variable selection	132
8.4	Level 5	132
8.4.1	BDT result	134
8.4.2	Pull-validation	135
8.4.3	Model Rejection Factor	136
8.4.4	Systematic Uncertainties	138
8.5	Results	141
8.5.1	Unblinding	141
8.5.2	Limits	142
9	Summary and Conclusion	145

III

Additions

A	Gauge symmetries	151
B	Planck's law	153
B.1	Electromagnetic waves in a cubical cavity	153
B.1.1	Classical approach	154
B.1.2	Quantum approach	154
Appendices	149	

C	Statistics	155
D	Distributions	157
D.1	Spherical random numbers	157
D.2	Power law distributions	158
D.3	Angular distributions	159
D.4	Weighting	160
E	AdaBoost: simple example	163
F	Resampling Methods	165
F.1	Bootstrapping	165
F.2	Cross-validation	165
G	Additional BDT Checks	167
H	Data Events at Final Level	169
10	Some useful things for LaTeX	173
10.1	Definitions	173
10.2	Remarks	173
10.3	Corollaries	173
10.4	Propositions	173
10.4.1	Several equations	174
10.4.2	Single Line	174
10.5	Examples	174
10.5.1	Equation and Text	174
10.5.2	Paragraph of Text	174
10.6	Exercises	174
10.7	Problems	174
10.8	Vocabulary	174
	Bibliography	175
	Index	189

Nederlandstalige Samenvatting

Lorem ipsum dolor sit amet, consectetuer adipiscing elit. Ut purus elit, vestibulum ut, placerat ac, adipiscing vitae, felis. Curabitur dictum gravida mauris. Nam arcu libero, nonummy eget, consectetuer id, vulputate a, magna. Donec vehicula augue eu neque. Pellentesque habitant morbi tristique senectus et netus et malesuada fames ac turpis egestas. Mauris ut leo. Cras viverra metus rhoncus sem. Nulla et lectus vestibulum urna fringilla ultrices. Phasellus eu tellus sit amet tortor gravida placerat. Integer sapien est, iaculis in, pretium quis, viverra ac, nunc. Praesent eget sem vel leo ultrices bibendum. Aenean faucibus. Morbi dolor nulla, malesuada eu, pulvinar at, mollis ac, nulla. Curabitur auctor semper nulla. Donec varius orci eget risus. Duis nibh mi, congue eu, accumsan eleifend, sagittis quis, diam. Duis eget orci sit amet orci dignissim rutrum.

Nam dui ligula, fringilla a, euismod sodales, sollicitudin vel, wisi. Morbi auctor lorem non justo. Nam lacus libero, pretium at, lobortis vitae, ultricies et, tellus. Donec aliquet, tortor sed accumsan bibendum, erat ligula aliquet magna, vitae ornare odio metus a mi. Morbi ac orci et nisl hendrerit mollis. Suspendisse ut massa. Cras nec ante. Pellentesque a nulla. Cum sociis natoque penatibus et magnis dis parturient montes, nascetur ridiculus mus. Aliquam tincidunt urna. Nulla ullamcorper vestibulum turpis. Pellentesque cursus luctus mauris.

Nulla malesuada porttitor diam. Donec felis erat, congue non, volutpat at, tincidunt tristique, libero. Vivamus viverra fermentum felis. Donec nonummy pellentesque ante. Phasellus adipiscing semper elit. Proin fermentum massa ac quam. Sed diam turpis, molestie vitae, placerat a, molestie nec, leo. Maecenas lacinia. Nam ipsum ligula, eleifend at, accumsan nec, suscipit a, ipsum. Morbi blandit ligula feugiat magna. Nunc eleifend consequat lorem. Sed lacinia nulla vitae enim. Pellentesque tincidunt purus vel magna. Integer non enim. Praesent euismod nunc eu purus. Donec bibendum quam in tellus. Nullam cursus pulvinar lectus. Donec et mi. Nam vulputate metus eu enim. Vestibulum pellentesque felis eu massa.

Quisque ullamcorper placerat ipsum. Cras nibh. Morbi vel justo vitae lacus tincidunt ultrices. Lorem ipsum dolor sit amet, consectetuer adipiscing elit. In hac habitasse platea dictumst. Integer tempus convallis augue. Etiam facilisis. Nunc elementum fermentum wisi. Aenean placerat. Ut imperdiet, enim sed gravida sollicitudin, felis odio placerat quam, ac pulvinar elit purus eget enim. Nunc vitae tortor. Proin tempus nibh sit amet nisl. Vivamus quis tortor vitae risus porta vehicula.

Fusce mauris. Vestibulum luctus nibh at lectus. Sed bibendum, nulla a faucibus semper, leo velit ultricies tellus, ac venenatis arcu wisi vel nisl. Vestibulum diam. Aliquam pellentesque, augue quis sagittis posuere, turpis lacus congue quam, in hendrerit risus eros eget felis. Maecenas

eget erat in sapien mattis porttitor. Vestibulum porttitor. Nulla facilisi. Sed a turpis eu lacus commodo facilisis. Morbi fringilla, wisi in dignissim interdum, justo lectus sagittis dui, et vehicula libero dui cursus dui. Mauris tempor ligula sed lacus. Duis cursus enim ut augue. Cras ac magna. Cras nulla. Nulla egestas. Curabitur a leo. Quisque egestas wisi eget nunc. Nam feugiat lacus vel est. Curabitur consectetur.

Suspendisse vel felis. Ut lorem lorem, interdum eu, tincidunt sit amet, laoreet vitae, arcu. Aenean faucibus pede eu ante. Praesent enim elit, rutrum at, molestie non, nonummy vel, nisl. Ut lectus eros, malesuada sit amet, fermentum eu, sodales cursus, magna. Donec eu purus. Quisque vehicula, urna sed ultricies auctor, pede lorem egestas dui, et convallis elit erat sed nulla. Donec luctus. Curabitur et nunc. Aliquam dolor odio, commodo pretium, ultricies non, pharetra in, velit. Integer arcu est, nonummy in, fermentum faucibus, egestas vel, odio.

Sed commodo posuere pede. Mauris ut est. Ut quis purus. Sed ac odio. Sed vehicula hendrerit sem. Duis non odio. Morbi ut dui. Sed accumsan risus eget odio. In hac habitasse platea dictumst. Pellentesque non elit. Fusce sed justo eu urna porta tincidunt. Mauris felis odio, sollicitudin sed, volutpat a, ornare ac, erat. Morbi quis dolor. Donec pellentesque, erat ac sagittis semper, nunc dui lobortis purus, quis congue purus metus ultricies tellus. Proin et quam. Class aptent taciti sociosqu ad litora torquent per conubia nostra, per inceptos hymenaeos. Praesent sapien turpis, fermentum vel, eleifend faucibus, vehicula eu, lacus.



Paragraphs of Text

Lorem ipsum dolor sit amet, consectetuer adipiscing elit. Ut purus elit, vestibulum ut, placerat ac, adipiscing vitae, felis. Curabitur dictum gravida mauris. Nam arcu libero, nonummy eget, consectetuer id, vulputate a, magna. Donec vehicula augue eu neque. Pellentesque habitant morbi tristique senectus et netus et malesuada fames ac turpis egestas. Mauris ut leo. Cras viverra metus rhoncus sem. Nulla et lectus vestibulum urna fringilla ultrices. Phasellus eu tellus sit amet tortor gravida placerat. Integer sapien est, iaculis in, pretium quis, viverra ac, nunc. Praesent eget sem vel leo ultrices bibendum. Aenean faucibus. Morbi dolor nulla, malesuada eu, pulvinar at, mollis ac, nulla. Curabitur auctor semper nulla. Donec varius orci eget risus. Duis nibh mi, congue eu, accumsan eleifend, sagittis quis, diam. Duis eget orci sit amet orci dignissim rutrum.

Nam dui ligula, fringilla a, euismod sodales, sollicitudin vel, wisi. Morbi auctor lorem non justo. Nam lacus libero, pretium at, lobortis vitae, ultricies et, tellus. Donec aliquet, tortor sed accumsan bibendum, erat ligula aliquet magna, vitae ornare odio metus a mi. Morbi ac orci et nisl hendrerit mollis. Suspendisse ut massa. Cras nec ante. Pellentesque a nulla. Cum sociis natoque penatibus et magnis dis parturient montes, nascetur ridiculus mus. Aliquam tincidunt urna. Nulla ullamcorper vestibulum turpis. Pellentesque cursus luctus mauris.

Nulla malesuada porttitor diam. Donec felis erat, congue non, volutpat at, tincidunt tristique, libero. Vivamus viverra fermentum felis. Donec nonummy pellentesque ante. Phasellus adipiscing semper elit. Proin fermentum massa ac quam. Sed diam turpis, molestie vitae, placerat a, molestie nec, leo. Maecenas lacinia. Nam ipsum ligula, eleifend at, accumsan nec, suscipit a, ipsum. Morbi blandit ligula feugiat magna. Nunc eleifend consequat lorem. Sed lacinia nulla vitae enim. Pellentesque tincidunt purus vel magna. Integer non enim. Praesent euismod nunc eu purus. Donec bibendum quam in tellus. Nullam cursus pulvinar lectus. Donec et mi. Nam vulputate metus eu enim. Vestibulum pellentesque felis eu massa.

Quisque ullamcorper placerat ipsum. Cras nibh. Morbi vel justo vitae lacus tincidunt ultrices. Lorem ipsum dolor sit amet, consectetuer adipiscing elit. In hac habitasse platea dictumst. Integer tempus convallis augue. Etiam facilisis. Nunc elementum fermentum wisi. Aenean placerat. Ut imperdiet, enim sed gravida sollicitudin, felis odio placerat quam, ac pulvinar elit purus eget enim. Nunc vitae tortor. Proin tempus nibh sit amet nisl. Vivamus quis tortor vitae risus porta vehicula.

Fusce mauris. Vestibulum luctus nibh at lectus. Sed bibendum, nulla a faucibus semper, leo

velit ultricies tellus, ac venenatis arcu wisi vel nisl. Vestibulum diam. Aliquam pellentesque, augue quis sagittis posuere, turpis lacus congue quam, in hendrerit risus eros eget felis. Maecenas eget erat in sapien mattis porttitor. Vestibulum porttitor. Nulla facilisi. Sed a turpis eu lacus commodo facilisis. Morbi fringilla, wisi in dignissim interdum, justo lectus sagittis dui, et vehicula libero dui cursus dui. Mauris tempor ligula sed lacus. Duis cursus enim ut augue. Cras ac magna. Cras nulla. Nulla egestas. Curabitur a leo. Quisque egestas wisi eget nunc. Nam feugiat lacus vel est. Curabitur consectetur.

Suspendisse vel felis. Ut lorem lorem, interdum eu, tincidunt sit amet, laoreet vitae, arcu. Aenean faucibus pede eu ante. Praesent enim elit, rutrum at, molestie non, nonummy vel, nisl. Ut lectus eros, malesuada sit amet, fermentum eu, sodales cursus, magna. Donec eu purus. Quisque vehicula, urna sed ultricies auctor, pede lorem egestas dui, et convallis elit erat sed nulla. Donec luctus. Curabitur et nunc. Aliquam dolor odio, commodo pretium, ultricies non, pharetra in, velit. Integer arcu est, nonummy in, fermentum faucibus, egestas vel, odio.

Sed commodo posuere pede. Mauris ut est. Ut quis purus. Sed ac odio. Sed vehicula hendrerit sem. Duis non odio. Morbi ut dui. Sed accumsan risus eget odio. In hac habitasse platea dictumst. Pellentesque non elit. Fusce sed justo eu urna porta tincidunt. Mauris felis odio, sollicitudin sed, volutpat a, ornare ac, erat. Morbi quis dolor. Donec pellentesque, erat ac sagittis semper, nunc dui lobortis purus, quis congue purus metus ultricies tellus. Proin et quam. Class aptent taciti sociosqu ad litora torquent per conubia nostra, per inceptos hymenaeos. Praesent sapien turpis, fermentum vel, eleifend faucibus, vehicula eu, lacus.

Theory and Experiment

1 The Standard Model of Particle Physics 13

- 1.1 What we call matter: fermions
- 1.2 How particles communicate: interactions
- 1.3 The Standard Model in theory
- 1.4 A success story
- 1.5 The need for physics beyond the Standard Model

2 Theoretical Motivation of the Analysis . 35

- 2.1 Introduction
- 2.2 Theory
- 2.3 Properties of the signal
- 2.4 Previous searches

3 Cosmic Rays and Neutrinos 41

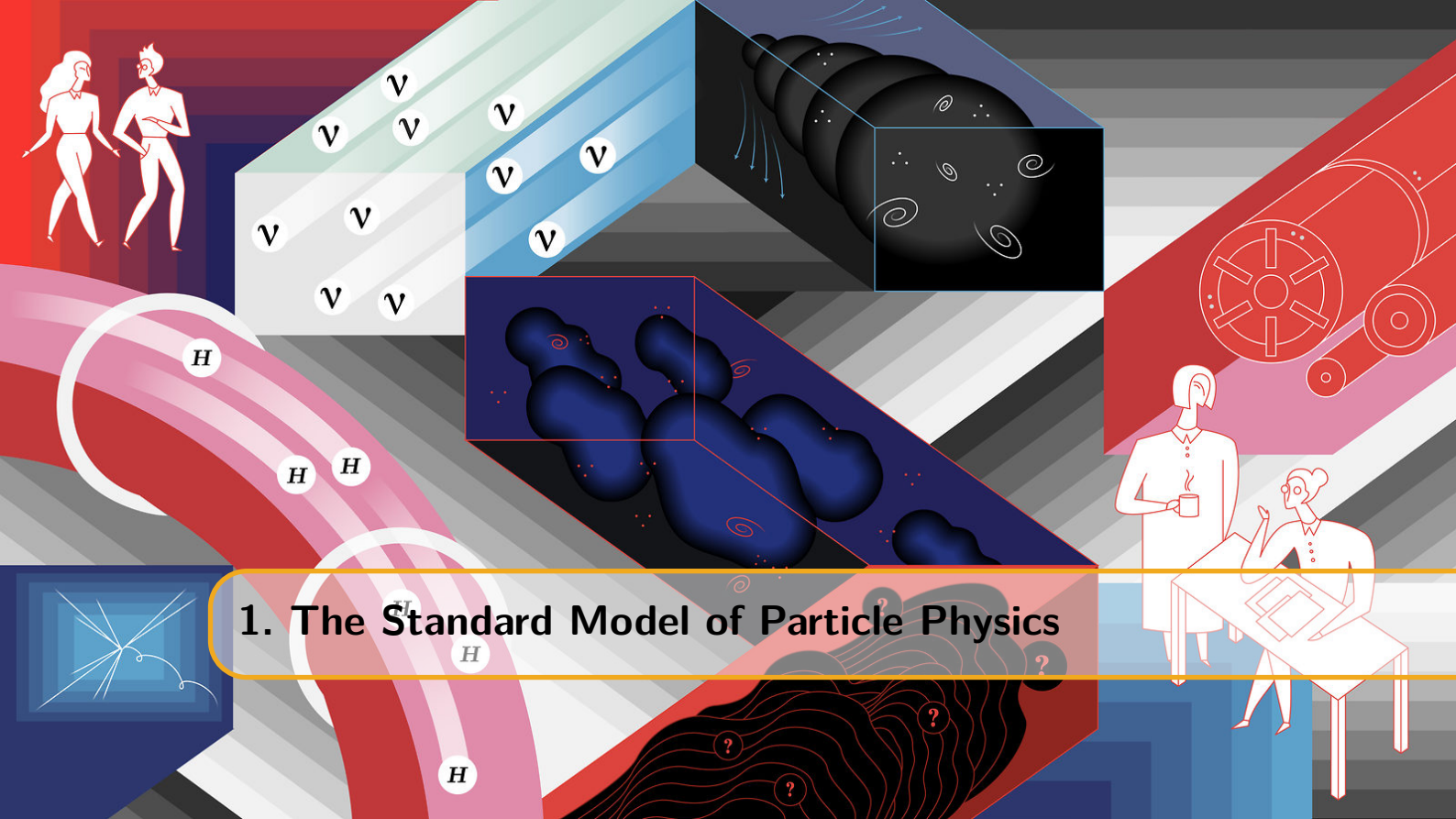
- 3.1 Cosmic rays
- 3.2 Neutrinos
- 3.3 Air showers
- 3.4 Cosmic ray and neutrino detectors

4 Relativistic Particles in Matter 59

- 4.1 Neutrino interactions
- 4.2 Cherenkov effect
- 4.3 Propagation
- 4.4 Energy loss formulae

5 The IceCube Experiment 69

- 5.1 Geometry
- 5.2 Antarctic ice
- 5.3 Hardware components
- 5.4 Deployment
- 5.5 Data taking
- 5.6 Search strategies
- 5.7 Future upgrades
- 5.8 Discussion



1. The Standard Model of Particle Physics

A physicist is an atom's way of knowing about atoms ~ George Wald

The aim of this chapter is to give a summary of the theoretical framework that is used in particle physics. This framework was developed in stages throughout the latter half of the 20th century and is known as the Standard Model of particle physics. This model is a quantum field theory that is able to describe most of what is seen in particle physics experiments and proved to be successful in predicting later experimental discoveries. In this chapter, a brief historical overview of the development of this theory will be given together with a limited description in order to familiarize the reader with concepts that will be used throughout this work. For a more in-depth and exhaustive discussion I refer to Refs. [1, 2, 3, 4]. We start with an overview of the constituent particles of the Standard Model, linking them to our everyday life. Secondly, a general description is given on the nature of forces. Thirdly, we go to a more mathematical and in-depth description of the Standard Model. Lastly, we present the many successes of this model and finalize with an argumentation of why there is a need for physics beyond this model.

1.1 What we call matter: fermions

Physics (from Ancient Greek: φυσική - *physikē*, “knowledge of nature”) is the natural science that studies matter. Matter is made up by *atoms* (from Greek: *atomos** , “indivisible”) that can bind together into molecules and accounts for what is around us in our everyday life. Atoms are made up of a positively charged *nucleus* that is surrounded by one or more *electrons*. The nucleus and electrons are bound to each other via the electromagnetic force. The nucleus is made up of one or more *protons* and, typically, an approximately equal amount of *neutrons*. Because of their similar characteristics, protons and neutrons are often referred to as *nucleons* and together they make up of more than 99.94% of an atom’s mass. Nucleons are made up of smaller particles called *quarks*,[†] which are, as far as we know, *fundamental particles*. This

*Coined by ancient Greek philosophers Leucippus and his pupil Democritus who believed matter was made up of discrete units.

[†]The word “quark” originally appeared in the novel *Finnegans Wake* written by the Irish author James Joyce (1882–1941). The protagonist of the book dreams that he is serving beer to a drunken seagull. Instead of asking for “three quarts for Mister Mark” the inebriated bird says “three quarks for Muster Mark”. Murray Gell-Man had the habit of using names like “squeak” and “squark” for peculiar objects and after encountering the sentence in the book the name struck him as appropriate since the (then hypothetical) particle came in threes.

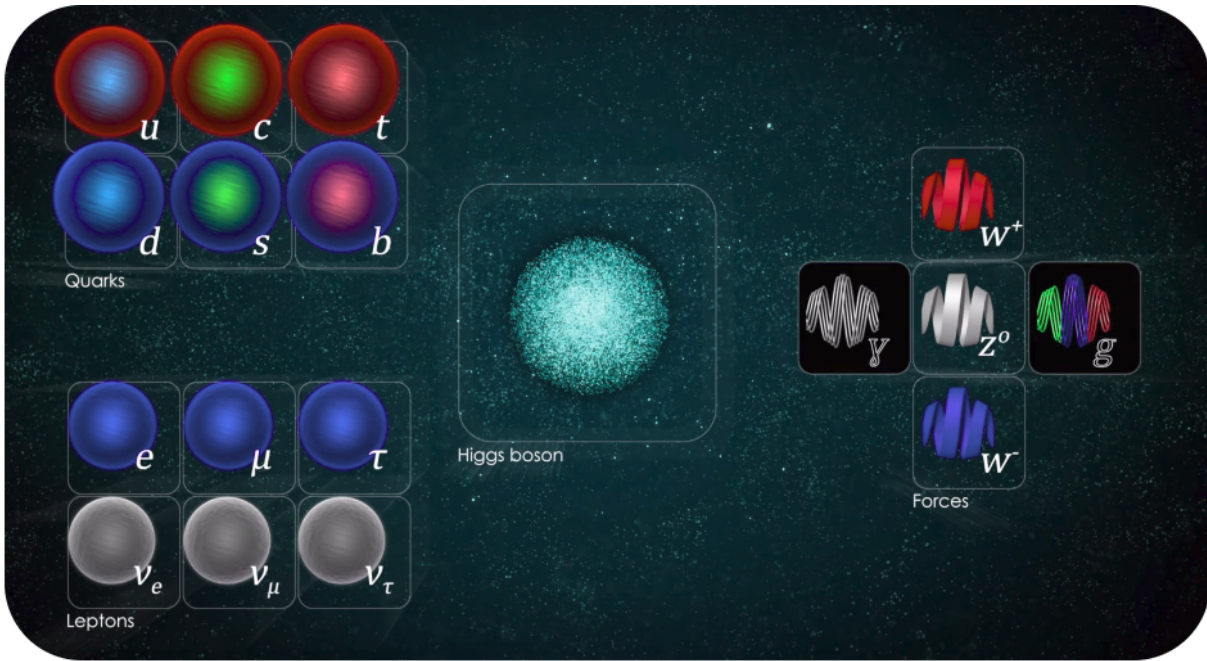


Figure 1.1: The Standard Model of particle physics distinguishes fermions (left) from bosons (right). The Brout-Englert-Higgs boson (middle) is more peculiar as it has no intrinsic spin and plays a special role in the theory. Charges for fermions are not explicitly written to account for antiparticles. Illustration from Ref. [5].

means that we believe that there are no smaller substructures making up these objects and are in essence mathematically best described as infinitely small. Because of this, they are often referred to as pointlike. In the Standard Model (SM), these particles are characterized as *fermions*, which have odd half-integer spins, obeying the laws of quantum mechanics. The spin of a particle is often illustrated with its classical counterpart in which an object is spinning and thus carries an intrinsic angular momentum. This analogy cannot be extrapolated to pointlike particles, but the property happens to hold the same units as the classical orbital momentum. The spin of a particle seems to be just another property particles have, like charge or mass. Fermions follow Fermi-Dirac statistics and therefore obey the Pauli exclusion principle. As a consequence, fermions cannot occupy the same place at the same time (more formally: no two fermions may be described by the same quantum numbers). This agrees with our macroscopic observations of matter in everyday life: matter interacts with matter; people cannot walk through walls!

In total, the SM distinguishes 24 different fermions that can be subdivided into two distinct classes: *quarks* and *leptons*. There are six quarks (up, down, charm, strange, top and bottom), and six leptons (electron, electron neutrino, muon, muon neutrino, tau and tau neutrino), along with the corresponding antiparticle for each of these fermions. A summary of all the particles in the Standard Model is given in Figure 1.1.

1.1.1 Leptons

Leptons* can be subdivided into two classes: electromagnetically charged particles (e^- , μ^- and τ^-) and the neutral neutrinos† (ν_e , ν_μ and ν_τ). Because of their charge, electrons are the well known particles that combine into atoms together with nucleons. Being the lightest of the three, the electron is said to be part of the first *generation*, together with the electron neutrino. Muons

*λεπτός (leptos) meaning thin, delicate, lightweight, or small. Originally leptons were considered the “light” particles and hadrons the “heavy” particles, but the discovery of the tau lepton in 1975 broke that rule.

†The Italian word for neutron (neutrono) sounds like the word neutral (neutro) with an augmentative suffix (-one) tacked on the end, making the word a little wordplay. In Italian, it sounds something like “big neutral”. Replace the augmentative suffix -one with the diminutive suffix -ino and you have a “little neutral”, which is a good description of what a neutrino is — a diminutive neutral particle.

differ only from electrons in mass* and make up the second generation together with muon neutrinos. Similarly, tau particles and tau neutrinos define the third generation. All leptons have a corresponding antiparticle indicated by a positive charge (e.g. e^+) or a bar (e.g. $\bar{\nu}_e$). Neutrinos are proven to have a very small mass [6] and interact only via the weak force (Section 1.2.3), making them inherently very hard to detect.

1.1.2 Quarks

The six quarks are called up, down, charm, strange, top and bottom quarks ($(u, d), (c, s), (t, b)$). One generation is made up of a particle with charge $1/3$ and one with $-2/3$ (also visualized in Figure 1.1). These charges are relative to the absolute electron charge. The difference between generations is again essentially the bare mass of the particles. Because quarks also interact through the strong force (see Section 1.2.4), they combine into *hadrons*[†] (of which nucleons are the best known examples). Due to their color charge and the intrinsic behaviour of the strong force, quarks cannot be observed freely: they always combine into color neutral particles; a property called *confinement*. When a hadron, with its constituent quarks, is pulled apart, the attractive force between the quarks does not fall down rapidly since gluons carry color charge themselves. When these particles are pulled apart far enough, it becomes energetically more favorable to produce new quark-antiquark pairs, which again combine into color neutral particles[‡]. The energy requirement for the production of new particles is far below the one to separate the quarks far enough from each other to observe them separately. Quark antiparticles are again denominated with a bar (i.e. \bar{u}).

Because of their ability to interact with the strong force, particle accelerators in the 1960's led to the discovery of a plethora of possible quark combinations. Something that is often referred to as the "particle zoo".

1.2 How particles communicate: interactions

There are four fundamental interactions known to exist: gravity and electromagnetism, which produce significant long-range forces, and the strong and weak forces that only express themselves at (sub)atomic distances and govern nuclear interactions. These are explained in more detail below and an overview is given in Table 1.1.

Particles interact with each other through the exchange of *gauge bosons* or *force carriers*[§]. Gauge bosons are bundles of energy, *quanta*, and can be seen as excitations of one of the force fields.

Fields are a mathematical approach used by physicists to describe what we observe in experiments. Although the use of fields is very natural, the concept might feel a bit unfamiliar. In the following, the known forces are described in more detail. Gravity plays less of a role in subatomic physics, but is added for completeness and is mainly used to make the reader more familiar with the concept of a field.

1.2.1 Gravity

Gravity (from Latin/old French: *gravitas*/grave, "weighty, heavy") is the phenomenon wherein massive objects are attracted to each other. Gravitation is famously described by the general theory[¶] of general relativity proposed by Albert Einstein in 1915. Compared to the other forces,

*This characteristic is often referred to as *lepton universality*.

[†]ἀδρός (adros) meaning thick, robust, massive, or large. This name alludes to the ability of the point-like quarks to bind together and form particles that are massive in a certain sense.

[‡]This process is called *hadronization* and results into the production of "jets" in particle accelerators [7].

[§]A classic and very simplistic way of looking at force carriers is to imagine two people standing on a boat. The force carrier is a heavy ball that can be thrown from one person to the other. Doing so, both persons will move in opposite direction.

[¶]A scientific theory is an explanation of an aspect of the natural world that can be repeatedly tested, in accordance with the scientific method, using a predefined protocol of observation and experiment. Established scientific theories have withstood rigorous scrutiny and embody scientific knowledge.

Table 1.1: Summary of the known forces and their properties. The relative strength is compared to the electromagnetic force, but depends on the energy scale.

Interaction	Gravitation	Weak Electroweak	Electromagnetic	Strong
Acts on	mass/energy	flavor	electric charge	color charge
Couples to	all particles	all fermions	electrically charged	quarks, gluons
Mediation	not yet observed	W^+, W^-, Z	γ	gluons
Rel. strength	10^{-35}	10^{-11}	1	10^2

gravity is intrinsically very weak* and is not described in the SM (see Section 1.3). This is why gravity is often left out in discussions of particle physics experiments, but is crucial for understanding astronomical objects and how they influence each other. It can however be used to explain the concept of a field in a very natural way.

A very good description of gravitation was already provided centuries ago. First published on July 5th, 1686 was Newton’s work *Philosophiae Naturalis Principia Mathematica* (“the Principia”) that described formula that are still widely used today. The equation of the force exerted by two massive bodies takes the following form,

$$F = G \frac{m_1 m_2}{r^2}, \quad (1.1)$$

where F is the gravitational force acting between two objects, m_1 and m_2 are the masses of the objects, r is the distance between their center of mass, and G is the gravitational constant.

Newton’s law states that two massive bodies will exert a force onto one another proportional to their masses, but inversely proportional to the square of the distance between them. Newton realized this would mean that at any given instant in time all massive objects in the universe would know from every other object in the universe where it is located and how massive it is†. Because of this, Newton himself believed his explanation could not be the final answer. The answer is fully described in Einstein’s work of general relativity, but was already explained by Pierre-Simon Laplace in 1783. Gravitation is the slope of a field that pervades space and therefore, one only needs to know the value of the field in a local region to calculate the attractional force at that specific location. Massive objects do not “feel” each other but distort space and time in such a way that objects that are attracted “fall” towards each other. Field theory makes it able to treat the laws of physics as a local property instead of an action at a distance.

To date, it has not been possible to describe gravity in the framework of quantum field theory like the other fundamental forces, although, there is still much ongoing work. The gauge bosons from such a quantum field theory for gravity are mostly referred to as *gravitons*.

1.2.2 Electromagnetism

The electromagnetic field (from Ancient Greek: ἥλεκτρον *elektron*, “amber”, and μαγνῆτις λίθος, *magnetis lithos*, which means “Magnesian stone”‡) presents itself in the electrical and magnetical forces. In the late 1870’s, the publication of James Clerk Maxwell’s *A Treatise on Electricity and Magnetism* showed that the electric and magnetic interactions of negative and positive charges are mediated by one force: electromagnetism. Particles carrying a quantity (charge) of one of these forces can attract or repel each other.

Similar to the theory of gravity, the electromagnetic field pervades all around us, providing the necessary description of how charged particles interact with each other. The interaction of nuclei, which have a positive electric charge, and electrons makes up most of what is described in chemistry.

*Two magnets that fit in the palm of your hand can deliver a force which is of similar strength than the force that our entire planet exerts on a human body.

†Imagine the attraction of the Moon towards the Earth: how are both “communicating”?

‡In 1641 Athanasius Kircher described the magnetic properties of the Magnesian stone in his book *Magne sive de arte magnetica opus tripartitum* [8].

The force carrier of electromagnetism is called a *photon*, or in other words: light.

1.2.3 Weak force

The weak force is one aspect of the overarching electroweak theory that combines electromagnetism and the weak force. As opposed to gravity and electromagnetism, it only takes place at very small subatomic distances*. One well known phenomenon that is described by the weak force is *beta decay* in which free neutrons decay into protons and produce an extra electron and anti-electron neutrino. Another beautiful example of the weak force is the driving mechanism in the Sun's thermonuclear process that makes it shine. This process cannot be explained by chemical processes but with the fusion of hydrogen atoms into deuterium. Two protons are squeezed together into a He atom that consists of a proton and a neutron. The conversion of the proton into a neutron can be explained by the weak force.

The force carriers of the weak force are the W^+ , W^- and Z bosons. Because of the mass of these force carriers, the coupling of particles with the weak field is inversely proportional to the square of their mass. This makes the force seem to be very weak, hence its name†.

The weak force also carries some peculiar properties that are unique in a number of respects:

- it is the only interaction that violates parity symmetry and even does so maximally (V-A interaction),
- its force carriers are massive as opposed to all other force carriers,
- it is the only force capable of changing quarks from one family into a quark of another family.

1.2.4 Strong force

As indicated in Section 1.1, nuclei are made up of protons and neutrons. However, up to now the forces described in this section cannot explain how they can make up a stable combination. The positive/neutral electromagnetic charge of the protons/neutrons would even suggest the opposite. Protons and neutrons are made up by quarks that carry a quantity called *color charge*. Particles carrying a color charge participate in interactions of the strong force. Due to the principle of *self interaction*, the strong force only manifests itself on very small scales‡. When nucleons are squeezed together (either due to high temperatures or pressure) and come close enough, the quarks that make up the nucleons interact and make up the binding energy between nucleons.

The force carriers of the strong force are called *gluons*. These gluons carry a color charge themselves and are massless.

Aside from holding nucleons together, the strong force is also responsible for around 99% of the mass of the nucleon's mass. The binding energy, which includes the kinetic energy of the quarks and the energy of the gluon fields that bind the quarks together, makes up the bulk of the mass via Einstein's $E = mc^2$ relation. Only a small percentage of the total nucleon mass comes from the bare quark masses.

1.2.5 A note about bosons

As opposed to fermions, which obey Fermi-Dirac statistics and cannot occupy the same quantum state, bosons follow Bose-Einstein statistics§. Bosons carry integer spins ($s = 0, 1, 2$, etc.), fermions carry half-integer spins ($s = 1/2, 3/2$, etc.). As a result, bosons have no problem occupying the same place at the same time (more formally: two or more bosons may be described by the same quantum numbers). As the particles that make up light and other forms of electromagnetic radiation, photons are the bosons we have the most direct experience with. In

*The reason being that the force carriers are massive, more info in Section 1.3.

†It was Enrico Fermi who first came up with a proper description of the beta decay in 1933. Although he described the interaction as a 4-point interaction, making it only valid up to energies below 100 GeV.

‡As opposed to the weak force where the short distance behaviour is explained due to the mass of the force carriers.

§The name "boson" originates from Paul Dirac who wanted to commemorate the contributions of Indian physicist Satyendra Nath Bose who, together with Albert Einstein, theorized the characteristics of elementary particles that follow Bose-Einstein statistics [9].

our everyday experience, we don't see beams of light crash into one another. Photons can go through each other with no effect.

1.3 The Standard Model in theory

Most of the text below is based on the very elaborate book from Franz Mandl and Graham Shaw, *Quantum Field Theory* [10].

The Standard Model is a *quantum field theory*, meaning its fundamental objects are fields of a quantum nature that are defined at all points in spacetime. These fields are

- fermion fields, ψ , which account for “matter particles”;
- electroweak boson fields, W^1, W^2, W^3 and B ;
- gluon fields, G^a ; and
- the Higgs field, ϕ .

Quantum field theory treats particles as excited states of one of these underlying fields, so called *field quanta*. The difference between classical and quantum fields is that they are operator-valued. Classical fields can in principle take on distinct values at each point in space whereas a quantum field accommodates observations of quantum mechanics such as

- the quantization of energy, meaning that only discrete energy values are possible;
- these discrete energy levels are equally spaced;
- the lowest achievable energy is not equal to absolute zero, but has a zero-point energy*.

The dynamics of the quantum state and the fundamental fields are determined by the Lagrangian density \mathcal{L} . Writing the time and space coordinates in the form $(t, \mathbf{x}) = (x^0, x^1, x^2, x^3) = x^\mu$, the equations of motion of these fields can be written as:

$$\frac{\partial}{\partial x_\mu} \left[\frac{\partial \mathcal{L}}{\partial (\partial \phi / \partial x^\mu)} \right] - \frac{\partial \mathcal{L}}{\partial \phi} = 0, \quad (1.2)$$

which follow from the principle of least action. The lagrangian function depends on the fields and how these fields change in spacetime: $\mathcal{L}(\phi, \nabla \phi)$. Quantization of these fields can be obtained by interpreting the coordinates and momenta as Heisenberg operators, and subjecting these to canonical commutation relations.

Furthermore, the Standard Model is a gauge theory in which the Lagrangian is invariant under certain Lie groups (referred to as the symmetry group or the gauge group of the theory) of local transformations. For quantized gauge groups, the quanta of the gauge fields are referred to as *gauge bosons*. A gauge theory is a mathematical model that has a gauge freedom; there are mathematical degrees of freedom that are redundant. In other words: different mathematical expressions describe the exact same physical system and are in that sense unphysical. An experiment could never uniquely determine their values, even in principle[†]. If the phase of the wavefunction is changed by a different amount at each point in spacetime and the physics remains unchanged, the Lagrangian is said to follow a *local phase symmetry*[‡].

The Standard Model is defined by the local $SU(3) \times SU(2) \times U(1)$ gauge symmetry. Each element gives rise to three fundamental forces.

1.3.1 **SU(3): quantum chromodynamics**

The quantum chromodynamics (QCD) sector defines the interactions between quarks and gluons. Since leptons do not carry color charge, they do not participate in this interaction. The Dirac Lagrangian of the quarks coupled to the gluon fields is given by

*This is in accordance with the well known Heisenberg uncertainty principle that states that because of the zero-point energy, the position and momentum of a particle are not fixed but have a small range of variance: $\sigma_x \sigma_p \geq \frac{\hbar}{2}$.

[†]Imagine a perfect cylinder that can be twisted without deforming. It is not possible to distinguish a cylinder that has been twisted or not. To be able to determine it, an initial gauge has to be present. A horizontal line drawn on the cylinder can determine if the cylinder has been deformed or not.

[‡]See appendix A.

$$\mathcal{L}_{QCD} = \sum_{\psi} \bar{\psi}_i \left(i\gamma^{\mu} \left(\partial_{\mu} \delta_{ij} - ig_s G_{\mu}^a T_{ij}^a \right) - m_{\psi} \delta_{ij} \right) \psi_j - \frac{1}{4} G_{\mu\nu}^a G_a^{\mu\nu}, \quad (1.3)$$

where we sum over the fields of the strong charge and

ψ_i is the Dirac spinor of the quark field (the subscript $i = r, g, b$ represents the color charges);

γ^{μ} are the Dirac matrices;

G_{μ}^a is the 8-component ($a = 1, 2, \dots, 8$) SU(3) gauge field;

T_{ij}^a are the 3×3 Gell-Mann matrices (generators of the SU(3) color group);

$G_{\mu\nu}^a$ are the field strength tensors for the gluons;

g_s is the strong coupling constant;

m_{ψ} corresponds to the quark masses.

1.3.2 $SU(2) \times U(1)$: electroweak

The electroweak (EW) sector is a Yang-Mills gauge theory with the symmetry group $SU(2)_L \times U(1)$. The Lagrangian is given by

$$\begin{aligned} \mathcal{L}_{EW} &= \sum_{\psi} \bar{\psi} \gamma^{\mu} \left(i\partial_{\mu} - \frac{g'}{2} Y_W B_{\mu} - \frac{g}{2} \vec{\tau}_L \vec{W}_{\mu} \right) \psi - \frac{1}{4} W_a^{\mu\nu} W_{\mu\nu}^a - \frac{1}{4} B^{\mu\nu} B_{\mu\nu} \\ &= \bar{Q}_i i D_{\mu} \gamma^{\mu} Q_i + \bar{u}_i i D_{\mu} \gamma^{\mu} u_i + \bar{d}_i i D_{\mu} \gamma^{\mu} d_i + \bar{L}_i (i D_{\mu} \gamma^{\mu}) L_i + \bar{e}_{R,i} (i D_{\mu} \gamma^{\mu}) e_{R,i} \\ &\quad - \frac{1}{4} W_a^{\mu\nu} W_{\mu\nu}^a - \frac{1}{4} B^{\mu\nu} B_{\mu\nu}, \end{aligned} \quad (1.4)$$

where

B_{μ} is the U(1) gauge field;

Y_W is the weak hypercharge* (the generator of the U(1) group);

\vec{W}_{μ} is the 3-component SU(2) gauge field;

$\vec{\tau}_L$ are the Pauli matrices (infinitesimal generators of the SU(2) group with subscript L to indicate that they only act on left-chiral fermions);

g' (weak isospin) and g (weak hypercharge) are the U(1) and SU(2) coupling constants respectively;

$W_a^{\mu\nu}$ ($a = 1, 2, 3$) and $B^{\mu\nu}$ are the field strength tensors for the weak isospin and weak hypercharge fields;

Q, u and d are the left-handed doublet, right-handed singlet up and right-handed singlet down quark fields;

L and e are the left-handed doublet and right-handed singlet electron fields.

The field strengths are given by

$$\begin{aligned} W_{\mu\nu}^a &= \partial_{\mu} W_{\nu}^a - \partial_{\nu} W_{\mu}^a + g \epsilon^{abc} W_{\mu}^b W_{\nu}^c, \\ B_{\mu\nu} &= \partial_{\mu} B_{\nu} - \partial_{\nu} B_{\mu}, \end{aligned}$$

and the covariant derivative for the left- and right-handed fermions by,

$$\begin{aligned} D_{\mu} \psi_L &= \left(\partial_{\mu} - i \frac{g}{2} \tau_a W_{\mu}^a - i \frac{g'}{2} Y_W B_{\mu} \right) \psi_L, \\ D_{\mu} \psi_R &= \left(\partial_{\mu} - i \frac{g'}{2} Y_W B_{\mu} \right) \psi_R, \end{aligned}$$

where one simply has to fill in the appropriate weak hypercharge for the corresponding quark and lepton fields.

It is worth noting that no terms are included for fermion masses. These would have the form of $m \bar{\psi} \psi$ but are forbidden as they would break the $SU(2)_L \times U(1)$ gauge invariance. Neither is it possible to add explicit mass terms for the U(1) and SU(2) gauge fields.

*The weak hypercharge follows the relation $Y_W = 2(Q - T_3)$ where Q is the electric charge and T_W the third component of the weak isospin.

1.3.3 Brout-Englert-Higgs mechanism

To come to a viable description of the elementary particles one is required to introduce masses into a chiral theory. The masses of the W and Z bosons are explained by the use of the Brout-Englert-Higgs (BEH) mechanism formulation. Introducing one or more scalar fields, the Higgs fields, which can acquire a vacuum expectation value, make it possible to spontaneously break a symmetry in the Lagrangian. We say that electroweak symmetry is broken down to electromagnetism. According to the Goldstone theorem, every spontaneously broken continuous symmetry results in a massless scalar particle: the Goldstone boson. Hence, the number of Goldstone bosons in a theory is equal to the number of broken generators of the symmetry group.

Since the electroweak theory after symmetry breaking should contain three massive gauge bosons (W^+ , W^- and Z), the scalar fields of the Higgs fields should contain at least three degrees of freedom. The simplest approach to do this is by introducing a complex, scalar $SU(2)$ doublet Φ with positive hypercharge ($Y_W = 1$),

$$\Phi = \begin{pmatrix} \phi^+ \\ \phi^0 \end{pmatrix} = \frac{1}{\sqrt{2}} \begin{pmatrix} \phi_1 + i\phi_2 \\ \phi_3 + i\phi_4 \end{pmatrix}, \quad (1.5)$$

Similar to the $SU(2)$ symmetry of the EW theory, four new gauge particles are introduced: H^+ , H^- , H^0 and H .

Massive bosons

Having introduced this scalar doublet, one needs to add the corresponding Lagrangian term to the electroweak Lagrangian from Eq. 1.4,

$$\mathcal{L}_S = (D^\mu \Phi)^\dagger (D_\mu \Phi) - V(\Phi), \quad \text{with } V(\Phi) = \mu^2 \Phi^\dagger \Phi + \lambda (\Phi^\dagger \Phi)^2. \quad (1.6)$$

The first term is the kinetic term while the second corresponds to the potential of the scalar field*. The quartic term in the potential needs to be positive to ensure an absolute minimum in the Lagrangian. The quadratic term can either be positive or negative, depending if $\mu^2 > 0$ or $\mu^2 < 0$. This is illustrated in Fig. 1.2. In the former case the scalar potential has an absolute minimum at the origin:

$$\langle 0 | \Phi | 0 \rangle \equiv \Phi_0 = \begin{pmatrix} 0 \\ 0 \end{pmatrix}. \quad (1.7)$$

From Eq. 1.6 and 1.7, one can see that the kinetic term does not give rise to massive particles in this scenario†. In the case of $\mu^2 < 0$, the minimum is no longer located at the origin of the fields: $\partial_{|\Phi|} V(|\Phi|) = 0$ for $|\Phi| = \sqrt{-\frac{\mu^2}{2\lambda}}$, hence one possible solution is‡

$$\langle 0 | \Phi | 0 \rangle \equiv \Phi_0 = \begin{pmatrix} 0 \\ \frac{v}{\sqrt{2}} \end{pmatrix}, \quad \text{with } v = \sqrt{-\frac{\mu^2}{\lambda}}. \quad (1.8)$$

v is referred to as the *vacuum expectation value* to reflect that the Higgs field is always “on”. To investigate the terms, we can expand the field around the minimum:

$$\Phi(x) = \begin{pmatrix} \theta_2(x) + i\theta_1(x) \\ \frac{v+H(x)}{\sqrt{2}} - i\theta_3(x) \end{pmatrix} = e^{i\theta_a \tau_a} \begin{pmatrix} 0 \\ \frac{v+H(x)}{\sqrt{2}} \end{pmatrix}. \quad (1.9)$$

Implementing this into Eq. 1.6 would yield the existence of unphysical fields $\phi_{1,2,3}$ that give rise to three extra degrees of freedom that were not present in the original Lagrangian§. Since a

*The form of the potential is not known from first principles, but is the simplest form that can explain the spontaneous symmetry breaking mechanism.

†Easy to see when substituting $v = 0$ in Eq. 1.13.

‡It is not possible for the charged part of the fields to have a vacuum expectation value as this would not be in agreement with electromagnetism. The upper part in Eq. 1.8 is therefore set to zero.

§In Eq. 1.6, the vector fields are massless and each give rise to 2 d.o.f. The vev would make the three vector fields massive, thus adding 3 d.o.f. and introduce three unphysical fields.

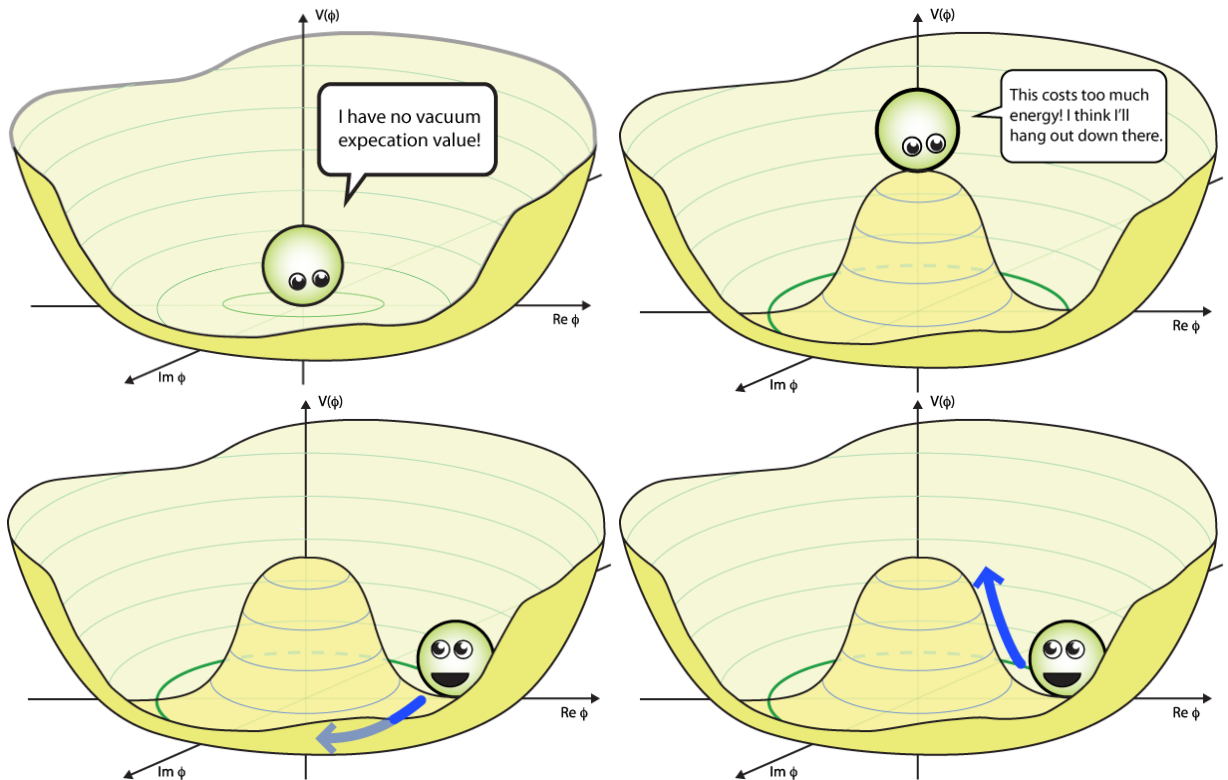


Figure 1.2: In this example the Higgs potential is illustrated in function of a complex scalar field (2D). The principal is the same for a complex scalar doublet but a lot harder to visualize. *Top left:* the Higgs potential with $\mu^2 > 0$, there is no vacuum expectation value. *Top right:* $\mu^2 < 0$, the origin is now a maximum and not stable; the scalar field will move to the lowest possible energy state. *Bottom left:* a flat direction in the potential corresponds to a massless Goldstone mode (remember there are two extra scalar fields in the full theory, meaning there are a total of three). *Bottom right:* the concave shape of the potential near the minimum defines the Higgs boson mass. Illustrations from Ref. [11].

change of variables cannot alter the number of d.o.f. of a system, one can conclude that three fields do not represent physical fields. They can be removed by fixing a gauge, the unitary gauge, that breaks the original symmetry of the system!

$$\Phi(x) \rightarrow e^{-i\theta_a \tau_a} \Phi(x) = \begin{pmatrix} 0 \\ v+H(x) \\ \sqrt{2} \end{pmatrix}, \quad (1.10)$$

where we have introduced a new scalar field $H(x)$. After inserting this in the kinetic part of the scalar Lagrangian (Eq. 1.6) and redefining the gauge fields as

$$\begin{aligned} W_\mu^\pm &= \frac{1}{\sqrt{2}} (W_\mu^1 \mp iW_\mu^2), \\ Z_\mu &= \frac{1}{\sqrt{g^2 + g'^2}} (gW_\mu^3 - g'B_\mu), \\ A_\mu &= \frac{1}{\sqrt{g^2 + g'^2}} (gW_\mu^3 + g'B_\mu), \end{aligned} \quad (1.11)$$

we find for the kinetic part of the scalar Lagrangian:

$$|D_\mu \Phi|^2 = \frac{1}{2} (\partial_\mu H)^2 + \frac{1}{2} g^2 (v + H)^2 W_\mu^+ W^{-\mu} + \frac{1}{8} (v + H)^2 (g^2 + g'^2) Z_\mu Z^\mu. \quad (1.12)$$

Since mass terms enter this equation in the general form of $M_W^2 W_\mu W^\mu$ for the W bosons and $\frac{1}{2} M_Z^2 Z_\mu Z^\mu$ for the Z boson, the mass terms of the gauge bosons after spontaneous symmetry breaking can be written down as:

$$\begin{aligned} M_W &= \frac{1}{2} vg, \\ M_Z &= \frac{1}{2} v \sqrt{g^2 + g'^2}, \\ M_A &= 0, \end{aligned} \quad (1.13)$$

where it is clear that the photon remains massless*.

Corollary 1.3.1 — Eating the gauge bosons. A vev can give rise to massless Goldstone bosons. These particles correspond to the infinite possibilities of its phase in the potential. However, this would also lead to extra degrees of freedom in the Lagrangian. Therefore, one has to fix a gauge that results in the disappearance of the bosons and making the vector bosons of the original fields massive.

Specifically, the two massless W^1, W^2 bosons in the electroweak theory (2×2 polarizations^a = 4 d.o.f.) and two charged Higgses (2 d.o.f.) sum to a total of six degrees of freedom. In the broken theory, we have two massive W^+, W^- bosons (2×3 polarizations), which again total to six degrees of freedom.

Similarly, the W^3, B (2×2 d.o.f.) and H^0 (2 d.o.f.) combine into the neutral Z (massive, 3 d.o.f.), the γ (2 d.o.f.) and the scalar H (1 d.o.f.).

Similar to the nucleons having a mass that is much greater than the summed mass of its constituents, the Higgs fields gives rise to the mass of these gauge bosons. In the case of nucleons, it is primarily the potential energy of the strong force that is responsible for the total mass following $E = mc^2$. The coupling of the gauge bosons to the Higgs field gives a sense of inertia to the particle. The particle does not float freely in vacuum but interacts with the ever present Higgs field (with a vev $\neq 0$) making it massive.

*A massless particle cannot have a third polarization, similar to a photon: it is traveling at the speed of

^aBecause the W and Z bosons are massive, it costs energy to produce them and so the weak force is only really effective over a short distance. This is in contrast to the massless photons that result into a long range electromagnetic force. Thus, the Higgs field is responsible for the “weakness” of the weak force.

light so it cannot have a polarization in the direction of propagation, only longitudinal.

Using the potential term in Eq. 1.6 together with the vev in Eq. 1.10, we find for the Lagrangian of the Higgs boson

$$\mathcal{L}_H = \frac{1}{2} (\partial_\mu H) (\partial^\mu H) - \lambda v^2 H^2 - \lambda v H^3 - \frac{\lambda}{4} H^4. \quad (1.14)$$

The first term again corresponds to the kinetic term, whereas the third and forth refer to the three- and four-point self-interactions of the Higgs respectively. Scalar masses have the general form $\frac{1}{2} m\phi^2$; the Higgs boson mass is thus equal to

$$m_H = 2\lambda v^2 = -2\mu^2, \quad (1.15)$$

and needs to be determined experimentally.

Working through the interaction terms of the Lagrangian, one can show that the electric charge e is related to the couplings of the weak isospin g and hypercharge g' .

$$e = g \sin \theta_W = g' \cos \theta_W, \quad (1.16)$$

where the Weinberg angle is denoted as θ_W and indicates the magnitude of rotation of the boson fields after spontaneous symmetry breaking:

$$\begin{pmatrix} \gamma \\ Z \end{pmatrix} = \begin{pmatrix} \cos \theta_W & \sin \theta_W \\ -\sin \theta_W & \cos \theta_W \end{pmatrix} \begin{pmatrix} B^0 \\ W^0 \end{pmatrix}, \quad (1.17)$$

and is related to the weak isospin and hypercharge:

$$\cos \theta_W = \frac{g}{\sqrt{g^2 + g'^2}} \quad \text{and} \quad \sin \theta_W = \frac{g'}{\sqrt{g^2 + g'^2}}. \quad (1.18)$$

Massive fermions

A term like $-m\bar{\psi}\psi = -m [\bar{\psi}_L\psi_R + \bar{\psi}_R\psi_L]$, where we have decomposed the equation into the left- and right-handed chiral states* is not gauge invariant in the Lagrangian. The left-handed fermions form an isospin *doublet* and the right-handed fermions form isospin *singlets*. They transform differently under $SU(2)_L \times U(1)_Y$:

$$\begin{aligned} \chi_L &\rightarrow \chi'_L = \chi_L e^{i\tau_L^3 \vec{W} + i\alpha Y_W}, \\ \psi_R &\rightarrow \psi'_R = \psi_R e^{i\alpha Y_W}. \end{aligned} \quad (1.19)$$

It is possible for the fields to couple to the complex Higgs doublet, defined in Eq. 1.5, by adding Yukawa couplings. This results into terms that are singlets under $SU(2)_L$ and $U(1)_Y$:

$$\mathcal{L}_{Yuk} = \lambda_e \overline{L} \Phi e_R - \lambda_d \overline{Q} \Phi d_R - \lambda_u \overline{Q} \tilde{\Phi} u_R + h.c., \quad (1.20)$$

where we have introduced the conjugate of Φ , $\tilde{\Phi} = i\tau_2 \Phi^*$, which has a negative hypercharge. After spontaneous symmetry breaking (Eq. 1.10), we find:

$$\begin{aligned} L_{Yuk} &= -\frac{1}{\sqrt{2}} \lambda_e (\bar{\nu}_e, \bar{e}_L) \begin{pmatrix} 0 \\ v + H(x) \end{pmatrix} e_R + \dots \\ &= -\frac{1}{\sqrt{2}} \lambda_e (v + H(x)) \bar{e}_L e_R + \dots, \end{aligned} \quad (1.21)$$

where we highlighted only the electron part. Fermion mass terms have the general form $m_f \bar{f}_L f_R + h.c.$. Therefore, one finds:

$$m_e = \frac{\lambda_e v}{\sqrt{2}}, \quad m_u = \frac{\lambda_u v}{\sqrt{2}}, \quad m_d = \frac{\lambda_d v}{\sqrt{2}}. \quad (1.22)$$

* $\psi_L = P_L \psi = \frac{1-\gamma^5}{2} \psi$ and $\psi_R = P_R \psi = \frac{1+\gamma^5}{2} \psi$

The mass of the fermions is again not predicted as the Yukawa coupling parameters are free parameters.

1.3.4 Particle mixing

In Eq. 1.20, we introduced Yukawa coupling constants to explain the mass of fermions. In its most general realizations, these couplings are not constants but matrices. This will introduce possible mixing of *flavor eigenstates* into different *mass eigenstates*. Let us write out the second term in Eq. 1.20:

$$\begin{aligned} \lambda_d \overline{Q_L} \Phi d_R &= \Lambda_{ij}^d \overline{Q_{Li}^I} \Phi d_{Rj}^I = \Lambda_{ij}^d (\text{up-type down-type})_{Li}^I \begin{pmatrix} \phi^+ \\ \phi^0 \end{pmatrix} (\text{down-type})_{Rj}^I \\ &= \begin{pmatrix} \Lambda_{11} \overline{(u\ d)_L^I} \begin{pmatrix} \phi^+ \\ \phi^0 \end{pmatrix} & \Lambda_{12} \overline{(u\ d)_L^I} \begin{pmatrix} \phi^+ \\ \phi^0 \end{pmatrix} & \Lambda_{13} \overline{(u\ d)_L^I} \begin{pmatrix} \phi^+ \\ \phi^0 \end{pmatrix} \\ \Lambda_{21} \overline{(c\ s)_L^I} \begin{pmatrix} \phi^+ \\ \phi^0 \end{pmatrix} & \Lambda_{22} \overline{(c\ s)_L^I} \begin{pmatrix} \phi^+ \\ \phi^0 \end{pmatrix} & \Lambda_{23} \overline{(c\ s)_L^I} \begin{pmatrix} \phi^+ \\ \phi^0 \end{pmatrix} \\ \Lambda_{31} \overline{(t\ b)_L^I} \begin{pmatrix} \phi^+ \\ \phi^0 \end{pmatrix} & \Lambda_{32} \overline{(t\ b)_L^I} \begin{pmatrix} \phi^+ \\ \phi^0 \end{pmatrix} & \Lambda_{33} \overline{(t\ b)_L^I} \begin{pmatrix} \phi^+ \\ \phi^0 \end{pmatrix} \end{pmatrix} \cdot \begin{pmatrix} d_R^I \\ s_R^I \\ b_R^I \end{pmatrix}, \end{aligned} \quad (1.23)$$

where the superscript I implies that the fermion fields are expressed in the *interaction (flavor)* basis. The subscript i stands for the three generations.

This means that after symmetry breaking the quark mass terms break down into

$$\begin{aligned} -\mathcal{L}_{Yuk}^{\text{quarks}} &= \Lambda_{ij}^d \overline{d_{Li}^I} \frac{v}{\sqrt{2}} d_{Rj}^I + \Lambda_{ij}^u \overline{u_{Li}^I} \frac{v}{\sqrt{2}} u_{Rj}^I + \dots \\ &= M_{ij}^d \overline{d_{Li}^I} d_{Rj}^I + M_{ij}^u \overline{u_{Li}^I} u_{Rj}^I + \dots \end{aligned} \quad (1.24)$$

where we have omitted the hermitian conjugate terms and the Higgs field interaction terms. Note that the u - and d -terms in the equation still each represent the three up- and down-type quarks respectively. There is mixing between the flavor fields as there is no reason why the matrix M should be diagonal*.

To obtain proper mass terms, one has to diagonalize the mass matrices M^u and M^d and find proper eigenstates. We introduce unitary matrices V as follows

$$\begin{aligned} M_{\text{diag}}^d &= V_L^d M^d V_R^{d\dagger}, \\ M_{\text{diag}}^u &= V_L^u M^u V_R^{u\dagger}, \end{aligned} \quad (1.25)$$

which can be done when the matrices V are unitary ($V_L^{d,u\dagger} V_L^{d,u} = \mathbb{1}$). Eq. 1.24 can now be expressed as follows:

$$\begin{aligned} -\mathcal{L}_{Yuk}^{\text{quarks}} &= \overline{d_{Li}^I} M_{ij}^d d_{Rj}^I + \overline{u_{Li}^I} M_{ij}^u u_{Rj}^I + \dots \\ &= \overline{d_{Li}^I} V_L^{d\dagger} V_L^d M_{ij}^d V_R^d V_R^{d\dagger} d_{Rj}^I + \overline{u_{Li}^I} V_L^{u\dagger} V_L^u M_{ij}^u V_R^u V_R^{u\dagger} u_{Rj}^I + \dots \\ &= \overline{d_{Li}^I} \left(M_{ij}^d \right)_{\text{diag}} d_{Rj}^I + \overline{u_{Li}^I} \left(M_{ij}^u \right)_{\text{diag}} u_{Rj}^I + \dots \end{aligned} \quad (1.26)$$

,

where the V matrices have been absorbed in the quark flavor eigenstates and have formed mass eigenstates. These mass eigenstates, which are the eigenstates one sees in experiments, couple

*The question and answer of flavor/mass mixing can be put as: Q: “Why is there mixing?”; A: “Because it can.”

differently to the gauge fields of the weak interaction. Working out one term from Eq. 1.4, the mixing of the flavor eigenstates is clearly visible

$$\begin{aligned}\mathcal{L}_{kinetic}(Q_L) &= i\overline{Q_{Li}^I}\gamma_\mu D^\mu Q_{Li}^I \\ &= \frac{g}{\sqrt{2}}\overline{u_{Li}^I}\gamma_\mu W^{-\mu}d_{Li}^I + \frac{g}{\sqrt{2}}\overline{d_{Li}^I}\gamma_\mu W^{+\mu}u_{Li}^I + \dots \\ &= \frac{g}{\sqrt{2}}\overline{u_{Li}}(V_L^u V_L^{d\dagger})_{ij}\gamma_\mu W^{-\mu}d_{Lj} + \frac{g}{\sqrt{2}}\overline{d_{Li}}(V_L^d V_L^{u\dagger})_{ij}\gamma_\mu W^{+\mu}u_{Lj} + \dots\end{aligned}\quad (1.27)$$

The combination of matrices $(V_L^d V_L^{u\dagger})_{ij}$, a unitary 3×3 matrix is known as the *Cabibbo-Kobayashi-Maskawa (CKM)* mixing matrix. By convention, the interaction and flavor eigenstates of the up-type quarks are chosen to be equal. The down-type quarks are therefore chosen to be rotated:

$$\begin{aligned}u_i^I &= u_i, \\ d_i^I &= V_{CKM}d_i,\end{aligned}\quad (1.28)$$

or explicitly:

$$\begin{pmatrix} d^I \\ s^I \\ b^I \end{pmatrix} = \begin{pmatrix} V_{ud} & V_{us} & V_{ub} \\ V_{cd} & V_{cs} & V_{cb} \\ V_{td} & V_{ts} & V_{tb} \end{pmatrix} \begin{pmatrix} d \\ s \\ b \end{pmatrix}. \quad (1.29)$$

Because the choice of the global phases of the quark fields is arbitrary and the matrix is unitary, the nine unknown complex elements can be reduced to three real numbers and one phase*. The matrix is most often written as:

$$V_{CKM} = \begin{pmatrix} c_{12}c_{13} & s_{12}c_{13} & s_{13}e^{-i\delta} \\ -s_{12}c_{23} - c_{12}s_{23}s_{13}e^{i\delta} & c_{12}c_{23} - s_{12}s_{23}s_{13}e^{i\delta} & s_{23}c_{13} \\ s_{12}s_{23} - c_{12}c_{23}s_{13}e^{i\delta} & -c_{12}s_{23} - s_{12}c_{23}s_{13}e^{i\delta} & c_{23}c_{13} \end{pmatrix}, \quad (1.30)$$

where $c_{ij} = \cos(\theta_{ij})$ and $s_{ij} = \sin(\theta_{ij})$ for $i < j = 1, 2, 3$ and δ is the *CP*-violating phase.

The mixing of the flavor quantum states is necessary to explain charged current interactions changing the strangeness with one [12] and *CP*-violating processes [13].

Without going into detail, it is worth noting that a similar matrix exists that connects the lepton flavor and mass eigenstates. In contrast to the quarks, the down-type interaction doublet states are chosen to be the same as the mass eigenstates. The mixing of the mass and interaction eigenstates is in the neutrino sector. This matrix is known as the Pontecorvo-Maki-Nakagawa-Sakata (PMNS) matrix [14],

$$\mathcal{U} = \begin{pmatrix} 1 & 0 & 0 \\ 0 & c_{23} & s_{23} \\ 0 & -s_{23} & c_{23} \end{pmatrix} \begin{pmatrix} c_{13} & 0 & s_{13}e^{-i\delta} \\ 0 & 1 & 0 \\ s_{13}e^{-i\delta} & 0 & c_{13} \end{pmatrix} \begin{pmatrix} c_{12} & s_{12} & 0 \\ -s_{12} & c_{12} & 0 \\ 0 & 0 & 1 \end{pmatrix} \cdot \text{diag}(e^{i\alpha_1/2}, e^{i\alpha_2/2}, 2). \quad (1.31)$$

1.4 A success story

Over the course of multiple decades, the Standard Model was built up into an extremely comprehensive theory. The first building blocks necessary for its construction came from experiments in the early 19th century when its quantum characteristics became more apparent. The theory was formulated as a gauge theory in the 1960s and 1970s and for decades it has been rigorously tested and checked, leading to extremely accurate experimental precision measurements that agree with the theory. Apart from precision measurements it has led to predictions of particles and their interactions, which could only be tested years or decades after they were first proposed. In the following, we give a brief overview of some astonishing experimental results.

*This phase is responsible for *CP-violation*.

1.4.1 Wave-particle duality

One of the most striking features of the SM is that particles may be partly described in terms of not only particles, but also of waves. The classical concepts of “particles” or “waves” is insufficient in describing the behaviour of quantum-scale objects. In the late 18th and early 19th century, physicist were puzzled by the successful approaches to well known problems of electromagnetic phenomena, which were widely accepted as fields, with quantizations (particles). Black body radiation and the photoelectric effect are described below. In quantum field theory, particles are defined as excited states of a field. The wave-nature is evident in the calculated *probability distributions* for a given reaction.

1.4.1.1 Photoelectric effect

At the close of the 19th century, J.J. Thomson found that electricity is caused by *particles* that can fly through vacuum. But, since electromagnetism was known to be a wave that is generated by a changing electric or magnetic *field*, a particle description of electricity and charge was, in a way, flawed by construction. A first step towards quantization came when the ultraviolet catastrophe seemed to be solved if black-body radiation is not explained by the classical equipartition theorem (Appendix B), but a quantization of the electromagnetic field: Planck’s law. Planck denounced these particles of light as a limitation of his approximation, not a property of reality. It was only later, when Einstein combined this theory with the photoelectric effect, that light quanta/photons became more accepted.

The photoelectric effect describes that when a material is shined upon by light, electrons or other free carriers can be emitted. In a classical theory perspective, an alteration in the intensity of light would induce changes in the kinetic energy of the particles emitted from the material. Instead, these particles are dislodged only by the impingement of photons when those photons reach or exceed a threshold frequency/energy. Changing the intensity of the light bundle only changes the amount of particles released, but does not alter its kinetic energy. This is easy to explain in a quantum view and resulted in the Einstein’s Nobel Prize in 1921.

1.4.1.2 Double-slit experiment

The double-slit experiment was first performed by Thomas Young in the early 19th century. If a beam of light shines through two slits of a screen onto a second screen behind the first, an interference pattern can be seen as illustrated in Fig. 1.3. This proved the wavelike nature of light.

In later years, similar experiments for electrons were done to prove the wavelike properties of particles [17, 18]. The same double-slit experiment was finally performed in the 60s [19] and for single electrons in 1974 [20]. Single photon [16] (shown in Fig. 1.3) and single electron double-slit experiments show the same results, illustrating the wave probability interpretation of particles and fields.

1.4.2 Predictions

By 1932, scientists knew that atoms were made up by protons, neutrons and electrons. Together with the photon, a total number of four particles were known. Four grew to five when Anderson discovered the existence of positrons [21] (predicted by Dirac [22]). Then came the pion [23] and muon [24]. By the 1960s, there were hundreds of “fundamental particles” with no good guiding principles to link them together. They were often referred to as the “particle zoo”.

By a series of insights by several individuals, the Standard Model as a quantum field theory became more widely accepted. Since then, the model has predicted the results of experiment after experiment. Some of them are:

- Neutral weak currents. Postulated by A. Salam, S. Weinberg and S. Glashow, the theory of electroweak interactions predicted the existence of a new type of weak interaction, in which the reacting particles do not change their charges. The first observation was made in 1973 at the European nuclear research laboratory, CERN.
- Weak gauge bosons. Again postulated by the abovementioned people. These particles were also discovered in CERN, 1984.

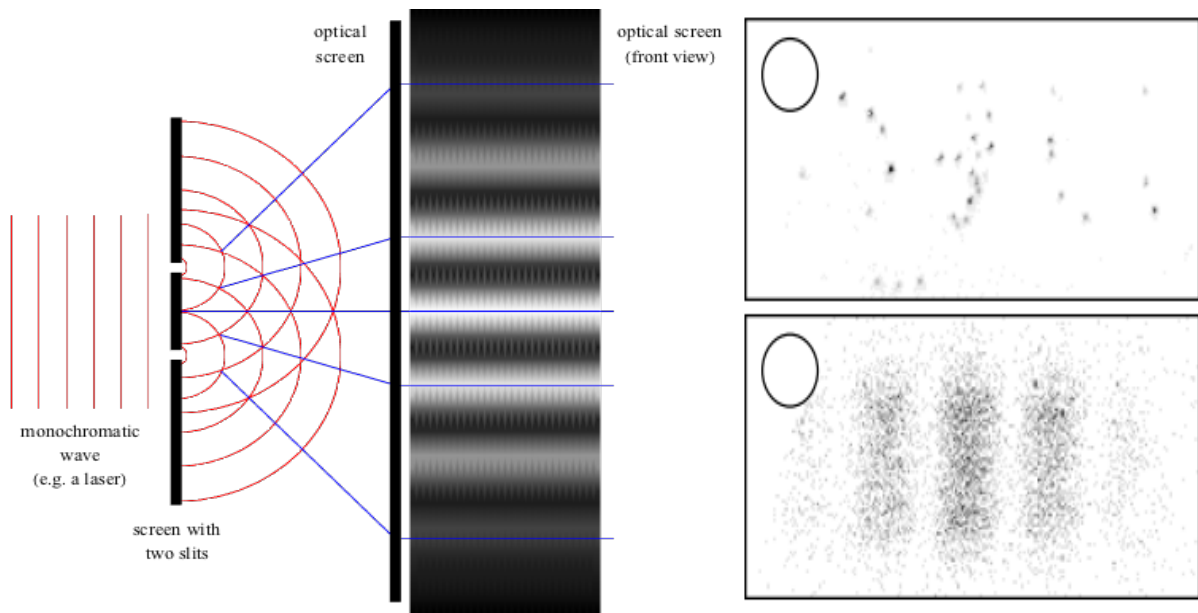


Figure 1.3: *Left:* Schematic view of interference pattern as in Young’s experiment [15]. *Right:* (top) a single 20 ms time frame showing several individual photon arrival points; (bottom) image obtained after integrating for a few seconds: the diffraction pattern emerges [16].

- Heavy quarks. To explain the *CP*-violations in kaon decays, M. Kobayashi and T. Maskawa predicted the existence of a third generation of quarks: the *top* and *bottom* quarks. The bottom quark was discovered in 1977 at Fermilab [25]. It took another 18 years for the top quark to be found in the same institute [26].
- Gluons. The gauge bosons of quantum chromodynamics were discovered in 1978 and 1979 [27].
- Higgs boson. On July 4, 2012, physicists at CERN announced the discovery of the only fundamental particle predicted by the Standard Model that was not yet discovered.

1.4.3 Precision tests

Inconsistencies between experiment and theory can be signs of wrong or incomplete theories. Below, a small subset of many precision tests is given:

- *Lamb shift*, a difference in energy between two energy levels of the hydrogen atom that was not predicted by the Dirac equation. This phenomenon is explained with the theory of QED. [REF](#).
- *Andere goede voorbeelden? Precision measurements in IceCube? vb: Neutrino cross-section: IceCube/Nature <https://www.nature.com/articles/nature24459>*

Because of this, experimentalists are continuously testing theoretical parameters of the Standard Model. These precision tests are most often done for the theory of QED. With the use of *renormalization theory*, many parameters of the theory can be calculated in great detail. High-precision measurements of various observables have been performed at LEP 1 and SLC [28, 29, 30, 31, 32, 33] for physics at the Z-boson mass ($\sqrt{s} \approx M_Z$) and other observables at Tevatron [34, 35], LEP 2[35], ATLAS[36, 37] and CMS[38, 39]. Some of them are listed in Table 1.2. From this it is clear that the SM is very consistent with what we see in experiments.

1.5 The need for physics beyond the Standard Model

Despite its incredible success, many physicists believe the Standard Model is certainly not the full story. There are a number of features that seem arbitrary, but also some that cannot be explained by the theory alone. Below, I give a list of open questions:

- Why are there **three families** for both leptons and quarks? Why not two? Or four? Or a thousand even?

Table 1.2: Observables compared with the SM best fit predictions. Errors are the total (experimental plus theoretical) uncertainties. Results are taken from Tables 10.4 and 10.5 in [40].

Parameter	Experimental value	Theoretical value	Standard deviation
m_t [GeV]	172.74 ± 0.46	172.96 ± 0.45	-0.5
m_W [GeV]	80.387 ± 0.016	80.358 ± 0.004	1.8
	80.376 ± 0.033		0.6
	80.370 ± 0.019		0.6
	2.046 ± 0.049		-0.9
Γ_W [GeV]	2.195 ± 0.083	2.089 ± 0.001	1.3
	125.14 ± 0.15		0.0
$g_V^{\nu e}$	-0.040 ± 0.015	-0.0398 ± 0.0001	0.0
$g_A^{\nu e}$	-0.507 ± 0.014	-0.5063	0.0
τ_τ [fs]	290.75 ± 0.36	290.39 ± 2.17	0.1
$\frac{1}{2}(g_\mu - 2 - \frac{\alpha}{\pi})$	$(4511.18 \pm 0.77) \times 10^{-9}$	$(4508.63 \pm 0.03) \times 10^{-9}$	3.3
M_Z [GeV]	91.1876 ± 0.0021	91.1884 ± 0.0020	-0.4
Γ_Z [GeV]	2.4952 ± 0.0023	2.4942 ± 0.0008	0.4
$\Gamma_Z(\text{had})$ [GeV]	1.7444 ± 0.0020	1.7411 ± 0.0008	-
$\Gamma_Z(\text{inv})$ [MeV]	499.0 ± 1.5	501.44 ± 0.04	-
$\Gamma_Z(l^+l^-)$ [MeV]	83.984 ± 0.086	83.959 ± 0.008	-

- What is the **cause of the symmetries** we see in the Standard Model. Why is, for example, QCD not an SU(4) gauge theory?
- There are a number of **parameters** in the SM that cannot be explained by first principles. We have no good explanation why the top quark is 75 000 times heavier than the up quark. Why is the vev of the Higgs potential 246 GeV? Why is the Higgs mass 125 GeV? There are in total 19 parameters in the SM that are tuned by experiments and can be found in Table 1.3.
- Why does the Higgs potential have this **Mexican hat shape**? In other words, why is μ^2 in $\lambda (\Phi^\dagger \Phi)^2 + \mu^2 (\Phi^\dagger \Phi)$ negative? Also, the vev, the mass of the Higgs boson and the mass of the fermions due to the Yukawa couplings all appear in Table 1.3. This makes us believe there is something we do not fully understand about the BEH mechanism.
- Right-handed neutrinos can be introduced into the SM. They are singlets with respect to the strong and weak interaction and would therefore not carry an electric charge, weak hypercharge or weak isospin. Due to this lack of charge, right-handed neutrinos would be extremely difficult to detect. They have Yukawa interactions with other leptons and the Higgs boson, but its coupling would be extremely small. Neutrinos can become massive with Dirac mass terms in the same way charged leptons become massive in the BEH mechanism. Their **extremely small masses** suggest another mechanism in which the very light left-handed neutrinos are accompanied with extremely heavy right-handed neutrinos. This mechanism is called the Seesaw mechanism and requires the addition of Majorana mass terms*.

Aside from these, there are a number of unexplained phenomena that probably cannot be explained in a simple extension of the Standard Model but need a non-trivial approach. For example:

- It is a natural assumption that the universe is neutral with all conserved charges. Both the SM and general relativity give no explanation on the **matter-antimatter imbalance** we see in the universe. The Big Bang was expected to produce equal amounts of matter and anti-matter, yet we see that the observable universe consists almost exclusively out

*Oscillation of the massive neutrinos is described in the PMNS matrix and adds 7 new parameters to the SM: the three mass terms $m_{\nu_1}, m_{\nu_2}, m_{\nu_3}$, the mixing angles θ_{12}, θ_{13} and θ_{23} and the CP -violating phase δ_{CP} .

of baryonic matter*. The most likely explanation is that in the early universe physical laws we know today were absent or have acted differently. The observed CP -violation is insufficient to account for the observed baryon asymmetry of the universe given the limits on baryon number violation.

- The stars, planets, interstellar clouds, etc. we see in space consist of baryonic matter. Assuming general relativity is the correct theory to describe gravity on cosmological scales, the Lambda-CDM model predicts that the matter we see is only around 15% of the total matter present in our visible universe [41]. To explain the galaxy rotation curves [42], galaxy velocity dispersions [43], galaxy cluster masses [44], gravitational lensing [45], and many more, it is predicted that around 85% of the mass is not yet observed. This matter is referred to as **dark matter** as it cannot interact electromagnetically because it would have already been observed otherwise. No known particles in the SM can explain this phenomenon.
- Similar to dark matter, the Lambda-CDM model predicts that the total energy in the visible universe should consist mostly out of a constant energy density for the vacuum called **dark energy**. 5% of the total energy consists of baryonic matter, 26% should be dark matter and the remaining 69% of dark energy is necessary to explain the expansion of the universe[†].
- General relativity is generally accepted to describe gravity on cosmological scales. Thusfar, it has not been possible to describe **gravity** on a quantum scale as is the case for the Standard Model and still be valid on very large scales. The inclusion of the graviton would for example not recreate what is observed experimentally without other modifications to the SM, which have not been observed. Contradictory to popular belief, it is not true that general relativity and quantum mechanics are incompatible. There is a need for a more complete theory beyond the range of their combined applicability [47].
- Why is the CP -violation in the strong interaction extremely small or even zero?
- Often referred to as a muon g-2 anomaly there are possible hints of new physics as the theoretical prediction of magnetic moment of the muon and experimental values have a small but significant offset [48].
- Why is there much more mixing in the lepton sector (PMNS) compared to the quark sector (CKM)?
- To explain the apparent quantum fluctuations on cosmological scales together with the horizon [REF](#), flatness [REF](#) and magnetic monopole [REF](#) problems we have a theory of exponential expansion of space in the early universe: **cosmic inflation**. The theory states that between 10^{-36} and 10^{-32} seconds after the Big Bang a rapid exponential expansion happened. This could explain the apparent thermal equilibrium between parts of the visible universe that are not in causal contact with each other and the even distribution of the cosmic microwave background. The hypothetical field that is thought to be responsible for inflation, inflaton, is not yet observed and would be an extension of the Standard Model.
- With the use of renormalization theory, it is possible to show that bare parameters should not be the same as parameters measured in experiments. These parameters, as the mass of particles, depends on the energy scale at which they are probed and physics far beyond the scope of the probed energy scale can influence these parameters. An example is the screening effect that is described in more detail in Section 1.5.1. Similarly, one-loop corrections to the Higgs boson mass[‡] will have radiative corrections with a quadratic dependence on the cutoff scale. Virtual particles in one-loop corrections can have infinite momenta that should

*Why are there protons, neutrons and electrons everywhere while it is perfectly possible for antiprotons and antineutrons to form atomic nuclei with positrons?

[†]If there is only matter and the Big Bang acceleration only happened in the beginning of the creation of the universe, then one would expect the expansion to diminish due to the gravitational pull of matter. Measurements say the opposite is true: the universe is expanding and in an accelerating rate. This was famously first described by E. Hubble [46].

[‡]Fermions and bosons are not effected by higher energy physics in the same way as a scalar particle is. There is a logarithmic dependence.

Table 1.3: The 19 free parameters in the Standard Model that have to be measured experimentally. If one wants to include neutrino masses and the PMNS mixing angle, 7 new parameters have to be added: $m_{\nu_1}, m_{\nu_2}, m_{\nu_3}$, the mixing angles θ_{12}, θ_{13} and θ_{23} and the CP -violating phase δ_{CP} .

Parameter	Description	Value
m_e	Electron mass	511 keV
m_μ	Muon mass	105.7 MeV
m_τ	Tau mass	1.78 GeV
m_u	Up quark mass	1.9 MeV
m_d	Down quark mass	4.4 MeV
m_c	Charm quark mass	1.32 GeV
m_s	Strange quark mass	87 MeV
m_t	Top quark mass	173.5 GeV
m_b	Bottom quark mass	4.24 GeV
θ_{12}	CKM 12-mixing angle	13.1°
θ_{23}	CKM 23-mixing angle	2.4°
θ_{13}	CKM 13-mixing angle	0.2°
δ_{CP}	CKM CP violation phase	0.995
g_1 or g'	U(1) gauge coupling	0.357
g_2 or g	SU(2) gauge coupling	0.652
g_3 or g_s	SU(3) gauge coupling	1.221
θ_{QCD}	QCD vacuum angle	≈ 0
v	Higgs vacuum expectation value	246 GeV
m_H	Higgs mass	125 GeV

contribute to the total mass of the Higgs boson. Since we expect new physics to be present at energies close to the Planck mass ($\approx 10^{18}$ GeV), these loop corrections should push the Higgs mass to similar energy ranges. But, we see that the Higgs mass is around 125 GeV. This would mean that there are other parameters which should almost *exactly* cancel these absurdly large numbers. This is called *fine-tuning*, and it's the intuition of most physicists that this incredible fine-tuning has a deeper, yet unknown, meaning. This problem is often referred to as the **hierarchy problem**.

Many of these problems can be seen as “environmental”. Why there are three families and why so many parameters in the Standard Model have no fundamental explanation could just be because it's just the way it is. Maybe there is a multiverse, a plethora of universes with similar Standard Models, which have slightly or vastly different parameters. Some questions might even be impossible to answer because of a lack of statistics: we only have one universe and mankind has not been around very long in the timescale of the universe. This consideration might be valid but again not answers all our questions, it does not solve the question around dark matter for example.

This argument should not prevent us in trying to find a more general theory for the Standard Model and general relativity. A better explanation could be fairly simple, but infinitely hard as well. There is only one way in trying to find a better understanding: experiments.

Unification is the most popular approach in describing physics beyond the Standard Model. Unification would mean that well-established theories are low-energy approximations of a more grand unified theory. Historically, this has worked very well: the unification of celestial gravitation of Kepler with terrestrial gravitation of Galileo into universal gravitation and the unification of electricity, magnetism, and later optics into electromagnetism. Gravity was overhauled by the much broader theory of general relativity. Lastly, the birth of gauge theories have combined QED and the weak interaction into the combined electroweak theory. The similarities in QCD and the electroweak theory, both being gauge theories, has led people to believe a unification is possible. This would unify the forces and particles known from the Standard Model into a *Grand Unified*

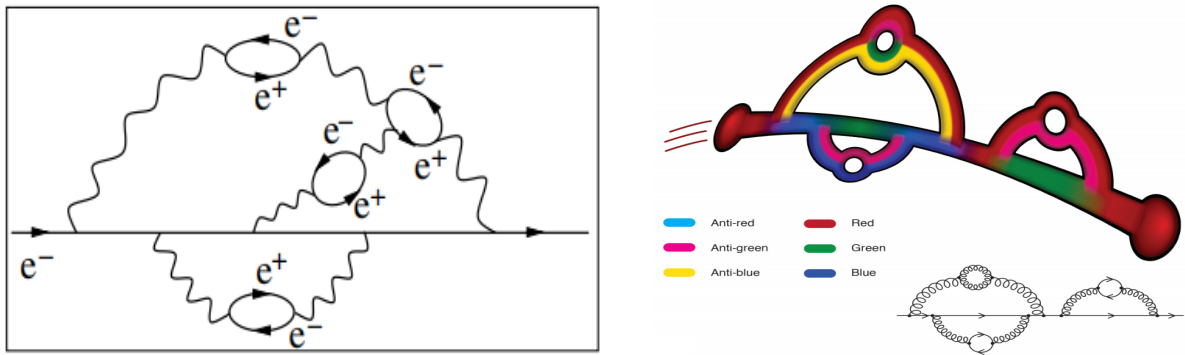


Figure 1.4: *Left:* virtual pairs of positrons and electrons can be produced in vacuum. Positrons are attracted to the bare electron resulting into an apparent lower charge of the bare particles from larger distances. This effect is referred to as *screening*. *Right:* quark and antiquark pairs have a similar screening effect in color charge as the case for electrical charges. There is an anti-screening effect due to gluons that “extract” color from the bare quark and is stronger than the screening effect of quark-antiquark pairs. At small distances, the dilution of the initial color charge is larger than at large distance. This drawing should not be taken literally and the concept of self-interaction is very hard to illustrate. One could interpret the initial red color with a gluon emission as a conservation of the red color, thus the red quark can only become blue if a gluon with a red and anti-blue color is emitted (gluons need to be color+anti-color pairs). In the first, top loop, two gluons are created but cannot have a combined color: anti-green with red (first) and green with anti-blue (second) is possible since green and anti-green have a net zero color charge. Figures from [49].

Theory or GUT. A theory that would add gravity is called a *Theory Of Everything* or TOE.

1.5.1 Running of the coupling constants

The coupling constants in the Standard Model are actually not constants. They depend on the energy of the system. Quantum fluctuations in vacuum have a non-negligible contribution in the apparent charge of particles. The effects of screening and anti-screening are visualized in Fig. 1.4 and can be mathematically formulated as a beta function. The function encodes the dependence of a coupling parameter, g , on the energy scale μ :

$$\beta(g) = \frac{\partial g}{\partial \log(\mu)}. \quad (1.32)$$

More coupling in shorter distances (i.e. higher energies) would give rise to a positive beta function and is the case in QED. In QCD, gluons carry a color charge and enter the beta function with a negative sign

$$\beta(g) = - \left(11 - \frac{2n_f}{3} \right) \frac{g^3}{16\pi^2}, \quad (1.33)$$

with n_f the number of fermions that participate in the strong interaction. This decrease in coupling strength in function of energy scale is called *asymptotic freedom*. Alternatively, we can write down the coupling constants in function of the energy

$$\alpha_i^{-1}(Q) = \alpha_i^{-1}(m_Z) + \frac{b_i}{2\pi} \log \frac{Q}{m_Z}, \quad (1.34)$$

with $b_1 = -\frac{4}{3}n_g - \frac{1}{10}n_h$, $b_2 = \frac{22}{3} - \frac{4}{3}n_g - \frac{1}{6}$ and $b_3 = \frac{11}{-3}$ the U(1), SU(2) and SU(3) constants in which n_g denotes the number of quark and lepton generations and n_h is the number of Higgs doublet fields. These three couplings seem to converge, leading people to believe a more universal theory at higher energies would unify these parameters into one and is shown in Fig. 1.5.

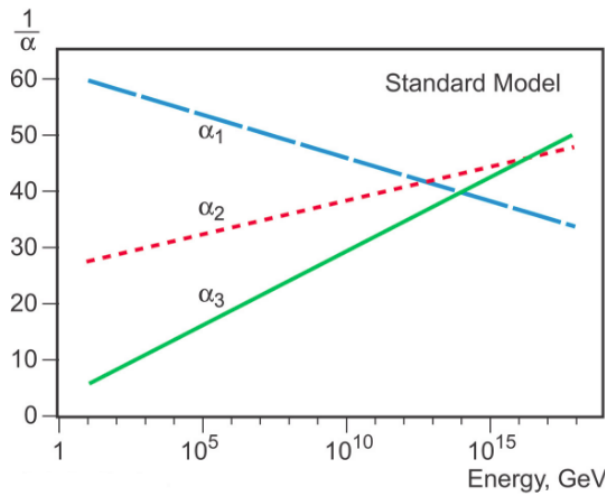


Figure 1.5: Running of the coupling constants in the Standard Model. Figure from [50].

1.5.2 Unifying theories

Linking the seemingly arbitrary parameters in the Standard Model has been ongoing for the last couple of decades. Linking these theories is not easy since they exhibit very different behaviors. Electromagnetism is long-ranged, the weak force is short-ranged and the strong force is weak in high-energy environments such as the early universe and strong where the probing energy is low. Many GUTs predict that quarks and leptons are part of a single representation of a gauge group with one single hypercharge and would explain why the electric charge of electrons and protons seem to be exactly the same [51].

The simplest GUT is SU(5), which would break down into the Standard Model at lower energies due to spontaneous symmetry breaking. Other possible extensions are SO(10) [REF](#), SU(8) [52] and O(16) [REF](#) Lie groups.

Without experimental results there is still much ongoing debate into which theory is the correct one. Multiple viable theories still remain. A subset of a handful are given in the following sections.

Supersymmetry

Supersymmetric models impose a new symmetry, supersymmetry (SUSY), that relates fermions and bosons. Every fermion would have a, yet unseen, bosonic supersymmetric partner and vice versa. This theory is highly motivated due to its ability in canceling the quadratically divergent terms in the mass correction of the Higgs boson. Unbroken SUSY would lead to partners with the same mass as the particles we know from the SM and would have been discovered long ago. Because of this, one assumes the symmetry to be broken.

The last couple of years, SUSY was regarded as the most promising extension of the SM with tremendous efforts from big collaborations such as the experiments at the Large Hadron Collider (LHC) in search for proof. Unfortunately, to this date no evidence for SUSY has been found.

Little Higgs

String theory

1.5.3 How to look for new physics

In general one could say there are two possible ways to look for new physics. Almost all of the physics in our solar system can be explained with what we know from the Standard Model. Interactions in controlled laboratory environments are currently on the order of ~ 10 TeV in the experiments at the LHC. This could still be well below the energy levels to produce new, exotic, particles. In the energy frontier it is the goal to reach the highest energies possible in order to get as close to the energy requirements where new physics become more prominent. As a consequence, more and more cosmic ray experiments have found an interest in searches for physics beyond the Standard Model. This is sometimes called the *cosmic frontier*. This

analysis tries to explore this possibility in more detail for the IceCube experiment. Cosmic ray experiments have the disadvantage that they are not fully contained experiments and information is lost as the primary interaction is unknown and important parameters as energy, direction, type,... of the particle have to be reconstructed.

The other approach tries to extract information from precision experiments and are therefore reliant on limiting statistical and systematical uncertainties. In these experiments, the intensity of the beam of particle accelerators is pushed to their highest values and is therefore referred to as the intensity frontier. This strategy tries to generate huge numbers of particles needed to study rare or exotic subatomic processes. Rare processes could gain us a lot of information on unknown physics. Some parameters which can be calculated in the SM have a small offset in what is measured in experiment. It is possible that new physics enter in Feynman diagrams and have a non-negligible contribution, however rare they are.

I'd like to finish this chapter with quotes from Steven Weinberg in an interview with Nova REF about his vision on string theory. It shows the apparent stalemate phycisist seems to find themselves into: there are no theoretical breakthroughs regarding long standing problems.

"I believe that there is a simple theory that governs everything—the four forces we know about, perhaps other forces as well. I'm not sure that's true. It may be that nature is irreducibly messy. I'm sure that we should assume it's not, because otherwise we're never going to find a fundamental theory. But even so, we're not guaranteed that we'll find it. We may not be smart enough. Dogs are not smart enough to understand quantum mechanics. I'm not sure that people are smart enough to understand the whatever-it-is that unifies everything. I think we probably are, because of our ability to link our minds through language, but I'm not certain."

"There was a marvelous period from, I'd say, the mid-'60s until the late '70s when theoretical physicists actually had something to say that experimentalists were interested in. Experimentalists made discoveries that theoretical physicists were interested in. Everything was converging toward a simple picture of the known particles and forces, a picture that eventually became known as the Standard Model. I think I gave it that name. And it was a time when graduate students would run through the halls of a physics building saying they had discovered another particle and it fit the theories, and it was all so exciting."

"Since the late '70s, I'd say, particle physics has been in somewhat of a doldrums. Partly it's just the price we're paying for the great success we had in that wonderful time then. I think cosmology now, for example, is much more exciting than particle physics. The string theorists are trying to push ahead without much support from relevant experiments, because there aren't any relevant experiments that can be done at the kind of scales that the string theorists are interested in."



2. Theoretical Motivation of the Analysis

The world is divided into people who think they are right ~ Anonymous

As seen in Chapter 1, there is much ongoing debate which beyond-the-Standard-Model physics models could help explain questions we do not have answers for. Over the last decades, this quest has proven to be non-trivial since many anticipated accelerator experiments have not given any clear hints towards physics that cannot be explained by the Standard Model. A big part of the physics community is trying its best to help answer these riddles and dedicated experiments have been constructed in their search for new physics. Other collaborations try to make use of their detector in the most efficient way possible. These experiments most often try to look for beyond-the-Standard-Model physics by searching for signals in their detector that could not be explained by the particles we know today. One example, and also being the subject of this work, is to try to look for particles that have a lower electromagnetic, non-zero, charge than the charged particles of the Standard Model.

2.1 Introduction

As seen in Chapter 1, all free particles have an electromagnetic charge that is a multitude of the absolute electron charge, e , equal to 1.602×10^{-19} C. Elementary particles such as (anti)quarks have fractional charges equal to $\pm \frac{1}{3}e$ and $\pm \frac{2}{3}e$, but have never been seen as isolated particles due to *confinement* as explained in Section 1.1.2. No other particles are expected to have a charge lower than e and are therefore perfect candidates for searches for beyond the Standard Model. Different experiments have sought for these anomalously charged particles and are referred to as *Lightly Ionizing Particles (LIPs)* or *Stable Massive Particles (SMPs)*. Throughout this work the latter denomination is used, indicating they do not rapidly decay and have masses significantly higher than the lightest leptons.

2.2 Theory

In Section 1.5.2, possible extensions of the Standard Model were already introduced. One of the simplest possible extensions of the $SU(3) \times SU(2) \times U(1)$ group is the $SU(5)$ gauge group. It is the smallest Lie group that can contain the group of the Standard Model without introducing any new fermions. It could explain charge quantization [51], has complex representations and can accommodate fractional charges. In this scheme, new vector bosons, usually called X and

Y bosons, occur with charges $\frac{4}{3}$ and $\frac{1}{3}$. Extensions of the SU(5) models allow for color singlet particles with charges $\frac{1}{3}$ and $\frac{2}{3}$ [53]. Other possible extention are the SU(7) [54], SU(8) [52], SO(14) [55], SO(18) [56], SO(10) \times SO(8) [57].

It should be noted that the simplest form of an SU(5) gauge group is already highly constrained as proton decay is allowed in this model and estimated to be around $10^{30} - 10^{31}$ years, but experimental results have shown the lifetime to be $> 1.67 \times 10^{34}$ years ($\tau(p \rightarrow \pi^0 e^+)$) [58] and $> 6.6 \times 10^{33}$ years ($\tau(p \rightarrow \pi^0 \mu^+)$) [59].

There are also some string theories where massive particles with a fractional charge are also predicted [60, 61], which was later confirmed to occur very often in certain compactifications [62].

More recently, there has been an increasing interest in searches for millicharged particles. New particles could couple to the Standard Model via a “kinetic mixing” or “hypercharge portal” [63, 64]. And in recent years, they were studied as possible candidates for dark matter [65, 66, 67, 68]. The charges of these particles are however often $< 10^{-3}e$ and no ideal candidates in neutrino Cherenkov experiments. It is possible to look for them in neutrino experiments [69], but are more targeted toward future experiments such as DUNE [70] and SHiP [71]. A more detailed explanation of these particles can be found in [72]. The most stringent upper limit in millicharged particles known to the author is given in Ref. [73].

There are many other possible extensions but go beyond the scope of this work. One could just keep in mind that no free particles with an anomalous charge less than e are expected and that, if seen, would give clear hints of beyond-the-Standard-Model physics and would help in finding a more clear picture of what is possibly lurking beyond the realms of our understanding.

2.3 Properties of the signal

Because there are many possible scenarios what these particles are, originate, or are produced from, one has to make certain assumptions about the properties of the signal. A particle traveling at the speed of light with a lifetime < 0.1 seconds traversing a detector will not give the same signal properties as one that has a very long lifetime. Therefore, I have assumed that the particles I am looking for

- behave leptonically, similar to muons;
- have a long lifetime and will not decay within the detector, or have a very low probability;
- follow an energy spectrum with a spectrum of -2^{*};
- are assumed to produce a uniform flux in angle space close to the detector.

These assumptions are consistent with previous searches that are mentioned in Section 2.4. The behaviour of these particles in the detector will depend on the charge (see Section 4.3.2.1) and, to a lesser extent, the mass. In this work the particles are assumed to have a

- charge of 1/3, 1/2 and 2/3;
- mass of 10 GeV, 100 GeV, 1 TeV, 10 TeV and 100 TeV,

where I have referred to the charge of the particles as relative to the absolute electron charge, e^\dagger . The possible combinations result into a total of 15 unique signal samples which will be searched for.

2.4 Previous searches

There are several ways on can assume to produce fractional charge particles. Different assumptions lead to different possible searches with previous and current detectors. In the following, the results of several experiments are shown.

2.4.1 Searches with accelerators and fixed targets

The total energy of the interaction should be large enough to produce particles of a certain mass. The square of the centre of mass energy is given by:

^{*}More information about spectra can be found in Section 3.1.2.

[†]This will be done throughout this work from this point on.

Table 2.1: Highest-energy fractional charge particle searches in electron-positron colliders. No evidence for fractionally charged particles was found.

Energy (GeV)	Charges sought	Collider	Reference
1-1.4	$\frac{2}{3}$	VEPP-2M	[76]
29	$\frac{1}{3}, \frac{2}{3}$	PEP	[77]
130-209	$\frac{2}{3}, \frac{4}{3}, \frac{5}{3}$	LEP	[78]
130-136, 161 and 172	$\frac{2}{3}$	LEP	[79]
91.2 (m_Z)	$\frac{2}{3}, \frac{4}{3}$	LEP	[80]
91.2 (m_Z)	$\frac{4}{3}$	LEP	[81]

$$\begin{aligned} s &= (p_1 c + p_2 c)^2 \\ &= m_1^2 c^4 + m_2^2 c^4 + 2E_1 E_2 - 2\vec{p}_1 \cdot \vec{p}_2 c^2, \end{aligned} \quad (2.1)$$

where $p_{1,2}$ are the four-momenta of the two particles and c is the speed of light. Assuming E is the energy of the incoming particle and m the mass of a target particle in rest, the maximal mass reach of a search is given by:

$$m_{max} \approx \sqrt{2mE}. \quad (2.2)$$

If I is the incoming particle from the input beam and N a nucleus, the production of exotic particles can then be depicted as

$$I + N \rightarrow F + X, \quad (2.3)$$

where F stands for the fractional charged particle and X for the other particles that are produced in the interaction. No experiments that used accelerators and fixed targets found evidence for the existence of fractional charge particles [74]. The highest-energy search used muons with a muon beam of 200 GeV, resulting in an m_{max} of $19 \text{ GeV}/c^2$ [75].

2.4.2 Colliders

Particle colliders can reach much higher energies than most fixed-target experiments. The maximal mass of new particles in a storage ring which is colliding particles of energy E , Eq. 2.1 gives

$$s = 4E^2. \quad (2.4)$$

There is a big difference in lepton and hadron accelerator experiments since much less particles are being produced in the former due to the absence of strong interactions. The production is “cleaner” and the sought particles are easier to distinguish from other productions. But, it is more difficult to reach higher energies for lepton accelerators*. An overview of electron-positron colliders is given in Table 2.1. No evidence for fractionally charged particles was found.

Experiments that use proton-antiproton colliders have reached large masses but have also found no evidence of fractionally charged particles. An overview is given in Table 2.2.

A more recent search was performed at the LHC, a proton-proton collider, when operating at an energy of 7 TeV. No evidence of particles with fractional charge was found. An upper limit of 95% confidence level was set for particles with electric charge $\frac{2}{3}$ up to a mass of 310 GeV and 140 GeV for those with charge $\frac{1}{3}$ [85].

*The radiative power of synchrotron radiation scales with a factor of m^{-4} : particles with low mass lose much more energy in circular accelerators with a fixed radius.

Table 2.2: Highest-energy fractional charge particle searches in proton-antiproton colliders. No evidence for fractionally charged particles was found.

Energy (TeV)	Charges sought	Collider	Reference
0.54	$\frac{1}{3}, \frac{2}{3}$	SPS	[82]
1.8	$\frac{2}{3}, \frac{4}{3}$	Tevatron	[83]
1.8	$\frac{1}{3}, \frac{2}{3}$	Tevatron	[84]

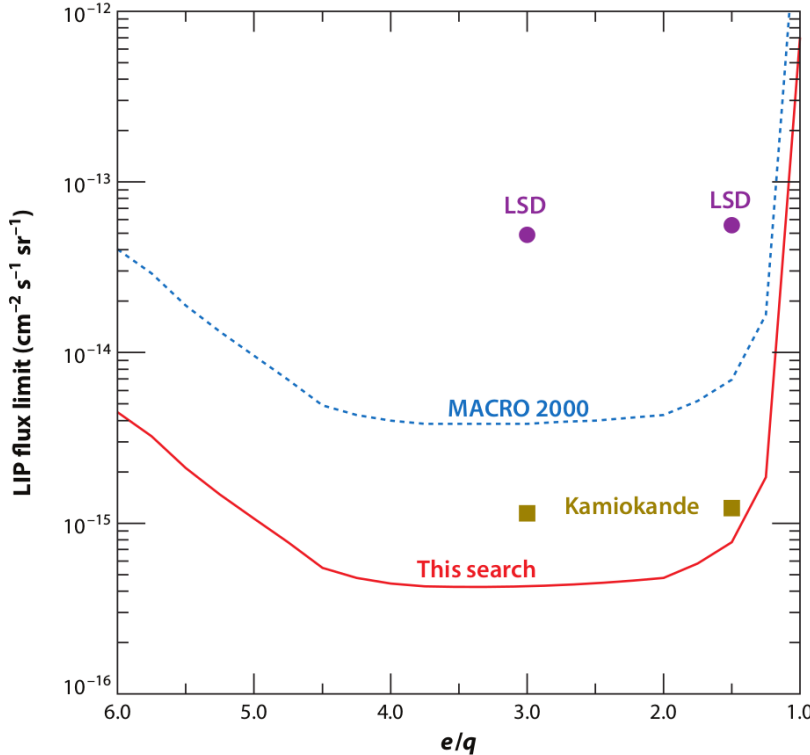


Figure 2.1: Upper limits on fluxed of particles close to the repective detectors. LIP stands for *Lightly Ionizing Particles*. From Ref. [87].

2.4.3 Searches for particles with telescopes

There are several ways particles with a fractional charge could be produced in cosmological events;

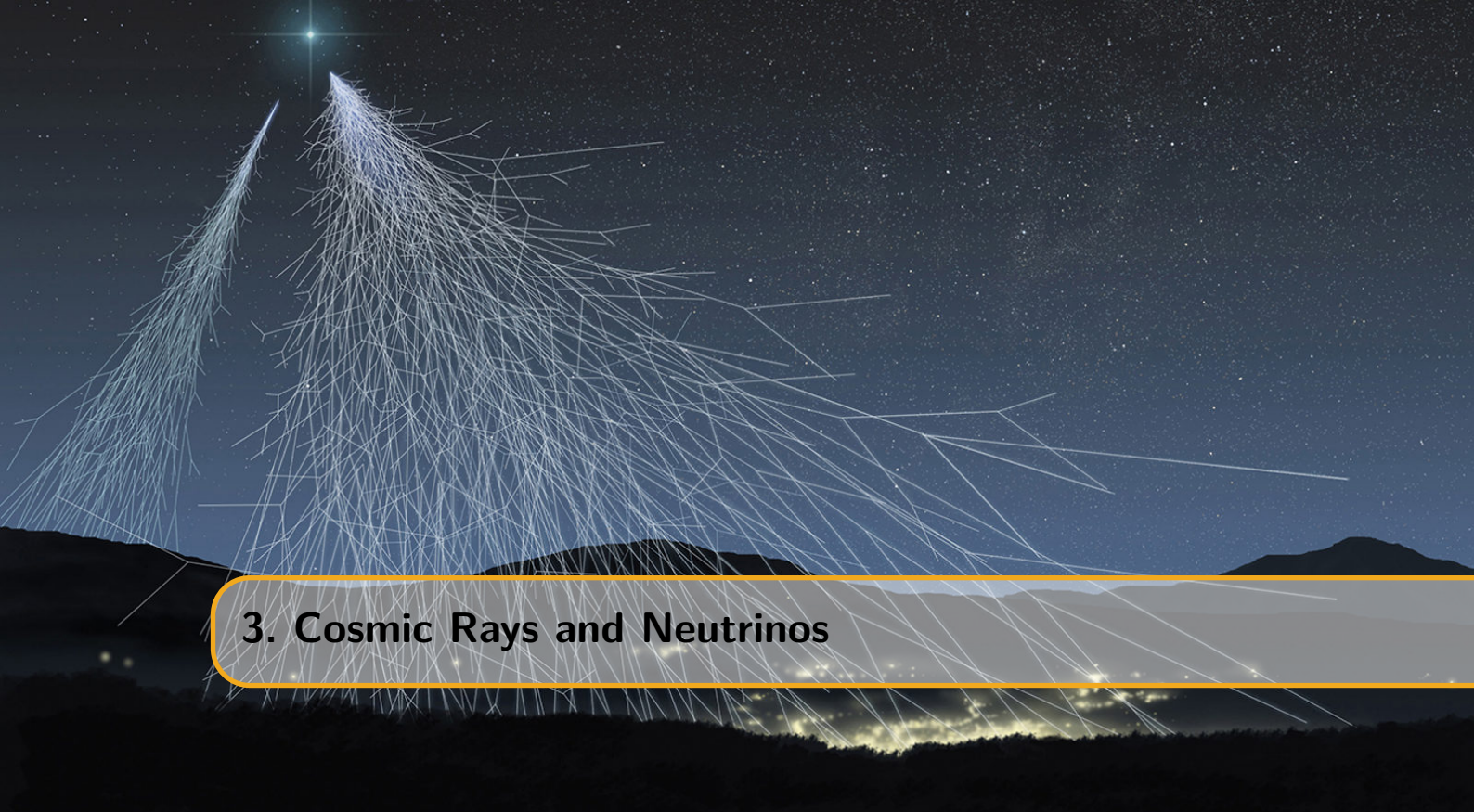
- the particles were produced early on in the Universe and are a stable component of the present material;
- the particles are rare but can be continuously produced in high-energetic astrophysical event; or
- the particles are produced in cosmic ray processes on Earth.

Because there is no clear preference in one of these possibilities, most telescope experiments therefore express their search sensitivity in function of an incoming flux close to the detector in units of $\text{cm}^{-2} \text{s}^{-1} \text{sr}^{-1}$. This analysis has adopted the same search strategy and aims to improve upon previous results. The most stringent upper limit was realized by the MACRO experiment found on the arXive that compares results from older searches and can be found in Figure 2.1. The best published result is set by Kamiokande II with upper limits of $2.1 \times 10^{-15} \text{ cm}^{-2} \text{s}^{-1} \text{sr}^{-1}$ and $2.3 \times 10^{-15} \text{ cm}^{-2} \text{s}^{-1} \text{sr}^{-1}$ for particles with charges $\frac{1}{3}$ and $\frac{2}{3}$ respectively [86].

Volgend stukje tekst ergens in verwerken?

Particle physicists don't look for a needle in a haystack as what is sometimes used for an analogy to make clear in what we are doing. We are in fact looking at hay in a haystack. The hay we are looking for has slightly different properties. It can be a bit drier or a bit longer, but it takes an

enormous amount of time and clever thinking to be able to distinguish the hay from normal hay. But sometimes errors can slip in, or you can have a very long normal piece of hay while you could have smaller pieces of new hay so finding a new one doesn't give you a hundred percent assurance that you've indeed found something new. You need to find enough of the new ones to be able to say that there are too many found that could be obtained by pure chance from the normal set.



3. Cosmic Rays and Neutrinos

We sit in the mud, my friend, and reach for the stars ~ Ivan Turgenev

Cosmic rays, contrary to its name, almost exclusively refer to particles with a finite rest mass. The term *rays* was historically attributed to these particles as they were thought to be mostly electromagnetic radiation. They are particles coming from outer space, impinging our atmosphere and producing large showers of electromagnetic radiation. The interest of cosmic rays within the field of particle physics and modern particle physics is clear: multiple new particles were discovered from the interactions at energies that were higher than most experiments could reach. Positrons, muons, pions, and kaons were first discovered in cosmic ray experiments in the 1930s and '40s. Today, high-energy cosmic ray interactions are still of interest as the highest energies of these particles go beyond what is feasible at the most powerful accelerators such as the LHC. Neutrinos are expected to be produced together with cosmic rays, near the source or close to Earth, making neutrino astronomy a powerful and important part of modern day astronomy. This chapter serves as an overview of the origin of cosmic rays and neutrinos with their properties. For a more exhaustive description of cosmic rays I refer the reader to Ref. [88].

3.1 Cosmic rays

3.1.1 Discovery of cosmic rays

With the use of electrometers, Victor Hess performed multiple ground-breaking balloon flight experiments in 1912 to prove that the amount of radiation increases with altitude [89]. This was in strong contradiction with the widespread belief that radiation on Earth's surface mostly originates from radioactive substances in its crust. Hess concluded that an extremely penetrating radiation existed. He described this radiation to be coming from space that then enters Earth's atmosphere. This proved to be correct, but it was wrongfully attributed to electromagnetic radiation by Robert Millikan in the 1920s [90].

Hess later ruled out the possibility that cosmic rays originate from the Sun as his observations showed no particular differences in night and day and during solar eclipses. In the late 1920s, first evidence was found that cosmic rays were charged due to a variation of their intensity with latitude, which indicated that they were deflected by the geomagnetic field [91].

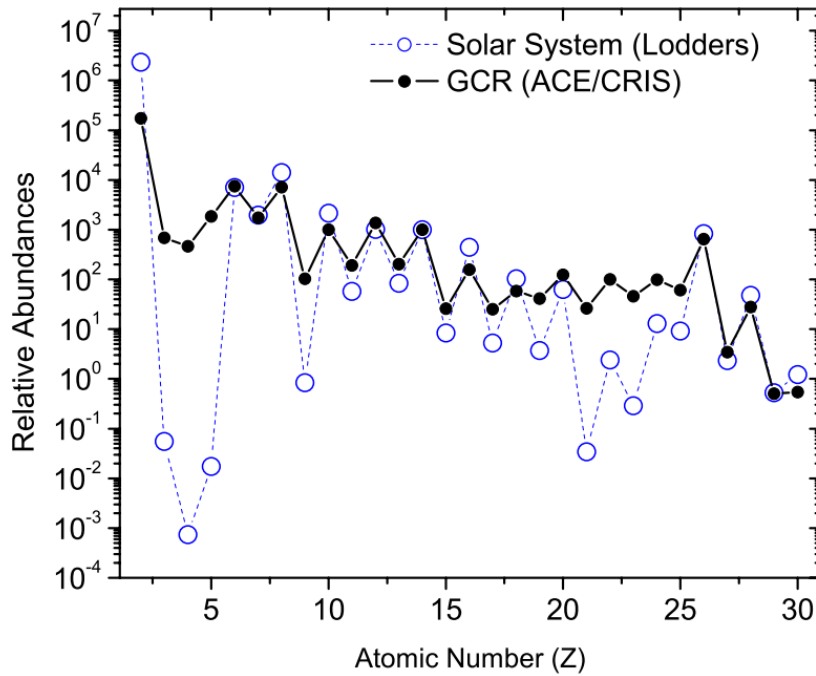


Figure 3.1: The cosmic ray elemental abundances measured on Earth compared to the solar system abundances, all relative to carbon = 100. Figure from ACE news archive [92].

3.1.2 What are cosmic rays?

Cosmic rays are, almost exclusively, the collection of nuclei that are stripped of their electrons, making them electrically charged, heavy particles. Around 90% of the particles are ionized hydrogen atoms, or protons. 9% are alpha particles and 1% are nuclei of heavier elements. There is a striking resemblance between the relative abundance of cosmic rays and elements in the solar system as seen in Figure 3.1. A much smaller fraction of incoming particles are electrons, positrons and antiprotons.

There are however two important differences between cosmic rays and elements from our solar system. Firstly, the two groups of elements Li, Be, B and Sc, Ti, V, Cr, Mn are many orders of magnitude more abundant in cosmic rays than in the solar system. This is due to their absence in stellar nucleosynthesis and are therefore not expected to be produced in large numbers. More massive cosmic rays (mainly C, O and Fe) can produce these nuclei in the process of *spallation*; they are produced by collisions of cosmic rays with the interstellar medium. Therefore, these nuclei are sometimes referred to as *secondary nuclei*. The second difference is that nuclei with an atomic number $Z > 1$ are much more abundant with respect to hydrogen for cosmic rays. This phenomenon is not yet well understood but could be attributed to the difficulty to ionize hydrogen, necessary for acceleration processes.

The amount of cosmic rays seen on Earth is expressed in units of $[m^{-2}s^{-1}sr^{-1}]$. We can see in Figure 3.2 that the cosmic ray flux follows a energy power law spectrum

$$dN \propto E^{-\gamma} dE, \quad (3.1)$$

where γ is called the *spectrum index*. Because of the steepness of the spectrum it is often multiplied by a higher power of energy*.

We can divide the global spectrum in four regions. Between 10 GeV and 1 PeV the differential spectrum index is around -2.7. From 10 PeV to 1 EeV it's around -3.1. Above 10 EeV, the

*The broad range in both energy and flux, visible in Fig. 3.2, should convince the reader that many types of detectors are necessary to study the behaviour of cosmic rays. Low-energy particles are abundant and high-energy particles are much more rare. Both the energy and the incoming flux will determine the type and size of the detector.

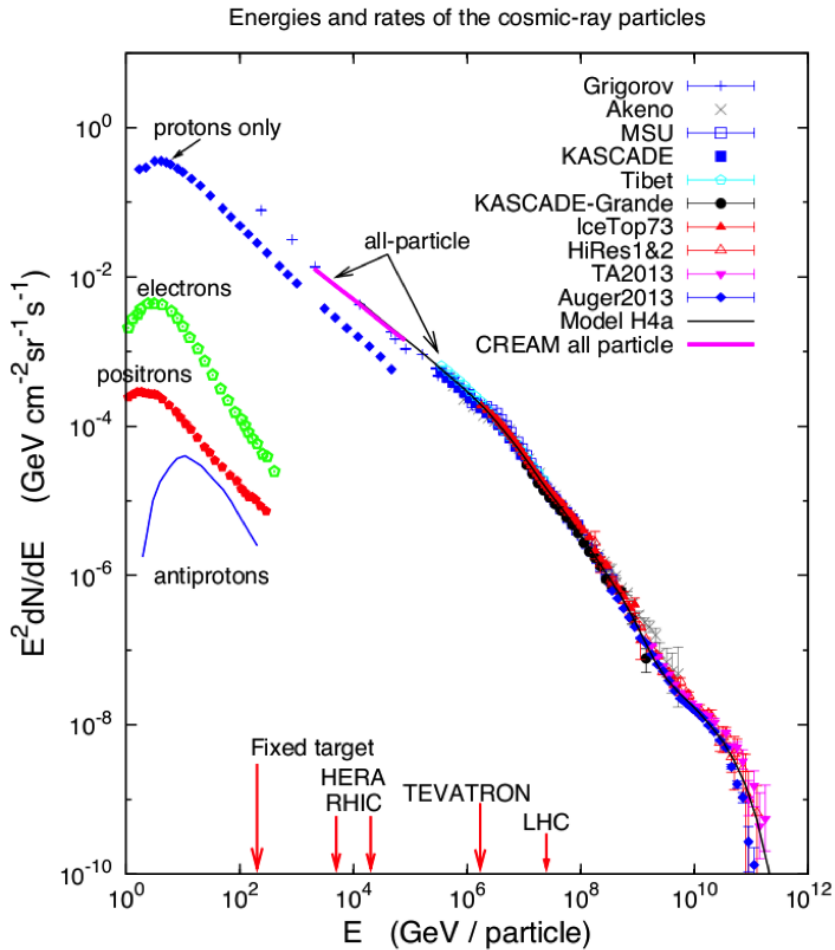


Figure 3.2: Spectrum of cosmic rays at Earth. The all-particle spectrum measured by different experiments is plotted together with the proton-only spectrum. Subdominant contributions to the total flux from electrons, positrons and antiprotons as measured by the PAMELA experiment are also shown. Figure from Ref. [93].

spectrum again flattens to an index around -2.6 and an apparent cutoff region is present at around 10^{20} eV. The transition of this first to second region at around 3 PeV is referred to as the *knee*. The second to third region transition is called the *ankle*. It is possible to describe the full cosmic-ray spectrum with sources within our galaxy. However, a more generally accepted theory is that the knee in the spectrum originates from the end of a population of particles that are accelerated within our Milky Way [94]. Around 100 PeV is the *second knee*, believed to be a feature of the iron drop-off.

The origin of cosmic rays has been a topic of discussion for many years. We know now that most particles originate from sources in the local galaxy, having spent on average 10^7 years in diffusive motion in the interstellar medium [94]. This is consistent with the resemblance of the relative abundances of cosmic rays and elements from our solar system. However, there is no general consensus about the origin of the cosmic rays with energies above 3×10^{18} eV. In the following, the abovementioned energy regions are discussed in more detail.

3.1.2.1 Solar modulation

In the solar system, a stream of charged particles is released from the Sun. This stream is mostly made up of electrons, protons and alpha particles with kinetic energies ranging between 0.5 and 10 keV. Within this solar wind plasma, there is a magnetic field. Cosmic rays coming into the solar system interact with these particles and magnetic field. The influence is greatest on particles with the lowest energies. This effect is called *solar modulation*. In effect, we see a strong suppression of cosmic rays at energies of 10 GeV and below.

3.1.2.2 Galactic component

The most probable acceleration mechanism for cosmic rays originating from our Galaxy is by shocks driven by expanding supernova remnants [95]. Other possible sources are superbubbles, pulsars, magnetic reconnection, AGN episodes (see Section 3.1.4.2), starburst episodes, GRBs (see Section 3.1.4.3), etc. It is expected that these many possible sources dominate in the low-energy cosmic rays. This was later proved by observations of a lower gamma-ray emissivity from π^0 decay from Magellanic clouds compared to the Milky-Way [96]. From the ratio of primary to secondary nuclei, it can be inferred that cosmic rays travel distances thousands of times greater than the thickness of the disk of the Galaxy. There is also an apparent decrease in the amount of matter that is traversed by cosmic rays with higher energies than with lower. Higher-energy cosmic rays seem to spend less time in the Galaxy than lower-energy ones and suggests that cosmic rays are accelerated before most propagation occurs [88].

The way the spectrum is fit is not set in stone. Here I will use the convention used by Gaisser, Stanev and Tilav described in reference [94]: the spectrum is subdivided in three populations. The first population corresponds to the particles primarily accelerated by supernova remnants, with the knee signaling the cutoff of this population. The second population is a higher-energy galactic component of unknown origin. The third generation will be described in more detail in Section 3.1.2.3. Assuming that the primary spectrum depends on the *magnetic rigidity*^{*},

$$R = \frac{pc}{Ze}, \quad (3.2)$$

where Ze is the charge of a nucleus of total energy $E_{tot} = pc$ and relates to the gyroradius of a particle in a given magnetic field B as

$$r_L = \frac{R}{B}. \quad (3.3)$$

If there is a characteristic rigidity, R_e , above which a particular acceleration process reaches a limit, then the feature will show up in total energy first for protons, then for helium and so forth for heavier nuclei according to

*An assumption that is experimentally favored over other assumptions. Rigidity is an appropriate variable for interpreting changes in the spectrum due to propagation and acceleration in magnetic fields.

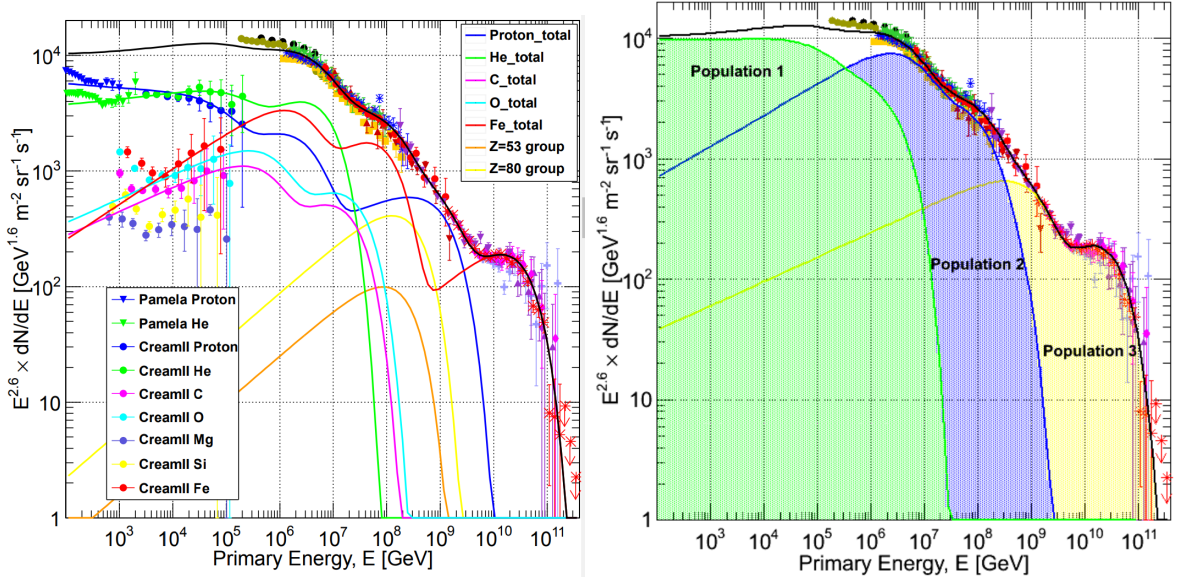


Figure 3.3: Overview of the categorization of the cosmic-ray spectrum as done in Ref. [94]. The individual components are shown on the left, and the total contribution of the three proposed populations are shown on the right.

$$E_{tot} = Ze \times R_e. \quad (3.4)$$

This effect is visualised in Figure 3.3 and indicates that as one population reaches its maximum, the composition becomes heavier. The second knee, reported by KASCADE-Grande [97] and GAMMA [98] could be explained with an “iron knee” bump.

3.1.2.3 Extragalactic component

The flux at the highest energies is exceedingly small. The number of events per year at energies above 5×10^{19} eV is around one per square kilometer per century. There are only two experiments in the world capable of detecting the highest-energy cosmic rays in a statistical meaningful way: Telescope Array, located in the Northern Hemisphere (instrumented area of $\approx 700 \text{ km}^2$) and the Pierre Auger Observatory in the Southern Hemisphere (instrumented area of $\approx 3000 \text{ km}^2$).

Both experiments see a suppression of the flux above 6×10^{19} eV. The exponential cutoff is consistent with the expected Greisen-Zatsepin-Kuzmin (GZK) effect [99, 100] where cosmic rays interact with the cosmic microwave background radiation (CMB)



or



Particles with energies above 5×10^{19} eV would interact with the CMB, leading to an exponential cutoff (if the incoming particles above these energies would be relatively young it is still possible for them to reach the detector). The Pierre Auger experiment reported to see higher compositions at the highest energies [101]. If the particle is a nucleus with A nucleons, then the GZK limit applies to its nucleons, which carry only a fraction $1/A$ of the total energy. For iron nuclei this would for example result in a limit of 2.8×10^{21} eV. In contrast, the TA experiment interpreted their data as implying a light primary composition (mainly p and He) at the highest energies. Both experiments use a different interpretations for crucial quantities of these measurements and a thorough joint analysis conducted by both experiments states that, at the current level of statistics and understanding of systematics, both data sets are compatible with being drawn from the same parent distribution [40].

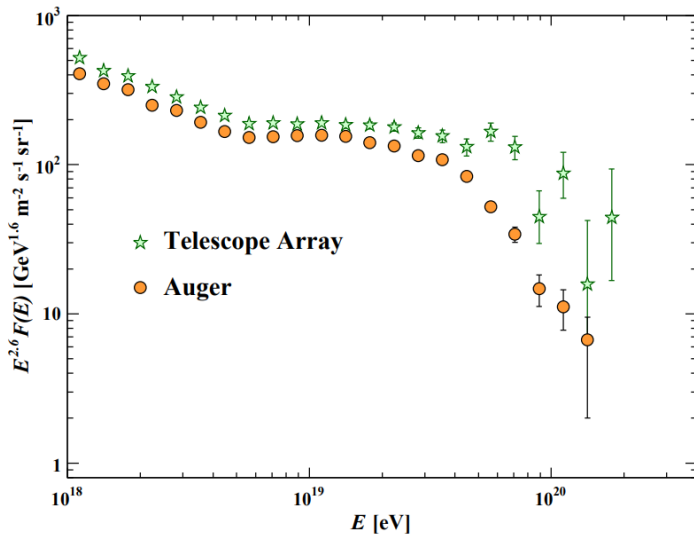


Figure 3.4: Expanded view of the highest energy portion of the cosmic-ray spectrum from data of the Telescope Array and the Pierre Auger Observatory [40].

The Pierre Auger Observatory also reported evidence in an anisotropic distribution of the arrival directions of the highest-energy cosmic rays in a direction where the distribution of galaxies is relatively high and does not coincide with the galactic plane [102]. These observations, together with our lack of known possible sources within our galaxy for these ultra-high energies shows compelling evidence that these particles have an origin from outside our galaxy. From pion decay, there is also an expected flux from extragalactic neutrinos (more information in Section 3.2.3 and 5.6.1). The flux, spectrum and angular distribution of the excess neutrino signal detected by IceCube between ≈ 50 TeV and ≈ 2 PeV are also inconsistent with those expected for Galactic sources [103].

To put it simply, understanding cosmic rays and determining their origin can help us answer fundamental questions about the origins of the universe, our galaxy and, more philosophically, ourselves. With the words of Carl Sagan:

“The nitrogen in our DNA, the calcium in our teeth, the iron in our blood, the carbon in our apple pies were made in the interiors of collapsing stars. We are made of starstuff.”

3.1.3 Acceleration mechanism

How cosmic rays got their signature slope in the energy spectrum and its intricate details have been under discussion for multiple decades. To this date, there is no clear picture how these particles are accelerated in full detail. It is beyond the scope of this work to give a comprehensive overview of all possible acceleration mechanisms or possible sources. Most calculations are left out and for a more detailed discussion the reader is referred to specialized books or the references in the text.

The acceleration of the particles can be subdivided into two questions. First, where are the particles accelerated? Does it happen on large scales, cosmological distances in galaxies or near specific sources? Secondly, how are these particles exactly accelerated? What is the driving mechanism? Since primary cosmic rays are all electromagnetically charged particles, these mechanisms should clearly be sought for in places where electric and/or magnetic fields play a dominant role.

3.1.3.1 Galactic accelerators

With their approximate energy density around 0.5 eV/cm³ in our local galaxy, the bulk of cosmic ray acceleration could very well be explained by **supernovae**. This density results into a total

power of around

$$L_{CR} = 7 \times 10^{40} \text{ erg/s}, \quad (3.7)$$

where erg is a unit often used in astronomy*. If one assumes a supernova explosion of around one per every 30 years, then the total power output of type II supernovae with a mass output of around ten times the mass of the Sun at a velocity close to $5 \times 10^8 \text{ cm/s}$ would result in a power of

$$L_{SN} \sim 3 \times 10^{42} \text{ erg/s}. \quad (3.8)$$

These numbers are not set in stone and hold large uncertainties, but it shows that with an acceleration efficiency on the order of a couple of percent supernova explosions are a prominent source of energetic cosmic rays, if not the dominant one.

3.1.3.2 Extragalactic accelerators

We will see in Section 3.1.4.1 that the maximum energy from shock acceleration by a supernova remnant is insufficient to explain Ultra High Energy Cosmic Rays (UHECR). Particles can be accelerated if the trajectory of the particles can be changed and energy can be transferred multiple times. The magnetic fields responsible for the course change of these particles have to be sufficient in magnitude in order for these particles not to escape and go beyond the grasp of the source responsible for the acceleration. This limitation is expressed by the gyroradius in the accelerator, $r_L = E/ZeB$ similar to Eq. 3.3, requiring it to be smaller than the radius of the accelerator: $r_L < R$ or $E < ZeBR$.

Even if only qualitative, this relation provides an interesting criterion to identify possible sources of UHECRs by looking at the accelerator related term BR . This was done in a classic paper by Hillas [104], illustrated in the more recent Figure 3.5. Accelerators necessary to explain the amount of UHECRs are not populated (enough) in our galaxy, making them more likely to be of extra-galactic origin. Active galactic nuclei, gamma ray bursts, starburst galaxies, and galaxy clusters are therefore also briefly explained.

3.1.4 Sources

3.1.4.1 Supernova (remnants)

Supernovae can be broadly subdivided into two categories: type I and type II. Type I supernova explosions happen in binary star systems. In those systems, one of the two stars is a carbon-oxygen white dwarf that accretes matter from the second star. When the total mass of the white dwarf reaches the Chandrasekhar limit of around 1.44 solar masses, it cannot longer hold itself under the gravitational pressure and collapses in on itself. Within seconds, the carbon component in the white dwarf starts nuclear fusion and enough energy is released to produce an explosion brighter than the Sun with a factor of around 5 billion. A resulting shock wave can reach up to around 3% the speed of light.

Type II supernova explosions differ by being single star systems. When a star reaches the end of its lifecycle the subsequent fusion reactions reach to a halt. If the star has enough mass (at least 8 times the mass of the Sun), it is possible for the inner core to again reach the Chandrasekhar limit and collapse in on itself due to the lack of *electron degeneracy*. Without the outward pressure of nuclear fusion reactions and the support of the core, the outer layers of the star collapse under the gravitational pressure. The compression of the electrons and protons into neutrons results into a very hot, dense, neutron core. The velocity of the inwards falling layers can reach to a staggering 23% of the speed of light and recoil when hitting the remaining core. Neutrinos are produced in this violent core collapse and the outward going shockwave hits the remaining outer layers forming the supernova explosion†.

*1 erg = 10^{-7} J .

†To get a better feeling of how extraordinary these events really are, I'd like to illustrate what it would be like if one could be close to a supernova event. From Figure 3.11, one can calculate that the number of solar neutrinos going through our hand per second is around *one trillion*. Yet they are so weakly interacting that, on

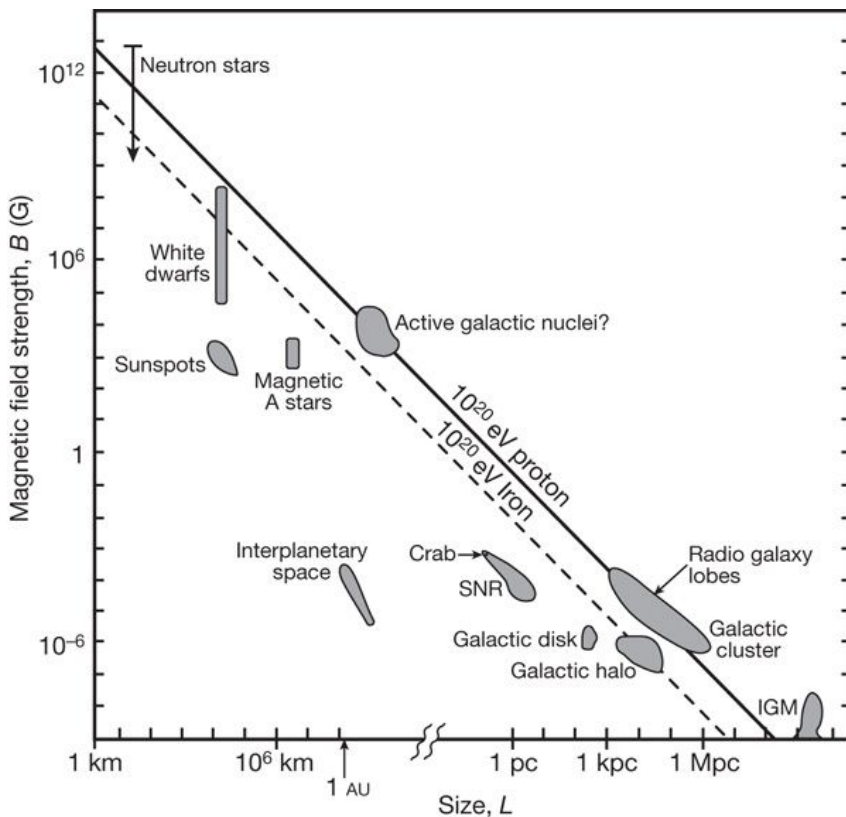


Figure 3.5: The Hillas plot of potential cosmic ray accelerators locates objects according to size and magnetic field. Objects to the left of the diagonal lines cannot accelerate particles to 10^{20} eV (proton: solid, iron: broken). Image obtained from Ref. [105].

Because of their brightness, supernovae within our galaxy can be seen with the naked eye (provided they are not too far away). The last recorded supernova from our galaxy was by Johannes Kepler in 1604 but earliest recordings go back to 185 AD by Chinese astronomers*. The question remains how supernovae can serve as cosmic ray accelerators. In 1949, Enrico Fermi proposed a mechanism where particles can gain energy by collisions with moving interstellar ionized gas clouds. Only later, it was realized that a large, plane shock front moving with a certain velocity is able to accelerate charged particles much more efficiently. This first mechanism results into an energy transfer proportional to the squared velocity of the cloud and is thus called *second order Fermi acceleration*. Shock front acceleration energy transfer is proportional to the velocity and is called *first order Fermi acceleration*. Supernova remnants provide an explanation for the origin of these shock fronts.

First- and second-order Fermi acceleration

Suppose we have a magnetic cloud in the interstellar medium travelling with a certain velocity \vec{V} and a particle with velocity \vec{v} enters the cloud under an angle θ_1 (see Figure 3.7). If we assume collisionless scattering can occur (no energy is dissipated from the particle to the cloud) due to the magnetic fields in the cloud, the magnitude of the momentum in the rest frame of the cloud will not change ($E'_1 = E'_2$, where the apostrophe denotes the cloud rest frame). From special relativity we know that:

average, only one will interact with an atom in your body every few years. Supernova explosions are so vast that around 10^{57} neutrinos can be released. This number is so big that even if an observer is a distance of 2.3 AU away from the event, he would still receive a fatal radiation dose of *neutrinos alone*. As another example: looking at a supernova as far away as 1 AU is 10^9 times brighter than detonating a hydrogen bomb pressed against your eyeball.

*From observations of other galaxies, supernovae are expected to occur, on average, once every thirty years. Not all of these will be visible to the naked eye, but would almost certainly be observable with modern astronomical telescopes.

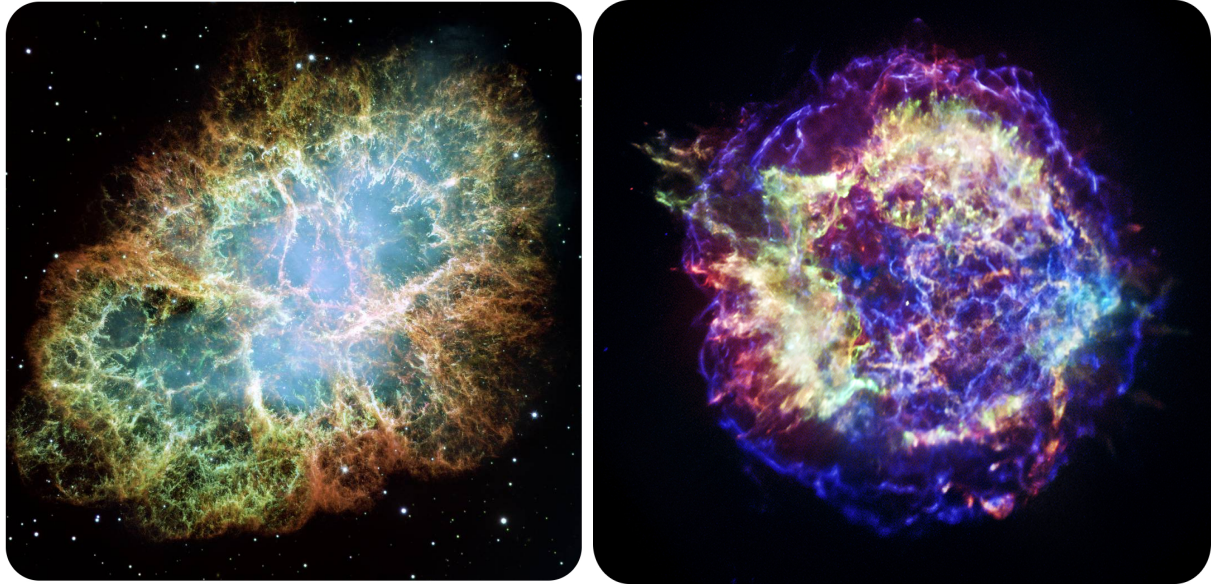


Figure 3.6: *Left:* the Crab Nebula is the supernova remnant approximately one thousand years old. The supernova was noted by Chinese astronomers in the year 1054 AD. *Right:* Chandra X-ray observatory picture of the Cassiopeia A supernova remnant (pictures from NASA).

$$\begin{aligned} E'_1 &= \gamma (E_1 - p_{1,\parallel} V) \\ &= \gamma E_1 (1 - \beta \cos \theta_1), \end{aligned} \tag{3.9}$$

with $\beta = V/c$ and γ the Lorentz factor. Similarly and using $E'_1 = E'_2$

$$\begin{aligned} E_2 &= \gamma E'_2 (1 + \beta \cos \theta'_2) \\ &= \gamma^2 E_1 (1 - \beta \cos \theta_1) (1 + \beta \cos \theta'_2) \end{aligned} \tag{3.10}$$

and

$$\frac{\Delta E}{E} = \frac{E_2 - E_1}{E_1} = \frac{1 - \beta \cos \theta_1 + \beta \cos \theta'_2 - \beta^2 \cos \theta_1 \cos \theta'_2}{1 - \beta^2} - 1. \tag{3.11}$$

By hypothesis, the escaping particles are isotropic in the cloud frame: $\langle \cos \theta'_2 \rangle = 0$. One can show that $\langle \cos \theta_1 \rangle = -\frac{\beta}{3}$ [88], leading to

$$\frac{\Delta E}{E} = \frac{4}{3} \frac{\beta^2}{1 - \beta^2} \approx \frac{4}{3} \beta^2, \tag{3.12}$$

showing that for molecular clouds, the energy gain is indeed proportional to the square of β for second-order Fermi acceleration.

If a particle is incoming to an expanding shock (see Figure 3.7), $\langle \cos \theta_1 \rangle$ is equal to $-2/3$ and $\langle \cos \theta'_2 \rangle$ is equal to $2/3$, leading to

$$\frac{\Delta E}{E} = \frac{\frac{4}{3}\beta + \frac{13}{9}\beta^2}{1 - \beta^2} \approx \frac{4}{3}\beta, \tag{3.13}$$

where β is now equal to $u_1 - u_2$, as explained in the caption of the figure. We have shown that for shock fronts the energy gain is indeed proportional to β for first-order Fermi acceleration. From both the outcome as the discussion it is clear that the energy gain enters through relativistic effects, making an intuitive approach not straightforward.

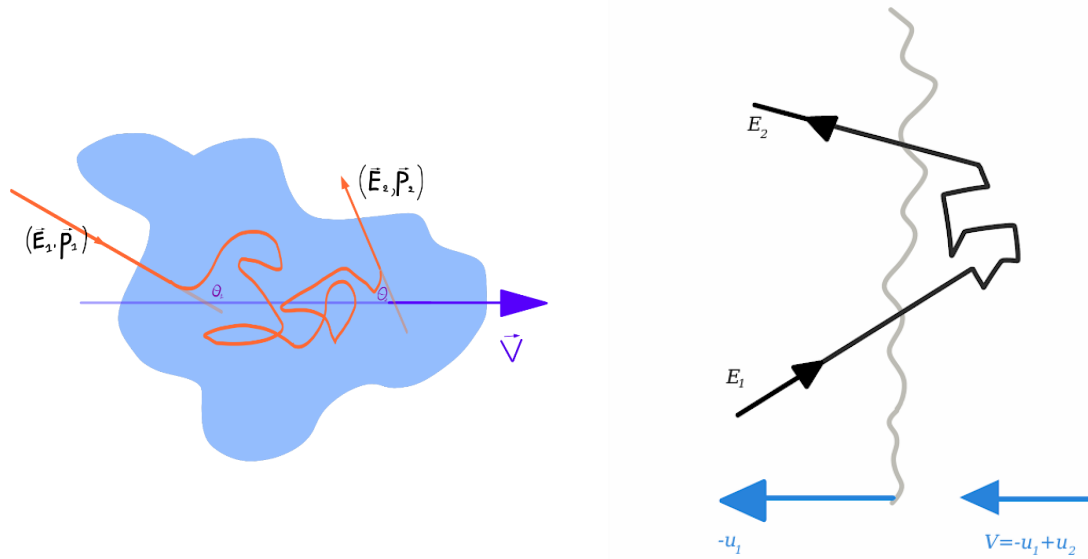


Figure 3.7: *Left:* magnetic cloud showing second-order Fermi acceleration. *Right:* shock waves typically have magnetic inhomogeneities both preceding (downstream) and following them (upstream). If a charged particle travels through the shock wave, it can gain velocity through first-order Fermi acceleration. In the illustration, a particle travels from upstream to downstream and back upstream. At every back and forth movement, the particle effectively gains in energy. For a particle with a velocity u_1 relative to the shock front, the front seems to come at him with velocity $-u_1$. The downstream medium has a velocity relative to the shock front of $u_2 < u_1$ making it seem coming towards the particle with velocity $u_1 - u_2$.

Power

The energy gain of a “single collision” results into the power law spectrum when considering a process in which a test particle increases its energy by an amount proportional to its energy with each encounter. Let us assume $\Delta E = \xi E$, then, after n encounters:

$$E_n = E_0 (1 + \xi)^n, \quad (3.14)$$

where E_0 is the energy when the particle first enters the accelerator medium. To reach a certain energy E' , the particles must encounter a number of collisions

$$n(E') = \frac{\ln\left(\frac{E'}{E_0}\right)}{\ln(1 + \xi)}. \quad (3.15)$$

To reach energies of E' or higher, the number of collisions will be proportional to

$$\begin{aligned} N(\geq E') &\propto \sum_{m=n}^{\infty} P_{present}(m) = \sum_{m=n}^{\infty} (1 - P_{esc})^m \\ &= (1 - P_{esc})^n \left((1 - P_{esc}) + (1 - P_{esc})^2 + \dots \right) \\ &= \frac{(1 - P_{esc})^n}{P_{esc}}, \end{aligned} \quad (3.16)$$

where $P_{present}$ is the probability of a particle still being present in the accelerator and P_{esc} the probability of the particle to escape per collision. Making use of $a^{\ln b} = e^{\ln a \ln b} = b^{\ln a}$ and inserting Eq. 3.15

$$N(\geq E') \propto \frac{1}{P_{esc}} \left(\frac{E'}{E_0} \right)^{-\gamma}, \quad (3.17)$$

with

$$\gamma = \frac{\ln\left(\frac{1}{1-P_{esc}}\right)}{\ln(1+\xi)} \approx \frac{P_{esc}}{\xi}. \quad (3.18)$$

The power law spectrum becomes visible in the derivative of the number of particles in energy

$$\frac{dN}{dE} \sim E^{-(\gamma+1)}, \quad (3.19)$$

in agreement with Eq. 3.1 (alough γ is not the same variable here). Shock wave fronts have an expected $\gamma \approx 1$, giving rise to a different spectrum to what is seen on Earth but which can be explained by propagation from the source to Earth (this is beyond the scope of this work, [tenzij je het uitlegt in 3.1.5](#)). The spectrum from Fermi shock acceleration is thus expected to follow an E^{-2} powerlaw behavior.

Maximum energy

The highest energies that particles can be accelerated to can be defined by

- the differential energy gain per collision dE/dt , and
- the total time the particle can be accelerated.

The energy gain is given by

$$\frac{dE}{dt} = \frac{\xi E}{T_{cycle}}, \quad (3.20)$$

where T_{cycle} is the characteristic time for one acceleration cycle. T_{cycle} depends on the diffusion coefficients and velocities of the upstream and downstream regions and is set to $T_{cycle} \geq 20E/(3u_1ZeB)$ by Lagage and Cesarsky [106] for a strong shock and arguing that the diffusion lenth, λ_D , cannot be smaller than the Larmor radius of the parcticle. Particles with a Larmor radius greater than the irregularities holding a magnetic field are not prone to be heavily influenced by them. Lagage and Cesarsky therefore concluded that

$$E_{max} \leq \frac{3}{20} \frac{u_1}{c} ZeB(u_1 T_{ST}), \quad (3.21)$$

where T_{ST} is the Sedov-Taylor time where particles are less prone to escape and is ~ 1000 years. For $u_1 \sim 10^9$ cm/s [107] and $B \sim 3\mu G$ the Lagage and Cesarsky limit reads

$$E_{max} \leq Z \times 2.4 \times 10^5 \text{ GeV}. \quad (3.22)$$

3.1.4.2 Active Galactic Nuclei

Active Galactiv Neuclei (AGNs) are no stars at the end of their life cycle but active black holes located in the center of galaxies. In most older galaxies, the stars at the center have reached the end of life and have gone supernova, leaving behind white dwarfs or black holes. It is believed that most massive galaxies have supermassive black holes in their centers by the accretion of matter from surrounding large gas clouds [108, 109]. Their masses in current models range from 10^6 to 10^{10} solar masses [110].

The efficient conversion from gravitational potential energy to kinetic energy and radiation make AGNs the most luminous persistent sources of electromagnetic radiation in the universe, and as such very good means in discovering distant objects. The accretion discs heat up due to the inward falling and produce light peaking in the ultraviolet waveband. Certain emission lines are also expected due to the radiation from excited cold atomic material. Some accretion discs produce jets, which point opposite each other, and their direction is defined by either the spin of the black hole, the accretion disc or a combination of both. The most powerful AGNs are classified as *quazars* and AGNs with a jet pointing toward the Earth is called a *blazar*.

Charged particles have large cyclotron radii in AGNs and the relativistic jets could provide the necessary mechanisms to accelerate particles to ultra-high energies. The Pierre Auger collaboration hinted to a correlation of the highest-energy cosmic rays with the positions of nearby active galactic nuclei [111]. Recently, a collaborative effort of IceCube, Fermi-LAT,



Figure 3.9: *Left:* artist impression of a blazar. Illustration from DESY, Science Communication Lab. *Right:* Image from the Hubble telescope where we see a jet streaming out from the center of galaxy M87.

MAGIC and others observed a coincidence of high-energy neutrinos and a blazar, making them very good candidates of sources of extragalactic neutrinos [112].

3.1.4.3 Gamma Ray Bursts

The most catastrophic deaths of massive stars or mergers of neutron-neutron stars or a neutron star and a black hole result into Gamma Ray Bursts (GRBs). GRBs are named after the burst of gamma rays that is followed by a longer-lived afterglow of electromagnetic radiation at longer wavelengths. These bursts are the most energetic explosions in the electromagnetic spectrum and occur when a high-mass star collapses to form a neutron star or black hole. A typical burst releases as much energy in a few seconds than the Sun will do in its entire 10 billion-year lifetime and temporarily outshines the rest of the galaxy*. GRBs are isotropically distributed, making them extragalactic in origin [114].

An often used model to explain how charged particles could reach extremely high energies is called the *fireball model*. This internal-external shock model assumes that kinetic energy of an ultra-relativistic flow is dissipated in internal collisions. When the shock hits the surrounding matter, it is slowed down and gives rise to the signature afterglow [115]. After an initial progenitor phase (see below), a plasma of photons, electrons, positrons, and baryons develops into the formed jets. In this initial phase, the fireball is radiation-dominated and optically thick for photons, making it invisible in the electromagnetic spectrum. Due to radiative pressure, the fireball expands at relativistic speeds (γ -factors > 100) to the point that it becomes more and more transparent. If the central engine produces multiple shocks with different velocities, there will be internal shocks, which give rise to the observed burst emission. In this mechanism, the ultra-relativistic matter can transfer its kinetic energy to the acceleration of particles, explaining cosmic ray production. Later shocks of the jets with surrounding matter would explain the signature afterglow seen in GRBs.

Although there is still much ongoing discussion, GRBs are sometimes subdivided into two regions: *long gamma ray bursts* ($t_{burst} > 2$ s) and *short gamma ray bursts* ($t_{burst} < 2$ s). Long bursts originate from collapsars: a massive star core-collapse forms a black hole and surrounding matter is pulled into an accretion disk. Short bursts hint to progenitors that are extremely compact, where neutron-neutron star or neutron star and black hole mergers are the most probable explanation. The recent detection of the gravitational waves can provide a significant contribution to the understanding of these sources [116, 117, 118, 119, 120].

*GRBs were first discovered in the late 1960s by accident. The Vela satellites had additional gamma ray detectors designed to detect very fast bursts of gamma rays that are expected to be produced by nuclear tests in space [113].

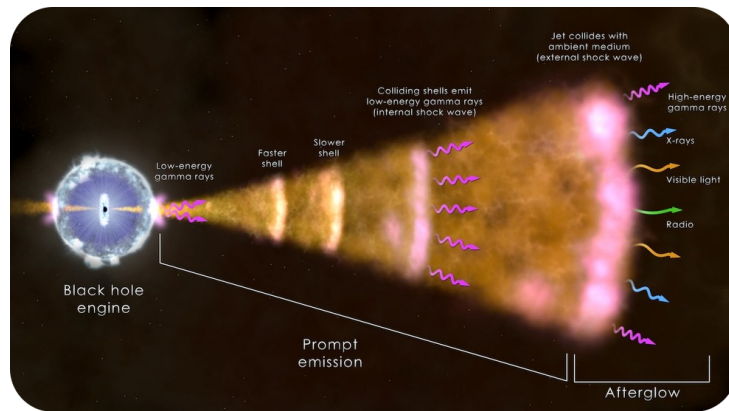


Figure 3.10: Schematic view of the fireball model. In the beginning, the fireball is opaque. After propagation, it becomes transparent, releasing γ -rays due to high-temperature plasma. Charged particles are accelerated in the shock waves and hit the interstellar medium, emitting optical and X-ray light. Image from NASA Goddard space flight center.

3.1.4.4 Starburst galaxies

Galaxies that undergo an episode of large-scale star formation, are called *starburst galaxies*. Most of these are in the midst of a merger or close encounter with another galaxy. Several experiments have shown their gamma ray emission at several hundred GeV to be two to three orders of magnitude of that in our own galaxy [121, 122]. Galactic scale winds from the central regions are possible sources for cosmic ray acceleration.

3.1.4.5 Galaxy clusters

When galaxies are bound together by gravity, they are referred to as *galaxy clusters*. They can contain around 100 to 1000 galaxies and have typical mass ranges around $10^{14} - 10^{15}$ solar masses. Through merging and accretion of dark matter and baryonic gas, galaxy clusters are expected to generate powerful shock waves on large scales. Shocks with significant velocities could provide the necessary conditions for cosmic ray acceleration [123].

3.1.5 Propagation

Doen of niet? Al veel uitleg bij mogelijke bronnen... Gedetailleerde propagatie mss teveel van het goede. In 3.1.4.1 zeg je al dat je er niet in detail gaat op ingaan, mss toch een klein woordje uitleg?

3.2 Neutrinos

As by-products of cosmic ray collisions with matter, neutrinos provide incontrovertible evidence for hadronic acceleration. Since these particles are weakly-interacting, they can escape much denser environments and hold crucial information about the origins of their production environments. Because these particles barely interact, their detection is difficult. Similar to cosmic rays, neutrinos cover a broad range in energy (see Figure 3.11), calling for different types of detectors to cover this large spectrum.

Cosmic rays are deflected in inter- and extragalactic magnetic fields and therefore their arrival direction at Earth does not hold much pointing information (Figure 3.12, left). Light ranging from radio to gamma rays on the electromagnetic spectrum is of a crucial importance in astrophysics but has its limitations: photons can be absorbed by interstellar medium, or are trapped in opaque sources. At higher energies ($\approx 10^{14}$ eV), photons interact and produce electron-positron pairs ($\gamma + \gamma \rightarrow e^+ + e^-$). Unless the sources are closeby, no photons are capable of reaching Earth (see Figure 3.12, right). Neutrinos escape from the sources more easily and are not deflected by magnetic fields, making them key messengers in identifying cosmic ray accelerators. In the following, we will go over the different types of neutrinos that are detectable on Earth.

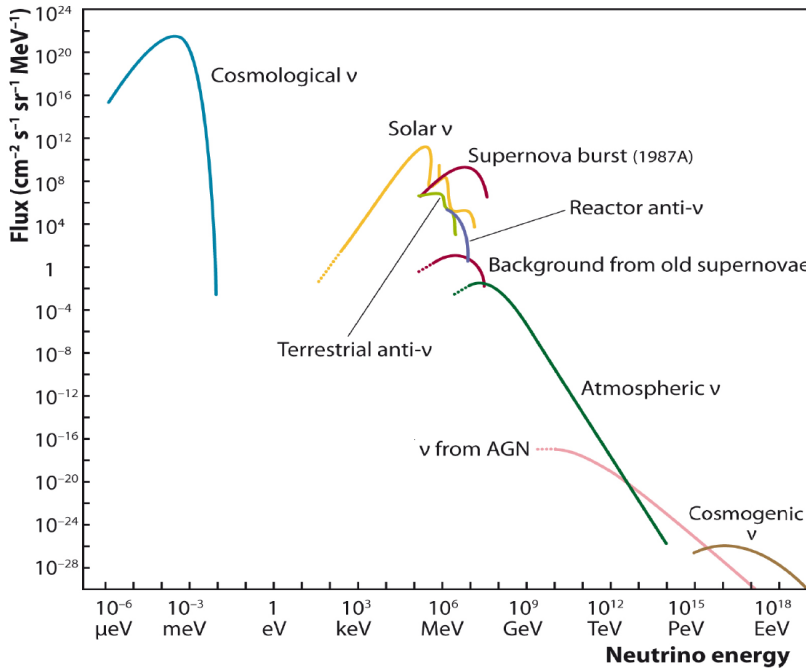


Figure 3.11: Plot illustrating several neutrino fluxes that cover a huge range of energy. Illustration from Ref. [124].

3.2.1 Conventional

Neutrinos are produced in large abundances in air showers (see Section 3.3; Eq. 3.34 and 3.35). The neutrinos that are produced with low to high energies (\approx MeV to PeV range) are called *atmospheric* or *conventional* neutrinos. They are primarily produced in pion or kaon decay. Due to helicity effects, pion and kaon decay to electrons/electron neutrinos is strongly suppressed compared to decays into muons/muon neutrinos. As a result, the ratio of electron neutrinos to muon neutrinos is a factor of around two

$$\frac{N(\nu_\mu + \bar{\nu}_\mu)}{N(\nu_e + \bar{\nu}_e)} \approx 2, \quad (3.23)$$

which should be clear when we look at the example of pion decay where the muon decays as well

$$\begin{aligned} \pi^+ &\rightarrow \mu^+ + \nu_\mu \\ &\rightarrow e^+ + \nu_e + \bar{\nu}_\mu + \nu_\mu. \end{aligned} \quad (3.24)$$

The most referred to calculations for the atmospherical neutrino flux were done by Honda et al. [125].

3.2.2 Prompt

Charmed mesons, also called D mesons, are the lightest particles that contain charm quarks*. Hints of charm particles were first seen in cosmic rays in 1971 by Niu et al. [127]. The production of these particles is strongly suppressed, but are expected to exhibit a harder spectrum than conventional neutrinos do. These mesons have short lifetimes (hence the name: prompt) and decay into neutrinos independent of their energy and arrival direction. Therefore, their energy spectrum is expected to follow that of primary cosmic rays. Their contribution at higher energies can be non-negligible or even become dominant. To this date, it has not been possible to observe this prompt component, but remains an interesting signal in diffuse neutrino searches and could contribute significantly to background expectations. The most referred to calculations for the prompt neutrino flux were done by Endberg et al. [128].

* $D^0 : c\bar{u}, \bar{D}^0 : u\bar{c}, D^+ : c\bar{d}, D^- : d\bar{c}$

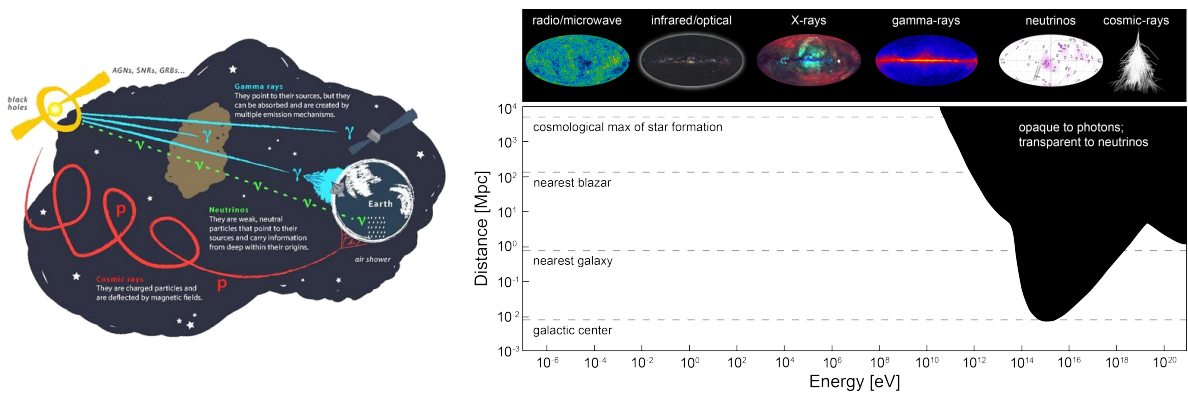


Figure 3.12: *Left:* Artist impression of the path that several types of particles travel before reaching Earth. *Right:* Illustration of the visibility of sources in function of their distance and the photon energy. The signature dip in the photon visibility comes from the pair production peak when photons interact with the CMB. Both illustrations from the IceCube collaboration.

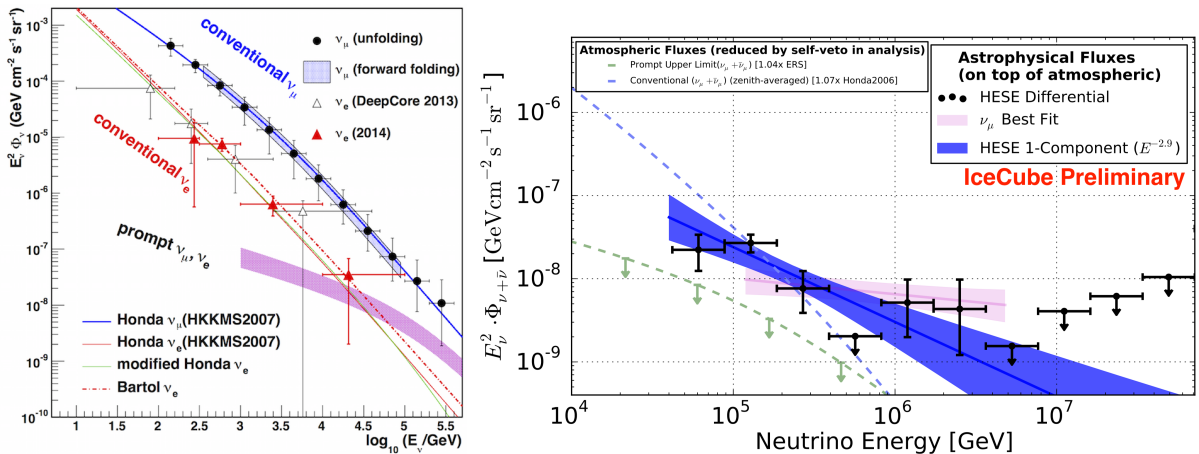


Figure 3.13: *Left:* Measurement from the IceCube collaboration showing the difference in ν_e and ν_μ flux. *Right:* Measured differential astrophysical flux using contained events (points) and a fit to that data (blue line and band), compared with the best fit obtained from through-going ν_μ (pink line and band). From Ref. [126].

3.2.3 Astrophysical

Astrophysical neutrinos are expected to be created when cosmic rays interact close to their interaction sites. Because they are neutral and are unlikely to be absorbed, astrophysical neutrinos are expected to reveal more information about these sources. To first order, these neutrinos would follow the spectrum of cosmic rays at their production. As indicated in Section 3.1.4.1, this is equal to an E^{-2} powerlaw spectrum from Fermi shock acceleration. The majority of these neutrinos are expected to arise from decays from pions that were created in these cosmic-ray interactions ($\pi \rightarrow \mu + \nu_\mu$) followed by the muon decay ($\mu \rightarrow e + \nu_e + \nu_\mu$). The resulting flavor ratio fraction is $\nu_e : \nu_\mu : \nu_\tau = 1 : 2 : 0$ at the source. Neutrino oscillations* across cosmological distances give an expected $\nu_e : \nu_\mu : \nu_\tau = 1 : 1 : 1$ expectation at Earth. As can be seen in Fig. 3.13.

The spectrum is expected to follow a harder spectrum compared to the conventional and prompt neutrinos and dominate at the highest energies.

*Explained in Section 1.3.4.

3.2.4 Other neutrino sources

The abovementioned neutrino sources are most important for high-energy neutrino research. Other, more abundant sources, play less of a role in kilometer scaled detectors but are briefly mentioned below.

3.2.4.1 Cosmological

Similar to the photons from the CMB, neutrinos would have been able to decouple from matter only seconds after the Big Bang. Due to the expansion of the universe, the temperature of the neutrinos has dropped to ≈ 1.95 K due to redshift. At these energies, direct detection is near to impossible. They have no measureable effect in large-scale neutrino detectors.

3.2.4.2 Solar

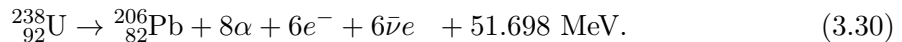
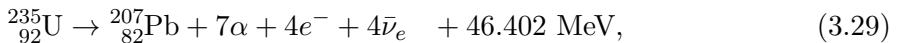
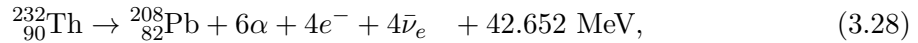
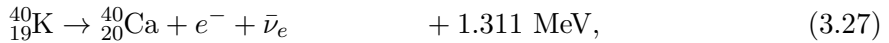
Nuclear fusion in the Sun is responsible for the production of electron neutrinos and is the largest contribution of neutrinos that can be detected on Earth. 86% of neutrinos are produced by the proton-proton reaction

$$p + p \rightarrow d + e^+ + \nu_e. \quad (3.25)$$

The remaining part is produced by reactions that involve more heavy particles. Having energies < 20 MeV, these neutrinos have no measurable effect in neutrino telescopes.

3.2.4.3 Terrestrial neutrinos

Radioactive decays from ^{40}K , ^{232}Th and ^{238}U account for almost all geoneutrinos. The reactions give rise to neutrinos from beta decay [129]



The maximal energies of these neutrinos are again too low to give a contribution to neutrino telescopes.

3.2.4.4 Reactor neutrinos

Nuclear reactors harness energy from the splitting (fission) of heavy nuclei into lighter fission products. These neutron-rich daughter particles undergo beta decays ($n \rightarrow p + e^- + \bar{\nu}_e$). Reactor neutrinos are therefore always antineutrinos. The energy spectrum reaches a maximum around 10 MeV, making them again invisible for neutrino telescopes.

3.2.4.5 Supernova neutrinos

The core collapse of stars where electrons and protons are compressed into neutrons as described in Section 3.1.4.1 dissipates most of its energy in the production of neutrinos ($e^- + p^+ \rightarrow n + \nu_e$) [130]. Depending on the distance of the source to the detector, supernovae are only visible in a collective raise of the dark noise of the equipment [131].

3.3 Air showers

Moeten air showers als aparte sectie? Zou ook als onderdeel van cosmic rays kunnen geschreven worden...

When primary cosmic ray particles hit the Earth's atmosphere, they give rise to a large shower of secondary particles. At low- to mid-energy ranges, the abundance of cosmic rays is large enough for these showers to be analyzed with balloon or satellite experiments. As indicated in Section 3.1.2, the flux of high-energy cosmic rays is so small that there is a need for very

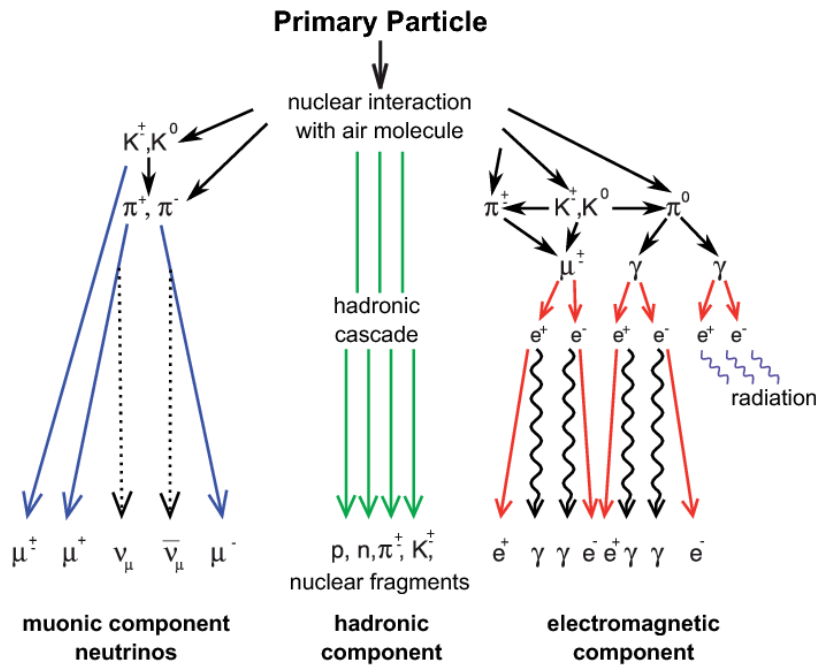


Figure 3.14: Schematic view of an extensive air shower with a clear distinction between the three components. Image from the KASKADE collaboration.

large-scale detectors, measuring kilometers in instrumented area.

The interaction length of nuclei with high energies is too small for them to be able to travel further than tens of kilometers in height. They will interact with an atmospheric nucleus and produce secondary particles. These particles, on their turn, decay or further interact with the atmosphere and give rise to an *extensive air shower* (EAS) if the production of new particles is large enough. Some of these particles will be stopped, but others are capable of reaching the Earth or even penetrate deep inside it. Although air showers are of significant importance in cosmic ray studies, we will only give a brief summary of the most noteworthy features and its main importance for this analysis. An air shower has three components: the hadronic, muonic and electromagnetic. The hadronic component can be seen as the core of the shower, consisting of high-energy hadrons. The interactions and subsequent decays of these hadrons fuel the electromagnetic and muonic parts. A schematic overview is given in Figure 3.14. If the primary particle is a photon, the shower is made up almost exclusively of an electromagnetic component. Because the lateral size of an electromagnetic cascade is caused by multiple scatterings of electrons and positrons, the lateral size of these showers is relatively small (radius around 1 km for a transversely downgoing 100 TeV photon). In hadronic cascades, on the other hand, the lateral size is caused by the transverse momenta of the secondary particles making these showers much larger (radius around 4 km for a transversely downgoing 100 TeV proton) [132].

3.3.1 Hadronic component

When a proton interacts with a nucleus, it interacts with a proton or neutron and will most often produce charged or neutral pions

$$\begin{aligned} p + N &\rightarrow p + N + k\pi^+ + k\pi^- + r\pi^0, \\ p + N &\rightarrow n + N + (k+1)\pi^+ + k\pi^- + r\pi^0, \end{aligned} \tag{3.31}$$

where N stands for a nucleon of an atmospheric nucleus and k and r are the multiplicities of the produced pions. The example for heavier nuclei from this is straightforward. On average, one-third of the hadron production will be neutral pions, which decay immediately into electromagnetic particles

$$\pi^0 \rightarrow \gamma + \gamma \quad (98.8\%) \text{ or} \quad (3.32)$$

$$\pi^0 \rightarrow e^+ + e^- + \gamma \quad (1.17\%). \quad (3.33)$$

The other two-thirds will be charged particles and have a lot longer lifetime, making them much more probable to interact with air nuclei. After having traveled a distance corresponding to their mean interaction length, charged particles interact again with air nuclei if their energy is large enough. 90% of these charged particles are new pions and 10% of the daughter particles are kaons. Pions almost exclusively decay into muons ($\pi^+ \rightarrow \mu^+ + \nu_\mu$) and the most dominant kaon decay modes are (similar for K^-) [40]

$$\begin{aligned} K^+ &\rightarrow \pi^+ + \pi^0 & (20.7\%), \\ K^+ &\rightarrow \mu^+ + \nu_\mu & (63.6\%), \\ K^+ &\rightarrow \pi^0 + e^+ + \nu_e & (5\%), \\ K^+ &\rightarrow \pi^0 + \mu^+ + \nu_\mu & (3.4\%), \end{aligned} \quad (3.34)$$

where the first decay mode fuels the hadronic component further. The remaining decay modes enter in the EM and muonic components. The total number of hadrons reaching sea level is very small and when they do, they are immediately stopped.

3.3.2 Muonic component

Muons are the dominant component of particles reaching sea level (around 80%). Most muons that are produced in an EAS are able to reach so far due to their relativistic velocities and lifetime of $2.2 \mu\text{s}^*$. They have relatively low ionization losses compared to electrons, making them very penetrating and are therefore referred to as the *hard component*. Muons can also decay and contribute to the electromagnetic component via

$$\begin{aligned} \mu^+ &\rightarrow e^+ + \nu_e + \bar{\nu}_\mu, \text{ and} \\ \mu^- &\rightarrow e^- + \bar{\nu}_e + \nu_\mu. \end{aligned} \quad (3.35)$$

3.3.3 Electromagnetic component

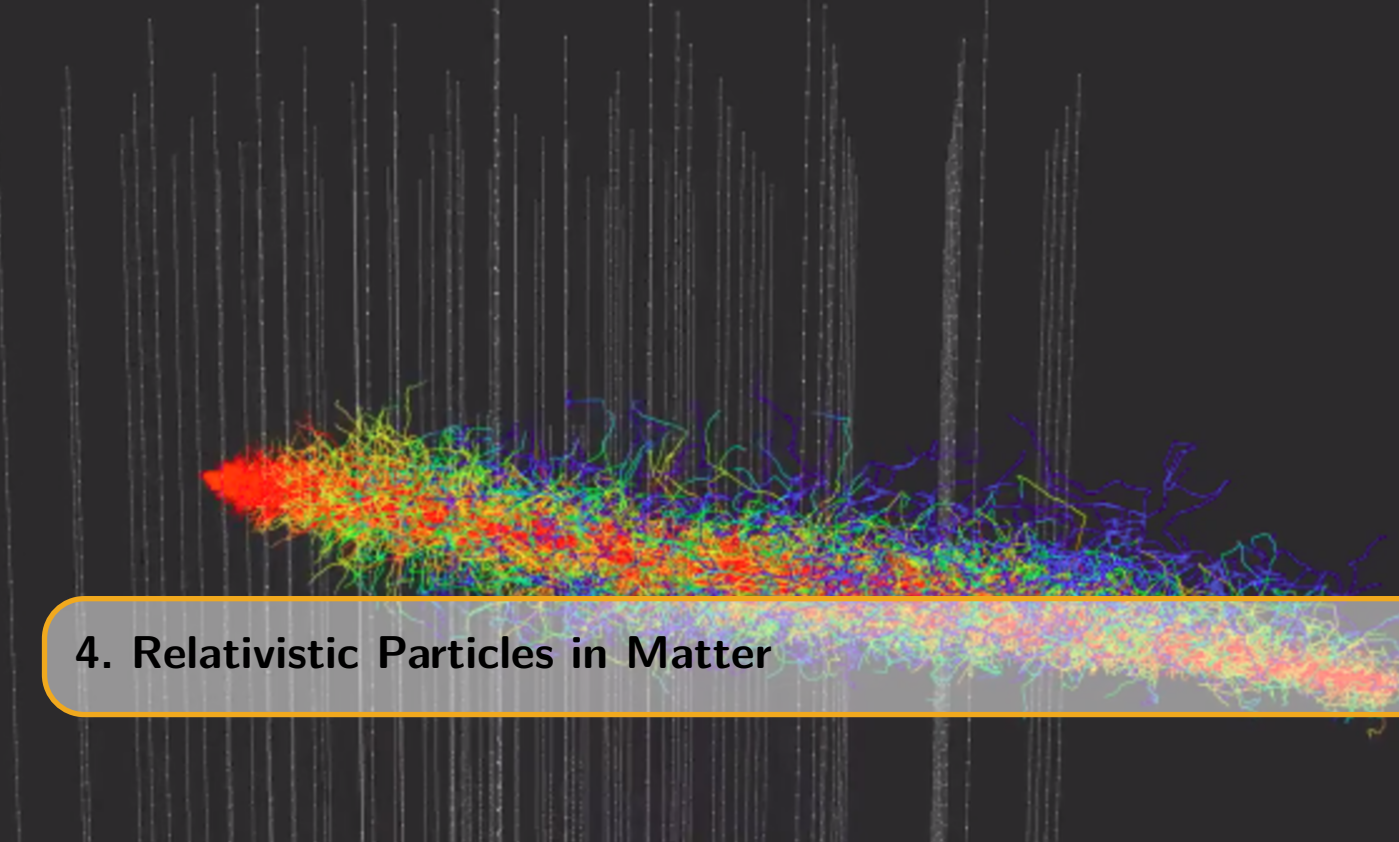
At each hadronic interaction, slightly more than a third of the energy goes into the electromagnetic component. Since most hadrons re-interact, eventually most of the primary energy finds its way into the electromagnetic component. Muons can produce delta electrons or electron-positron pairs from pair production (see Section 1.3.3).

At energies above a few MeV, photons interact with matter via pair production and convert into an electron-positron pair. High-energy electrons and positrons primarily emit photons via bremsstrahlung. These two processes are repeated until the photons fall below the pair production threshold and bremsstrahlung energy loss starts to dominate. Because electrons lose their energy fast, they are almost immediately stopped when they reach dense matter (Earth's surface) and hence referred to as the *soft component*.

3.4 Cosmic ray and neutrino detectors

Doen of niet? Kan een interessante overgang geven naar hoofdstuk 5 en IceCube meer introduceren... Kan ook teveel info zijn. In 10-tal zinnen?

*The half-survival length of 5 GeV muons is $L = \ln(2) \times \gamma \times 2.2 \mu\text{s} \times 0.9998 \times c = \gamma \times 456 \text{ m} \approx 23 \text{ km}$. The relativistic time dilation is of crucial importance here!



4. Relativistic Particles in Matter

*Hofstadter's Law: It always takes longer than you expect, even when you take into account
Hofstadter's Law*

Neutrinos are notoriously difficult to detect. When high-energy neutrinos interact with matter, they produce secondary particles that travel fast enough to produce Cherenkov radiation. As indicated in Section 3.4, cubic-sized experiments try to exploit these properties by using natural ice or water as the instrumented volume. In this chapter an overview of the behaviour of relativistic matter is given. The experiment that is used here is the IceCube detector and therefore, there will be a larger focus on ice.

4.1 Neutrino interactions

Neutrinos interact with matter in both charged current (CC) and neutral current (NC) processes. In the former, the mediator particle is a charged W boson resulting in a charged lepton in the final state. In the latter, the mediator particle is the neutral Z boson. Both interaction types have a resulting hadronic component as daughter particles. The interactions can be written as

$$\nu_l (\bar{\nu}_l) + N \xrightarrow{W} l^- (l^+) + X^{+(-)} \quad (CC) \quad (4.1)$$

$$\nu_l (\bar{\nu}_l) + N \xrightarrow{Z} \nu'_l (\bar{\nu}'_l) + X \quad (NC), \quad (4.2)$$

where l is the lepton flavor (e, μ, τ), N denotes the initial hadronic state of the nucleus and X the final hadronic state. These interactions are illustrated in Figure 4.1.

The charged leptons and hadrons lead to light production via gamma ray production and Cherenkov radiation. With the right material, it is possible to detect this light production and reconstruct some of the neutrino's characteristics.

4.2 Cherenkov effect

From Einstein's works on special and general relativity, it follows that the speed of light in vacuum, c , is a universal constant. The speed of light in matter can be significantly lower than

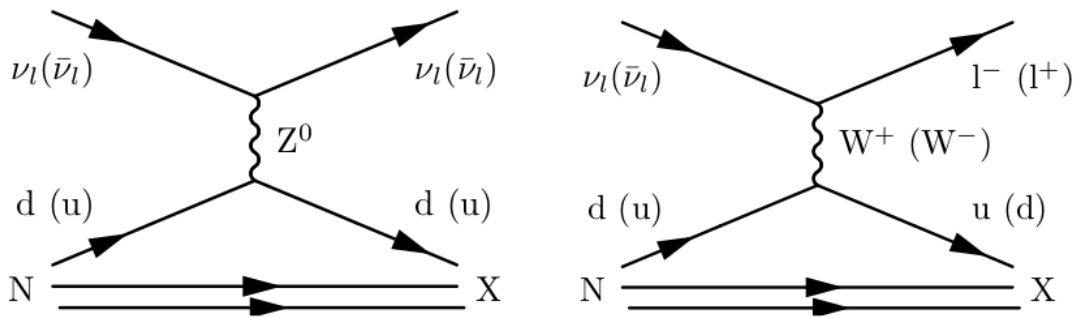


Figure 4.1: Feynman diagrams of the NC (*left*) and CC (*right*) neutrino interactions. l is the lepton flavor (e, μ, τ), N denotes the initial hadronic state of the nucleus and X the final hadronic state. The antineutrino interactions are given in between brackets.

that. If a particle travels through a dielectric medium at a speed that is greater than the phase velocity of light in that medium, electromagnetic radiation is emitted. This radiation is called *Cherenkov radiation* and is named after the first person who was able to detect it experimentally, Pavel Cherenkov. He was awarded the Nobel Prize in 1958 for his findings together with Frank and Tamm on their theoretical work on the subject [133].

As can be seen in Appendix B, Eq. B.1, the velocity of a propagating wave is given by

$$\nabla^2 \psi = \frac{1}{v^2} \frac{\partial \psi}{\partial t}, \quad (4.3)$$

where ψ is the wave function and v its group velocity. From Maxwell's equations and some vector calculus, it is straightforward to find that the wave equation for electromagnetic radiation becomes

$$\nabla^2 E = \mu \epsilon \frac{\partial E}{\partial t}, \quad (4.4)$$

where E is the electric field and μ and ϵ the permeability and permittivity of the medium respectively. From these equations it is clear that for light in a dielectric medium

$$v = \frac{1}{\sqrt{\mu \epsilon}} = \frac{1}{\sqrt{\mu_r \epsilon_r}} \frac{1}{\sqrt{\mu_0 \epsilon_0}} = \frac{1}{\sqrt{\mu_r \epsilon_r}} \times c \leq c, \quad (4.5)$$

where $1/\sqrt{\mu_0 \epsilon_0} = c$ and μ_r and ϵ_r are the relative (to vacuum) permeability and permittivity respectively and are ≥ 1 . These terms are also written as the refractive index $n = \sqrt{\mu_r \epsilon_r}$: $v = c/n$.

When a charged particle moves inside a dielectric medium, it excites the molecules of the medium to the higher levels and excited states. The molecules emit photons in the form of electromagnetic radiation upon returning back to their ground state. According to the *Huygens principle*, the emitted waves move out spherically at the phase velocity of the medium (which can be less than the speed of light in vacuum). If the motion of the particle is slow, the radiated waves bunch up slightly in the direction of motion, but they do not cross. However, if the particle moves faster than the light speed, the emitted waves add up constructively leading to a coherent radiation at angle θ_c with respect to the particle direction; Cherenkov radiation. The coherent interference is enough to be visible to the naked eye*. The signature of the effect is a cone of emission in the direction of particle motion. Fig. 4.2 shows a schematic view of the Cherenkov radiation, illustrating the typical spherical wavefront and the resulting radiation†.

From the figure we can derive that

*The typical blue light in the cooling water at nuclear reactor sites is also due to this Cherenkov radiation.

†Note of the author: the typical cone shape of this effect can be easily seen when observing ducks. If a duck is traveling in a straight line in the water, individual concentric waves can be distinguished and a cone shaped wave is produced behind them.

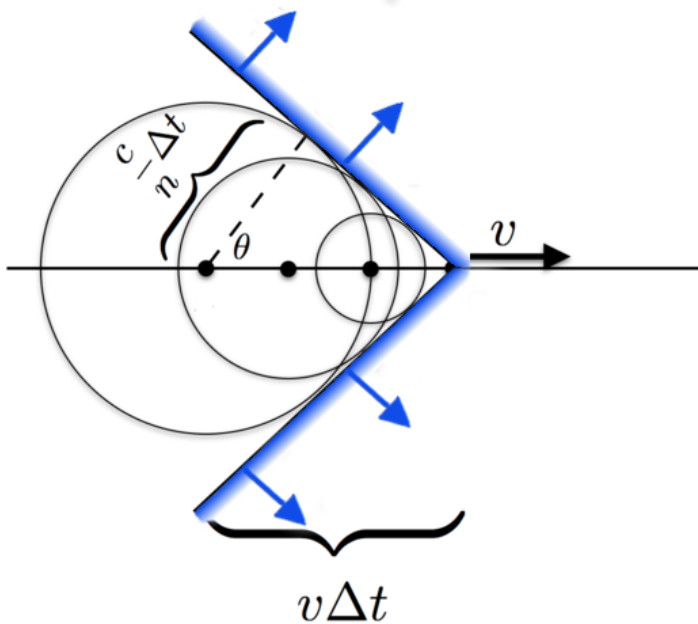


Figure 4.2: Schematic overview of Cherenkov radiation from a particle traveling at a velocity v .

$$\cos \theta_c = \frac{c}{v\Delta t} = \frac{c}{vn} = \frac{1}{\beta n}. \quad (4.6)$$

Because $-1 \leq \cos \theta_c \leq 1$, the velocity of the charged particle must be $v \geq c/n$. Typical values of n are on the order of 1-2, requiring the particles to be relativistic in order to emit Cherenkov radiation. The number of photons produced per unit path length of a particle with charge ze and per unit energy interval of the photon was calculated by Frank and Tamm, and is often referred to as the Frank-Tamm equation [40]

$$\begin{aligned} \frac{d^2N}{dEdx} &= \frac{\alpha z^2}{\hbar c} \sin^2 \theta_c = \frac{\alpha^2 z^2}{r_e m_e c^2} \left(1 - \frac{1}{\beta^2 n^2(E)} \right) \\ &\approx 370 \sin^2 \theta_c(E) \text{ eV}^{-1} \text{cm}^{-1} \quad (z=1), \end{aligned} \quad (4.7)$$

where r_e is the classical electron radius, m_e the electron mass and α the fine-structure constant. Equivalently, this equation can be written in function of the wavelength of the photon

$$\frac{d^2N}{dxd\lambda} = \frac{2\pi\alpha z^2}{\lambda^2} \left(1 - \frac{1}{\beta^2 n^2(\lambda)} \right), \quad (4.8)$$

where it is clear that the charge of the particle will influence the total Cherenkov light yield. A charge of 1/3 will reduce the light output with a factor of 9! As an example, air Cherenkov telescopes such as MAGIC, H.E.S.S and VERITAS look for the direct and indirect Cherenkov light from gamma rays and cosmic rays. Because the refractive index of air is close to 1 (1.000293 at sea level and smaller with increasing height) the opening angle of the Cherenkov cone is small ($\approx 1^\circ$). The particles need to be very relativistic in order for Cherenkov radiation to occur*.

In water and ice, the refractive index is ≈ 1.33 , making $\beta_{min} = 0.75$ and $E_{min} = 1.51 \cdot m_0$. Experiments using water or ice as the interaction medium are Super-Kamiokande, ANTARES and the IceCube experiment.

*Let us assume the refractive index of air at sea level, then, from $E^2/m^2 = \gamma^2 = 1/(1 - \beta^2)$, it follows that the minimal energy is ≈ 41 times its rest mass. Since the refractive index decreases in function of height, the energies of particles interacting with the atmosphere must be even higher.

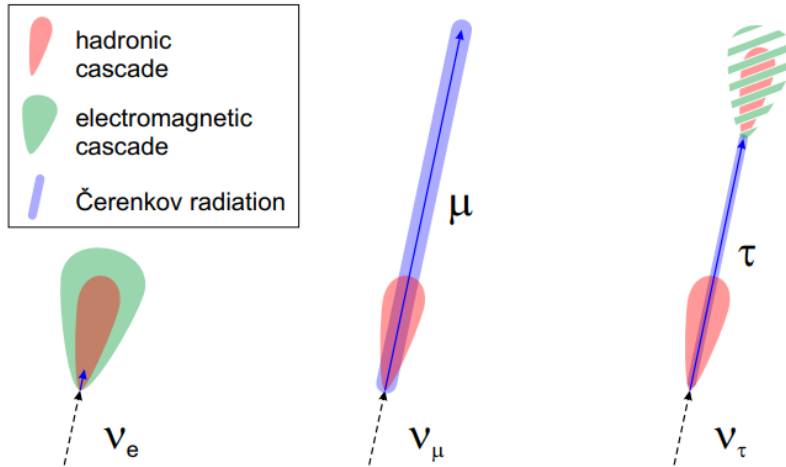


Figure 4.3: Schematic view of the neutrino signatures in matter. At each interaction point there is a hadronic cascade (red). Every hadronic cascade has electromagnetic sub-showers which are not illustrated here. Muons and energetic taus can give rise to tracks. Illustrations from Ref. [134].

4.3 Propagation

As described in Section 4.1, neutrinos will give rise to several types of interactions in the surrounding medium. There are three characteristic signatures, which are the main interest in the IceCube detector (illustrated in Figure 4.3).

4.3.1 Cascades

4.3.1.1 Electrons and photons

In a charged current neutrino interaction, the energetic electron will give rise to a shower of gamma rays (bremsstrahlung) and positrons and electrons (pair production). Positrons and electrons will in their turn emit new gamma rays and this process continues until the photon energies fall below the pair production threshold. Because electrons/positrons lose their energy fast, they are almost immediately stopped, giving an *electromagnetic cascade* a spherical shape.

Let us assume E_0 is the energy of the incoming electron. In a very simplistic toy model one can say that an electron emits one photon after one radiation length, X_0 . A photon will decay into an electron-positron pair after approximately one radiation length too*. At every decay or radiation process it is assumed that the daughter particles carry 1/2 of the energy. After t steps, the energy is equal to

$$E(t) = \frac{E_0}{2^t}. \quad (4.9)$$

The number of particles will be equal to

$$N(t) = 2^t. \quad (4.10)$$

At a critical energy E_c , the multiplication process stops (as pair production dominates over bremsstrahlung) and we find

$$t_{max} = \frac{\ln\left(\frac{E_0}{E_c}\right)}{\ln 2}, \quad (4.11)$$

the total longitudinal length of an electromagnetic shower is thus approximately equal to

*In fact one radiation length implies $1/e$ times the initial energy. Assuming the electron loses half its energy into the photon, then $0.63/0.5 \approx 1$. After one radiation length, a high energy photon loses $\approx 7/9$ times its energy via bremsstrahlung, again we assume ≈ 1 .

$$X = X_0 \frac{\ln\left(\frac{E_0}{E_c}\right)}{\ln 2}. \quad (4.12)$$

This logarithmic dependence on the energy of the initial particle will therefore result into elongations of a couple of meters at most. Typical values in ice are $X_0 \approx 40$ cm and $E_c \approx 80$ MeV.

4.3.1.2 Hadrons

In the case of neutral current events, the breakup of the struck nucleus leads to charged byproducts. These byproducts can reinteract in the medium and produce neutral pions that decay into gamma rays. These particles again die out quickly, resulting in a spherical emission of light for *hadronic cascades*. The basic development of hadronic cascades in space is very similar to that of electromagnetic ones, but with important differences in energy losses, particle content, lateral spread and fluctuations. Hadronic cascades contain particles heavier than electrons, that have a higher Cherenkov threshold. A fraction of them are slow neutrons, which do not produce any light. Neutral pions produce gamma rays. Charged pions, on the other hand, can decay into muons and muon neutrinos; long-ranged particles that do not contribute to the cascading process. Finally, a non-negligible fraction of the energy is lost in the hadronic binding processes.

The light yield will be smaller than the one obtained from an electromagnetic cascade of equal initial energy and with much larger event-by-event variations.

4.3.2 Muon tracks

Muons are produced in charged current muon neutrino interactions and travel much further than electrons and positrons. The relativistic muon will produce light according to the Frank-Tamm equation, Eq. 4.8, resulting in *direct Cherenkov radiation*. Ionization, bremsstrahlung, pair production, and photonuclear interactions (see Section 4.4) are also capable of producing relativistic secondary particles that will produce *indirect Cherenkov radiation*. Both effects result in a Cherenkov cone with a diffuse light emitting out from the track in all directions behind it.

4.3.2.1 Energy loss

Below 1 TeV, muons will lose most of its energy to ionization losses. A charged particle traversing matter will ionize the material around it. When the energy transfer is high enough, electrons can be stripped away from their atoms, resulting in *delta electrons*. As can be seen in Figure 4.4, ionization losses have only a very weak energy dependence. It is therefore very difficult to distinguish for example a 50 GeV from a 500 GeV muon as the direct Cherenkov light production will be similar (Eq. 4.8) and the energy loss will be from the energy-independent ionization.

Above 1 TeV, however, the muon will on average lose more energy to stochastic* effects. Here, effects such as bremsstrahlung, pair production and the photonuclear effect dominate over ionization. Indirect Cherenkov production starts to dominate and make the energy estimation much easier.

The average energy loss along the muon trajectory can be parametrized by

$$-\frac{dE}{dx} = a + b \cdot E_\mu, \quad (4.13)$$

where a and b are obtained by fitting and can be found in Table 4.1†. The muon range can be found by integrating Eq. 4.13

$$R_\mu \approx \frac{1}{b} \ln\left(\frac{E_\mu}{E_{th}} + 1\right), \quad (4.14)$$

*In this context we mean the energy losses are not deterministic: it is impossible to know when an interaction of this kind will occur. One can only make estimations on their *expected* effects.

†Mwe stands for “meter water equivalent”, a unit often used in cosmic ray physics. A detector shielded by matter equal to 100 mwe would be equally shielded from cosmic rays if it were 100 meters below water.

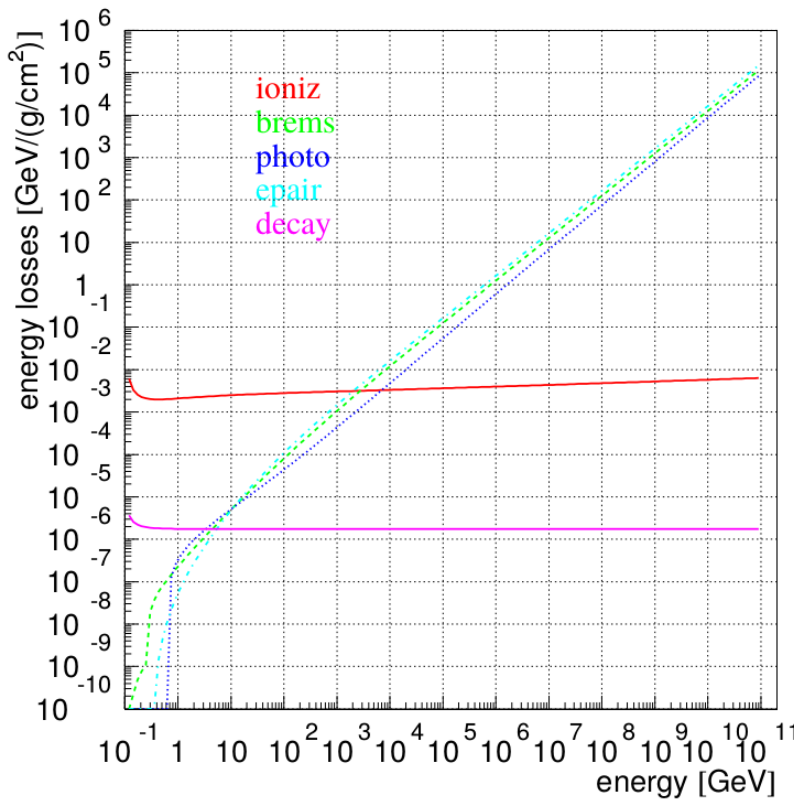


Figure 4.4: Muon energy loss from ionization (upper solid curve), bremsstrahlung (dashed), photonuclear (dotted), pair production (dashed-dotted) and decay (lower solid curve).

Table 4.1: Best fits for muon energy loss parameters a and b from Eq. 4.13. Fits from [135].

Medium	$a \left(\frac{\text{GeV}}{\text{mwe}} \right)$	$b \left(\frac{10^{-3}}{\text{mwe}} \right)$
Air	0.281	0.347
Ice	0.259	0.363
Fr. Rock	0.231	0.436
St. Rock	0.223	0.463

with $E_{th} = a/b = 720$ GeV, the energy threshold above which stochastic effects are dominant. Contained muon events can therefore have a decent energy estimation as well.

4.4 Energy loss formulae

As mentioned in Section 4.3.2.1, secondary interactions become non-negligible at certain energies. These effects are accounted for in IceCube simulations and are of great importance for muons. Since these interactions are electromagnetic in nature, they will also play a role for SMP particles. In this section we go over the four main components of secondary interactions. This section is largely based on the findings in [135]. The energy of the secondary particles will be expressed with $\nu = vE$, with E the energy of the incident particle and v the fraction of the energy transfer. Secondary interactions occur at all energy levels and become continuous in nature below a certain energy threshold. Therefore, in many codes v_{cut} is implemented as a lower bound (more information see Section 4.4).

Ionization

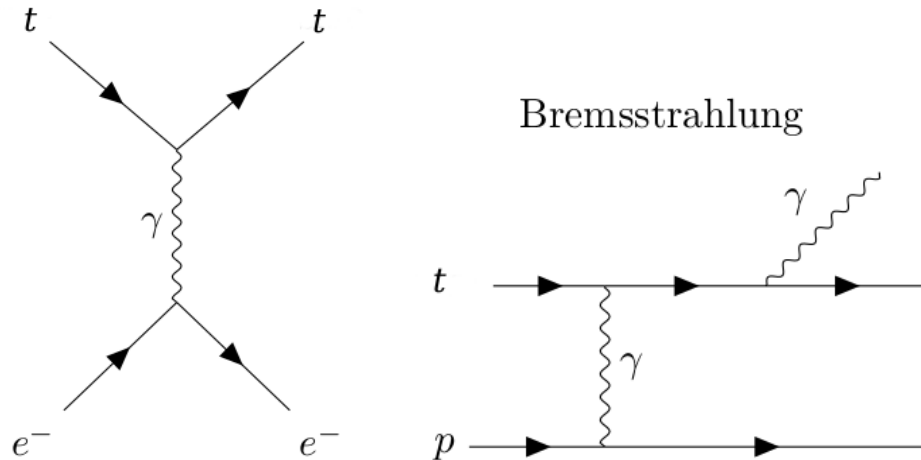


Figure 4.5: Feynman diagrams of the an ionization interaction (left) and bremsstrahlung (right). t denotes the throughgoing particle.

4.4.1 Ionization

Fast charged particles that move through matter will interact with the electrons of atoms in the material. The interaction will excite or ionize* the atoms. The Feynman diagram of this interaction is given in Fig. 4.5 (left). This interaction will lead to an energy loss of the traveling particle and is expressed via the Bethe-Bloch formula

$$\begin{aligned}
 -\left\langle \frac{dE}{dx} \right\rangle = & K z^2 \frac{Z}{A \beta^2} \left[\frac{1}{2} \ln \left(\frac{2m_e \beta^2 \gamma^2 \nu_{upper}}{I(Z)^2} \right) - \frac{\beta^2}{2} \left(1 + \frac{\nu_{upper}}{\nu_{max}} \right) + \frac{1}{2} \left(\frac{\nu_{upper}}{2E(1+1/\gamma)} \right)^2 - \frac{\delta}{2} \right], \\
 \text{where } \nu_{upper} = & \min(\nu_{cut}, \nu_{max}) \quad \text{and} \quad \nu_{max} = \frac{2m_e(\gamma^2 - 1)}{1 + 2\gamma \frac{m_e}{m_t} + \left(\frac{m_e}{m_t} \right)^2}
 \end{aligned} \tag{4.15}$$

where K is equal to $4\pi N_A r_e^2 m_e c^2$, N_A is Avogadro's number, r_e the classical electron radius, m_e the electron mass, z the charge of the particle (in multiples of the electron charge), Z the atomic number of the absorber, A the atomic mass of the absorber, I the mean excitation energy of the absorber and m_t the mass of the throughgoing particle. The density correction δ can be found in the corresponding literature.

For particles in the region of $0.1 \leq \beta\gamma \leq 1000$ this is the dominant factor in the mean energy loss. The cross section giving rise to this energy loss equation is expressed as

$$\frac{d^2N}{d\nu dx} = \frac{1}{2} K z^2 \frac{Z}{A} \frac{1}{\beta^2} \frac{1}{\nu^2} \left[1 - \beta^2 \frac{\nu}{\nu_{max}} + \frac{1}{2} \left(\frac{\nu}{E(1+1/\gamma)} \right)^2 \right], \tag{4.16}$$

where negligible terms are left out.

4.4.2 Bremsstrahlung

Charged particles that decelerate by another charged particle lose kinetic energy that is converted into radiation. This phenomena is known as *bremsstrahlung* and is illustrated in Fig. 4.5 (right). The cross section may be represented by the sum of an elastic component and two inelastic components,

*In this case, one often refers to these electrons as *delta electrons*. These electrons can be relativistic and produce Cherenkov radiation.

$$\sigma = \sigma_{el} + \Delta\sigma_a^{in} + \Delta\sigma_n^{in}, \quad (4.17)$$

where σ_{el} denotes the cross section of the Coulomb scattering of the particle from the atomic center and the two other terms are corrections that account for additional processes, in which the bremsstrahlung is accompanied by the changing of electron and nuclear structure of the atom in the final state.

4.4.2.1 Elastic component

$$\sigma_{el}(E, v) = \frac{\alpha}{v} \left(2z^2 Z \frac{m_e}{m_t} r_e \right)^2 \left(\frac{4}{3} - \frac{4}{3}v + v^2 \right) \left[\ln \left[\frac{m_t}{\delta} \right] - \frac{1}{2} - \Delta\sigma_a^{el} - \Delta\sigma_n^{el} \right], \quad (4.18)$$

where $\delta \approx \frac{\mu^2 \omega}{2E(E - \omega)}$,

where α is the fine structure constant and ω the photon's frequency. The atomic and nuclear formfactors are

$$\begin{aligned} \Delta\sigma_a^{el}(\delta) &= \left[1 + \frac{1}{\delta \sqrt{e} B Z^{-1/3} / m} \right] \\ \Delta\sigma_n^{el}(\delta) &= \left[\frac{D_n}{1 + \delta(D_n \sqrt{e} - 1) / m_t} \right] ; D_n = 1.54 A^0 . 27. \end{aligned} \quad (4.19)$$

Other constants are as defined in Eq. 4.15. Other parametrizations can be found in the corresponding literature.

4.4.3 Inelastic component

The effect of nucleus excitation can be evaluated as

$$\Delta\sigma_n^{in} = \frac{1}{Z} \Delta\sigma_n^{el}; (Z \neq 1), \quad (4.20)$$

where $\Delta\sigma_n^{el}$ is defined in Eq. 4.19.

In the atomic excitation, one accounts for bremsstrahlung whereby photons can radiate from the throughgoing particle and where photons radiate from the electrons of the atom. This contribution is

$$\Delta\sigma_a^{in} \approx \frac{1}{Z} \ln \left[\frac{m_t / \delta}{\delta m_t / m_e^2 + \sqrt{e}} \right] - \ln \left[1 + \frac{m_e}{\delta \sqrt{e} B' Z^{-2/3}} \right], \quad (4.21)$$

where $B' = 1429$ for $Z > 2$ and $B' = 446$ for $Z = 1$.

4.4.4 Photonuclear

The photonuclear interaction of leptons is the process by which a lepton scatters inelastically with a nucleon or nucleus. Through a virtual photon exchange, hadrons are produced, as is illustrated in Fig. 4.6. The cross section formula is given by

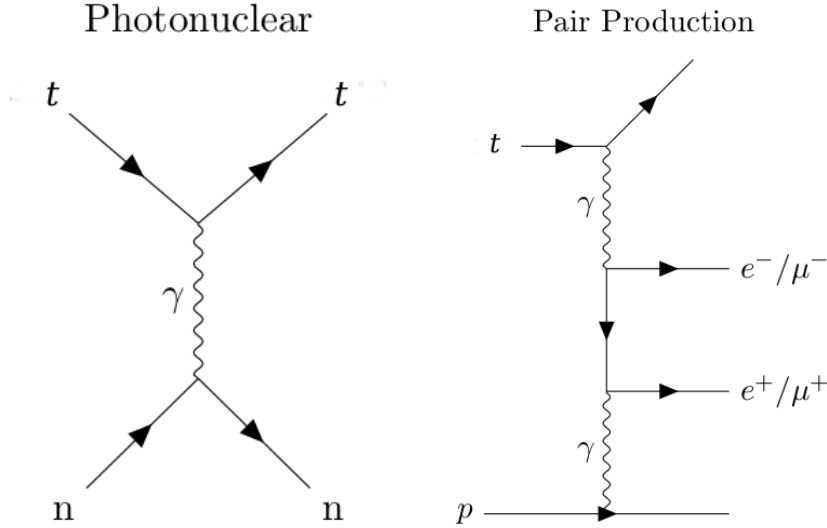


Figure 4.6: Feynman diagrams of the a photonuclear interaction (left) and pair production (right). t denotes the throughgoing particle.

$$\frac{d\sigma}{dv} = \frac{z^2 \alpha}{2\pi} A \sigma_{\gamma N} v \left\{ 0.75 G(x) \left[\kappa \ln \left(1 + \frac{m_1^2}{t} \right) - \frac{\kappa m_1^2}{m_1^2 + t} - \frac{2m_t^2}{t} + \frac{4m_t^2}{m_1^2} \ln \left(1 + \frac{m_1^2}{t} \right) \right] + 0.25 \left[\left(\kappa + \frac{2m_t^2}{m_2^2} \right) \ln \left(1 + \frac{m_2^2}{t} \right) - \frac{2m_t^2}{t} \right] + \frac{m_t^2}{2t} \left[0.75 G(x) \frac{m_1^2 - 4t}{m_1^2 + t} + 0.25 \frac{m_2^2}{t} \ln \left(1 + \frac{t}{m_2^2} \right) \right] \right\}, \quad (4.22)$$

where $t = Q_{max}^2 = \frac{m_t^2 v^2}{1-v}$, $\kappa = 1 - \frac{2}{v} + \frac{2}{v^2}$,
 $m_1^2 = 0.54 \text{ GeV}^2$, and $m_2^2 = 1.8 \text{ GeV}^2$.

Parameters that aren't defined here can be found in the corresponding literature.

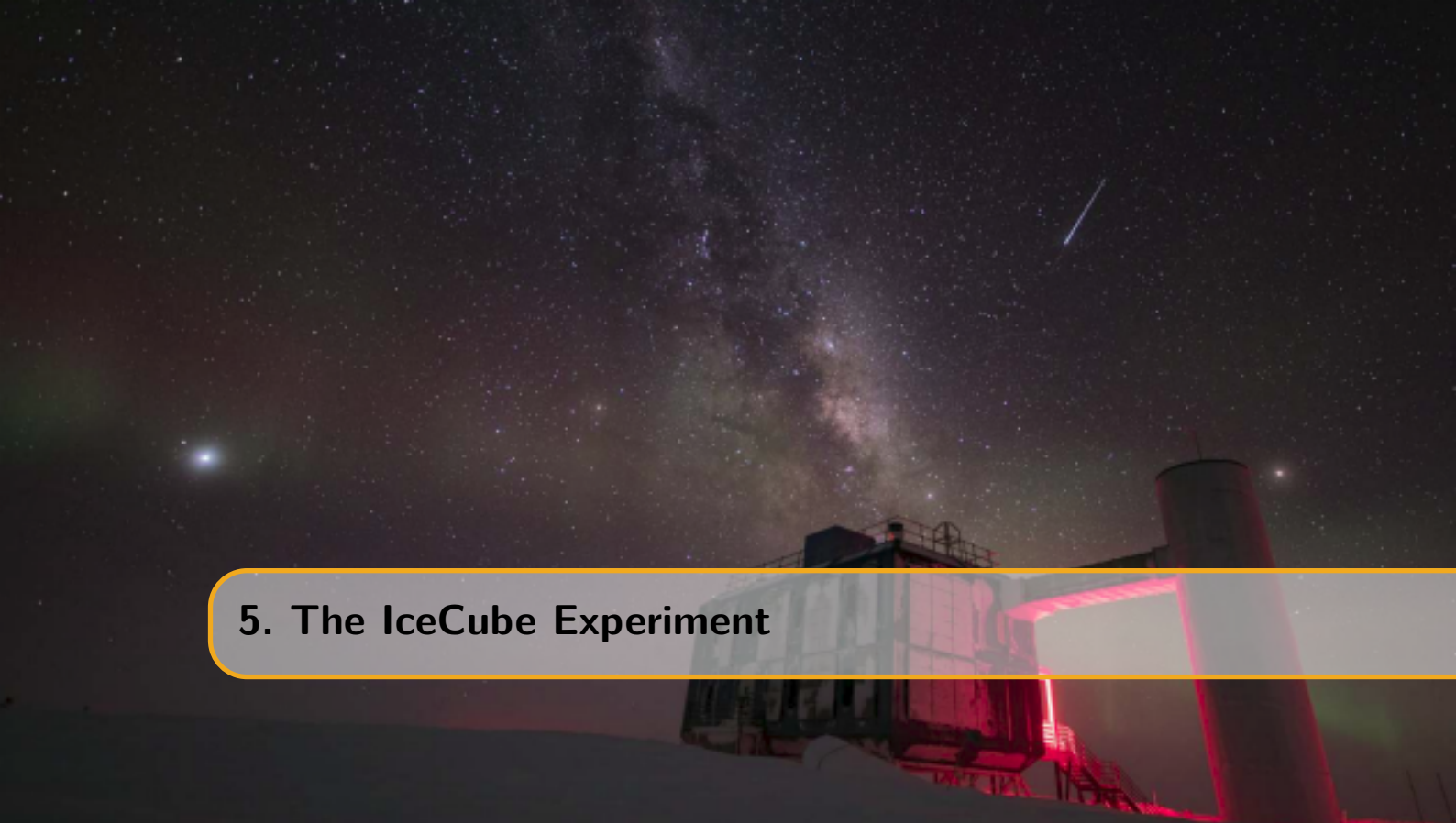
4.4.5 Pair production

Pair production occurs when the virtual photon radiated from the throughgoing particle or proton splits into an electron-positron pair or muon-antimuon pair, the differential cross section is equal to

$$\frac{d\sigma(E, v, \rho)}{dv d\rho} = \frac{2}{3\pi} Z(Z + \zeta)(z\alpha r_e)^2 \frac{1-v}{v} \left(\Phi_e + \frac{m_e^2}{m_t^2} \Phi_\mu \right), \quad (4.23)$$

where $v = (\epsilon_+ + \epsilon_-)/E$, $\rho = (\epsilon_+ - \epsilon_-)/(\epsilon_+ + \epsilon_-)$,

and ϵ_+ and ϵ_- denote the energies of the positively and negatively charged electrons/muons. The parameters not described in detail can be found in the corresponding literature.



5. The IceCube Experiment

Computers are useless; they can only give you answer ~ Pablo Picasso

IceCube is a neutrino observatory located near the Amundsen-Scott South Pole Station close to the geographic South Pole. As already introduced in Section 3.4, experiments that search for astrophysical neutrinos need to be constructed with enormous instrumented volumes. IceCube is the first gigaton neutrino detector ever built and was designed specifically for this case. It is buried beneath the surface of the Antarctic ice, starting from around 1450 meters of depth and extending to around 2,500 meters (\sim 300 meters above bedrock). The ice acts as a medium for both the interaction of a neutrino and light propagation. This chapter serves as a general overview of the several components of IceCube detector together with an introduction to the data processing.

The main goal of the IceCube experiment is to learn more about the distant sources that we believe to be responsible for the detection of the highest-energy cosmic rays. As indicated in Section 3.2, neutrinos are crucial in gaining information about these far away sources. Large-scale detectors are necessary to cover the faint flux of neutrinos with very high energies. Detecting the Cherenkov radiation (Chapter 4) from neutrino interactions is the best way to observe these weakly interacting particles. As hadronic, electromagnetic and muonic components from these interactions require a medium that extends to a couple of kilometers and has good light propagation characteristics, the South Pole ice sheet acts as a near ideal component of the detector. As a proof of concept, the AMANDA (Antarctic Muon And Neutrino Detector Array) experiment was built between 1996 and 2000 to show that neutrinos with energies above 50 GeV could be detected in the Antarctic ice [136, 137]. After construction was finalized, the detector was made up of 677 optical modules mounted on 19 separate strings that are spread out in a rough circle with a diameter of around 200 meters. These strings were deployed by first “drilling” holes in the ice with a hot-water hose, showing that the technique works. After some years of data taking, it was clear that high-energy neutrinos could be observed, paving the way for the much larger IceCube project [138].

5.1 Geometry

The IceCube detector consists of three main parts that act as different purpose physics detectors. On the surface of the ice, water tanks with optical modules inside are spread out over an area of

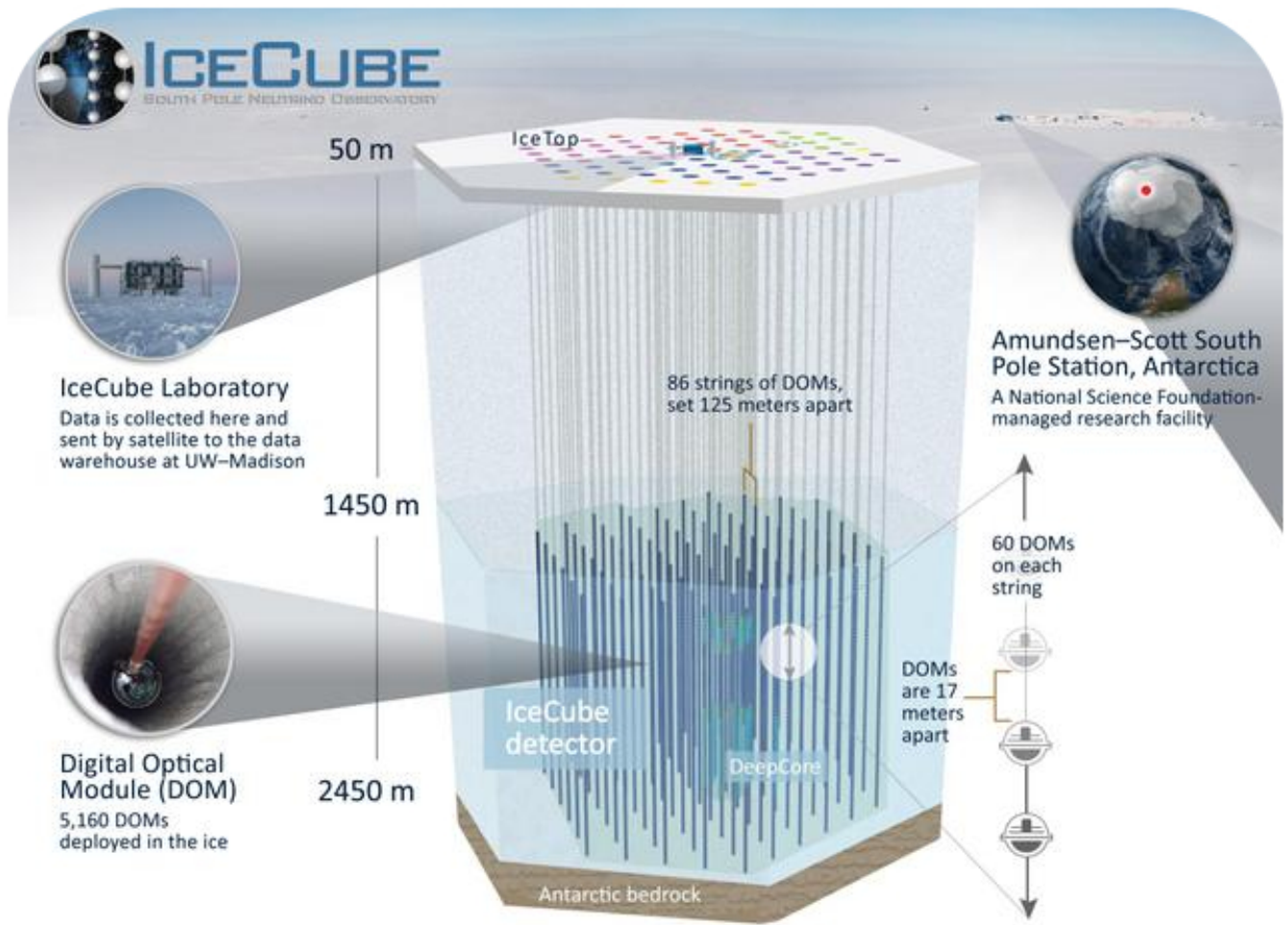


Figure 5.1: Illustration of the IceCube South Pole neutrino observatory.

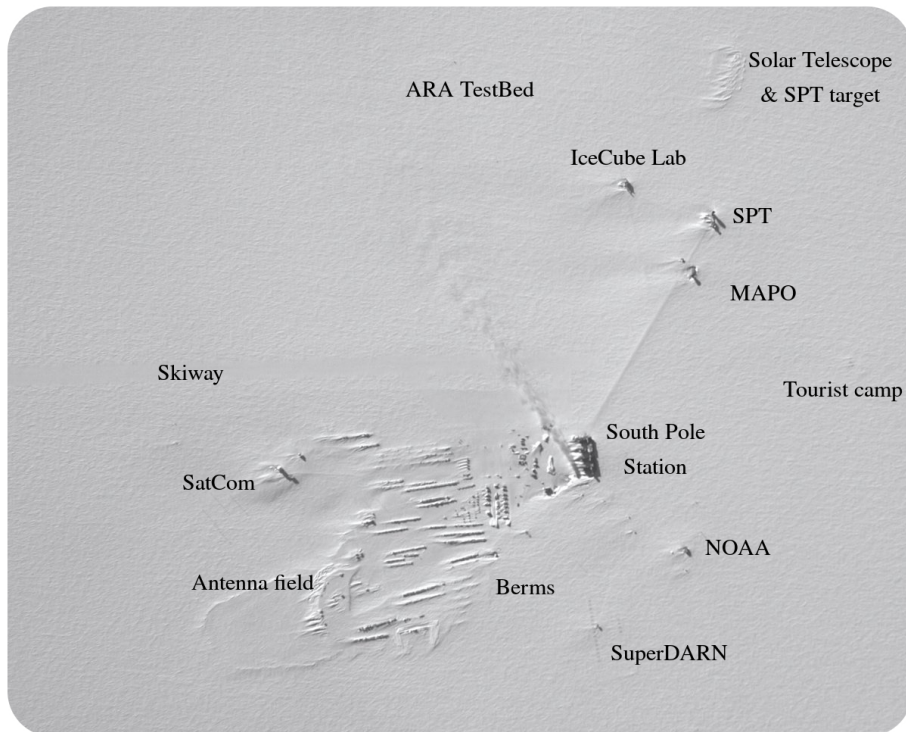


Figure 5.2: Aerial view of the South Pole. The main buildings and experimental setups are indicated in the figure. The exhaust of the South Pole Station is also visible.

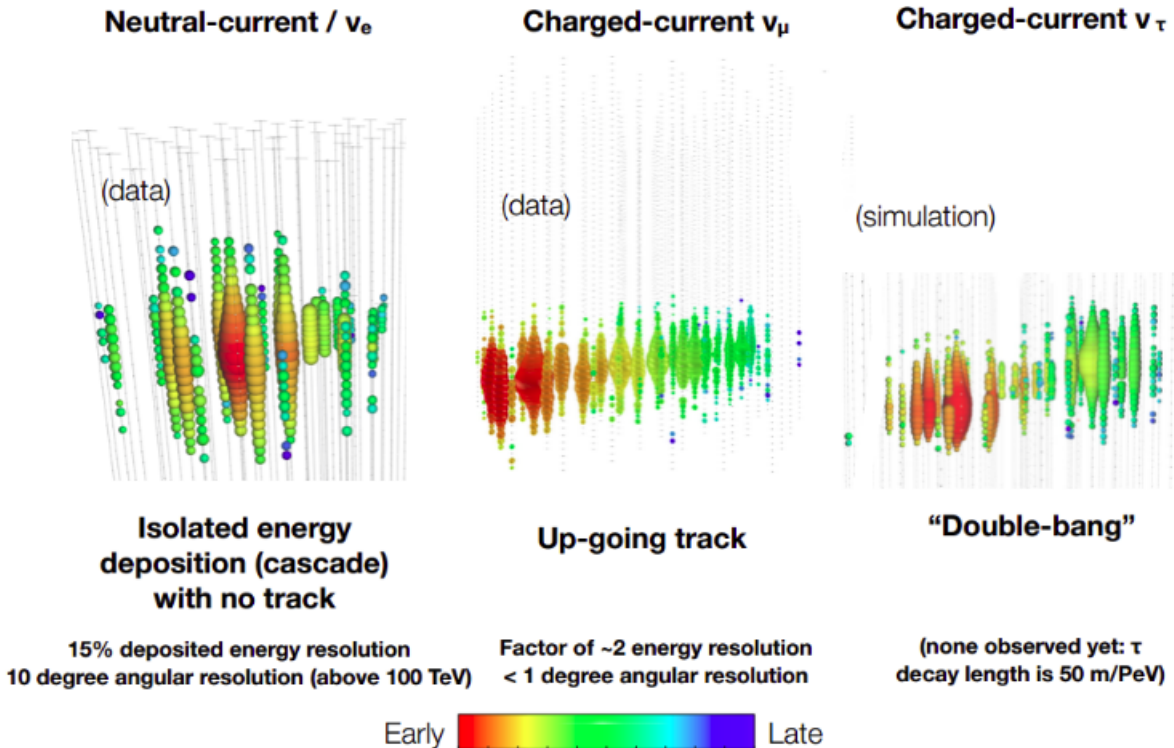


Figure 5.3: Neutrino interactions in the IceCube detector have two distinct types of interactions: cascades and tracks. Energetic taus are theorized to have double-bang signatures but have not undeniably been seen. Colors determine the timing of hits in the optical modules in the ice. Illustrations from the IceCube collaboration.

approximately 1 km² and make up the *IceTop detector*. This surface array was built as a cosmic ray detector and veto for the in-ice array. The *in-ice IceCube* detector is the main component and consists of 4680 digital optical modules. In its core, a denser subdetector, *DeepCore*, significantly enhances the capabilities for low-energy events of the observatory in a limited volume. 480 sensors form the center of the DeepCore array. The three components combined make the facility a clear multipurpose physics detector. Fig. 5.1 shows the layout of the detector.

5.1.1 In-ice array

The in-ice array consists of 4680 digital optical modules (DOMs) that are able to register light that is scattered and propagated through the ice (more info about these modules can be found in Section 5.3.1). The DOMs are attached to cables and are frozen vertically in the ice. In total, 78 of these “strings” were frozen into boreholes and arrayed over a cubic kilometer in a hexagonal shape. Because the ice is only transparent deep within, the DOMs are attached to the strings starting from a depth of 1450 meters to 2450 meters. The strings, as viewed from above, are spaced around 125 meters apart and along each string, 60 DOMs are attached with a vertical separation of 17 meters. This design was chosen in order to meet up to the primary science requirement of detecting astrophysical neutrinos in the energy range of $\mathcal{O}(\text{TeV})$ – $\mathcal{O}(\text{PeV})$.

In general, there are two event topologies that form the standard signatures of neutrinos in IceCube as indicated in Section 4.3. *Track-like events*, originating from charge-current muon neutrino interactions, provide an angular resolution at a typical angle of 1° for well contained and reconstructed tracks at 1 TeV and improves to $\sim 0.3^\circ$ for neutrinos with an energy of 1 PeV [Binnenkort gepubliceerd]. *Cascades*, originating from electromagnetic or hadronic cascades, result in a more spherical light generation in the detector. Well contained shower events have an average deposited energy resolution of around 15%. These event types are shown in more detail in Figure 5.3.

5.1.2 DeepCore

A subset of in-ice DOMs is deployed along eight extra strings in the central region of the in-ice array. The optical modules are deployed deeper than 1750 meter with a denser instrumented volume. Seven strings additional strings, belonging to the standard in-ice strings, are also combined with the DeepCore strings to optimize the instrumented volume for this detector. The inter-string spacing on the eight specialized DeepCore strings varies from 41 meters to 105 meters. The DOM-to-DOM spacing is 7 meters for the bottom 50 optical modules (which are deployed at depths of 2100 to 2450 meters). The remaining 10 DOMs on each string are located from depths shallower than 2000 meters with a spacing of 10 meters. This extra “layer” serves as a veto for downgoing atmospheric muons. Each string is instrumented with 60 DOMs, resulting in a total of 480 DOMs. Instrumentation in the ice between 2000 to 2100 meters proved to be less useful due to the *dust layer* (see Section 5.2) and was therefore left out. Six out of the eight specialized strings are also instrumented with DOMs using PMTs of higher quantum efficiency. The two remaining strings are instrumented with regular IceCube DOMs.

The DeepCore design allows us to detect neutrinos of much lower energies in the range of $\mathcal{O}(10 \text{ GeV})$ – $\mathcal{O}(100 \text{ GeV})$. Experiments for neutrino oscillation experiments, WIMP dark matter annihilation, galactic supernova neutrinos and point sources are made possible, or more feasible, with this dense subarray [139].

5.1.3 IceTop

IceTop is a cosmic ray air shower array, located on the surface of the ice and 2835 meters above sea level. As discussed in Chapter 3, air showers die out when they are propagating to Earth’s surface but as a consequence of the high altitude of IceTop, showers are observed near maximum, resulting in a good energy resolution for the detector. This is important if one wants to measure changes in composition as a function of energy. In total, 162 ice-filled tanks are distributed across 81 stations (two tanks per station) in a similar grid on which the in-ice array is deployed. Similar to the denser DeepCore infill, there are eight stations in the center of IceTop placed more closely together. The two tanks per station are separated 10 meters apart from each other and each tank contains two regular IceCube DOMs. One is operated at a “low-gain” and one at “high-gain”, making them more fitted for air shower detection. The tanks measure the Cherenkov light that is produced in the ice of a tank due to the particles in a shower (electrons, positrons, muons and hadrons). The IceTop design allows to fully cover the knee of the energy spectrum and is primarily sensitive from PeV to EeV energies. The denser infill allows the threshold to be lowered to 100 TeV. The detector is used in studies of the composition, gamma rays, high- p_T muons, etc.

5.1.4 IceCube laboratory

The central building to which the modules of all the detectors are connected is the IceCube Laboratory (ICL). Cables/strings from the arrays run up two cable towers on either sides of the structure. A picture of the ICL is shown as the header image of this chapter (pg. 69); one of the towers is visible. Inside the main part of the building there is a server room to which the cables in the towers are connected. The server room is protected against electromagnetic interference with a metal mesh. All data acquisition and online filtering computers are housed inside the server room together with the main IceCube computing system called the “South Pole System” (more information on this in Section 5.5).

5.2 Antarctic ice

Relativistic particles traveling through the ice produce photons in a Cherenkov cone of around 41° . How these photons propagate from the point of emission to the receiving sensors is determined by absorption and scattering within the ice. These propagation effects are important for both simulation and reconstruction of IceCube data requires a good understanding of the underlying properties of the medium. The most important parameters necessary to describe the photon propagation in ice are:

- the average distance to absorption,
- the average distance between successive scatters of photons, and
- the angular distribution of the new direction of a photon at each given scattering point.

There has been a large effort into measuring and modeling the Antarctic ice that is still ongoing. A good summary (which is a bit outdated) can be found in reference [140].

5.2.1 Ice simulation

To be able to characterize and simulate the ice, each DOM was instrumented with 12 LEDs that are aimed in six different azimuth angles (with 60° spacing) and along two different zenith angles. The LEDs were chosen to have a wavelength spectrum centered at around 400 nm to approximate the typical wavelength of detected Cherenkov photons.

The ice is modeled by the six-parameter ice model introduced in Ref. [141]. In this model, the ice is described by a table of depth-dependent parameters $b_e(400)$ and $a_{dust}(400)$ related to scattering and absorption at a wavelength of 400 nm. These two parameters are described by the relative temperature $\delta\tau$, which changes in function of depth, and six global parameters. The effective scattering coefficient is equal to $b_e = b \cdot (1 - \langle \cos \theta \rangle)$, where b is the geometrical scattering coefficient that determines the average distance between successive scatters and θ is the deflection angle at each scatter. The absorption coefficient a determines the average distance traveled by a photon before it is absorbed and is the sum of two components: one due to dust and the other a temperature dependent component for pure ice.

$$b_e(\lambda) = b_e(400) \cdot \left(\frac{\lambda}{400} \right)^{-\alpha}, \quad (5.1)$$

$$a(\lambda) = a_{dust}(\lambda) + Ae^{-B/\lambda} \cdot (1 + 0.01 \cdot \delta t), \quad \text{with} \quad a_{dust}(\lambda) = a_{dust}(400) \cdot \left(\frac{\lambda}{400} \right)^{-\kappa}. \quad (5.2)$$

α, κ, A and B are determined in [141]*, $\delta\tau$ is equal to

$$\delta\tau(d) = T(d) - T(1730\text{m}), \quad \text{with} \quad T(d) = 221.5 - 0.00045319 \cdot d + 5.822 \cdot 10^{-6} \cdot d^2. \quad (5.3)$$

Using flasher data with 400 nm wavelengths, it is possible to measure the values of $b_e(400)$ and $a_{dust}(400)$ at certain depths and use the six-parameter ice model to extrapolate scattering and absorption for other wavelengths.

In 2008, a flasher run was launched where each DOM on string 63 was producing flashes. The layout of the detector at the time of the flasher run and results of fits to $b_e(400)$ and $a(400)$ vs. depth can be found in Fig. 5.4. At a depth between 2000 meters and 2100 meters, a large increase in scattering and absorption is clearly visible. A *dust layer*, presumably originating to volcanic ash is characterized by an increase of dust in the ice, responsible for the higher scattering and absorption factors.

Over the years, multiple different ice models have been constructed. For this analysis the SPICELea[†] model has been set as nominal. This was the most recent model that had significant Monte Carlo background simulations available. It includes an angular sensitivity estimation according to the *hole ice*, a column of ice approximately 30 cm in radius immediately surrounding the strings with an increased amount of scattering. More information about this model can be found in Ref. [142].

*The remaining two parameters D and E were not used here.

[†]SPICE stands for South Pole Ice. Lea is an addition to distinguish the different model types, but has (as far as the author knows) no special meaning.

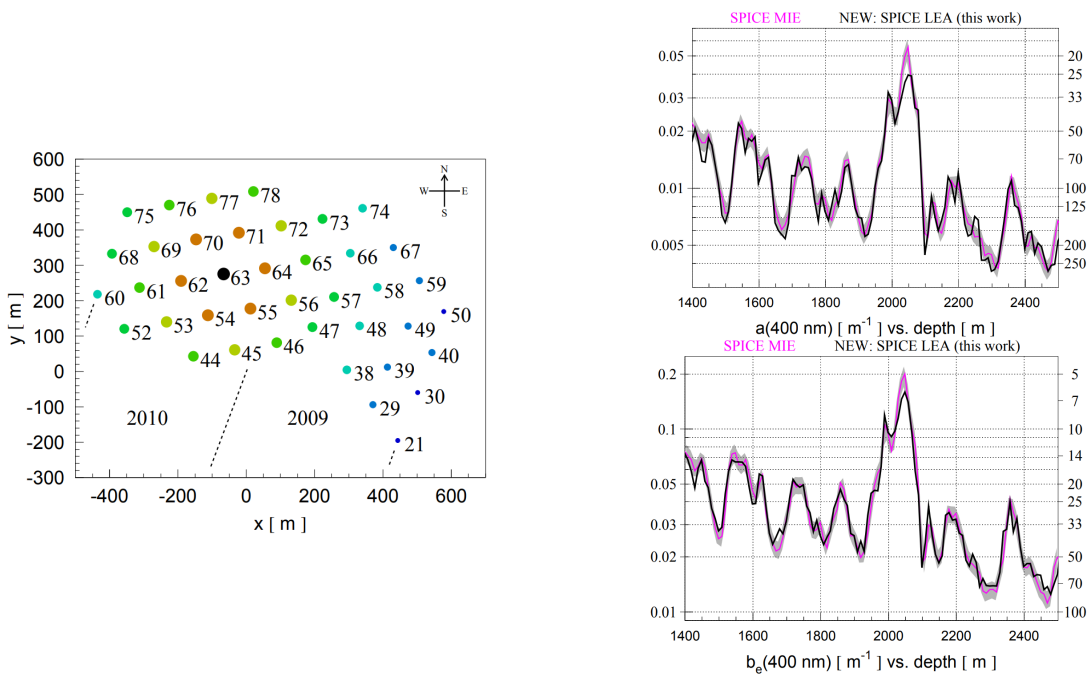


Figure 5.4: *Left:* Top view of the 2008 detector configuration when DOMs on string 63 were used to flash LEDs in a flasher run. Same colors are used for strings located at a similar distance to the central string. *Right:* values of $b_e(400)$ and $a(400)$ vs. depth for two different ice models. Both illustrations from Ref. [142].

5.2.2 Systematic uncertainties

The complex nature of the characteristics of the ice such as the dust particles, the tilt in the ice sheets, etc. result into non-negligible uncertainties in the ice model. Data from the flasher runs are compared to simulation and this verification was used to quantify the uncertainty on the measured values of $b_e(400)$ and $a(400)$. From this, it was determined that $(+10\%, 0), (0, +10\%)$ and $(-7.1\%, -7.1\%)$ uncertainties on the scattering and absorption coefficients was a conservative estimation.

5.3 Hardware components

5.3.1 Digital optical modules

The Digital Optical Modules, or DOMs, in the ice convert light into electrical signals and have the necessary hardware installed to perform some basic processing of the electrical pulses. A downward facing 10"-diameter photomultiplier tube (PMT) is able to detect light produced by electrons or muons typically ranging from 10 GeV to 10 PeV and distances up to 500 m away. The high voltage of the PMTs is set at 2 kV, resulting in a gain of 10^7 [143]. The amplitude of the resulting waveforms ranges from 1 mV up to and beyond the linearity limit of the PMT (~ 2 V) with the width ranging from 12 ns to 1500 ns. This wide dynamic range of waveform characteristics are processed by onboard electronics: the main board and delay board. The main board controls all the devices in the DOM (high voltage power supply for the PMT, the flasher board and pressure, temperature, and power supply voltage monitor sensors), digitizes the PMT waveforms, communicates with the data acquisition (DAQ) on the surface, houses an internal clock that is regularly calibrated with the DAQ on the surface and exchanges LC pulses with the adjacent DOMs (explained in Section 5.5). An illustration on the mechanical components of the optical module and a schematic view of the data flow starting from the PMT is shown in Fig. 5.6. The optical module is housed in a 13" glass sphere of 0.5" thick and is made from borosilicate. It is separated into two halves and held together with an aluminium waistband. The sphere was tested up to 690 bar hydrostatic pressure and is able to withstand the enormous pressure that the DOM is exposed to deep within the ice and during freezing (see Section 5.4). A penetrator

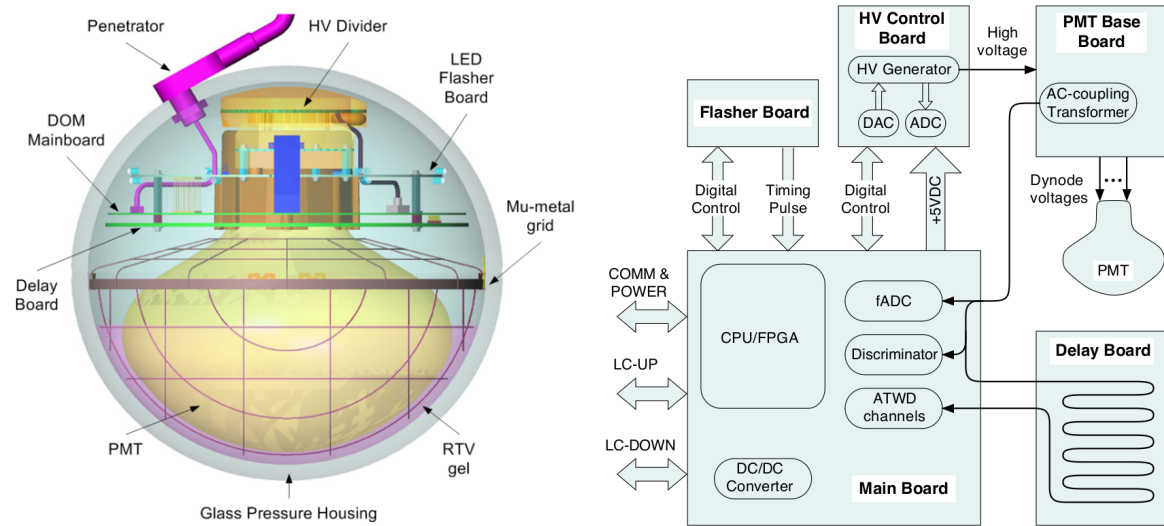


Figure 5.6: *Left:* illustrations of the mechanical DOM components. *Right:* Scheme of the functional connections.

inside the glass sphere brings out three wires pairs housed in a cable. One wire pair is connected to the string and ultimately to the ICL, the other two wires to the neighboring DOMs directly above and below for LC pulses. A detailed description is given in the detector paper [143].

5.3.1.1 PMTs

The 10" (or 25 cm) diameter PMT comes in two types: Hamamatsu R7081-02 for standard IceCube DOMs and a high-quantum-efficiency (HQE) version, Hamamatsu R7081-02MOD for the specialized DeepCore strings [144]. The peak quantum efficiency is around 25% (34% for HQE) at a wavelength of approximately 390 nm. However, the total acceptance of the optical module is the convolution of the quantum efficiency with the glass transmission (93% at 400 nm, decreasing to 50% at 340 nm and 10% at 315 nm at a normal incidence). The resulting acceptance is illustrated in Fig. 5.7. The PMTs are faced downwards and are housed in a mu-metal grid to shield it from the Earth magnetic field and a silicone gel necessary for optical coupling and mechanical support.

5.3.1.2 Main board and delay board

The PMT signals are sent to two ATWD (Analog Transient Waveform Digitizer) and one fast ADC (fADC) with a delay of about 75 ns. This delay is necessary because signals are only processed if they pass a discriminator setting that only passes if the signal exceeds a voltage that corresponds to 0.25 SPE (one SPE is the voltage that is typically corresponding to the voltage produced by a single photoelectron). Once this threshold is crossed, the signal is compressed and included into a “DOMlaunch” or “hit”. Signals that pass the LC requirement have their full waveforms compressed, whereas for isolated events only a time stamp and brief charge summary is sent. For each hit, an FPGA (Field Programmable Gate Array) opens up one of the two ATWD chips. Each of the two chips is provided with three amplifier gains with nominal values of 16, 2 and 0.25. Most pulses use the highest-gain channel while the other lower-gain recordings are used as needed when pulses reach 75% of the range of a higher-gain channel. The ATWD recording duration is 427 ns, which should include light that is produced within tens of meters of a DOM. The fADC is used when light reaches the DOM after the ATWD time window and samples continuously. The FPGA is programmed to save an interval of 6.4 μ s after the launch. ATWD chips digitize the waveform at 300 Msps, followed by a 10-bit digitization. The fADC captures the information with a 10-bit 40 Msps.

The two sets of ATWD chips are operated alternately in order to reduce deadtime. After 50 ns, the second chip is available to be launched during the digitization step of the first. The digitization procedure is terminated for isolated hits and the ATWD is reset, reducing the DOM

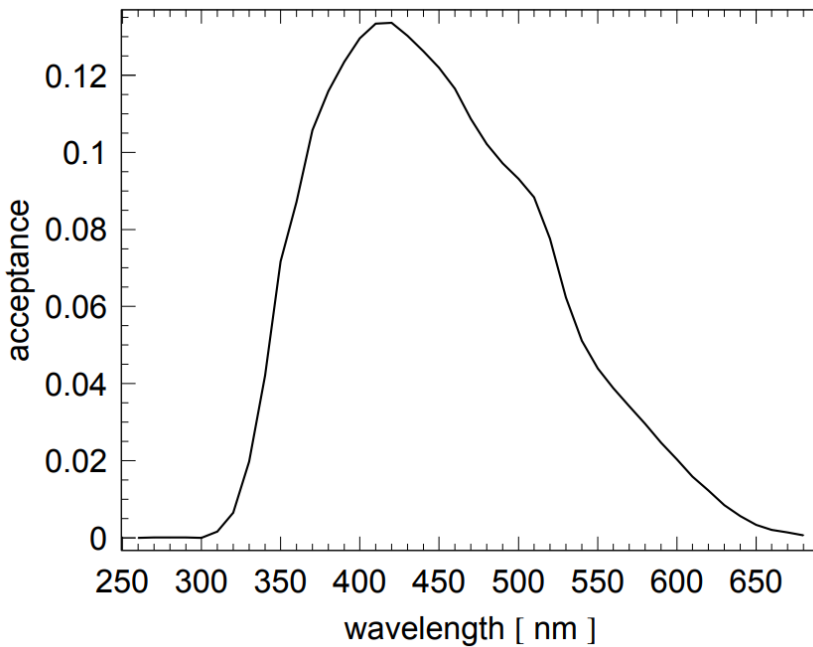


Figure 5.7: Fraction of photons arriving from a direction parallel to the PMT axis in function of the photon wavelength. Glass and gel transmission, PMT quantum and collection efficiencies are all included.

dead time.

The delay board consists of a 10 m-long copper trace that is able to delay the signal for 75 ns necessary to be able to record the full waveform, even before the discriminator threshold.

5.3.2 Calibration devices

Regular calibration of the components is necessary to be able to convert the DOM waveforms into physical constants. Some calibration procedures do not allow for simultaneous data-taking and are performed as few as possible, without losing significant confidence in the calibration of the devices. In-ice DOMs are calibrated yearly with the DOMCal procedure. Global time calibration can be done in parallel with data-taking and is provided by the RAPCal procedure. Optical efficiencies of the devices were determined in the lab before deployment and are also done *in situ*. “Dark noise” results in the vast majority of the background hits and needs to be properly understood for low-energy neutrino analyses, supernova searches, and detector simulations. The total rate of dark noise averages at around 560 Hz for in-ice DOMs and 780 Hz for HQE DOMs. The origins of the noise are non-trivial and include electronic noise, thermionic emission, Cherenkov light from radioactive decays, field emission within the PMT, and scintillation/luminescence in the glass of the PMT and pressure sphere. They are simulated with a combination of uncorrelated (Poissonian) noise and a correlated component. More information about these procedures can be found in [143].

5.3.3 Cable systems

The DOMs are the eyes of the detector, but the cable system connects all the modules together and links them to the readout hardware at the surface. The in-ice cables, 2505 m long, are connected to 60 DOMs and terminate at a Surface Junction Box (SJB) between IceTop tanks. IceTop tanks also connect to the SJB and a surface cable was trenched 1 m deep at the time of deployment and runs to the ICL. One cable consists of 20 “quads”, a construction of four twisted wires. Four quads provide special instrumentation and local coincidence between connections and one is a spare. The remaining 15 quads are each connected to four DOMs with two wire pairs. A wire pair connects two adjacent DOMs and are attached to connectors at 30 breakouts spaced 34

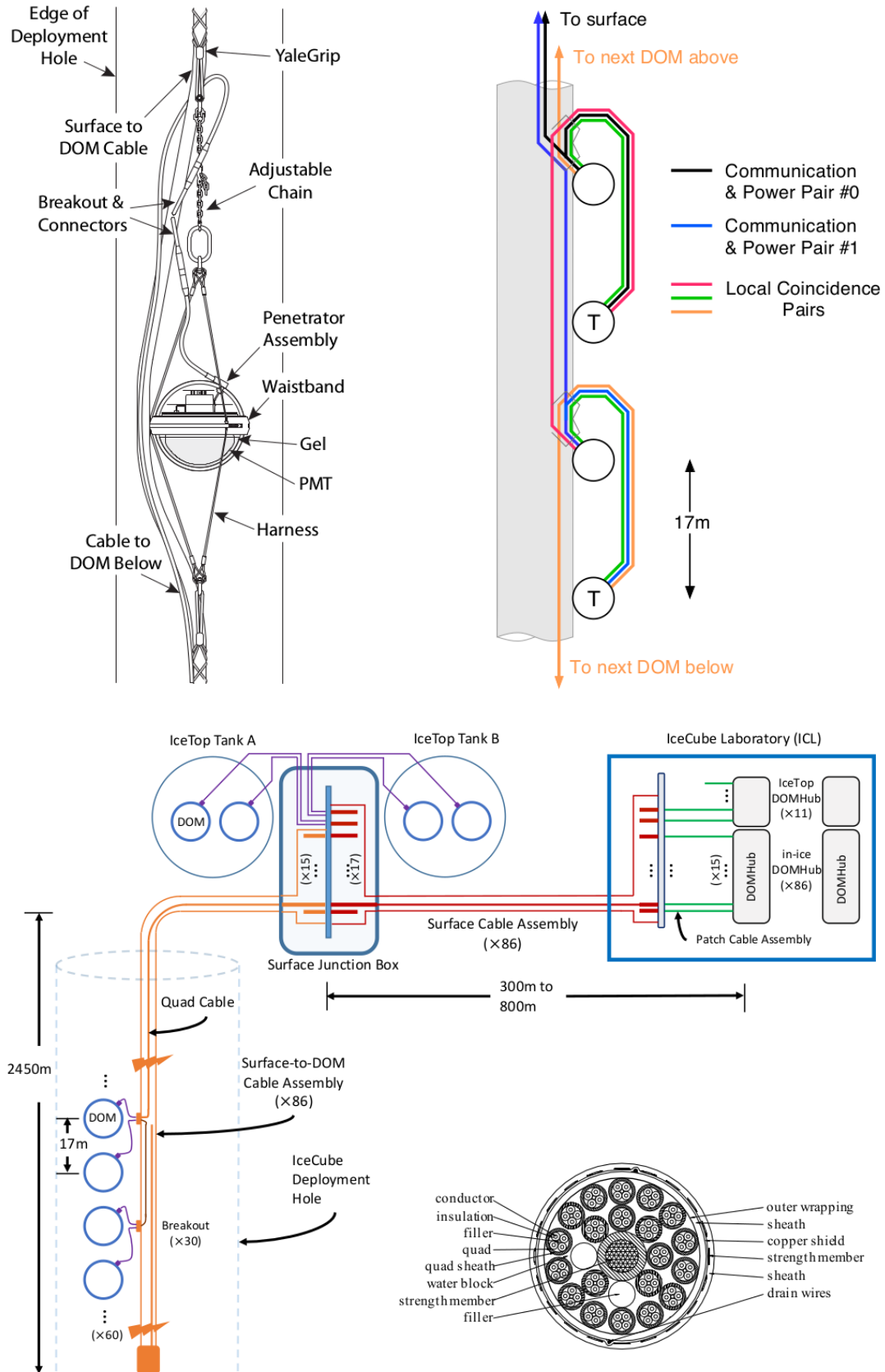


Figure 5.8: *Top:* Sketch of DOM cabling and schematic overview. The modules are connected to their nearest neighbors and the string. *Bottom:* General schematic overview of the IceCube cabling system and the connectivity of all components. All illustrations from Ref. [143].

m apart as can be seen in Fig. 5.8. A wire pair is used for bi-directional communication to the surface and power. As mentioned in Section 5.3.1, each DOM is connected to three wire pairs. The two remaining wires are dedicated to determine *Local Coincidence (LC)*. Each DOM is connected to its nearest neighbor above and below. If nearest or next-to-nearest neighbors are hit within a time window of $\pm 1 \mu\text{s}$, the hits are said to be in Hard Local Coincidence (HLC). Isolated hits are referred to as Soft Local Coincidence (SLC). In Section 5.3.1.2, the different processing of these hits is explained. LC requirements are able to drastically reduce the noise rate.

5.4 Deployment

In total, 86 holes had to be drilled for every IceCube and DeepCore string. The surface consists of a 50 m snow and firn region with a gradual transition into ice. The ice was melted with a 5 MW Enhanced Hot Water Drill (EHWD) capable of drilling around 1 hole per 48 hours as a maximum rate. The holes were 60 cm in diameter, providing enough clearance for the optical modules that were 35 cm in diameter, and with contingency time for delays that meant holes could shrink due to refreezing. Because melting snow and firn with hot water is not practical, a specialized drill with copper tubing through which hot water flows was used to melt the firn by contact.

The IceCube drilling was completed in seven field seasons during Arctic summers (early November to mid-January). The first season started in 2004-2005 and construction stopped in 2010 - 2011. At the end of each season, the Seasonal Equipment Site (SES) that provided electricity and a stable supply of hot pressurized water had to be decommissioned and positioned at the site for the next drilling season due to its size and complexity. From the SES a more flexible Tower Operations Site (TOS) was linked and held the drill tower, operations building, and hose and cable reels. There were two towers, where one was set up for drilling while the second one was still being used for deployment of the cables.

After drilling, all 60 DOMs were lowered one by one and connected to each other with the penetrator assembly as shown in Fig. 5.8. After deployment of all DOMs, the remaining 1,5 km of in-ice cable was lowered into the hole (known as the “drop phase”). The top of the cable was then secured by an anchor trenched into the snow and connected to the SJB.

In total 5484 (5160 IC + 324 IT) optical modules were deployed and as of 2018, there are 5396 still in data-taking mode (98.4%). 55 DOMs failed almost immediately during freeze-in while 34 DOM failures occurred post-deployment commissioning. This number includes modules on a wire pair which are taken out when the partner DOM on the same pair failed. The mean failure rate is estimated to be around $(4.1 \pm 1.2) \text{ yr}^{-1}$ and would result in a survival fraction of $(97.4 \pm 0.3)\%$.

5.5 Data taking

First processing of the photon detection is done inside the DOM as explained in Section 5.3.1.2: hits flagged as SLC are compressed more aggressively compared to HLC hits that have their entire waveform digitized. This information is sent along the cable/string to which all DOMs are attached and runs to the ICL. Each one of the strings is connected to one of the DOMHubs, which together with servers that run various online systems, comprised the South Pole System (SPS). An overview is given in Fig. 5.9.

The data acquisition (DAQ) system is run on the DOMHubs and recognizes patterns in hits that are most likely caused by particle interactions. This combination of hits is called an “event”. Most of the DAQ data rate originates from atmospheric muons with an event rate averaging around 2.7 kHz. The total bandwidth saved to tape (see Section 5.5.3) is approximately 1 TB/day.

To implement possible changes in the detector settings, triggers or filters, a physics run spans over one year, starting in May and ending in May the following year. Over the years, with the use of both online and on-site automatic alerts, the total uptime of the detector has a steady increase of clean uptime (usable data) from 89.75% in 2011 to 98.89% in 2018.

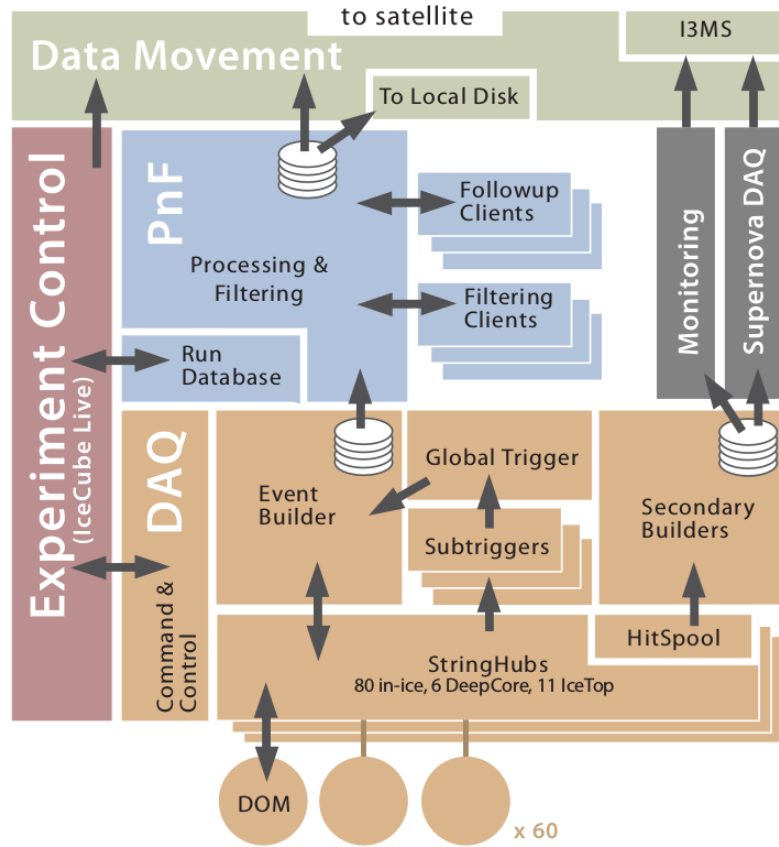


Figure 5.9: Schematic overview of the data flow in the primary IceCube online systems.

5.5.1 Triggers

To further reduce the noise rate, a system of triggers is set up to refine searches for physics events. The most important trigger is the Simple Multiplicity Trigger (SMT) used for the IceCube, DeepCore and IceTop arrays. The trigger setting requires a certain number of hits within a time window of the order of a couple of μs without any locality requirements. The Volume Trigger requires less HLC hits, but they have to be clustered in a certain cylindrical volume. Locality conditions are powerful for low-energy events that will not reach far in the detector but are more prone to produce hits in a small volume and time window. Low-energetic upgoing events passing along a single string therefore have a dedicated String Trigger. IceCube is also sensitive for, currently, hypothetical massive particles moving at subrelativistic speeds: magnetic monopoles. A dedicated Slow Particle (SLOP) trigger has therefore been developed. It searches for triplets of HLC pairs within a window, T_{\max} , and removes HLC pairs within a time window, T_{prox} , to remove hits originating from particles traveling at the speed of light. Other velocity and geometric requirements are set with the inner angle between triplets, α_{\min} and the “velocity” along the sides of the triangle. A Fixed Rate Trigger (FRT) reads out hit data from the full detector at fixed intervals, useful for DOM noise studies.

If a trigger condition is fulfilled, the start of the trigger window is determined as the first HLC hit of the triggered subdetector. The minimum length of the triggered window (as found in Table 5.1 for the different DOM sets) slides along with the hits until there is no more HLC after the last hit within the set minimum time window. The length of a triggered set of hits can therefore be longer than the minimum trigger window. As one event is capable of fulfilling multiple trigger requirements, the (sub)triggers are merged into one Global Trigger while keeping the information on the individual triggers. This data is subsequently sent to the Event Builder that writes DAQ events (also called *Q frames*) to a temporary file which is saved when it reaches a certain size. These events are eventually re-split into physics events (*P frames*) corresponding to a certain subtrigger before reconstruction and analysis. An example of one Global Trigger,

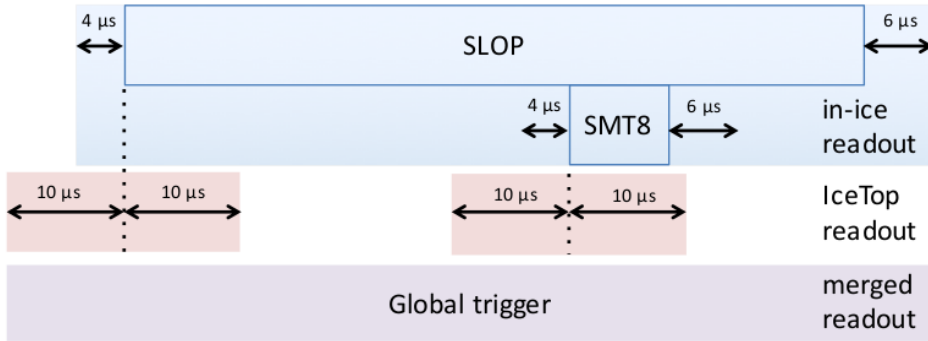


Figure 5.10: Example of a global trigger construction. Multiple triggers are combined due to their overlap with the long SLOP trigger.

Table 5.1: Parameter settings of triggers (as of May 2016) and typical trigger rates. **RELEVANT TRIGGERS HIGHLIGHTED IN BOLD**

Trigger	DOM set	N HLC hits	Trigger Window (μs)	Readout Window (IC) (μs)	Readout Window (IT) (μs)	Topology	Rate (Hz)
SMT	in-ice	8	5	-4, +6	± 10	-	2100
SMT	DeepCore	3	2.5	-4, +6	± 10	-	250
SMT	IceTop	6	5	± 10	± 10	-	25
Volume	in-ice	4	1	-4, +6	± 10	cylinder ($r = 175 \text{ m}$, $h = 75 \text{ m}$)	3700
Volume	IceTop	4	0.2	± 10	± 10	cylinder ($r = 60 \text{ m}$, $h = 10 \text{ m}$)	4
String	in-ice	5	1.5	-4, +6	± 10	7 adjacent vertical DOMs	2200
SLOP	in-ice	N_{triplet}	$T_{\text{prox}} = 2.5$	$-4, +6$	± 10	$\alpha_{\min} = 140^\circ$, $v_{\text{rel}}^{\max} = 0.5$	12
			$T_{\min} = 0$				
			$T_{\max} = 500$				
FRT	all	-	-	Combined: 10000	-	-	0.003

here mostly determined by the very long SLOP trigger, is shown in Fig. 5.10.

All triggers request all SLC/HLC hits of all DOMs, even the ones not directly involved in the trigger construction. For this, they use the StringHub software component located on every DOMHub that is capable of caching SLC and HLC hits in memory. Hits before and after the trigger window are also saved to the event to add information of early and late pulses. This is typically 4 μs before and 6 μs after the trigger window for in-ice triggers. The StringHub is also capable to save local “HitSpool” on-disc data and later request it if necessary from the Event Builder. This HitSpool data is able to store up to 16 hours of all waveforms overwriting the oldest data first and originally intended for the detection of Galactic supernovae. Such an event would give rise to a steady increase in apparent dark noise from its low-energy neutrinos without fulfilling the standard trigger requirements. Over the years, the HitSpool data has found multiple other usecases such as a neutron echo analysis, searching for delayed neutrons from hadronic interactions [145].

5.5.2 Filters

Events are sent through the online Processing and Filtering (PnF) system for further event processing of physics events. Around 25 filters per year search for a wide range of different type of particle interactions, ranging from low-energy neutrinos for oscillation measurements to the highest-energy neutrino interactions illuminating large parts of the detector. Some filters are designed to look for neutrino events of wide astrophysical interest to the scientific community and trigger alerts that are distributed to followup observatories worldwide. As a bonus, filtering reduces the data volume to a level of around 90 Gb/day, which is small enough to transfer to the North using a satellite. These filtered events had their waveforms further compressed using the Super Data Storage and Transfer format (SuperDST), which uses only 9% of the storage size of the full waveform information. Very fast, basic reconstructions are run on the SuperDST waveforms to compute the vertex position, energy, direction and goodness-of-fit that are necessary for the filter selections of possible interesting events.

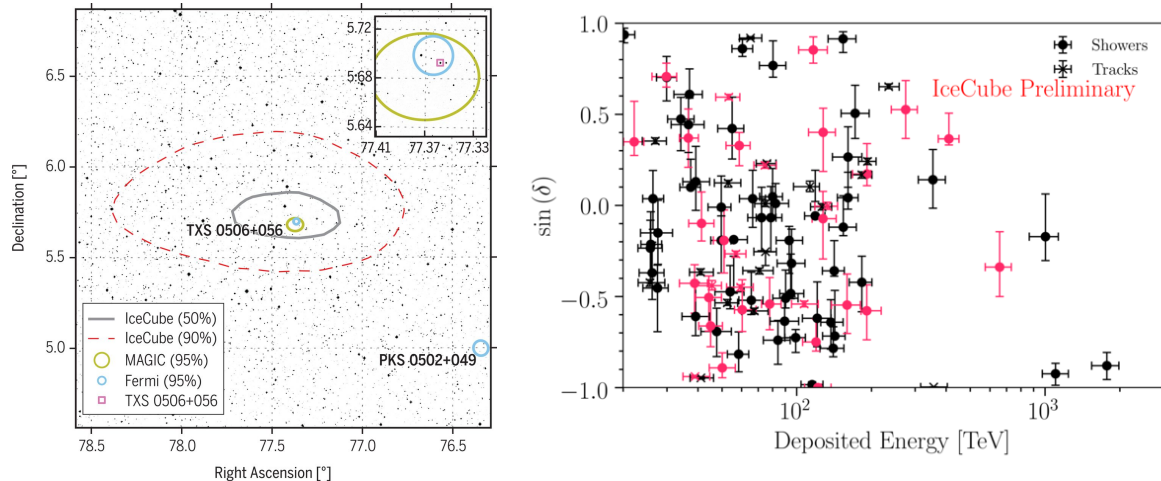


Figure 5.11: *Left:* Sky map around the presumable blazar source with the gamma-ray sources detected by Fermi and MAGIC overlaid. These are in excellent agreement with the IceCube neutrino containment region. *Right:* Map of showers (cascades) and tracks with their respective declination and deposited energy in the detector.

5.5.3 Data handling

Most of the data is processed with the PnF system. The geometry, calibration, and detector status (GCD) information from each 8 hour run is sent via the same satellite transfer that is used for the continuously running PnF system. All of the raw waveforms were written to tape before that system was retired in 2015. Since then, disks have been used to store the remaining archival data. This raw data is shipped to the North every year and are used if reprocessing of data is necessary. An example being the SPE correction for all runs starting from 2010 to 2016 referred to as *pass2 data*.

Files are stored in IceCube specific files and are called *i3files*.

5.6 Search strategies

The IceCube experiment consists of around 300 people from 50 institutions spread over 12 countries. A wide variety of senior scientists, graduate students, technicians, software specialists and engineers work on the continuous running operations to keep the detector live in both hardware and software. Most other people focus on physics analyses that range from low-energy oscillation physics to rare highest-energy neutrino interactions in the ice. Below I give a general and very brief overview of the IceCube experiments. Other examples, which are not mentioned below, are neutrino cross section measurements [146], inelasticity measurements [147], studies in hadronic interactions from cosmic ray interactions **SAMDRCITEREN**, and sterile neutrino searches [148].

5.6.1 Multimessenger astronomy and astrophysical neutrinos

The globally coordinated effort in joint searches and observations of cosmic rays, neutrinos, gravitational waves, and electromagnetic radiation is called *multimessenger astronomy*. As an example: a single source, such as a blazar, is expected to produce several signatures that would individually be prone to large uncertainties or even a lack of detection from background events. The IceCube collaboration has a good track record of detecting astrophysical neutrinos and measuring the diffuse flux [126, 149]. Individual sources long remained unidentified until the joint effort of multiple collaborations such as IceCube, Fermi-LAT, MAGIC, AGILE, and others* observed a coincidence with a high-energy neutrino from IceCube and a flaring blazar [112]. The

*A full list of participating collaborations can be found here [112].

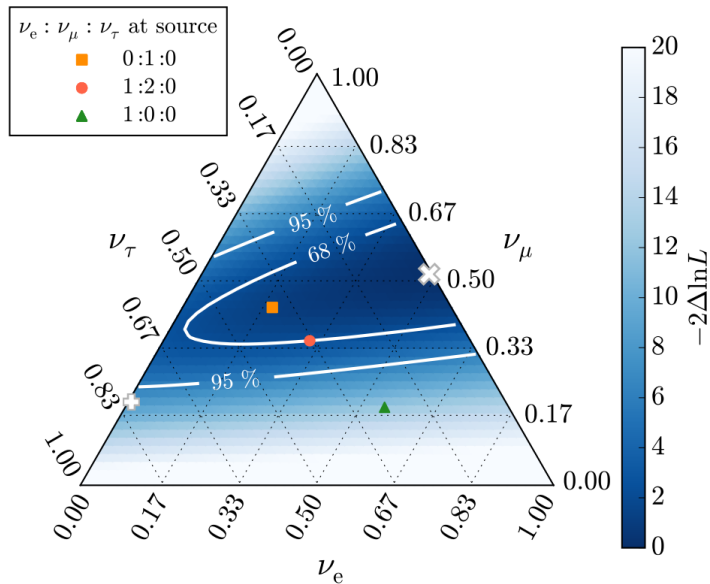


Figure 5.12: Scan of the flavor composition measured at Earth. The axes show the relative abundances of ν_e , ν_μ and ν_τ . The best fit is marked with an “x” and compared to three possible scenarios of neutrino abundances at the source. Propagation of neutrinos show different measurements at Earth due to oscillation effects. From Ref [150].

detection of the neutrino, referred to as IceCube-170922A, triggered an extensive multiwavelength search over the electromagnetic spectrum ranging from radio frequencies to γ -rays. Spatial and temporal coincidence of the estimated 290 TeV neutrino with a γ -ray emitting blazar suggest that high-energy neutrinos have blazars as possible origins. Results of the combined analysis for the blazar called TXS 0506+056 is shown in Fig. 5.11.

5.6.2 Oscillations

As discussed in Section 1.3.4, neutrinos oscillate in between flavor due to their mixing of mass and interaction eigenstates. Atmospheric neutrino “beams” that reach IceCube are ideal candidates to study this behavior at higher energies than most reactor- or accelerator-based experiments. As these particles arrive from all directions, they travel around 10 km (down-going) up to 12,700 km (up-going) before reaching the detector. As this path length is related to the measured zenith angle, a study that combines the measured energy with the angle is able to measure $\sin^2 \theta_{23}$ and $|\Delta m_{32}^2|$ comparable to world-leading experiments as shown in Fig. 5.13.

5.6.3 Galactic supernovae

A supernova explosion close by would result in a general rise of the noise rate of the detector (see Sections 5.5.1 and 3.1.4.1). The IceCube detector should, in theory be, sensitive to supernovae explosions not too far in our galaxy [152] and is a member of the Supernova Early Warning System (SNEWS) [153].

5.6.4 Beyond the Standard Model searches

As a main topic for this work, we focus on the apparent incompleteness of the Standard Model of particle physics. There is a large focus in the collaboration on searches for possible new scenarios that could explain some unexpected results. Some examples are listed below.

5.6.4.1 Lorentz invariance violation

Lorentz symmetry is one of the foundations of the SM: fundamental laws in nature are thought to be independent of the observer’s inertial frame. Some Standard-Model extensions allow for spontaneous breaking of Lorentz symmetry and can lead to Lorentz-invariance violating (LIV) effects. Examples are string theory or quantum gravity. Some effects that would follow from

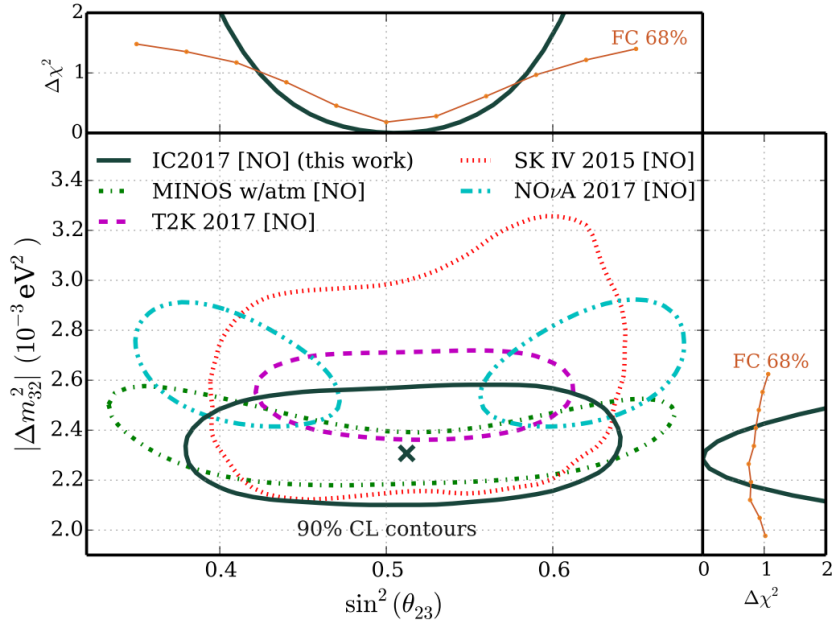


Figure 5.13: Comparison of the $\sin^2 \theta_{23}$ and $|\Delta m_{32}^2|$ measurements between IceCube, Super-K, T2K, MINOS and NO ν A. Normal mass ordering is assumed. Figures from Ref. [151].

these extensions are incorporated in the Standard Model Extension (SME) and although the size of LIV effects should be of the order of the Planck scale ($\approx 10^{19}$ GeV), they could manifest themselves in, e.g., oscillations of atmospheric muons. The LIV effects are often parametrised by two parameters: ρ_d and $\cos \theta$ (which are explained in the capture of Fig. 5.14), where d refers to the power of the operator in the Hamiltonian. The energy reach makes it possible to go to dimension up to 8 whereas most other experiments are sensitive up to dimension $d = 3$ or $d = 4$. This analysis was done first in the 40-string configuration [156] and later redone with the full detector configuration [155]. Results for $3 \leq d \leq 8$ are shown in Fig. 5.14.

5.6.4.2 Dark matter

The large amount of evidence to support the existence of dark matter (DM) was given in Section 1.5. Large ongoing experimental efforts are done to try to search for these elusive particles. Collider experiments try to produce these particles by SM interactions (*production searches*), other experiments try to measure its interaction with SM particles through nuclear recoil (*direct detection*). It should also be possible to search for the SM products that are produced when annihilation occurs and the corresponding daughter particles find their way to Earth (*direct detection*). Most searches focus on specific regions in the sky that are more prone to produce a measurable signal. As one characteristic of DM is its non-zero mass, they are expected to be gravitationally trapped in the halo of galaxies or to accumulate in heavy celestial objects nearby such as the Sun or the Earth itself. Since most SM particles would never reach us, neutrinos are the only possible messengers. Fig. 5.15 shows a comparison of upper limits on $\langle \sigma_A v \rangle$ versus WIMP mass*, for the annihilation channel $\chi\chi \rightarrow \tau^+\tau^-$ producing tau neutrinos. $\langle \sigma_A v \rangle$ is the WIMP-WIMP annihilation cross section and determines the strength of the expected neutrino flux. The analysis mentioned in the figure searched for signals from the center of the Milky Way [157]. Other IceCube analyses have searched for dark matter in the Sun [158, 159] and in the Earth [160].

5.6.4.3 Magnetic monopoles

The quantum theory of magnetic charge started with a paper by P. Dirac [161] in which he theorized the existence of magnetic monopoles in a similar fashion as he did to successfully predict the positron. If q_m is the magnetic charge and q_e the electric charge, Dirac found that the

*WIMP stands for Weakly Interacting Massive Particle and is one possible candidate for dark matter.

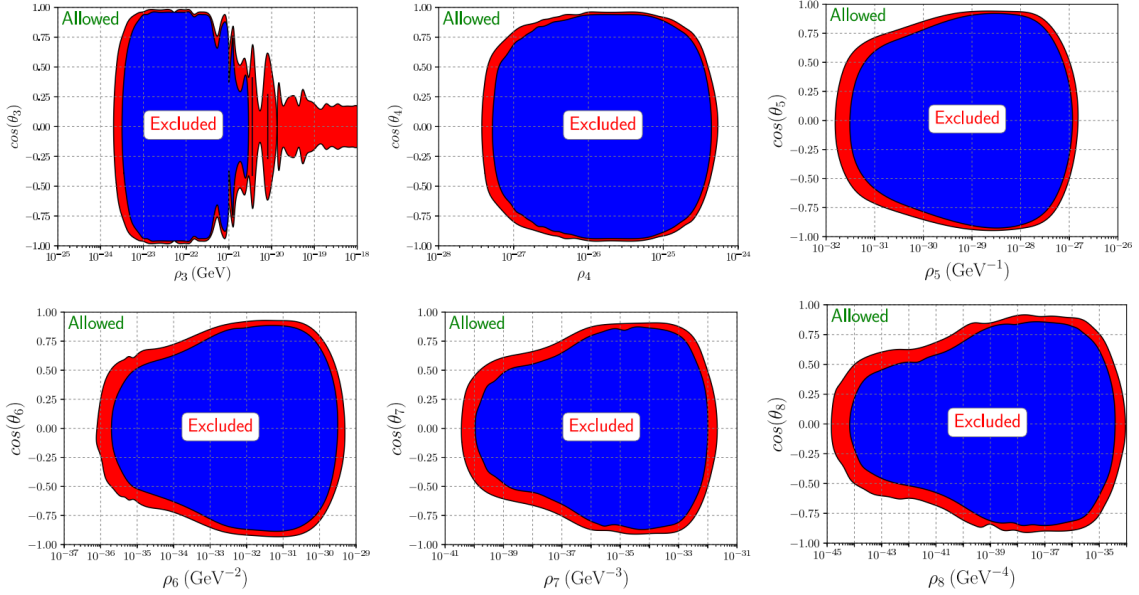


Figure 5.14: Regions excluded at 90% (99%) C.L. in the LIV parameter space in red (blue). ρ is related to the strength of the LIV and $\cos\theta$ is a combination of coefficients defining LIV in the effective Hamiltonian of Standard Model Extension [154]. The subscript d refers to the power of the corresponding operator in the Hamiltonian. More information in Ref. [155].

following condition should hold

$$q_m q_e = 2\pi n \quad (n \in \mathbb{Z}), \quad (5.4)$$

and could therefore explain why the electric charge is always quantized, i.e. in integer multiples of an elementary charge. The smallest possible magnetic charge would be*

$$g_D = 2\pi/e = e/2\alpha \approx 68.5e. \quad (5.5)$$

Magnetic monopoles appear automatically in certain Grand Unified Theories that would give rise to these particles after spontaneous symmetry breaking of the GUT group, similar to the Higgs mechanism [162, 163]. Masses are typically of the order of 10^{16-17} GeV and are searched for in IceCube analyses in multiple velocity ranges. Monopoles with velocities close to the speed of light in vacuum produce extremely bright tracks due to their high Dirac charge as shown in Eq. 5.5. At lower velocities ($\approx 0.5c$ to $0.76c$) secondary knock-off δ -electrons could have velocities above the Cherenkov threshold and produce light. Luminescence light from excitation of the ice dominates at low relativistic velocities ($\approx 0.1c$ to $0.5c$). For each of these speed ranges, searches for magnetic monopoles at the IceCube experiment are either in progress (luminescence) or have already set the world's best upper limits on the flux of magnetic monopoles over a wide range of velocities [164].

5.7 Future upgrades

The last couple of years there has been much ongoing work in improving the physics work that can be done in the collaboration. Several projects are in the pipeline, are under R&D, and/or have been funded to improve the full analysis case of the detector(s). Lower-energy neutrinos can be detected with a denser infill with other optical modules (the Upgrade, see Section 5.7.3), cosmic ray measurements can be improved with a complementary scintillator array to the IceTop tanks, and the detection of ultra high energy neutrinos could be made possible with a larger

*At the time of writing his paper, Dirac believed the smallest electric charge was from the electron. Since now we know the down quark holds an electric charge equal to $1/3e$, the minimal magnetic charge would be equal to $3g_D$.

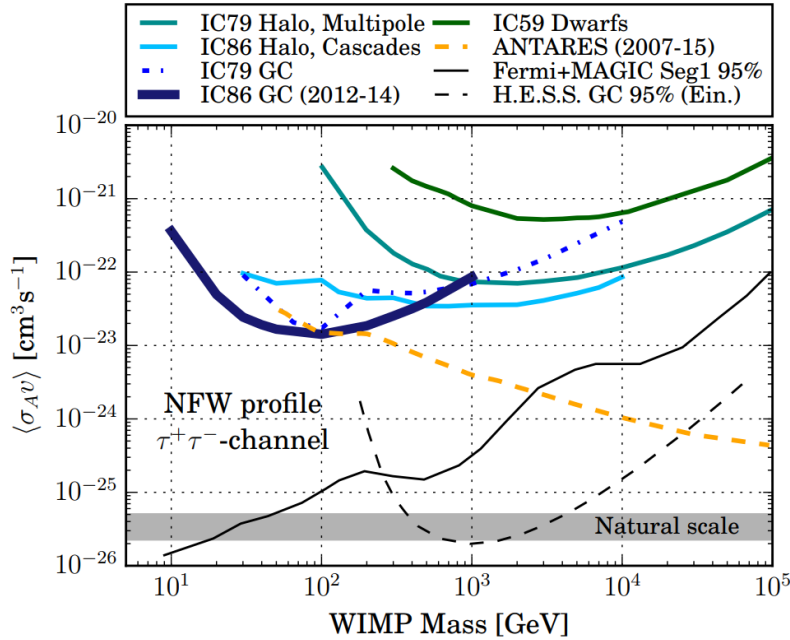


Figure 5.15: Upper limits of $\langle\sigma_A v\rangle$ in function of the WIMP mass from different experiments.

infill of the current IceCube in-ice array (Gen2) or radio antennas. Below a brief summary of future and ongoing projects is given.

5.7.1 Scintillators

During the Antarctic summer of the 2017/2018 season, several scintillator prototypes were installed as proof-of-concept for a full scintillator* array with a similar coverage of the current IceTop array. One station would consist of 7 scintillator panels; one as the center and the remaining six in a hexagonal shape around the center. A total of 37 stations result in 259 panels in total with an instrumented area of $\sim 388 \text{ m}^2$ [165]. This main purpose of this setup is twofold:

- **Measure the attenuation due to snow.** IceTop tanks suffer from snow accumulation and many IceTop analyses have this effect as their main systematic error. Electromagnetic components of air showers have short attenuation lengths in snow, resulting in a clear difference of signal rates for tanks that accumulated more snow than others in the course of the years since deployment. The uncertainty in the attenuation function, that depends on the distance to the shower axis, muon number, snow depth, energy, and zenith angle is expected to increase the estimated 6% systematic uncertainty on the energy spectrum in the following years. A reference signal from the scintillators can reduce this systematic uncertainty.
- **Improve low-energy detection efficiency.** Scintillators are able to efficiently detect air showers to lower energies than currently possible with IceTop detectors only.
- **Signal determination.** The setup could also be used in a similar fashion as the Pierre Auger upgrade was used to distinguish the muon and electromagnetic contributions [166].

5.7.2 IceAct

The main backgrounds in most IceCube analysis (including the one described in this work) are from atmospheric muons and muon neutrinos. IceTop has been shown to act as a veto for these events and is used in some analyses [167]. A possible complementary extension of the IceTop detector is based on small Air Cherenkov Telescopes (ACTs), called IceACT [168]. ACTs use air

*Scintillators collect light that is produced by particles travelling through matter that is excited by the relativistic particle (Bethe-Bloch formula).

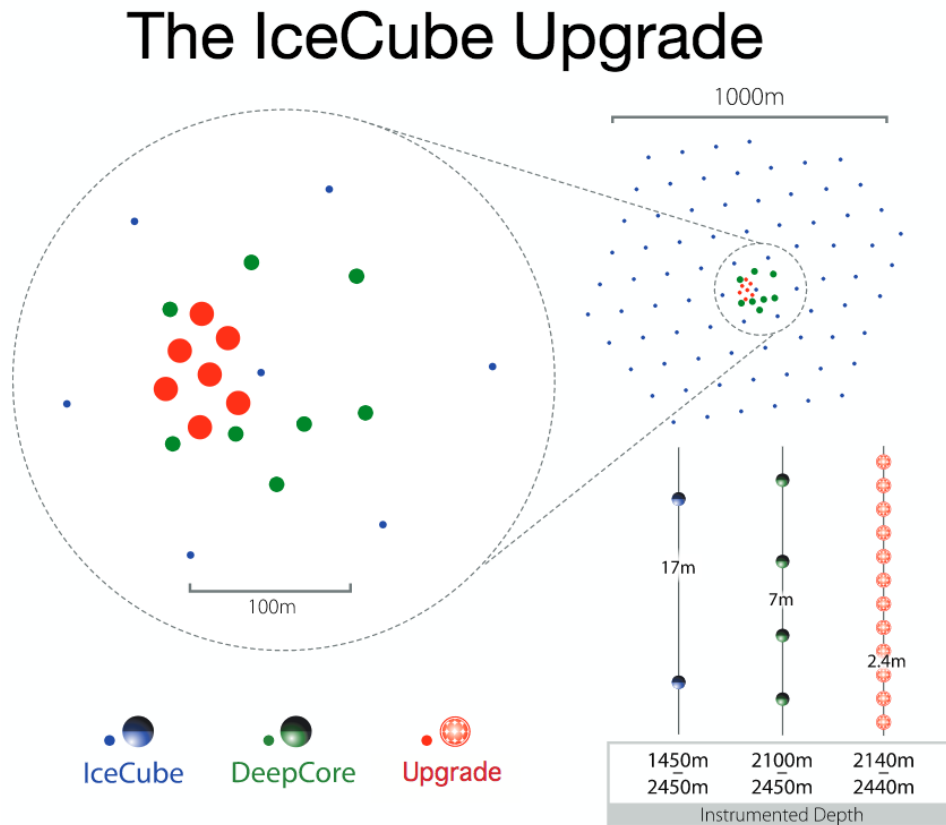


Figure 5.16: Top view of the Upgrade infill (red circles) within the DeepCore array (green) and the whole IceCube detector (blue). The area of the circles is representative of the instrumented photocathode density on a given string. From the IceCube collaboration.

as the active volume for light production and use cameras to detect light produced by cosmic rays. Downgoing atmospheric neutrinos could be vetoed as they are also accompanied by air showers on the surface. Currently, several prototype setups are deployed and tested on South Pole. One prototype telescope consists of 61 pixel SiPM camera with a 60 mm focal plane radius as the central part. One station would consist of a central telescope with six others surrounding it in a hexagonal shape. Each telescope would be oriented to a different point in the sky, optimizing the total field of view. An array covering the IceTop and IceCube detectors is proposed but still being discussed. Stations further away could also be included to further optimize the veto capabilities and would include fewer than 7 telescopes as the detection of a very inclined cosmic ray with one telescope shields more modules deep in the ice than vertical cosmic ray events.

5.7.3 IceCube Upgrade

In 2018, a funding proposal for a dense 7-string infill of DeepCore was accepted by the NSF and was effective from the beginning of October later that year. This infill would have DOMs separated 2.4 m apart and start from a depth of 2140 m, reaching to 2440 m deep in the ice along seven new strings (see Fig. 5.16). This very dense array would allow low-energy and oscillation experiments to reach much better sensitivities. As this project involves a restart of the drill and also serves as a testbed for new optical modules, the Upgrade is the first step towards the much bigger Gen2 project. New types of optical modules would be used with higher angular acceptances than the currently used DOMs that have one large downward facing PMT. Examples are D-Eggs, which have two PMTs at each end of an ellipsoid glass [169], and mDOMs, where multiple smaller PMTs are positioned in a ball-shaped optical module [170].

A camera system could also be included in the new optical module designs and should help to improve the properties of the ice after refreezing [171]. Another camera system, the Precision Optical Calibration Module (POCAM) should further improve our understanding of the ice

characteristics and accurately determine the efficiency and angular acceptance of the IceCube DOMs [172].

Deployment is currently planned for the 2022/2023 season.

5.7.4 IceCube Gen2

The IceCube Gen2 Facility

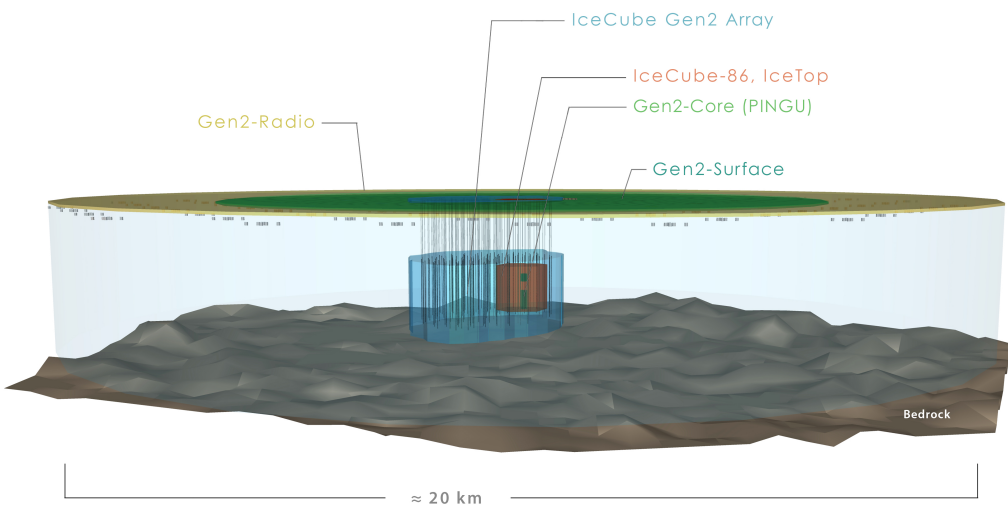


Figure 5.17: Impression of the possible Gen2 layout. The current IceCube in-ice and IceTop arrays are shown in red/brown. The 10x larger Gen2 in-ice array is given in blue. Possible layouts for the radio array (yellow) and surface array (green) are also listed. From the IceCube collaboration. **PINGU zit hier bij, maar nog geen idee of dat er van ga komen of dat het bij de upgrade gaat blijven...**

Although the IceCube in-ice array has successfully been able to determine the flux of astrophysical neutrinos and show the detection of a coincident neutrino with a blazar in an active state, a next generation larger detector infill would greatly improve the detection possibilities of astrophysical neutrinos [173]. A 10 km^3 volume of clear glacial ice would allow for a much higher detector acceptance of high-energy neutrino interactions, helping in searches for point sources, better characterizing the spectral and flavor properties, and search for cosmogenic neutrinos * among others. Point sources and cosmogenic neutrinos have, for now, not been observed even though the detector has been running stable for a couple of years. There is also only a small set of unambiguous astrophysical neutrinos. It would take extremely large running operations from the current detector (without hardware failures that are prone to happen more and more) to gather enough events for meaningful statistics. A much larger instrumented volume, such as the one proposed, is predicted to have an increase in sensitivity to transient source densities and rated by about two orders of magnitude [174]. Although much is undecided, the plans are to have an extra surface array for cosmic ray detection and a radio array for the highest energy neutrinos along the in-ice array.

Deployment is planned for ???

*These neutrinos are produced when UHECR hit the CMB.

5.7.4.1 In-ice infill

The current design for the Gen2 string configuration would be ~ 120 cables with an inter-string spacing around 250 m to 300 m. This much coarser spread of strings will result in a loss of sensitivity for neutrino events of the order of couple of TeV but would not affect the measurements of the very energetic astrophysical neutrinos. Measurements of the absorption lengths in function of the depth in the ice indicate that the instrumentation of the strings could be extended with an additional 250 m in total. This total depth is comparable to the current depth of the IceCube detector, meaning the surface area should reach to an exposed area of $\sim 10 \text{ km}^2$. This would result in a drastic sensitivity improvement of (near-)horizontal muons traversing the ice that are too energetic to be contained in the current detector.

5.7.4.2 Surface array

The size of the IceTop array is too limited for most analyses to be used as a veto for most analyses. Therefore, the prospects of a surface array for the Gen2 extension would have much larger designs [175]. The geometry and optimal type of detector that should be used for this configuration is still under design.

5.7.4.3 Radio array

To achieve an improved sensitivity to neutrinos in the $10^{16} - 10^{20}$ eV energy range, including GZK neutrinos, an additional radio-pulse neutrino detector could be constructed. At the critical energy of around 100 PeV, the origins of cosmic rays transitions from the highest-energy galactic sources to the even more extragalactic cosmic rays. A good review of radio emission from cosmic rays is given in Ref. [176]. There are ongoing experiments that act as a proof-of-principle for the radio technique in the ice: ARA (Askaryan Radio Array) [177], close to the IceCube detector at South Pole (see Fig. 5.2) and ARIANNA (Antarctic Ross Ice Shelf Antenna Neutrino Array) [178] on the Ross Ice Shelf at the antarctic coast.

5.8 Discussion

Nodig om over te gaan van deel 1 naar deel 2? Zou zeggen van wel. Kort.

Simulation, Processing and Analysis

6	Simulation: Event Generation and Propagation	91
6.1	Generation	
6.2	Propagation	
6.3	Detector simulation	
6.4	Processing	
6.5	Burn sample	
6.6	Event viewer	
7	Reconstruction, Cleaning and Analysis Techniques	103
7.1	Reconstruction	
7.2	Pulse cleaning	
7.3	IceHive	
7.4	CoincSuite	
7.5	Analysis techniques	
7.6	Boosted Decision Tree classifiers	
7.7	Minimal-Redundancy-Maximum-Relevance	
7.8	IceCube coordinate system	
8	The SPACE Analysis	119
8.1	Filter selection	
8.2	Level 3	
8.3	Level 4	
8.4	Level 5	
8.5	Results	
9	Summary and Conclusion	145

6. Simulation: Event Generation and Propagation

Soon there will be virtual reality, and augmented reality. If you assume any rate of improvement at all, then games will become indistinguishable from reality . . . , it would seem to follow that the odds we are in base reality are one in billions. ~ Elon Musk

To be able to search for new physics, one has to have a good handle on the detector response on known physics processes. Depending on the analysis, some processes are more interesting than others. In general, the particle interactions of interest are referred to as *signal events*. Other interactions, which mimic or obscure the signal events, are typically called *background events*. These events are simulated using Monte Carlo* (MC) simulations, where one makes use of a model that describes the interactions and their probability to occur. A typical MC simulation consists of hundreds to millions of events that are constructed using these models with the use of random number generators. To determine the detector response of a particle interaction, one first has to start with the particle generation, which sets the conditions of the initial interaction. Afterwards, the propagation of the particle in the detector (medium) is simulated as best as possible. Below, an overview of the important background and signal simulations that are used in this analysis is given. A flowchart of the simulations steps is shown in Fig. 6.1.

Corollary 6.0.1 — The software framework. *IceTray* is a modular framework written and used by the IceCube collaboration and mostly written in C++ for fast computation. A python interface for most modules is provided for fast and easy implementation of the code. The framework is used in both online and offline processing and is stream-based with modules that act on events in the stream and essentially follows a flowchart of modules that is provided by the user.

To process the large amount of simulation that is required for the collaboration, a data processing and management framework called *IceProd* was developed. The setup is very light-weight, running as a python application. It uses (complex) workflow DAGs (see below) across distributed computing grids in order to optimize usage of resources. A *dataset* is set

*While recovering from an illness in 1946, Stanislaw Ulam figured that the actual counting of successful attempts in playing a card game would yield him a much faster answer to the probability of success rather than doing the actual calculus. His work, shared with John von Neumann, needed to remain secret and adopted the code word “Monte Carlo”, referring to the gambling games in the Monte Carlo Casino in Monaco.

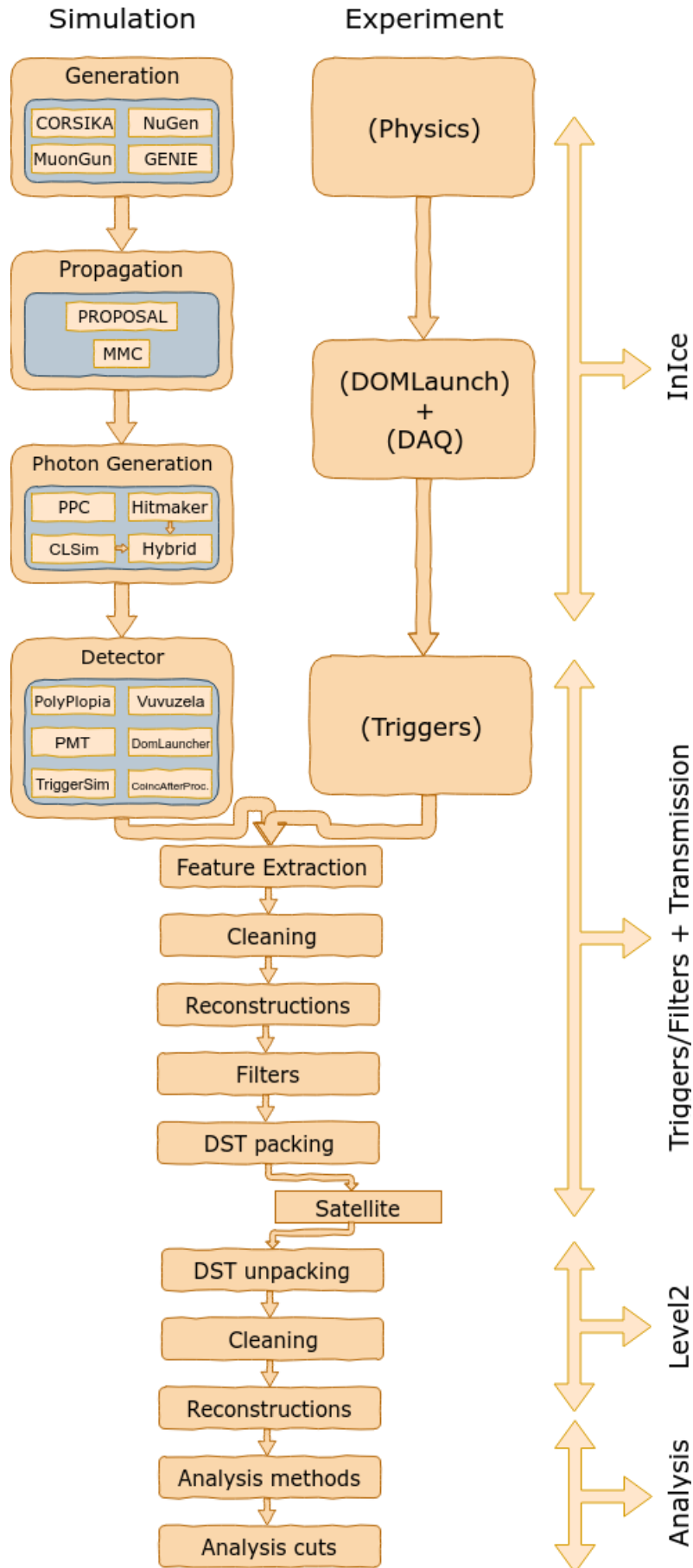


Figure 6.1: Flowchart of the simulation layout. On the left is shown that particles are injected and their interactions are simulated to digitized waveforms. The right part shows real data processing. After triggering, both data and simulation go through the same processing chain to prepare for analysis.

up by running hundreds to thousands of jobs in parallel over multiple computing resources all over the world. Each dataset has specific input parameters that are fixed. Distributions in physical parameters such as the direction, energy, position, etc. of the particle(s) are provided by random number generators [179].

HTCondor is an open source computing software that provides a job queueing mechanism, scheduling policy, priority scheme, resource monitoring, and resource management. Users submit their serial or parallel jobs to HTCondor and places them into a queue. It chooses when and where to run the jobs based upon a policy, carefully monitors their progress, and ultimately informs the user upon completion.

DAGMans (Directed Acyclic Graph Managers) are meta-schedulers for the execution of computations. They submit the programs to HTCondor in an order that is represented by a DAG and processes the results. DAGMans are often used by analyzers for bulk computations on large amounts of data.

6.1 Generation

Simulations start with setting up the starting conditions of the physical processes one wants to simulate. For example, a shower event by itself is not well defined. The type of primary particle (H, He, Fe,...), the energy, the inclination and so on will all define the properties of the full air shower that will be produced. Multiple different generators used in the IceCube collaboration serve other purposes; some are explained in more detail below.

6.1.1 Background simulation

6.1.1.1 CORSIKA

A free, publicly available software framework that is widely used in the astrophysics community for the simulation of cosmic ray interactions is called CORSIKA (COsmic Ray SImulations for Kascade). It was originally developed for the KASCADE experiment and now used by most people and collaborations to simulate air shower events. IceCube analyses, such as this one, use CORSIKA simulations to simulate the muonic component that is able to reach the in-ice detector.

The code is written in FORTRAN 77, but a C++ version is currently in the making [180].

A particle of specific type, energy, direction and position is injected in the top of the atmosphere and propagated. The distribution of particles in the shower is saved and read out according to a certain altitude. Because the flux of cosmic rays is exceedingly small at the highest energies, too many resources and too much time would be required to simulate an energy distribution as measured in experiments. Therefore, one often simulates a much harder spectrum and reweights the events accordingly later on (see Section D.4). Simulation datasets are often subdivided into a low-energy and high-energy dataset. In this analysis, the former ranges from primary energies between 600 GeV to 100 TeV and uses a spectral index that is close to what is measured. The spectral index of the latter is smaller, resulting in a harder spectrum, and the primary energy ranges from 100 TeV to 100 EeV. The lower limit of the energy range is due to the limited penetration depth of muons through the ice. An overview is given in Table 6.2.

The spectrum used for this analysis, after reweighting, follows the following energy distribution:

$$\Phi_i(E_{\text{prim}}) = \sum_{j=1}^3 a_{i,j} E^{-\gamma_{i,j}} \cdot \exp\left[-\frac{E}{Z_i R_{c,j}}\right]. \quad (6.1)$$

where we sum over the three populations that are mentioned in Section 3.1.2.2, γ is the spectral index, Z the particle atomic number and $a_{i,j}$ the normalization constants for primary i in population j . The 5 groups that are assumed to contribute significantly to the flux are: p, He,

Table 6.1: Best fit for parameters in Eq. 6.1. Numbers taken from Ref. [94].

j	R_c [V]	γ					$a_{i,j}$				
		p	He	CNO	Mg-Si	Fe	p	He	CNO	Mg-Si	Fe
1	$4 \cdot 10^{15}$	1.66	1.58	1.63	1.67	1.63	7860	3550	2200	1430	2120
2	$30 \cdot 10^{15}$			1.4			20			13.4	
3	$2 \cdot 10^{18}$			1.4			1.7			1.14	

CNO, Mg-Si and Fe. This is the convention that is used in Ref. [94]. Table 6.1 shows the best fits for the normalization constants to describe the data.

Interactions

The atmosphere composition is always set at 78.1% N₂, 21% O₂, and 0.9% Ar, which is a good description of reality. However, the density of the air above the detector changes significantly during the year because of temperature differences in the Arctic Summer and Winter. Most analyses treat the muonic component as a background and are not interested in the details of the showers and how it changes during the year and therefore use an average of the atmospheric density.

The shower propagation and composition depends on the models that are used to simulate these high-energy interactions. The lowest energies are simulated with FLUKA (FLUktuierende KAskade) [181]. This model covers the energy range that can be compared with accelerator experiments. Which model is the best for the highest energies is not known at the time of writing since there are no controlled laboratory measurements that are capable of reaching these energies. Several studies seem to indicate that the composition changes drastically at the highest energies **SAMCITEREN+andere**. Fortunately, this is of no importance for this analysis.

6.1.1.2 NuGen

The neutrino-generator (NuGen) is a neutrino event generator program that works with the IceTray framework. With this module, one can inject a primary neutrino on the surface of the Earth by specifying a few parameters in the steering file.

The physics implemented in this program is based on the ANIS-All Neutrino Interaction Generator [182]. However, the cross sections have been updated and the structure of the code has been changed significantly from ANIS to incorporate it in the IceTray framework.

The generator requires the first interaction to be near the detector and

- prepares a primary neutrino and injects it to the Earth,
- propagates the neutrino and works out interactions inside the Earth* (when they occur),
- makes a forced interaction inside the detection volume† (only if any neutrino reaches the detector site),
- stores injected neutrinos and all generated secondaries,
- stores interaction weight information.

The generator also does not distinguish between neutrino and antineutrino and assumes a ratio of (1:1).

The spectrum used for this analysis, after reweighting, follows the Honda2006 spectrum [125] for atmospheric neutrinos, SarcevicStd for the prompt component [128], and an astrophysical flux fit

* Possible interactions are CC, NC, Glashow resonance for $\bar{\nu}_e$ and tau decay for $\nu_\tau^{(-)}$. CC interactions produce no new neutrinos and the simulation stops at the vertex point. The other interactions create new secondary neutrinos.

† In most cases, a neutrino will not interact within the medium, but for computational reasons at least one neutrino is forced to interact and the simulation is reweighted afterwards accordingly.

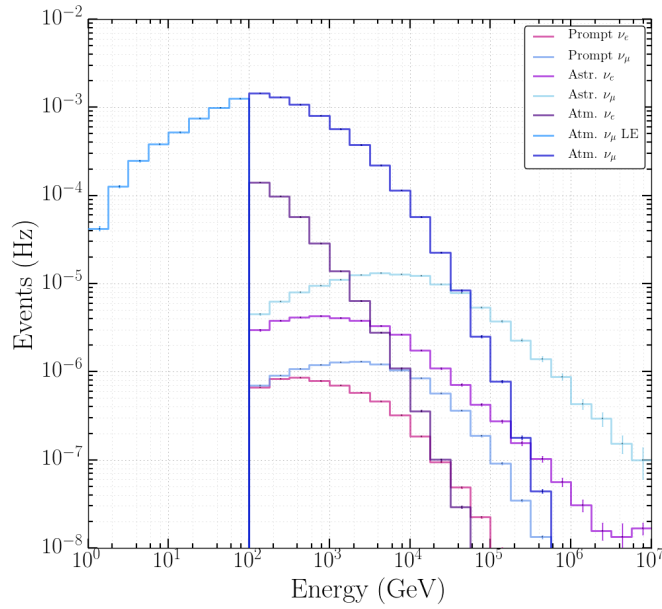


Figure 6.2: Distribution of weighted neutrino fluxes that were used for this analysis. The atmospheric ν_μ and ν_e fluxes were derived from Ref. [125], prompt from Ref. [128], and astrophysical from Ref. [183].

from Ref. [183] (see Section 3.2 for more information on these fluxes). The astrophysical flux measured by the IceCube collaboration follows an energy spectrum equal to

$$E^2(\Phi) = 1.5 \cdot 10^{-8} \left(\frac{E}{100 \text{ TeV}} \right)^{-0.3} \text{ GeV cm}^{-2} \text{s}^{-1} \text{sr}^{-1}. \quad (6.2)$$

The distribution for these different components can be seen in Fig. 6.2.

6.1.1.3 GENIE

To include the lowest energies, which are not accounted for by ANIS/NuGen, the GENIE (Generates Events for Neutrino Interaction Experiments) neutrino generator was implemented in IceTray. It is a well established generator, used by collaborations worldwide and written in C++ [184, 185].

The spectrum used for this analysis, after reweighting, follows the Honda2015 spectrum [186] for low-energy atmospheric neutrinos.

6.1.2 Signal simulation

As mentioned in Section 2.3, the signal flux is assumed to be isotropic close to the detector. The SMP starting points are randomly placed on a disk with a direction perpendicular to it as shown in Fig. 6.3. The disk has a radius of 800 m and is located at a distance of 1000 m from the detector center. The disk itself is randomly rotated around the detector center to simulate an isotropic flux. The distribution of the azimuth, ϕ , and cosine of the zenith*, $\cos(\theta)$, is shown in Fig. 6.4.

Because slow moving particles would require specialized treatment, the minimal velocity of the particles is set as $\beta > 0.95$ and simulated with an E^{-1} spectrum. The spectrum is later normalized to a flux of $10^{-14} \text{ GeV cm}^{-2} \text{ s}^{-1} \text{ sr}^{-1}$ with an E^{-2} spectrum (see Appendix D.2) where the absolute flux is only necessary for illustrative purposes, see Section [refer to this section](#)

*See Appendix D.3 why we show the cosine of the zenith.

Table 6.2: Overview of the datasets used in this analysis. GaisserH3a from Ref. [94], Honda2015 from Ref. [186], Honda2006 from Ref. [125], Sarcevic from Ref. [128], and astrophysical from Ref. [183].

Generator	Type	Range [GeV]	Simulated γ	Weighted γ	Ice	Dataset
CORS.	5-comp.	$10^5 - 10^{11}$	2	GaisserH3a	SpiceLea	11937
CORS.	5-comp.	$600 - 10^5$	2.6	GaisserH3a	SpiceLea	11499
CORS.	5-comp.	$600 - 10^5$	2.6	GaisserH3a	SpiceLea	11808
CORS.	5-comp.	$600 - 10^5$	2.6	GaisserH3a	SpiceLea	11865
CORS.	5-comp.	$600 - 10^5$	2.6	GaisserH3a	SpiceLea	11905
CORS.	5-comp.	$600 - 10^5$	2.6	GaisserH3a	SpiceLea	11926
CORS.	5-comp.	$600 - 10^5$	2.6	GaisserH3a	SpiceLea	11943
CORS.	5-comp.	$600 - 10^5$	2.6	GaisserH3a	SpiceLea	12161
CORS.	5-comp.	$600 - 10^5$	2.6	GaisserH3a	SpiceLea	12268
GENIE	ν_μ	$0.5 - 100$	1	Honda2015	SpiceMie	12475
NuGen	ν_μ	$100 - 10^8$	2	atmos.: Honda2006 prompt: Sarcevic astro.: Astro.	SpiceLea	11029
NuGen	ν_μ	$100 - 10^8$	2	atmos.: Honda2006 prompt: Sarcevic astro.: Astro.	SpiceLea	12346
NuGen	ν_μ	$100 - 10^8$	2	atmos.: Honda2006 prompt: Sarcevic astro.: Astro.	SpiceLea	11883
NuGen	ν_e	$100 - 10^8$	2	atmos.: Honda2006 prompt: Sarcevic astro.: Astro.	SpiceLea	12034
NuGen	ν_e	$100 - 10^8$	2	atmos.: Honda2006 prompt: Sarcevic astro.: Astro.	SpiceLea	12646

Table 6.3: Overview of the datasets used for systematic uncertainties. Polyg(onato) follows from Ref. [187], GaisserH4a from Ref. [188] and Bartol from Ref. [189].

Generator	Type	Range [GeV]	Sim. γ	Weighted γ	Ice	Dataset	Syst. Eff.
CORS.	Hoerandel	$600 - 10^5$	Polyg.	GaisserH3a	SpiceLea	11527	DOM eff. -10%
CORS.	Hoerandel	$600 - 10^{11}$	Polyg.	GaisserH3a	SpiceLea	11526	DOM eff. +10%
CORS.	5-comp.	$600 - 10^{11}$	2.6	GaisserH3a	SpiceLea	12388	Abs. +10% Scat. +10% Abs./Scat. -7.1%
CORS.	All datasets from Table 6.2			GaisserH4a	SpiceLea	Table 6.2	GaisserH4a
NuGen	ν_μ	$100 - 10^8$	2	Bartol (syst.)	SpiceLea	11029	Bartol flux
NuGen	ν_μ	$100 - 10^7$	2	Honda2006 + Bartol (syst.)	SpiceLea	11883	DOM eff. +10% DOM eff. -10% Abs. +10% Scat. +10% Abs./Scat. -7.1% Bartol flux
NuGen	ν_μ	$100 - 10^8$	2	Honda2006 + Bartol (syst.)	SpiceLea	12346	DOM eff. +10% DOM eff. -10% Abs./Scat. -7.1% Bartol flux

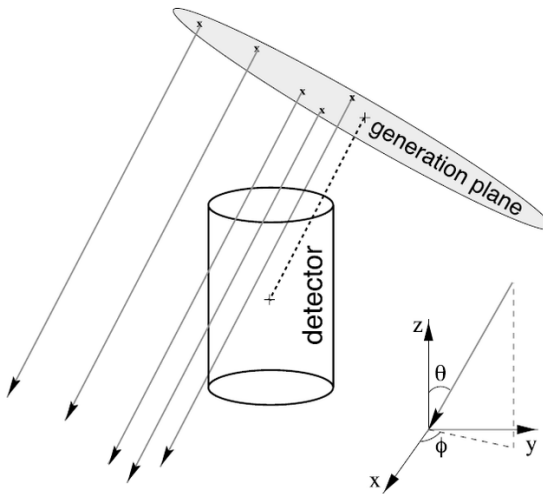


Figure 6.3: Illustration of how the particle injection works. The particle is first randomly positioned on a disk following a uniform distribution. The disk is then randomly rotated to simulate an isotropic flux.

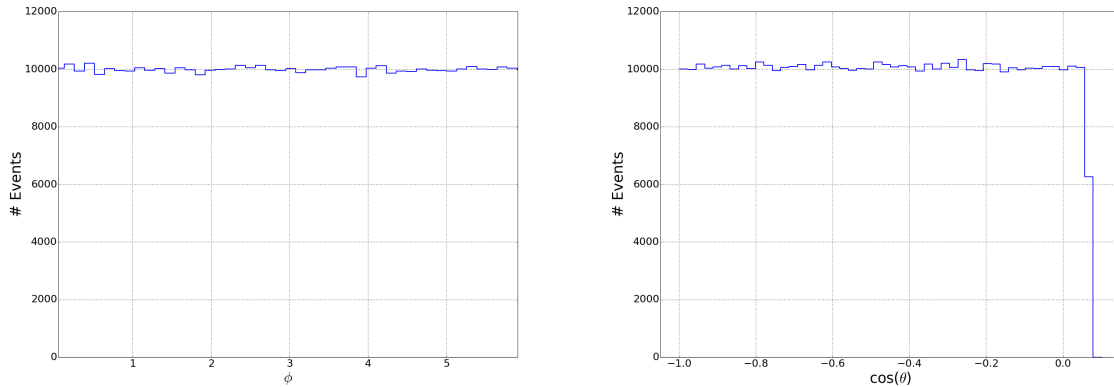


Figure 6.4: Illustration of uniform distributions of azimuth and cosine of the zenith for the particle injection in agreement with an isotropic flux (see Appendix D.1).

when it's written!.

Similar to the background, SpiceLea was used as the nominal ice model.

6.2 Propagation

After generation, the particles need to be propagated through the medium. The particles will interact, lose energy, produce new particles, and generate light. The particle interactions and light production are done in two different modules as photon simulation is done with GPU. The former module is called **PROPOSAL**, the latter **ppc**.

6.2.1 PROPOSAL

Using the cross sections of the important interactions, together with the properties of the traversing medium and the particles (mass, charge, spin, decay time, etc.), it is possible to simulate the energy losses, secondary production and the consequent interactions of these daughter particles. This is done in the software package **PROPOSAL** (the Propagator with Optimal Precision and Optimized Speed for All Leptons), fully written in C++. It was based on its predecessor **MMC** (Muon Monte Carlo), which was written in Java. In 2018, a substantial improved version of

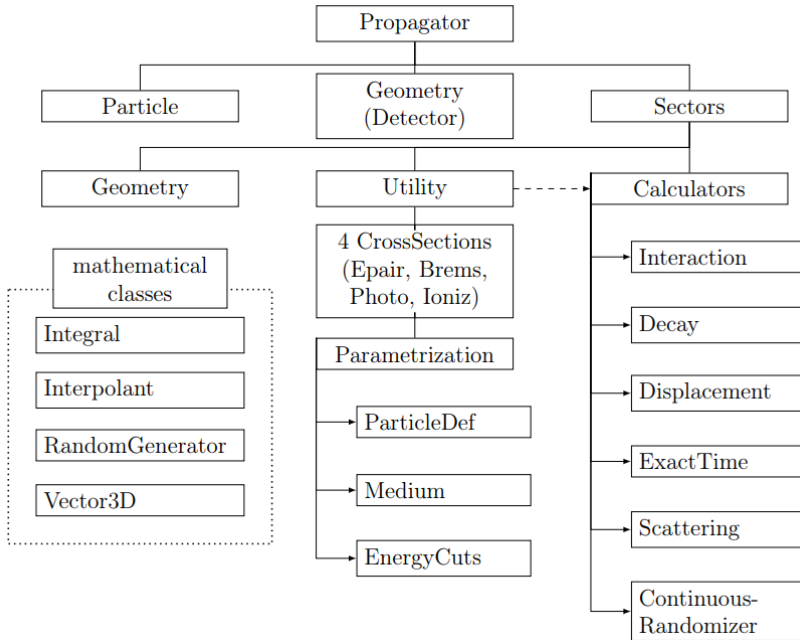


Figure 6.5: Overview of the class structure in PROPOSAL, from Ref. [190].

PROPOSAL was finalized. An illustration of the workings of the code is given in Fig. 6.5 and an in-depth documentation is given in Ref. [190].

PROPOSAL for SMPs

Since we assume the SMPs to behave leptonically, it was chosen to use PROPOSAL for the signal propagation as well. The mass and charge of the particle are set in the input parameters and the cross section dependence on these parameters can be seen in Section 4.4. In general, there is a small dependence on the mass and a squared dependency on the charge, except for bremsstrahlung that has a quadratic charge dependency. These effects only become prominent and important for highly relativistic particles, which as will be seen in Section *verwijs hiernaar als je dit geschreven hebt*, do not have a dominating contribution to the total signal.

The PROPOSAL module keeps track of all the particles that are produced during propagation and the accompanying energy losses in a tree-like structure (called an *I3MCTree*). This collection of particles and their interactions are forwarded to a light production computation module.

6.2.2 Photoelectron generators

In Section 5.2.1 we already explained how the ice is simulated in the IceCube detector. The parameters $b_e(400)$ and $a_{dust}(400)$ define the photon propagation through the ice and determine if they are absorbed or hit a DOM. To optimize computing time, the DOMs were scaled (nominally with a factor of 5) to force more photon interactions. The number of photons emitted was then appropriately scaled down with the square of this scaling factor*. The DOM acceptance curves, as shown in Fig. 5.7, together with the Frank-Tamm formula (Eq. 4.8) allow to calculate the expected number of photons produced per unit length:

$$\frac{dN}{dx} = \int_{\lambda_1}^{\lambda_2} \frac{2\pi\alpha}{\lambda^2} \sin^2(\theta_c) d\lambda = 2\pi\alpha \sin^2(\theta_c) \left(\frac{1}{\lambda_1} - \frac{1}{\lambda_2} \right). \quad (6.3)$$

From this formula, we find that the expected rate of a Cherenkov emission profile is equal to ≈ 350 photons/cm. Together with the DOM acceptance, which has an overall average of around 7%, the expected *seen* number of photons per meter is equal to 2450 m^{-1} .

*The surface of a sphere scales with the square of the radius.

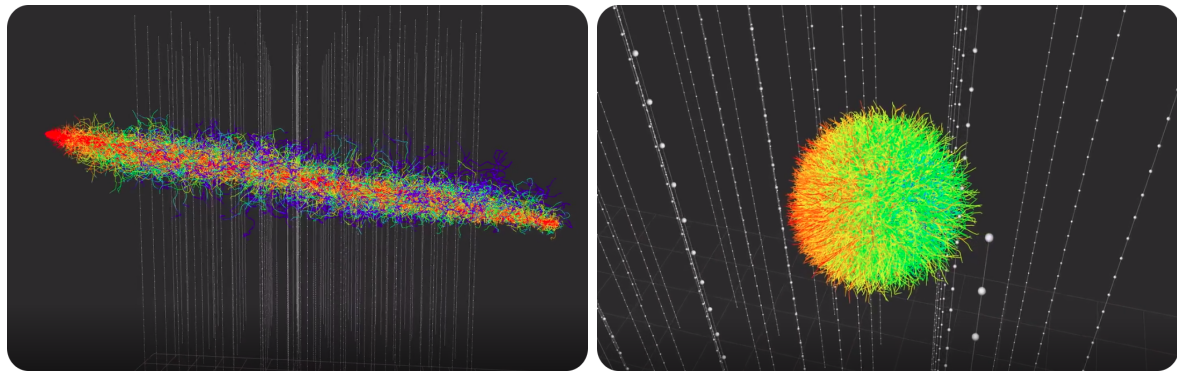


Figure 6.6: *Left:* simulation of a track event in IceCube. Each line represents a photon path and colors indicate how far they have traveled from their generation point. *Right:* simulation of a cascade event in IceCube.

PPC is a Photon Propagation Code, written in C++ and runs on graphic processing units (GPUs). This allows the code to run up to a hundred times faster than in a CPU-only environment. PPC employs both CUDA (NVIDIA GPU only) and OpenCL programming interface (both NVIDIA and AMD GPUs) together with multiple CPU environments. GPU environments allow the tracking of thousands of photons simultaneously, vastly improving the computational speed. For more information, see Ref. [191].

Previous photon propagation code, such as **Photonics** [192], produced 6-dimensional photon tables (3 spatial, 2 directional and 1 temporal). This meant that at least one set of tables had to be produced per particle type and per velocity and interpolation methods had to be used, with the accompanying inaccuracies. These tables also required significant disk space and the method was therefore replaced with the GPU-codes. Direct photon simulation also allows for other non-trivial implementations such as the tilting of ice layers.

Another photon propagation code is called **CLSim**, which uses GEANT4 to propagate particles. A hybrid version called **HybridCLSim** is often used. Muons are propagated using **PROPOSAL/MMC** and their stochastic losses (which are small showers) are simulated from tables whereas the “bare muons” (with their stochastics) are simulated using direct propagation. This avoids time loss for the rare but very computational high-energy cascade events.

An illustration of photon propagation in the IceCube detector for both a cascade and track simulation is shown in Fig. 6.6.

Nergens vermeldt hoe je je signaal verandert hebt hierop...

6.3 Detector simulation

Further processing of the simulations involve:

- **Polyplopia:** a project dedicated to merge multiple events to account for coincident events (that are simulated independently). An estimated 15% of CORSIKA events result in coincident events and make up the bulk of bad reconstructions where down-going muons are simulated as up-going (example see Fig. 7.5);
- **Vuvuzela:** the PMT noise is simulated as having an exponential component from thermal and radioactive decays, and a log-normal contribution for scintillation;
- **PMT:** the time from the first photon entering the PMT to the readout after passing along multiple dynodes has an uncertainty, referred to as “PMT jitter”. The amplification of photoelectrons by the PMT is also not constant and is simulated in this module. Additionally, the module accounts for prepulses, late pulses, afterpulses and saturation of the PMT. More information can be found in Refs. [144, 193].

- **DOMLauncher**: the digitization of the PMT pulses and other behavior of the DOM mainboard (as explained in Section 5.3.1.2) is done in this module. The three main features of the DOM that are simulated to generate launches are the discriminator, LC, and digitization.
- **trigger-sim**: simulation of the trigger behavior as explained in Sec. 5.5.1.

6.4 Processing

After a full particle propagation and detector response simulation, the sample is sent through the same PnF procedure as is done with the data (see Section 5.5.2). The different stages of processing are referred to as “Levels”, where basic conversion from PnF formats to i3files is called *Level0* done for data. Reconstructions, calibrations and hit cleaning necessary for the filters are done at *Level1* while the filter processing is done at *Level2*. These two levels are usually only run on simulation sets unless data is being reprocessed.

6.5 Burn sample

Getting the intricate details of physical events in non-trivial environments just right is not an easy task. In many steps of the way, simulations use fits and estimations. Some simulation datasets are reasonable to compare to the data, depending on the phase space one is looking at, while other datasets need other specifications. For example, analyses dedicated to measuring the cosmic ray interactions need much more fine-tuning in their models for the atmosphere, composition, interaction models, etc. than an analysis dedicated to search for muon tracks that first propagated through the Earth and have atmospheric muons as a background.

It is for this reason, most analyses select a certain subset of the data they want to analyze to compare to the Monte Carlo simulations. For this analysis, 10% of the total data, called the *burn sample*, was used to compare data to Monte Carlo. As indicated in Section 5.5.3, the data is saved in 8-hour runs and the burn sample consists of every run ending with a ‘0’. The burn sample also allows to estimate the robustness of certain reconstructions and variables regarding differences in data and simulation.

After the discovery of an SPE offset in the DOM response in 2015, it was decided that multiple years of data was to be reprocessed in what was called *pass2 reprocessing* [194]. Aside from the SPE correction, the raw pulses were reprocessed with 2017 PnF, making the data more uniform in the course of the years for easier comparison*. This analysis makes use of data starting in the years 2011 to 2015 and are referred to as IC86-1 to IC86-5 where IC86 stands for the complete 86-string IceCube detector configuration and the last digit refers to the year of the season start. Only runs were considered that had

1. a positive tag from run coordinators (status == “good_i3”),
2. at least 5000 active optical modules,
3. all strings active during runtime.

The *livetime* is the total time that the detector was up and running and non-corrupted data was processed. Due to the increase in detector uptime over the years, this also means that the livetime of the different datasets has increased. The livetime for the different years is equal to

- around 31 days of livetime for IC86-1,
- around 32.2 days of livetime for IC86-2,
- around 33.2 days of livetime for IC86-3,
- around 36.6 days of livetime for IC86-4,
- around 36.7 days of livetime for IC86-5,

resulting in a total burn sample livetime of around 170 days.

In tabel misschien? En data van start/einde...?

*Most filters did not undergo changes or only minor ones.

6.6 Event viewer

After a full simulation, it is possible to visualize the event in an event viewer called **Steamshovel**. Typical events in the IceCube detector are shown with this interface and are loaded from *i3files* that contain information about the detector geometry and the full event (DOM positions and calibrations, detector hits, timestamps, trigger hits, etc.). Simulated events also contain the true values of the particles and can be compared with reconstructed variables. Event viewers allow for first guesses in how background events are able to be separated from signal, although both can have wide varieties in possible outputs.

The number of photons seen per DOM is indicated by the size of the spheres; the larger the sphere, the more PEs were seen. The color of the modules indicates the time of the pulse registration. The color scale can be chosen, but usually a rainbow pattern is used where red indicates the earliest pulse hits and blue the last.

An example is given in Fig. 6.6.

en in eerste steamshovel verwijzen naar dit deel?.

7. Reconstruction, Cleaning and Analysis Techniques

Shall I refuse my dinner because I do not fully understand the process of digestion? ~ Oliver Heaviside

Because the in-ice IceCube detector is sparsely distributed, it is not straightforward to unambiguously reconstruct the particle (interactions). The scattering and absorption of photons, tilt of ice sheets, bubble column, etc. lead to uncertainties and make reconstruction challenging. Over the years, multiple reconstruction methods have been developed in the collaboration. They range from very fast (and simple) reconstructions, necessary for online filtering, to slow (and more refined) ones. Multiple reconstruction algorithms have been used in this analysis and are explained in more detail in this chapter.

7.1 Reconstruction

7.1.1 Likelihood

Reconstruction algorithms usually have no unique solutions to describe the set of measured values of an event. The likelihood $\mathcal{L}(\vec{x}|\vec{a})$ describes the probability of a set of parameters \vec{a} to be expressed in a set of experimentally measured values \vec{x} . The parameters, \vec{a} , typically define the particle's characteristics (energy, direction, position, type, etc.) while the measured values \vec{x} are determined from the detector response (number of PE, timing, position of hit DOMs, etc.). This likelihood is equal to the cumulative probability

$$\mathcal{L}(\vec{x}|\vec{a}) = \prod_i p(x_i|\vec{a}), \quad (7.1)$$

where $p(x, \vec{a})$ is the probability that we measure a certain value x from a set of independent values \vec{x} given an initial set of parameters \vec{a} . The best possible guess for the unknown parameters \vec{a} is the most likely set that will result into the experimental values. This is done by maximizing the likelihood \mathcal{L} . The reconstruction algorithms below rely on analyzing parameters that assume a single, long track

$$\vec{a} = (\vec{r}_0, t_0, \vec{p}, E_0), \quad (7.2)$$

where \vec{r}_0 is the position vector of the particle at a time t_0 with a direction \vec{p} and initial energy E_0 .

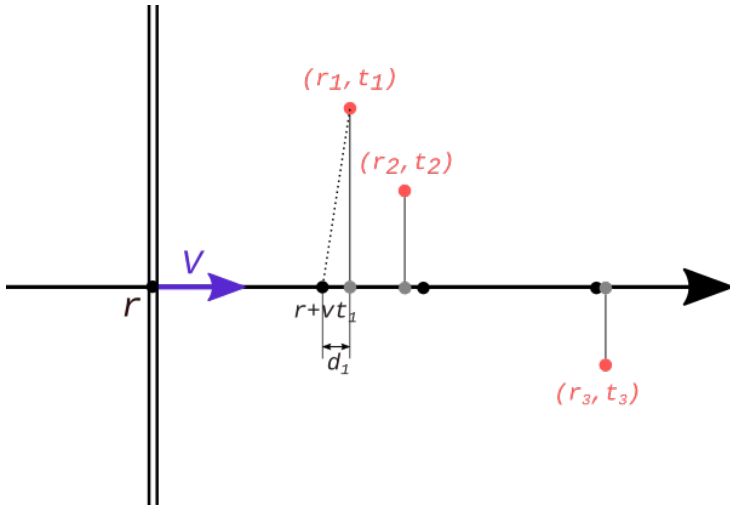


Figure 7.1: Figure illustrating how **LineFit** works. The position, \vec{r} , and velocity, \vec{v}_{part} minimizing the distance of the DOMs to the track is calculated. The dotted line is one of the distances that is minimized in Eq. 7.4.

7.1.2 Line-Fit

One of the most simple approaches in constructing a parameter profile is by calculating the track that, overall, has the closest approach of all the hit optical modules and is called **Line-Fit** (LF) [195]. If we assume that a particle starts at a position \vec{r} at a time 0 and travels at a velocity of \vec{v}_{part} , then its position at any given time is

$$\vec{r}' = \vec{r} + \vec{v}_{\text{part}}t. \quad (7.3)$$

We want to calculate the best possible estimate of the velocity \vec{v}_{part} and an initial position \vec{r} . Each DOM has a known location, \vec{r}_i , and measured time of a pulse, t_i . In this algorithm one assumes that a wavefront perpendicular to the particle's direction is traveling along with the particle. If the velocity \vec{v}_{part} is fixed, then the position of the particle at later times is known (black points in Fig. 7.1). However, the Cherenkov wavefront should be set at an angle and because scattering, PMT jitter, noise, etc. are not taken into account, this will not agree with the DOM position projected along the particle path (grey dots). The unknown velocity \vec{v}_{part} and position \vec{r} are the analytical solutions after minimizing the distances d_i as shown in the figure*

$$\begin{aligned} S(\vec{r}, \vec{v}_{\text{part}}) &\equiv \sum_{i=1}^{N_{\text{hit}}} \rho(\vec{r}, \vec{v}_{\text{part}}, \vec{r}_i, t_i)^2 \\ &= \sum_{i=1}^{N_{\text{hit}}} (\vec{r}_i - \vec{r} - \vec{v}_{\text{part}}t_i)^2, \end{aligned} \quad (7.4)$$

where N_{hit} are the number of pulse hits. The analytical solution by minimizing this equation is equal to

$$\vec{r} = \langle \vec{r}_i \rangle - \vec{v}_{\text{part}} \langle t_i \rangle \quad \text{and} \quad \vec{v}_{\text{part}} = \frac{\langle \vec{r}_i t_i \rangle - \langle \vec{r}_i \rangle \langle t_i \rangle}{\langle t_i^2 \rangle - \langle t_i \rangle^2}, \quad (7.5)$$

where $\langle x \rangle$ denotes the average of a parameter x over all hits i .

Because this is an analytical equation, this algorithm is very fast and therefore often used in online processing.

*Minimizing $r_i - r'$ (dotted line in Fig. 7.1) is the same as minimizing d .

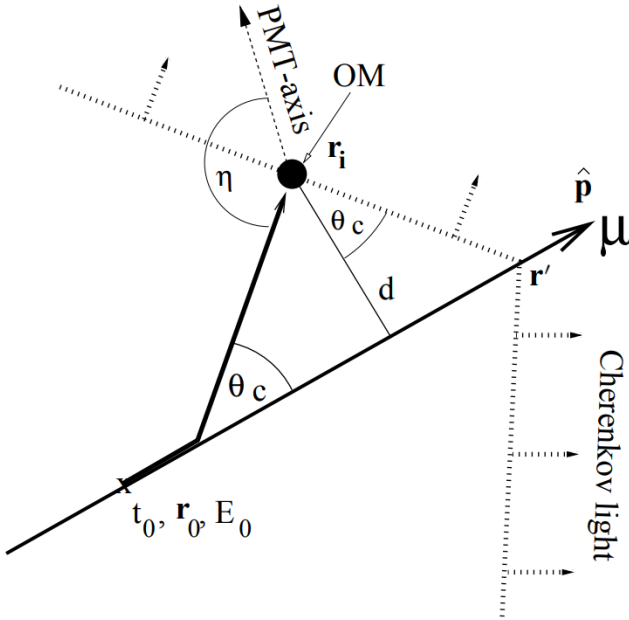


Figure 7.2: Figure illustrating a muon track passing close by an optical module and defining the parameters used in the reconstruction algorithms. Illustration from Ref. [195].

7.1.2.1 Improved Line-Fit

While disregarding the Cherenkov profile is inherent to the simplified LF model for computational reasons, removing hits generated by photons that scattered for a significant length of time will mitigate the effect of ignoring the photon scattering in the ice. It was found that a basic filter could identify these scattered hits, and improve accuracy by almost a factor of two by removing them from the dataset. More formally, for each hit h_i , the algorithm looks at all neighboring hits within a neighborhood of μ , and if there exists a neighboring hit h_j with a time stamp that is t earlier than h_i , then h_i is considered a scattered hit, and is not used in the basic reconstruction algorithm. Optimal values of μ and t were found to be 156 m and 778 ns by tuning them on simulated muon data [196].

This “delay cleaning” is done by computing the Huberfit on the remaining data points and minimizing

$$\sum_{i=1}^{N_{\text{hit}}} \phi(\rho(\vec{r}, \vec{v}_{\text{part}}, \vec{r}_i, t_i)), \quad (7.6)$$

where ρ is defined in Eq. 7.4 and the Huber penalty function ϕ is defined as

$$\phi(\rho) \equiv \begin{cases} \rho^2 & \text{if } \rho < \mu \\ \mu(2\rho - \mu) & \text{if } \rho \geq \mu \end{cases}. \quad (7.7)$$

Because of the overall performance increase of this method, all LF computations were done with the improved version (although still often referred to as “Line-Fit”).

7.1.3 SPE and MPE

A more intricate method of track reconstruction is done by taking the geometrical shape of the Cherenkov cone into account and relying on simulation fits where a seed track is implemented (usually from the fast Line-Fit algorithm).

Let us assume a particle is traveling close to a DOM with parameters defined in Eq. 7.2 as illustrated in Fig. 7.2. The minimal distance of the track to the DOM is equal to d and the PMT-axis (downwards relative to DOM) has an angle offset of η degrees of the Cherenkov wave

direction. In perfect conditions, the *time residual* (time between the observed hit time and the “expected” time) is a delta function centered around 0, where

$$t_{\text{res}} \equiv t_{\text{hit}} - t_{\text{geo}}, \quad (7.8)$$

with

$$t_{\text{geo}} = t_0 + \frac{\vec{p} \cdot (\vec{r}_i - \vec{r}_0) + d \cdot \tan(\theta_c)}{c_{\text{vac}}}, \quad (7.9)$$

which is equal to the time of the particle to travel from the position \vec{r}_0 to \vec{r}' as illustrated in the figure. The accompanying Cherenkov wavefront that sent out photons at a time t_0 from \vec{r}_0 will cross the DOM when the particle is at a position \vec{r}' . Due to noise effects, PMT jitter, light from secondary interactions, DOM orientation, etc. the time residual is smeared and shifted. The p.d.f. was estimated with photon simulations in ice and fitted to a Podel function [195]. The time likelihood profile for single photons i at the locations of the hit DOMs is then

$$\mathcal{L}_{\text{time}} = \sum_{i=1}^{N_{\text{hit}}} p_1(t_{\text{res}} | \vec{a} = d_i, \eta_i, \dots). \quad (7.10)$$

An initial particle position and direction are found by maximizing the likelihood and iterated a couple of times to find the global maximum instead of a local. This fitting is called the Single PhotoElectron (SPE) fit.

The description of single photons arriving at the optical modules cannot be correct since electrical and optical signal channels can only resolve multiple photons separated by a few 100 ns and \approx 10 ns, respectively. In the Multi-PhotoElectron (MPE) fit, one accounts for the fact that the early photons in a DOM hit scattered less in the ice. The p.d.f. for the first photon out of a total of N to arrive with a time residual of t_{res} is

$$p_N^1(t_{\text{res}}) = N \cdot p_1(t_{\text{res}}) \cdot \left(\int_{t_{\text{res}}}^{\infty} p_1(t) dt \right)^{(N-1)} = N \cdot p_1(t_{\text{res}}) \cdot (1 - P_1(t_{\text{res}}))^{(N-1)}, \quad (7.11)$$

where P_1 is the cumulative distribution of the single photon p.d.f..

7.1.4 Millipede

?? To have a better handle on the particle energy and cascades along the track, the module **Millipede** was developed. The number of photons seen at each optical module depends on multiple factors that were mentioned throughout this text, such as the ice characteristics, timing, etc. In this module, the expected number of photons is said to depend on the energy that was deposited along a track and a *light yield factor* that depends on the DOM position and the location of emission

$$\begin{aligned} N_{\text{exp},k} &= \rho_k + \sum_{i=1}^n \Lambda(\vec{r}_k, \vec{r}'_i) E_i \\ &= \rho_k + \vec{\Lambda}(\vec{r}_k, \vec{r}'_i) \cdot \vec{E}, \end{aligned} \quad (7.12)$$

where k refers to a certain DOM and i refers to a certain energy deposit such as illustrated in Fig. 7.3.

The likelihood is assumed to follow a Poisson distribution with a mean equal to the expected amount of photons, $N_{\text{exp},k}$

$$\mathcal{L}_k = \frac{(\vec{\Lambda} \cdot \vec{E} + \rho_k)^{N_{\text{seen},k}}}{N_{\text{seen},k}!} e^{-\vec{\Lambda} \cdot \vec{E} - \rho_k}. \quad (7.13)$$

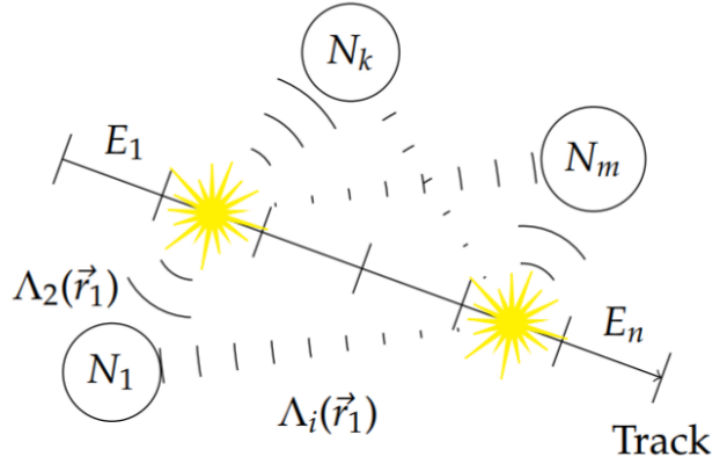


Figure 7.3: Illustration of the working principles of the **Millipede** toolkit. A track is subdivided into segments that each deposit a certain energy, E_i . Different segments can contribute to the total number photons seen per DOM, N_k .

For easier, faster and more accurate computation the logarithm of the likelihood is used

$$\begin{aligned} \ln \mathcal{L}_k &= N_{\text{seen},k} \ln \left(\rho_k + \sum_{i=1}^n \Lambda(\vec{r}_k, \vec{r}'_i) E_i \right) - \ln(N_{\text{seen},k}!) - \sum_{i=1}^n \Lambda(\vec{r}_k, \vec{r}'_i) E_i - \rho_k \\ &= N_{\text{seen},k} \ln \left(\rho_k + \vec{\Lambda}(\vec{r}_k) \cdot \vec{E} \right) - \vec{\Lambda}(\vec{r}_k) \cdot \vec{E} - \rho_k - \ln(N_{\text{seen},k}!) \end{aligned} \quad (7.14)$$

Maximizing the total likelihood (summing over all m DOMs) with respect to the energy gives

$$\nabla_{\vec{E}} \ln \mathcal{L} = \nabla_{\vec{E}} \sum_{k=1}^m \ln \mathcal{L}_k = \sum_{k=1}^m \left(\frac{N_{\text{seen},k} \vec{\Lambda}(\vec{r}_k)}{\vec{\Lambda}(\vec{r}_k) \cdot \vec{E} + \rho_k} - \vec{\Lambda}(\vec{r}_k) \right) = 0. \quad (7.15)$$

This equation holds if all terms in the sum vanish, i.e. if for all DOMs holds that

$$\begin{aligned} N_{\text{seen},k} &= \vec{\Lambda}(\vec{r}_k) \cdot \vec{E} + \rho_k \\ &\stackrel{\text{Eq. 7.12}}{=} N_{\text{exp},k}. \end{aligned} \quad (7.16)$$

This can be written in a set of linear equations

$$\vec{N} - \vec{\rho} = \mathbf{\Lambda} \vec{E}, \quad (7.17)$$

where

$$\mathbf{\Lambda} = \begin{pmatrix} \Lambda(\vec{r}_1, \vec{r}'_1) & \cdots & \Lambda(\vec{r}_1, \vec{r}'_n) \\ \vdots & \ddots & \cdots \\ \Lambda(\vec{r}_m, \vec{r}'_1) & \cdots & \Lambda(\vec{r}_m, \vec{r}'_n) \end{pmatrix}, \quad (7.18)$$

is the *response matrix* and has to be inverted to find the energies in the vector \vec{E} . It describes the DOM response to light output from certain segments along a track. The entries in this matrix come from simulations that produce spline tables. Simplified sources, such as minimum ionizing muons and isotropically emitting point sources are simulated in Monte Carlo simulations at certain discrete points. Interpolation is done using spline functions. More information, such as how timing information can be implemented, can be found in Refs. [197, 198].

7.1.5 FiniteReco

FiniteReco is a module that tries to reconstruct if particles are starting, stopping, contained or through-going. The hit DOMs around a seed track are checked to have seen light and the first and last emission points along the track are used to check the possible hypotheses.

Because the edges of the detector are not well defined*, the likelihoods of individual DOMs to have seen a hit lead to a total likelihood that doesn't give a conclusive answer, but the starting and stopping probabilities can be compared to a through-going track hypothesis.

7.1.6 Paraboloid

In Sections 7.1.2 and 7.1.3, we discussed how a particle's direction could be estimated. The **Paraboloid** module tries to provide an estimate for the error on this direction. A highly energetic muon with hundreds of hit DOMs will lead to a much better directional resolution than a dim track where only a handful of DOMs are hit. In general, the likelihood space around the estimated direction is scanned and compared to the likelihood of the initial track estimation. This method also gives a robust estimation if the initial track direction is in fact located at the global maximum likelihood or a local one. **Paraboloid** constructs a grid of zenith and azimuth points near the minimum and for each point on the grid it does a three-parameter minimization for the vertex holding the zenith and azimuth constant. The likelihood values for each point on the grid are then fit to paraboloid using a χ^2 minimization since the shape of the log-likelihood space near the minimum should have a paraboloid (2D parabola) shape. Of importance are the parameters of the corresponding error, which is assumed to correspond to an ellipse for the 1σ contours.

The module computes the lengths of the semimajor and semiminor axes of the 1σ error ellipse σ_1 and σ_2 [†]. It was found that the quadratic mean of both uncertainties provides for a good single-valued estimate for the angle uncertainty

$$\sigma_{\text{para}} = \sqrt{\frac{\sigma_1^2 + \sigma_2^2}{2}}. \quad (7.19)$$

Since σ_1 and σ_2 should follow univariate Gaussian distributions, σ_{para} will be the radius parameter in a bivariate distribution, meaning that the mean should be set to 1.177σ [‡]. This means, that if we calculate the great circle distance between the MC truth of the signal particle with the reconstruction direction and divide it with σ_{para} , the distribution should peak at 1.177 (mean). This variable is called the *paraboloid pull* and should be compared to an energy related variable (here the number of hit DOMs (NCh) is used). In Fig. 7.4, it is clear that there is an offset, which is seen in all analyses, that can be explained by multiple factors in Monte Carlo simulations but mainly stems from our incomplete knowledge and non-perfect simulations of the ice.

More information can be found in Ref. [199].

7.2 Pulse cleaning

As explained in Section 5.3.2, each DOM in IceCube has an intrinsic noise rate. This dark noise is observed in every triggered event and seen as random hits in the detector added to the hit pattern of tracks and cascades. These spurious hits are a large nuisance factor in event reconstructions, leading to misidentification and errors in the result. Noise cleaning should be done in early stages of event processing and analysis to reduce a large rate of bad reconstructed events that pass cut selections. One of the most conservative ways is to only look at HLC hits (*HLC cleaning*), but is too demanding for most low-energetic events that will have multiple hits from isolated DOMs.

*Imagine a cascade 20 m below the lowest DOMs. It is still possible for light to reach the bottom modules of the detector.

[†]The confidence intervals σ_θ and σ_ϕ can be found by rotating the minor and major axes σ_1 and σ_2 . How this is done can be found in the literature, but is of no importance here.

[‡]The CDF of the Rayleigh distribution $1 - e^{-x^2/2\sigma^2}$ is equal to the containment for a bivariate normal distribution. Implementing $x = 1.177\sigma$ yields a factor of 0.5.

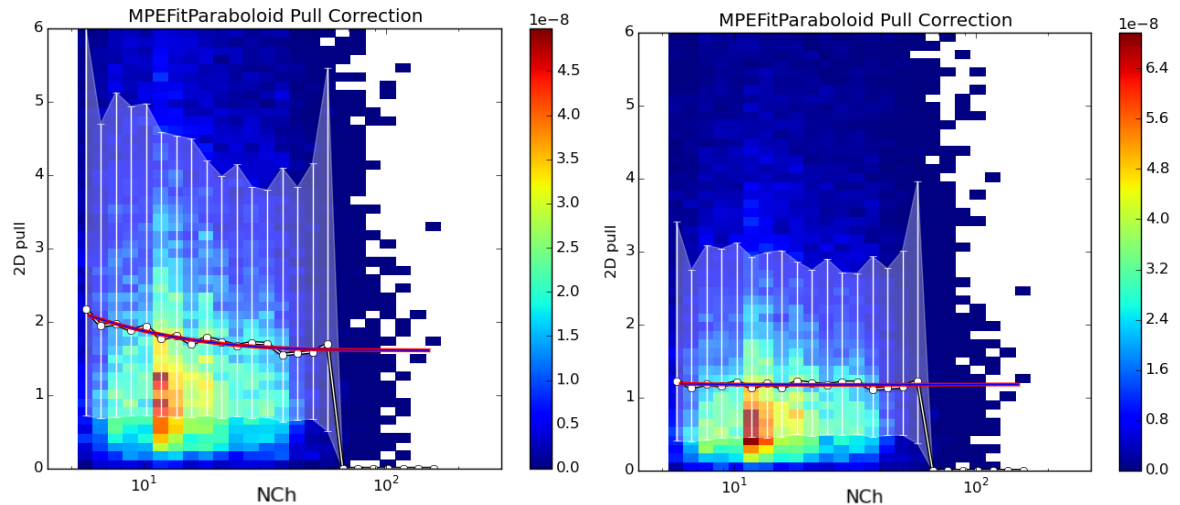


Figure 7.4: *Left:* Paraboloid pull in function of the number of hit DOMs shows that the global average (red/purple line) is not centered at 1.177. *Right:* Pull after correction.

Another, more conservative method, is the `seededRT` algorithm. This method relies on the “*RT-cut*”, which was already implemented in the time of AMANDA operations. R is a designed radius and T refers to the time between multiple possible pulse times (e.g. the pulse of one DOM starts during the time window of a second DOM’s pulse, or stops during the time window). The full description can be found in Ref. [200], but can be summarized as follows: DOMs are required to be in a temporal and spacial coincidence that is physically possible (e.g. signal between DOMs cannot exceed the speed of light in vacuum). This method is however computationally expensive since all DOM pairs have to be looped over*. The `seededRT` algorithm takes a subset of seeds that are considered to be mostly signal related hits. These seeds can be provided by, for example, using HLC information. By adding all further hits found within the seed’s *RT*-range to the list of seed hits and iterating until a convergence, only those (SLC) hits are kept that cluster around the initial seed hits. Outlying noise hits are supposedly not added and thus removed in the cleaned output. This method does not scale as drastically as the original *RT-cut* method.

7.3 IceHive

In Section 5.5.1, it was explained how multiple triggers were combined into one global trigger. In a first step, Q-frames are simply re-split into the individual events that belong to the different subtriggers. In about 15% of cases the data read out in one of these P-frames contains more than one primary interaction. This pile-up effect is referred to as *coincident events*. It is a direct result of the traversal time of a couple of microseconds in the detector[†], the large flux of low-energetic events and the trigger time windows of a couple of microseconds. This can be problematic for reconstructions, as can be seen in Fig. 7.5 where two downgoing muons can be reconstructed as an upgoing track.

There are two modules that try to clean events more thoroughly than pulse cleaning alone. The first is `TopolocalSplitter` (TS), which starts from the Q-frames and loops over pulses and splits the event into clusters of pulses that contain at least a number of causally[‡] connected pulses within a certain time window. Some extra cleaning, similar to `seededRT` cleaning, is done in addition and can split coincident events that have overlapping readout windows, but are geometrically separated.

*The number of pairs for n DOMs is equal to $\frac{1}{2}n(n - 1)$ and scales with n^2 .

[†]The speed of light in vacuum is equal to ≈ 0.3 m/ns, meaning the particle travels around 100 m in 0.3 μ s, without accounting for the delayed photon propagation necessary for detection.

[‡]The time between two DOM hits cannot be less than the time that light may have taken.

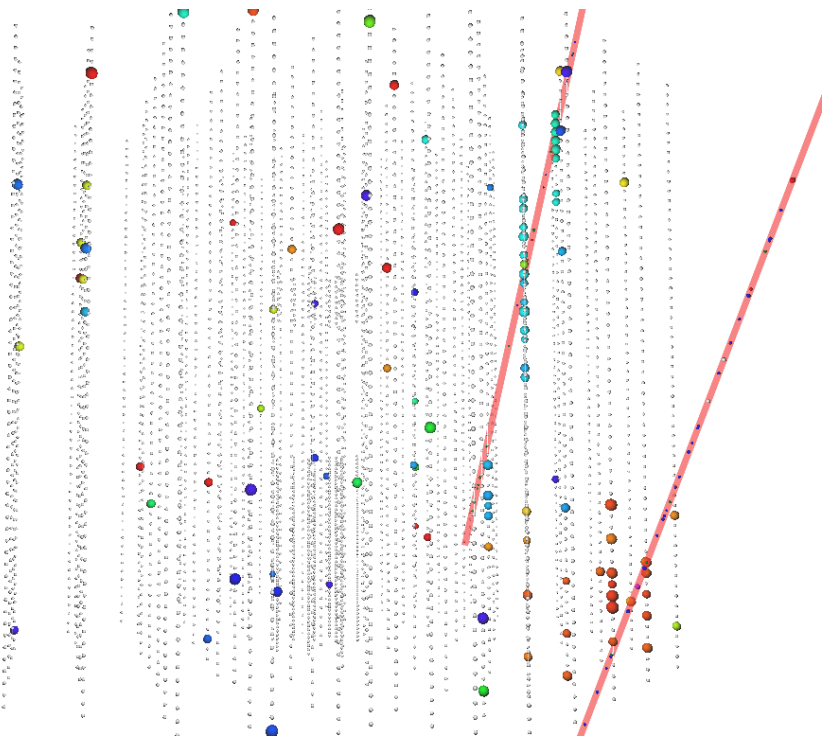


Figure 7.5: Event display of a simulated coincident event of two downgoing muons. The colors of the event range from red (early) to blue (late). The first muon hits the bottom of the detector, while the second traverses mainly the upper part. These events are often reconstructed as a single up-going event and therefore result in a large background contribution. The scattered isolated hits are due to noise effects and mostly removed by pulse cleaning.

The second module, and also used in this analysis, is called `IceHive`. A full description can be found in the doctoral thesis of M. Zoll [201]. The module consists of two main parts: one that splits events and handles coincident events, `HiveSplitter`, and another that has a refined pulse cleaning, `HiveCleaning`.

7.3.1 `HiveSplitter`

The module assumes that individual particles will create *clusters* of hits in the detector. A cluster can grow within a certain time window, but is separated from another cluster if it's not spatially connected. An initial cluster is formed if the multiplicity of hits exceeds a certain threshold (usually 3 or 4). The main difference in this module versus `TopologicalSplitter` is that it uses hexagons to describe the detector instead of assuming a spherical parameterization. It makes more sense to optimize the search volume, where hits are clustered together, with a shape that describes the detector well and uses a discrete spacing between larger volumes instead of a uniformly growing sphere. The hexagonal shape is set by defining three heights. The first height is defined along the string of the hit DOM and is equal to the vertical distance along the string. The second height is the vertical height along the neighboring strings. The third height is the vertical height along the next-to-neighboring strings. An example is shown in Fig. 7.6.

When the active region is set, there is an additional check to see if DOMs can be “connected”. `IceHive` assumes certain emission profiles (for both cascades as tracks) where light is produced. Three possible connections are assumed:

1. Hits occur at the same time, but at a spatial distance in agreement with the Cherenkov emission profile (hits C&1 and 2&3 in Fig. 7.6).
2. Hits occur at a different time and a different location, but in agreement with the Cherenkov emission profile (hits C&2 in Fig. 7.6).
3. Hits on topologically identical sites of an emission pattern that has moved along with the propagation of the particle (hits C&3 and hits 1&2 on Fig. 7.6).

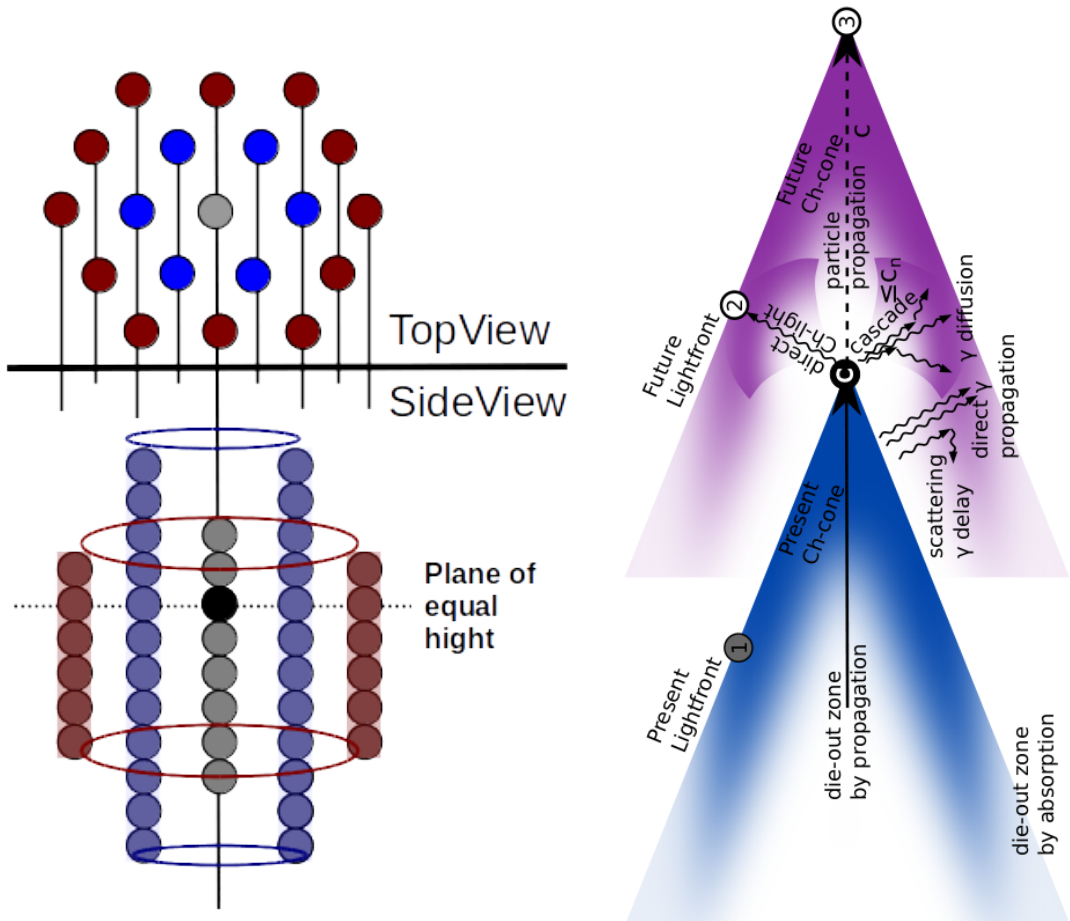


Figure 7.6: *Left:* The black circle illustrates a DOM that triggered a hit in the detector. The grey circles symbolize the DOMs along the string of the hit DOM. The number of DOMs that can be included in the active volume depends on the height defined by the module. The blue/purple DOMs belong to the neighboring strings and the red/brown DOMs to the next-to-neighboring strings. The heights of both these sets of DOMs are also set by the module. This example shows $h_2 > h_1 > h_3$, the heights are also asymmetric in this example. *Right:* Illustration of Cherenkov emission profile of a traversing particle. Both figures from Ref. [201].

These clusters are finally separated into different P-frames and thus regarded as distinct events.

7.3.2 HiveCleaning

Additionally, a similar cleaning as explained in Section 7.2 can be performed. Isolated hits that do not have neighboring hits occurring within a certain distance and time window, are removed. The main difference between this and `seededRT` cleaning is that the module again uses the hexagons as defined in the previous section.

7.3.3 Remark

The usage of `IceHive` has a great performance in separating coincident events, but often “overperforms” and splits clusters of hits that are originating from the same particle. This is predominantly the case for dim tracks that have large separations in between clusters (most of the triggered SMP events are of this type). It is because of this that the module `CoincSuite` was designed.

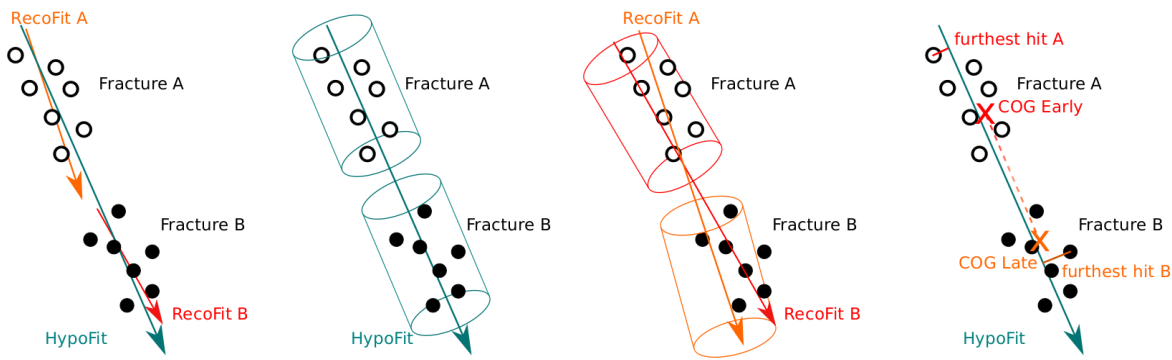


Figure 7.7: Schematic illustrations of possible recombination scenarios with the **CoincSuite** module. Two events are compared to each other or the combined event (HypoFit) in several different ways.

7.4 CoincSuite

Several testing algorithms allow to check if two or more split P-frames can originate from a single event. Five different scenarios were tested in this analysis, the first four are also chronologically shown in Fig. 7.7:

1. Cluster alignment: the reconstructed direction of the individual clusters is compared to the direction of a reconstruction that uses the combined hits (HypoFit). The directions should be within a certain criticle angle.
2. Cylinder cluster containment: the DOMs of the individual clusters should be able to be grouped together in a cylinder that has its center and direction along the HypoFit.
3. Cylinder cluster alignment: a cylinder around the reconstruction of each cluster is draw. The cylinders should overlap within a certain fraction.
4. COG* connection: the second quarter of the COG of the first cluster and the third quarter of the COG of the second cluster are computed. These COG should lie close enough and have to be in the vicinity of the HypoFit.
5. Velocity test: tests if the velocity of the HypoFit is close to the speed of light.

The combination of **IceHive**, which does a very good job in cleaning events, but often overperfromes and splits events that shouldn't be, and **CoincSuite**, which recombines events that were wrongfully split, leads to a very powerful tool to clean events.

7.5 Analysis techniques

Komt hier iets dat je gebruikt in het volgende hoofdstuk maar nog niet hebt uitgelegd?

7.6 Boosted Decision Tree classifiers

Given a certain event with a fixed set of variables that are constructed in an analysis, the question remains if the event is in fact a *signal* or *background* event. One can rely on Monte Carlo simulations to get a handle on the variable distribution in both sets. The most general and still widely used method is to use a cut-and-count approach where a cut is placed on a certain variable that discards events that fail the requirement. A Boosted Decision Tree (BDT) inspects a set of set variables and classifies an event with a score that ranges from -1 to 1. The higher the score, the more an event is regarded as signal-like. How this is done is given in more detail below. Boosted decision trees rely on multiple individual trees. Therefore, we will first explain how a single tree classification works.

*Similar to COM (Center Of Mass), the COG is a weighted average position of the hit DOMs. DOMs that register more light get a heigher weight.

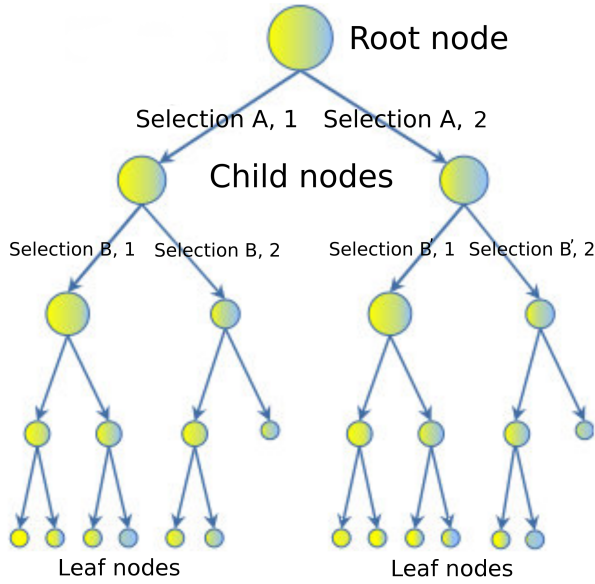


Figure 7.8: Illustration of decision tree scheme. Selection B and B' denote a selection on the same variable, but other requirement.

7.6.1 Structure

The goal of a decision tree is to determine if an event is signal- or background like. It uses a tree-like structure where certain selection criteria are used at different nodes as illustrated in Fig. 7.8.

A decision tree is a binary tree that places an event into a certain node depending on the selection at a node. The depth of a decision tree can be arbitrarily long, but is determined by a set of criteria defined in Section 7.6.2. An event consists of a certain set of variables $X = x_1, x_2, \dots, x_n$ that are used in the classification. Before any selection criteria, the event is said to be represented by the *root node*. A binary selection then determines to which *child node* the event should be classified, for example:

$$\begin{aligned} \text{Selection A} &= x_1 > y_1 \quad (\text{option 1}) \\ &= x_1 \leq y_1 \quad (\text{option 2}), \end{aligned} \tag{7.20}$$

where y_1 is the cut value for variable x_1 . Similarly, the other selections determine where the event is eventually placed. The last nodes are referred to as *leaf nodes* and hold the probabilities of whether an event is more signal- or background-like. These probabilities are translated into a score ranging between -1 (background) and 1 (signal).

7.6.2 Training

To construct a decision tree, one first has to “train” the algorithm. Given a certain “signal set” and “background set”, all variables used in the BDT are histogrammed and at each bin for each variable the “best cut” is set at the first node selection. To determine the optimal cut, we first define the purity of a node, p , by

$$p = \frac{\sum_s w_s}{\sum_s w_s + \sum_b w_b}, \tag{7.21}$$

where w_s and w_b refer to the weights of the signal and background events and the Gini index, g ,

$$g(p) = p(1 - p), \tag{7.22}$$

is used as a separation variable in this work*. Using the Gini index, the separation gain determines the effectiveness of the cut

$$\Delta S = g_p \cdot \sum w_p - \left(g_l \cdot \sum w_l + g_r \cdot \sum w_r \right), \quad (7.23)$$

where g_p and w_p denote the Gini index and weights of the parent nodes and similarly for the left and right child nodes. The cut that gives the highest separation gain is subsequently selected. The algorithm stops when one of the following criteria is met:

- a node only consists of signal or background events;
- a certain predefined maximal depth is reached;
- splitting would cause a child node to have less than a predefined minimal amount of events left;

and therefore determines the size of a tree. These selection criteria are necessary to avoid overtraining (see Section 7.6.4).

7.6.3 Boosting

As already implied in the text above, a BDT consists of a *forest* of decision trees. A user specified number of individual decision trees are trained sequentially, with a boosting process in between each training. Boosting consists of adjusting the weights of individual events according to whether the previously trained tree classifies them correctly. In this work, the AdaBoost[†] algorithm was used for boosting in which the score of an event is a weighted average of the scores the event receives from each tree in the forest [202].

A BDT may informally be called a “boosted decision tree”, but it must be understood that there are actually many trees (typically hundreds), and that boosting is a process that occurs between the training of consecutive trees. The approach makes use of the power of numbers: many weak single decision trees combined can be more powerful than one very good decision tree. In general, boosting follows the following steps:

1. Train a weak model on training data.
2. Compute the error of the model on each training example.
3. Give higher importance to examples on which the model made mistakes.
4. Re-train the model using “importance weighted” training examples.
5. Go back to step 2.

An example is given in Appendix E.

If $I(s, y)$ is a function equal to 0 when, after tree classification, the sample test score, s , is equal to its true identity, y , then the error rate for a tree is equal to

$$\epsilon = \frac{\sum_i w_i I(s, y)}{\sum_i w_i}. \quad (7.24)$$

The boosting factor for the tree is defined as

$$\alpha = \beta \cdot \ln \left(\frac{1 - \epsilon}{\epsilon} \right), \quad (7.25)$$

with β a user defined *boosting beta* and changes the weight of the tree to

$$\begin{aligned} w' &= w \cdot \exp(\alpha), & w' &= w \cdot \exp(-\alpha) \\ (\text{correct classification}) & & (\text{incorrect classification}), \end{aligned} \quad (7.26)$$

*Other possible separation variables include the cross entropy $-p \cdot \ln(p) - (1-p) \cdot \ln(1-p)$ or the misclassification error $1 - \max(p, 1-p)$

[†]Short for Adaptive Boosting.

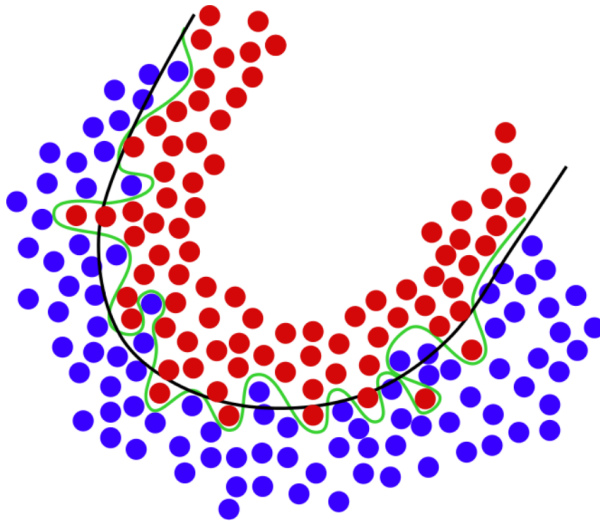


Figure 7.9: Example of overtraining. In black, the theoretical line between background (blue points) and signal (red points) is given. An overtrained BDT will have a (perfect) selection such as the green line. Illustration from [203].

after which the weights are renormalized so that $\sum w' = 1$. The process is repeated until the number of predefined trees is reached.

Due to its definition, the boost factor α will give good classifiers (which have low error rates) large boost factors. Events that are misclassified are then given larger weights, making the algorithm more likely to classify them correctly in the subsequent tree classifier.

Once the entire BDT is trained, the events can be given a score based on the multiple tree classifiers. This is done by taking the weighted average of all the scores in the individual tree classifiers, using its boost factor α as the weight of the tree. The score of an event i is then given by

$$s_i = \frac{\sum_m \alpha_m \cdot s_{i,m}}{\sum \alpha_m}, \quad (7.27)$$

where we loop over the individual trees denoted with index m .

7.6.4 Overtraining

BDTs are very powerful tools, but if not used correctly could lead to problems that are not easy to spot at first sight. Assume we train our BDT with a certain signal set and background set. If the BDT is trained up to the point of classifying statistical fluctuations, there is said to be *training sample overtraining*. An illustrative example is given in Fig. G.1. Another example is data/MC overtraining. The former can be dealt with with the use of *pruning*, while the latter should show clear data/MC agreement.

7.6.4.1 Pruning

The problem with overtraining is essentially that there are certain splits in a classifier tree that are too specific and less important. In the method of *cost complexity pruning*, for each node the complexity is calculated as

$$\rho = \frac{\Delta S}{n_{\text{leaves}} - 1}, \quad (7.28)$$

with ΔS the separation gain as defined in Eq. 7.23. The subtree of the node with the smallest value of ρ is removed and this is done repeatedly until a desired *pruning strength** is reached.

*A parameter on a scale from 0 to 100, which specifies the percentage of the pruning sequence to actually execute. 0 means no pruning is done and 100 signifies only a single root node remaining.

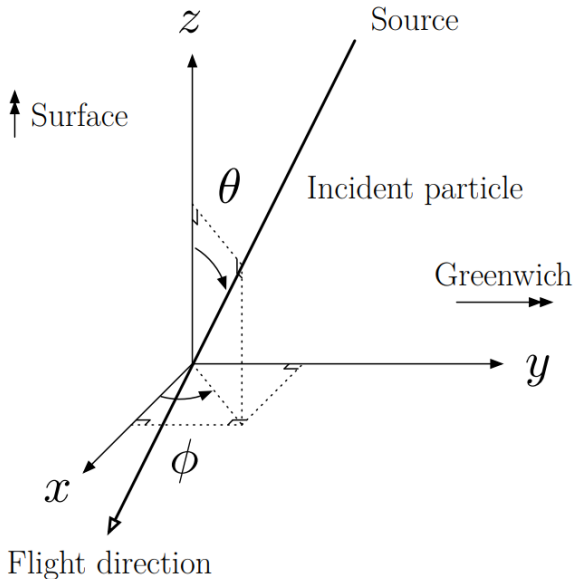


Figure 7.10: The IceCube Coordinate system.

BDTs are always trained and tested with different subsets of the same type (background or signal) of event. If the training set has significantly different scores than the testing set, the sample is most probably overtrained and one has to change the BDT input parameters. Typically, one uses Kolmogorov-Smirnov testing to indicate if the BDT score distributions from the training and testing sets could follow the same distribution pattern. As a rule of thumb, a $p_{KS} \lesssim 0.01$ indicates overtraining beyond the level of comfort.

7.6.4.2 Data-MC agreement

Nodig?

7.7 Minimal-Redundancy-Maximum-Relevance

Having multiple variables that are able to discriminate signal from background events is a necessary tool to ensure to conclude statements about a certain theory or exotic phenomenon. Single variables can show promising results, but when multiple variables are highly correlated much of the discriminative power diminishes. When using BDTs, analyzers often try to include variables and remove them if they show to be highly correlated in a trial-and-error fashion.

In this analysis, I made use of a technique that was originally developed for data in biological sciences but can be used for most analyses that involve “data mining”. Variables from a large sample set were selected with the condition of minimal-Redundancy-Maximal-Relevance (mRMR). To optimize the characterization of a certain class of events with a set of variables, these variables are selected with a *maximal relevance*. “Relevance” is characterized in terms of correlation of mutual information. Because combinations of individually good features do not necessarily lead to good classification performance, there is the additional requirement of *minimal redundancy* [204].

In this analysis, mRMR was used to rank variables from a large set according to their importance and proved to lead to low correlated variables (see Fig. ???).

7.8 IceCube coordinate system

Lastly, when referring to positions and directions one first has define a coordinate system to be able to uniquely define these variables. The system is shown in Fig. 7.10.

The center of the coordinate system is set close to the geometric center of the detector, at about 2000 m below the surface of the ice. The y-axis of the coordinate system is aligned with the Prime Meridian pointing toward Greenwich (United Kingdom). The x-axis is set perpendicular to the y-axis pointing in a, 90° clockwise direction. The z-axis is set perpendicular to the xy-plane, pointing upwards, normal to the Earth's surface.

A particle's direction is defined with zenith and azimuth angles, θ and ϕ respectively. The zenith angle is measured relative to the positive z-axis and the azimuth angle is measured counterclockwise from the positive xy-plane.



8. The SPACE Analysis

After introducing the detector workings, reconstruction and analysis techniques, background contributions and the signature of the signal, this chapter gives an overview of analysis. Starting from data processed with basic reconstructions and requirements a workflow was set up to try to discriminate events that are most likely of known physical interactions from the rare events that are sought for in this analysis. These events would originate from the theoretical particles with an anomalous charge (see Chapter 2). The analysis was adopted the "SPACE" analysis, which stands for a "Search for Particle with Anomalous ChargE".

8.1 Filter selection

As explained in Section 5.5.2, the data is processed through multiple filters. Since this analysis is the first of its kind in the collaboration, no processed dataset from other analyses was used. Filters had to be selected for proper comparison of data and Monte Carlo and I have chosen to optimize the signal to background ratio to select which filters should be included. An illustration is given in Fig. 8.1. This filter selection will be referred to as *Level2b*, as a simple addition to filter processing in Level2 (see Section 6.4).

8.1.1 VEF

The Vertical Event Filter (VEF) is designed to be used for oscillation and Earth WIMP analyses and makes use of the string trigger (see Section 5.5.1). An SMT that travel alongside a string, or closeby, can trigger optical modules while the total light yield of an event is low, making this filter an ideal addition to the filters that are selected. In addition, the filter removes HLC hits in the top 5 DOM layers to reduce the muonic component from air shower events. Other selection cuts, try to optimize the search efficiency for WIMP events in particular. For example, the LF zenith angle should be higher than 68.7° . More information can be found in Ref. [205].

8.1.2 LowUp

The LowUp filter is again mainly designed for WIMP searches, but also atmospheric neutrino analysis and is mainly designed to capture up-going muons with an energy below 1 TeV. The majority of the events that are selected by this filter make use of the in-ice Volume Trigger (see Table 5.1), but also the in-ice SMT8, in-ice String and SMT3-DeepCore triggers are run over for completeness. The selection cuts are loose selections required to look for up-going track-like particles. For example, the zenith angle of the reconstructed particle should have an angle of 80°

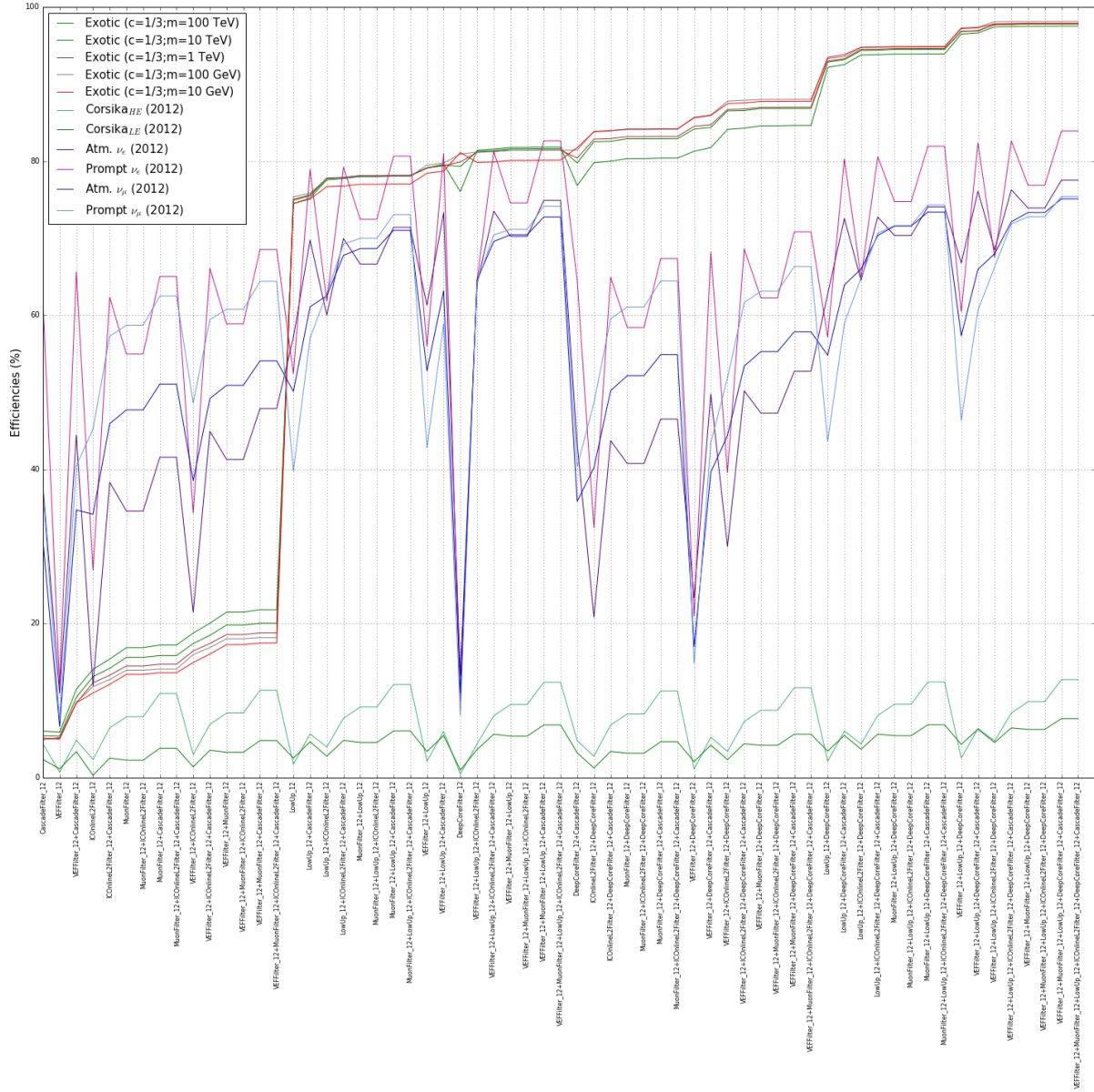


Figure 8.1: Illustration of the efficiencies of several filters and their possible combinations. The x-axis was determined by starting with filter selections that had a low efficiency in signal selection and range in function of performance. Five signal points for a fixed charge and different mass show similar results. Exotic SMPs with charges 1/2 and 2/3 show very similar results but are left out for a better visualization.

or higher and the difference between the maximal z-coordinate and minimal z-coordinate of hit DOMs should be less than or equal to 600 m. More information can be found in Ref. [206].

8.1.3 Online Muon L2

The Online Muon L2 filter is a subset of the Muon Filter (see Ref. ??) and tries to select the most interesting muon-like events while reducing the rate of the filter from around 30 Hz to 5 Hz, reducing the data with a factor of 6. Historically this subset was processed data from the Muon Filter, but after realizing that this could be done online and because many analyses made use of this selection, it was chosen to implement it as a separate filter. The filter tries to select both up-going and down-going muons, with different selection cuts depending on the zenith angle of the particle reconstruction. The four selection ranges are defined as:

- $180^\circ \geq \theta_{\text{MPE}} \geq 115^\circ$
- $115^\circ > \theta_{\text{MPE}} \geq 82^\circ$
- $82^\circ > \theta_{\text{MPE}} \geq 66^\circ$
- $66^\circ > \theta_{\text{MPE}} \geq 0^\circ$

where the particle reconstruction was done with MPE (Section 7.1.3), which was feasible if it only had to be done on the events passing the Muon Filter. The first two regions have an efficiency* higher than 99%. The down-going region require more stringent cuts to remove the less interesting muons from air showers. The variables used are the number of hit DOMs, likelihood parameters, number of PEs and so on. More information can be found in Ref. [207].

Verhoogt uw signaal niet zo veel omdat je enkel upgoing signaal gebruikte om dit te testen.

8.1.4 DeepCore

Additionally a DeepCore specialized filter was added to account for SMP tracks that partially traverse the more densely instrumented DC detector. Due to the low amount of light produced by these dim tracks, adding the DeepCore filter that is specialized for this part of the detector proved to be of significant importance.

The DeepCore filter was designed to look for very dim events coming from, e.g., dark matter, low-energy neutrino oscillations, and studies in observing atmospheric neutrinos below 100 GeV. The fiducial volume used for this filter consists of

- the bottom 22 DOMs on the IceCube strings 25, 26, 27, 34, 35, 36, 37, 44, 45, 46, 47 and 54;
- the bottom 50 DOMs on the DeepCore strings 79-86.

These strings are indicated in Fig. 8.2.

The filter uses the DeepCore SMT3 trigger and calculates the COG position. Two layers are used as a veto to remove events that probably originate from atmospheric muons. More information can be found in Ref. [208].

8.1.5 Burnsample checks

Before further processing, the burn sample (Section 6.5) is compared over the different years that are used in the analysis. This is shown in Figure 8.3. More information on the burn sample can be found in Section 6.5.

8.2 Level 3

The combined filter selection leads to a total rate of ~ 60 Hz, or ~ 1.9 billion events per year. The average event size at Level2 is around 15 kB, which would result into around 30 TB of data per year.

Therefore, five quality cuts are implemented with a goal that is threefold:

*Here defined as having a reconstruction within 3° of the MC truth.

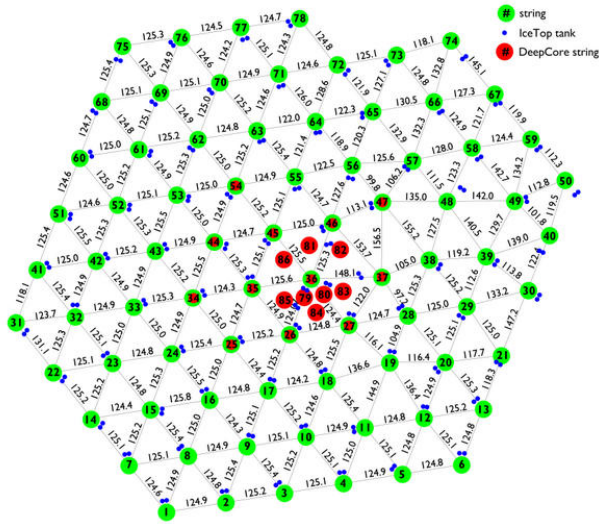


Figure 8.2: Aerial view of the IceCube strings (and IceTop tanks) where the DeepCore fiducial volume is defined by the DeepCore strings (red) and several surrounding in-ice IceCube strings (green and red).

1. reduce the total rate of the data,
2. improve the signal to background ratio, getting rid of uninteresting events,
3. improve the agreement between data and Monte Carlo.

These cuts are shown in Figs. 8.4, 8.5 and 8.6.

8.2.1 Zenith angle cut

Even though there are no up-going muons from air showers expected, the vast majority of events that pass the filter selection remain from misreconstructed muons. Even though there is only a small chance of these events to have a large misreconstructed zenith angle. The expected flux of air showers is so much larger compared to the assumed signal flux to such an extent that it dominates with orders of magnitude. The majority still has a reconstructed zenith angle lower than 90° . Therefore the zenith angle cut was set at an angle of

$$\theta_{\text{zen}}(\text{MPE}) \geq 85^\circ. \quad (8.1)$$

8.2.2 RlogL cut

The reduced log-likelihood, rlogL of the track reconstruction fit is used as a goodness-of-fit variable. The term “reduced” is used because the logarithm of the likelihood is normalized by the number of degrees of freedom (NDOF) in the track fit

$$\text{rlogL} = \frac{\log \mathcal{L}}{\text{NDOF}} = \frac{\log \mathcal{L}}{\text{NCh} - \text{NPara}}, \quad (8.2)$$

where NCh is the number of channels/DOMs and NPara the number of fitted parameters (3 for the position and 2 for the track). For Gaussian probability distributions this expression corresponds to the reduced chi-square. Lower values indicate better reconstructions, therefore the rlogL cut was set at a value of

$$\text{rlogL} < 15. \quad (8.3)$$

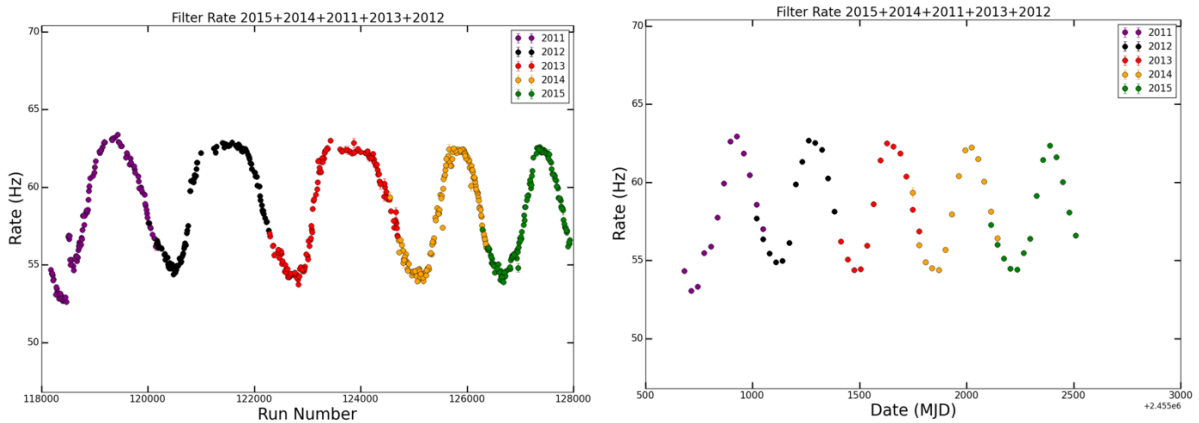


Figure 8.3: *Left:* Total rate of the combined filters in function of the run number. The sine wave pattern from seasonal variations in the atmosphere (see Section 6.1.1.1) is clearly visible and consistent throughout the years. The x-axis is more spread out in the first years as there were more test runs. The shift in data rate in early 2011 runs is due to the DOM software change that was introduced in the Summer of 2011 [209]. This phenomenon is well understood and since the changes are minimal it was chosen to keep these runs. *Right:* Total filter rate averaged per month. There is an overlap for each year because a new season doesn't necessarily start in the beginning of a month.

8.2.3 NPE cut

The number of photoelectrons seen in the detector has a clear correlation to the number of photons that were emitted from the track. From Eq. 4.8 it is clear that particles with a charge < 1 will produce less light. Therefore a cut on the total number of photoelectrons was set at a value of

$$\text{NPE} < 50. \quad (8.4)$$

8.2.4 Starting rlogL cut

The relative probability for tracks to be starting and/or stopping can be computed with FiniteReco (see Section 7.1.5). Because most low-energetic muons would be starting and/or stopping in the detector, these likelihoods prove to be a powerful tool in removing these events *. The llh is always compared to the llh of throughgoing tracks, hence the “relative probability”. It was chosen to place the starting rlogL at a value of

$$\text{rlogL} = \text{rlogL}(\text{starting}) - \text{rlogL}(\text{throughgoing}) > 0. \quad (8.5)$$

8.2.5 Stopping rlogL cut

Analogous to the previous cut, it was chosen to place the stopping rlogL at a value of

$$\text{rlogL} = \text{rlogL}(\text{stopping}) - \text{rlogL}(\text{throughgoing}) > 10. \quad (8.6)$$

8.3 Level 4

As can be seen in Figs. 8.4, 8.5 and 8.6, most of the background still originates from air showers (referred to as CORSIKA). Due to the Level 3 quality cuts, the total rate was reduced from around ~ 60 Hz to ~ 2 Hz, low enough for more elaborate variables to be computed and more elaborate cleaning. In Level 4 I have implemented the IceHive splitting and cleaning tools (see Section 7.3) and rerun the particle reconstructions on these “new” events. Additional quality

*High energetic muons will have a higher chance of being throughgoing, but would produce much more light than the dim tracks that are expected for the SMPs.

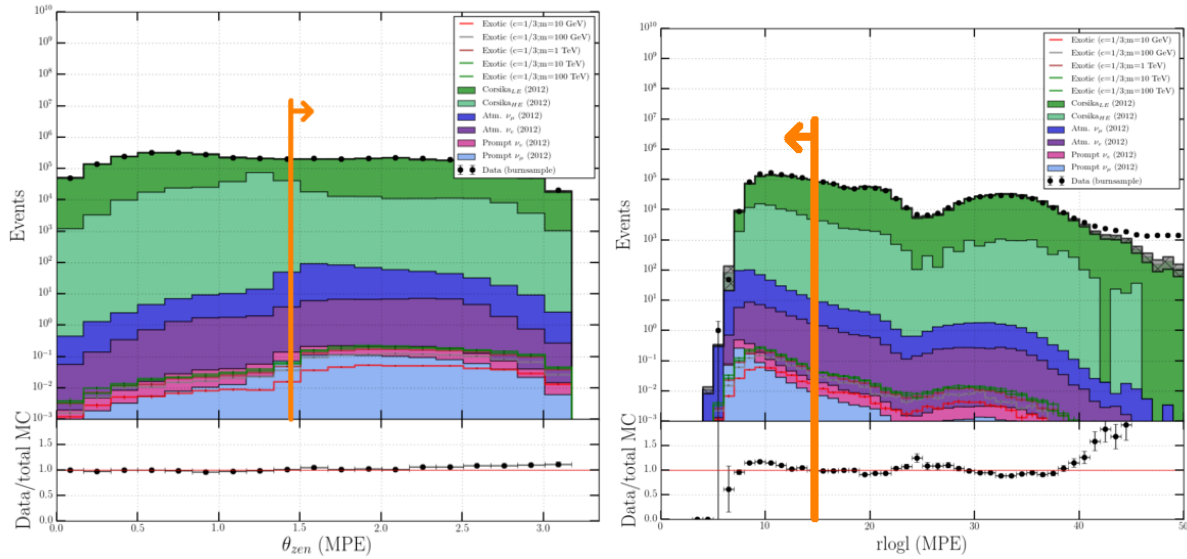


Figure 8.4: *Left:* Number of events in function of MPE reconstructed zenith angle normalized to the burn sample. The upwards trend to higher zenith angles is due to the filter selections that depend on the angle. *Right:* Number of events in function of rlogL normalized to the burn sample. The cuts are illustrated with an orange line, the arrow points towards the events that are kept.

Table 8.1: Overview of quality cuts in Level 4.

Variable	Definition	Cut	Motivation
nCh	Number of hit DOMs	≥ 5	Allows for better reconstructions
nStr	Number of hit strings	≥ 2	Allows for better reconstructions
nStr_in	The number of hit inner strings. An inner string is not located at the edge of the detector	≥ 1	Reduce leak-in events
Fitstatus MPE	Status of MPE reconstruction	Status == 'OK'	Remove bad reconstructions
θ_{HC} (MPE)	Zenith angle cut on HiveCleaned pulses	$\geq 85^\circ$	Similar to cut explained in ???: focus on up-going tracks
Innerstring domination	See text inline	== True	See text inline

cuts were added to this level to ensure higher quality events. An overview is given in Table 8.1. Finally, new variables were constructed to use in Level 5.

8.3.1 Cleaning and quality cuts

IceHive provides for a thorough cleaning method, sometimes resulting into events with a very low amount of hit DOMs. However, a minimal amount of hits is required to have reasonable and trustworthy particle reconstructions. Similarly, more than one string should have a hit to allow for better reconstructions due to the sparse distribution of the strings in the detector. Because light is able to reach the edge of the detector, even if the closest approach of the particle is tens or hundreds of meters away for very bright events, it would be near impossible to distinguish bright events far from the detector to dim tracks passing close by. Therefore, it was required that at least one string not on the edge of the detector should have hit DOMs to reduce these *leak-in events*. The zenith angle cut is re-introduced on the new event that should have better reconstructions due to cleaning and finally there is a requirement for “innerstring domination”.

Innerstring domination

There persist classes of events at the boundary of the detector, which can be a problem for an upgoing track analysis. This includes event classes as:

- (*Leak in*) Events which are heading towards the instrumented volume, but stop right before they reach it or pass next to, but not too far from, the detector. These leak light to the detector boundaries.
- (*Boundary*) Events that penetrate the detector very shallow on the boundary lines and

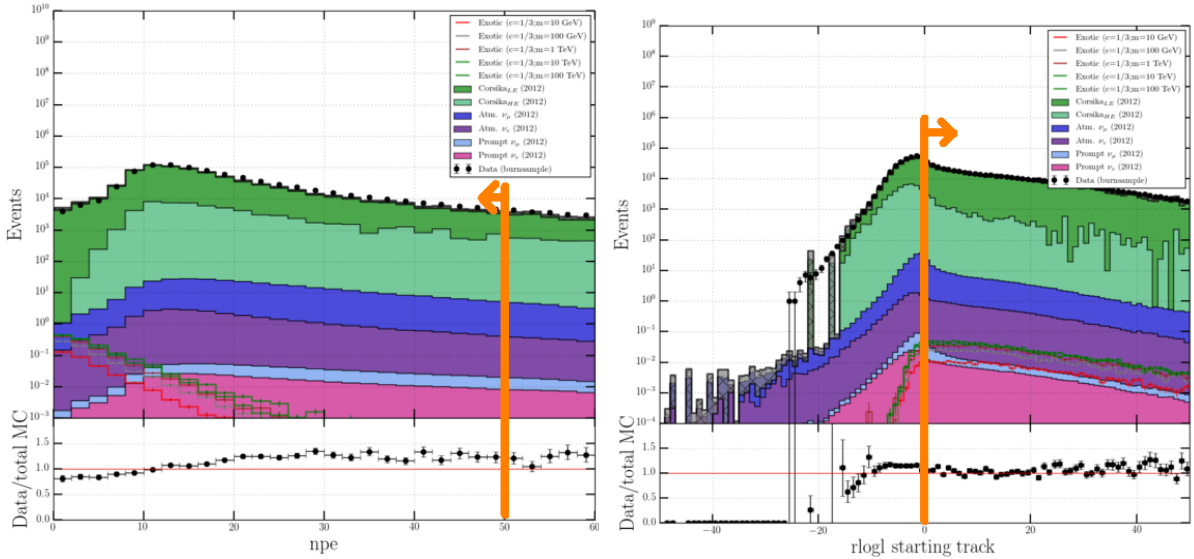


Figure 8.5: *Left:* Number of events in function of number of photoelectrons (NPE) seen in the detector. *Right:* Number of events in function of the starting likelihood. The cuts are illustrated with an orange line, the arrow points towards the events that are kept.

possibly have a cascade at the endpoint. The events have rather cascade like characteristics.

- (Corner-clippers) Events that are throughgoing on the corners of the detector that have a COG at a corner of the detector.
- (Leak out) Events originating from a neutrino passing through almost the entire length of the detector and only have an interaction vertex right before leaving the detector. Depending on position and angle, the reverse direction of reconstruction can be of similar probability and thus a nuisance.

All these event classes are not well reconstructable or have a high uncertainty in the reconstruction. It is more feasible to remove these class of events to maintain a sample of well reconstructable events. This is done here by the requirement of innerstring domination.

DOMs are defined as outer DOMs if they are one of the following:

- part of a string on edge of the detector,
- on the bottom of strings 1-78,
- on the top of strings 1-78.

The innerstring domination is set to `True` when

$$\frac{\#\text{outer DOMs}}{\#\text{inner DOMs}} < 0.5. \quad (8.7)$$

8.3.2 Variable construction

To distinguish signal from background events, variables that show a clear distribution difference prove to have the most discriminative power. In this part of the analysis, multiple new variables are introduced with this goal. Some variables used in Level 5 are already explained in the text and need no further introduction, they are shown in Fig. 8.17. A summary is given in Table ??.

8.3.2.1 Commonvariables

Variables that were often used in analyses often had subtle differences between them, making them prone to be a cause of errors. Multiple variable were therefore combined into one project, called “Commonvariables”. The variables used here can be subdivided into three categories: track characteristics, hit statistics and time characteristics and are summarized in Table 8.2. Their distributions are shown in Figs. 8.7, 8.8, 8.9 and 8.10.

Because DC and IC DOMs have different quantum efficiencies (see Section 5.1.2), the pulses

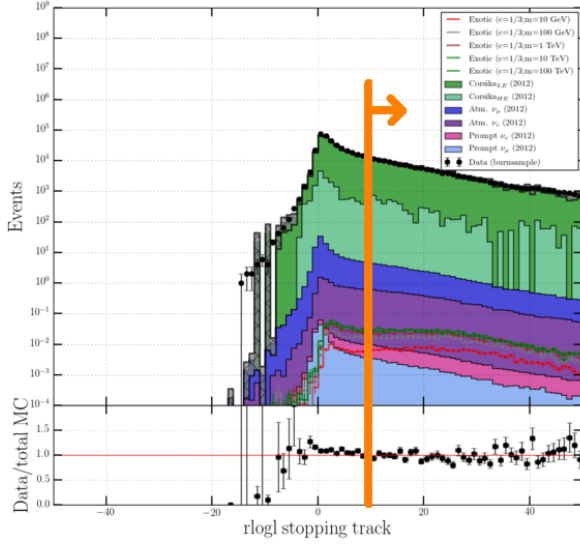


Figure 8.6: Number of events in function of the stopping likelihood. The cut is illustrated with an orange line, the arrow points towards the events that are kept.

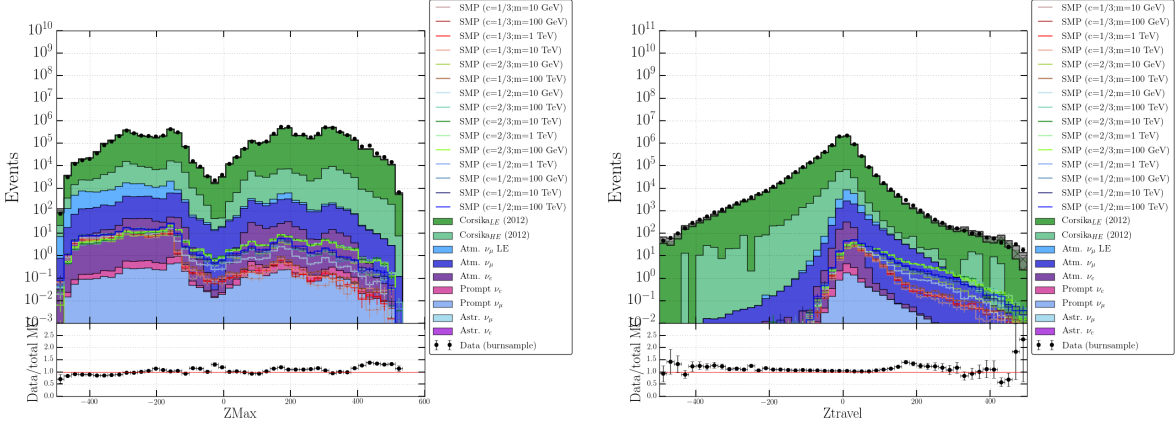


Figure 8.7: *Left:* Distribution of ZMax. The dip slightly below the origin is due to the dust layer. *Right:* Distribution of ZTravel. Negative values indicate down-going tracks, explaining the differences in signal and muons from air showers.

from DC and IC DOMs should not be mixed for an unambiguous definition. Therefore either only DC or IC pulses are used to compute these variables depending on if an event is *IC dominated* or *DC dominated*, where the former is set at $\frac{\#\text{DOMs}_{\text{IC}}}{\#\text{DOMs}_{\text{DC}}} \geq 0.5$ and the latter otherwise.

8.3.2.2 Millipede variables

The **Millipede** toolkit was introduced in Section ??, where it was explained how the energy deposition could be estimated from the light seen by the individual DOMs. Constructing multiple variables from this toolkit was the master thesis subject of Stef Verpoest and can be found in Ref. [210] for an elaborate explanation. The variables used in this analysis are explained below. Fig. 8.11 shows how the fit performed and can be helpful to explain the variables.

Mean loss

The most straightforward usage of the estimated mean energy loss rate is by taking the mean value and is referred to as *Mean_dEdX*. As can be seen from Fig. ??, the distribution of SMPs peaks at lower values than known backgrounds as expected. Energy losses that are reconstructed to come from outside the detector are removed (hence the *_contained* in the figure).

Due to the squared charge dependencies, an SMP of charge 1/3 is expected to have a relative

Table 8.2: List of Commonvariables used in this analysis.

Category	Variable	Description
Track Characteristics [†]	AvgDistToDom	The average distance of the DOMs to the reconstructed track, weighted by the total charge of each DOM.
	EmptyHits	The maximal track length along the reconstructed track that got no hits within a cylinder around the track.
	TrackSeparation	Distance how far the COG positions of the first and the last quartile of the hits are separated from each other.
	TrackDistribution	The track hits distribution smoothness value [-1;1] shows how smooth the hits of the given pulse series within the specified track cylinder radius are distributed along the track.
Hit Statistics	ZTravel	ZTravel is the average difference of the z value of all hit DOMs with the first (in time) quartile z value.
	ZMax	The maximum z of all hit DOMs.
Time Characteristics	ZPattern	All first pulses per DOM are ordered in time. If a DOM position of a pulse is higher than the previous ZPattern is increased with +1. If the second pulse is located lower in the detector ZPattern decreases with -1. In general this variable gives a tendency of the direction of a track.

[†] Whenever one of the track characteristics variables is shown/mentioned, the suffix (e.g. _50) refers to the track cylinder that was used around the track.

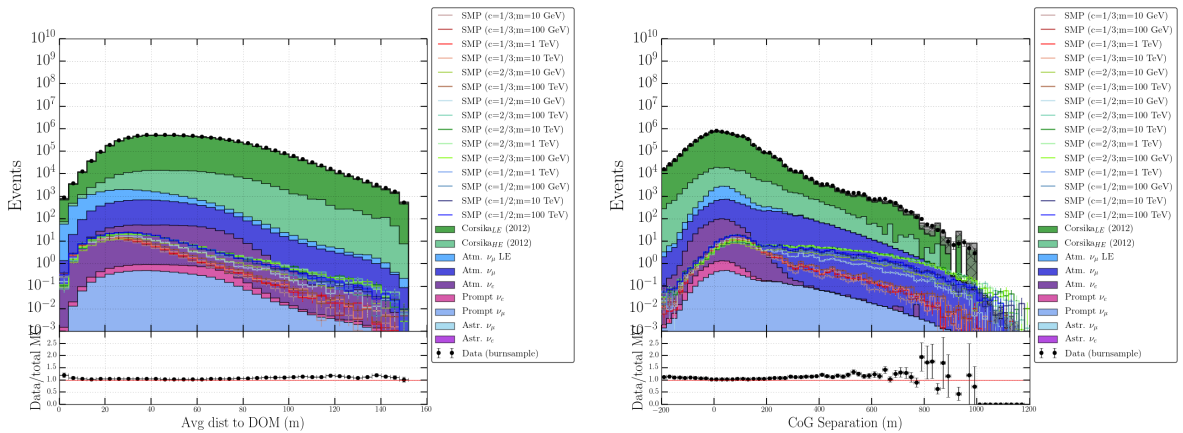


Figure 8.8: *Left:* Distribution of the average distance of a hit DOM to the seed track. Signal events produce less light, making it less probable for DOMs far away from the track to record light pulses. *Right:* Distribution of the TrackSeparation, or CoG separation, signal events show longer tails in the distribution compared to muons from air showers as expected. A cylinder radius of 150 m was used.

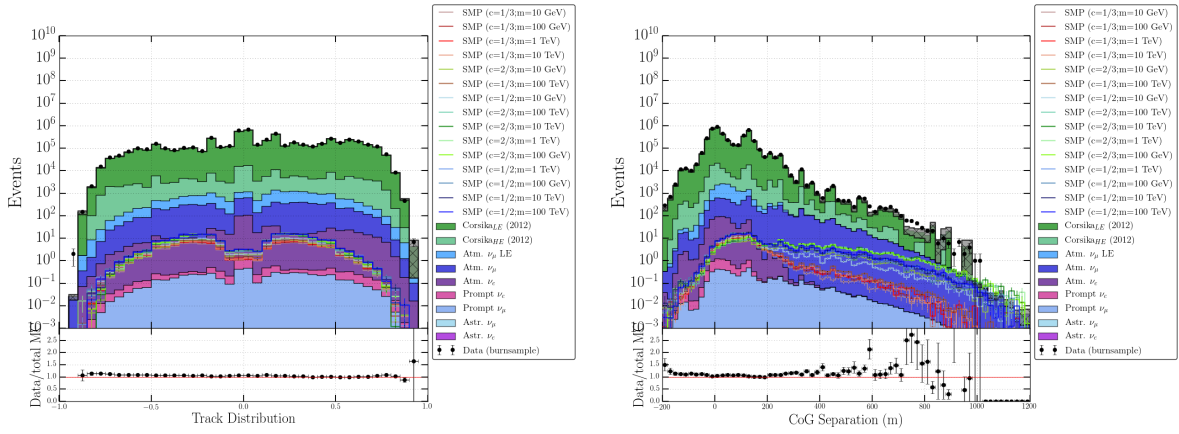


Figure 8.9: *Left:* Distribution of the smoothness of the track. *Right:* Distribution of the TrackSeparation, or CoG separation, with a cylinder radius of 50 m.

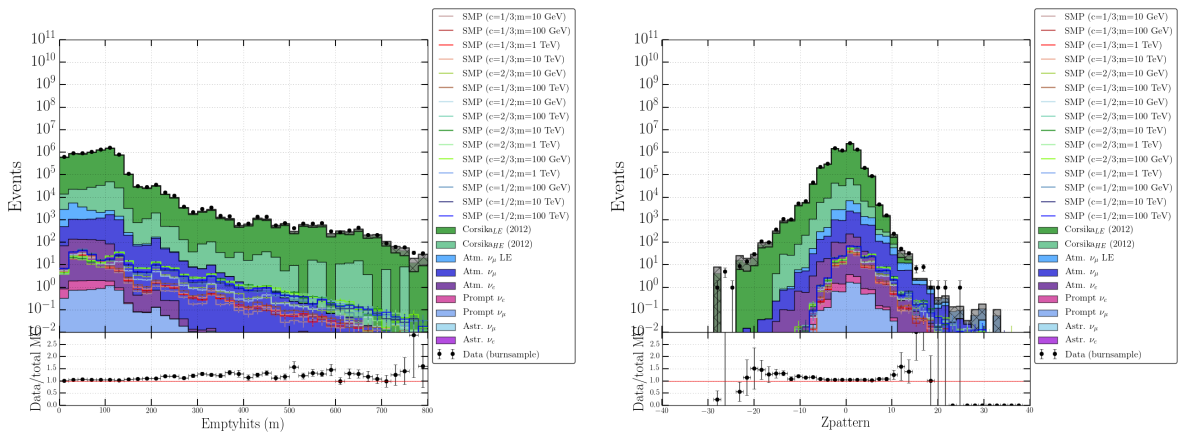


Figure 8.10: *Left:* Distribution of the length of empty hits along a track. Dim signal events show longer tails in the distribution than the backgrounds. *Right:* Distribution of the ZPattern of a track. Negative values indicate down-going tracks, explaining the different behaviour in signal and background.

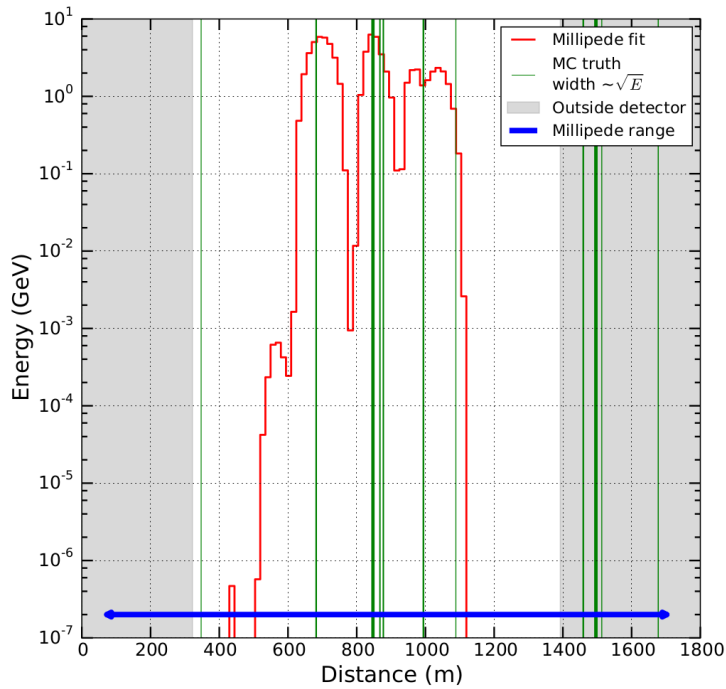


Figure 8.11: Output of a **Millipede** fit for an SMP with charge $\frac{1}{3}$ and mass 10 GeV. The x-axis shows the distance the particle traveled and starts after the first simulated energy loss event. The fit tries to estimate the energy of 15 m track segments. As a comparison, the true positions of energy deposits from the MC simulation are shown in green. Locations outside the detector are shaded in grey.

energy loss difference to muons with a factor of 9, which is the case when comparing to muons from neutrino interactions. Atmospheric muons in this level are almost entirely the result of misreconstructions, corner clippers, etc. making a comparison not valid.

Uniformity

Once the mean is computed, it is possible to count the amount of times the energy distribution curve (red curve in Fig. 8.11) to cross the mean value. This variable therefore parametrizes the uniformity of the track. The reasoning behind discriminating signal events from background is that most SMPs will have less uniform triggered hits due to the low amount of light that is produced. Particles therefore need to travel closer to a DOM to trigger a hit. In Fig. 8.12 we can see that the background distributions peak at lower values than the signal, which also has a slower dropoff.

Track length

Because of the lower energy losses, the SMP particles are also expected to travel larger distances than muons, supporting the idea to construct a variable that is sensitive to the distance traveled in the detector: a track length.

Since the tracks at this level are very dim, many segments from the **Millipede** output are reconstructed with zero energy. Therefore, it was chosen to use a certain part of the segments. The variables used here, *TrackLength_60*, used 60% of the length where energy was deposited. It is the distance between the points where 20% and 80% of the deposited energy track segment. We expected to see larger tails in the distribution of Fig. 8.13 in the signal compared to the background. Sub-optimal reconstructions result in bad millipede fits, giving a low and almost constant energy loss along the track. Additionally, coincident events that are not well separated also contribute to these events in the tail. However, most of the background events result into low values for this variable, still making it a powerful discriminative tool.

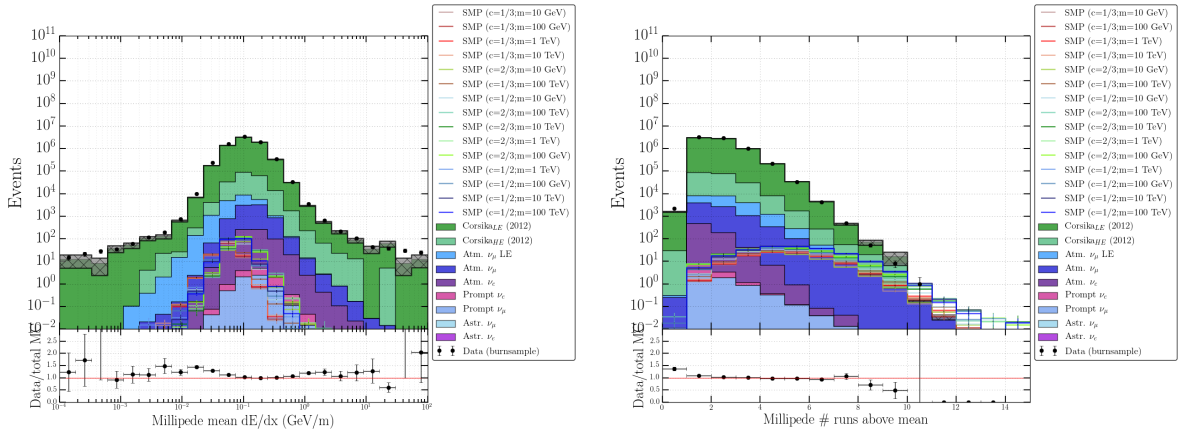


Figure 8.12: *Left:* Distributions for the estimated mean energy loss from the **Millipede** toolkit. *Right:* Distributions for the uniformity of the contained track.

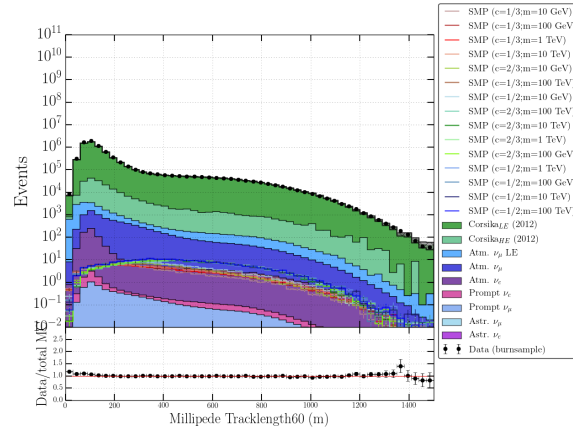


Figure 8.13: Distributions for the track length of the particle where the **Millipede** segments are used instead of the DOM pulses.

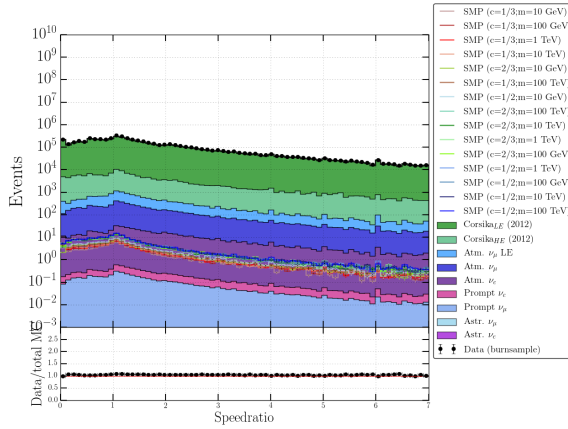


Figure 8.14: •

8.3.2.3 New variables

Speedratio

In addition, new variables were constructed. One was adopted from Jan Künnen's Earth WIMP analysis [211]. By looking at the "speed ratio" of the first to second and first to third HLC hits, it was used to remove wrongfully simulated detector noise, helping in data/MC disagreement. In this analysis, it showed to provide for a modest addition to discriminating variables*. The *Speedratio* is defined as

$$\frac{v_{12}}{v_{13}} = \frac{d(\text{HLC}_1, \text{HLC}_2) / \Delta t(\text{HLC}_1, \text{HLC}_2)}{d(\text{HLC}_1, \text{HLC}_3) / \Delta t(\text{HLC}_1, \text{HLC}_3)}, \quad (8.8)$$

where $d(\text{HLC}_i, \text{HLC}_j)$ is the distance between the DOMs that recorded the i th and j th HLC hits. $\Delta t(\text{HLC}_1, \text{HLC}_2)$ is the difference in time of the i th and j th HLC hits. This distribution is expected to peak at a value of 1, which is the expected result if one assumes that the photons originate from a particle traversing in a straight line and passes close to the DOMs. This is illustrated in Fig. 8.14.

NewLength

Because DC and IC pulses should not be mixed, essential information is lost regarding the length of a track. Many signal events are DC dominated (see Section 8.3.2.1), making those track length variables not optimal. This is especially the case for events that have hits in both IC and DC and are far away from each other, which is not expected from low-energetic muons. These should, on average, produce more light than SMPs and not travel very far unless they have significant energies that would result in much higher light outputs. I have constructed new variables that use the MPE track reconstruction as a seed. First, the event is required to have

- #DC pulses ≥ 4 ,
- #IC pulses ≥ 2 ,

since otherwise the contribution of noise infiltration is too high. Additionally, pulses that lie within a cylinder with the seed track as the center are selected. The radius can be chosen, but is of the order of 50-150 meters. This radius is shown with a suffix after the variable (e.g. `_100`), if the radius is infinite (all pulses are used), the suffix is "`_all`".

Then the first/last quartile in DC hits and the first/last half of the IC hits are determined. From these one can easily calculate the COG. To determine a length from four COGs, two have to be selected. The selection is based on the timing information on these COGs and given in the Table 8.3.

*Data and MC seem to agree well, which is probably due to the newer and better simulations.

Table 8.3: •

Timing	COG ₁
$DC_{f,q} < IC_{f,h}$	$DC_{f,q}$
$DC_{f,q} \geq IC_{f,h}$	$IC_{f,h}$
	COG ₂
$DC_{l,q} > IC_{l,h}$	$DC_{l,q}$
$DC_{f,q} \leq IC_{f,h}$	$IC_{l,h}$

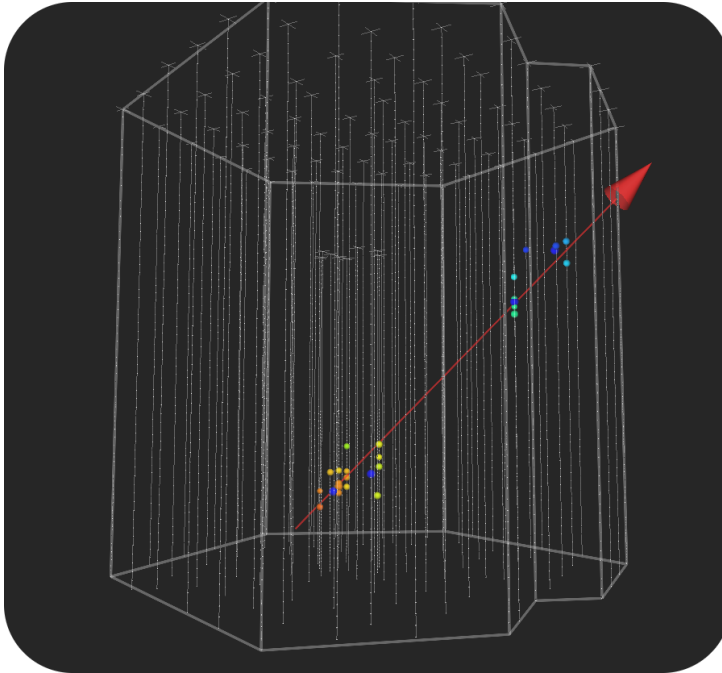


Figure 8.15: The NewLength variable is constructed by selecting the first quartile/half of the COGs of DC/IC and computing the distance from the last quartile/half of the COGs of DC/IC. Out of the four, the first and last in pulse time are chosen to compute the distance.

All in all one can say that the NewLength variable is another attempt in defining the track length of the track in the detector. The suffix “_z” is used for the variable that only uses the z-coordinate. Negative values occur when the timing of the two selected COGs is inverted when compared to the seed track (e.g. if the seed track is downgoing but the first CoG in time is located below the second COG) and most often occurs when the reconstruction was not optimal.

An illustration how the NewLength variable is constructed is shown in Fig. 8.15 and the distributions in Fig. 8.16.

8.3.3 Variable selection

The variables that are used in the BDT in Level 5 were selected by using the mRMR technique explained in Section 7.7. The 17 most important variables were used in the BDT. Less variables meant a lower performance while more variables did not show to add additional power in the BDT performance and meant more computational power. An overview of these variables is shown in Tab. 8.4.

8.4 Level 5

The last part of the analysis makes use of the variables that were constructed and the 17 that were estimated from the mRMR technique as the most powerful. First, the result from a single BDT is shown. Due to the lack of statistics in the final selection, the pullvalidation method was

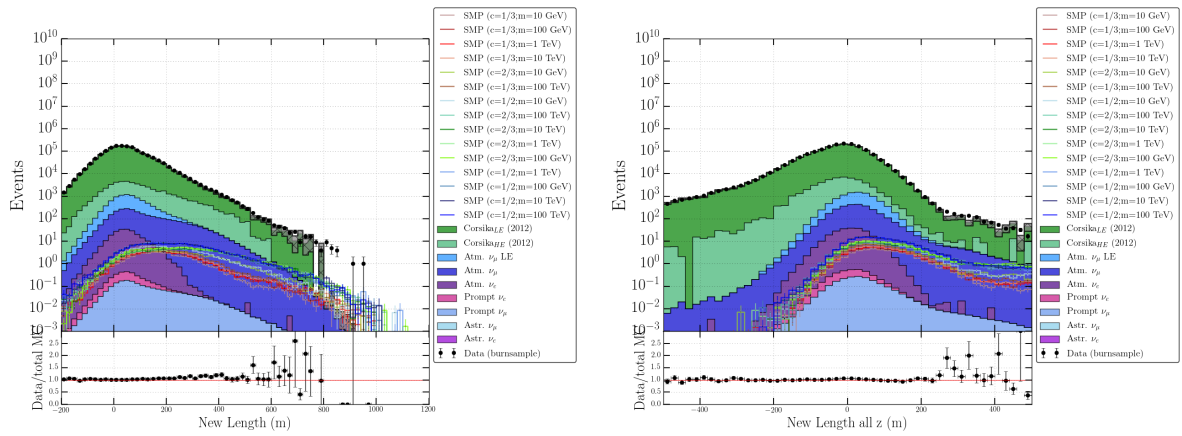


Figure 8.16: •

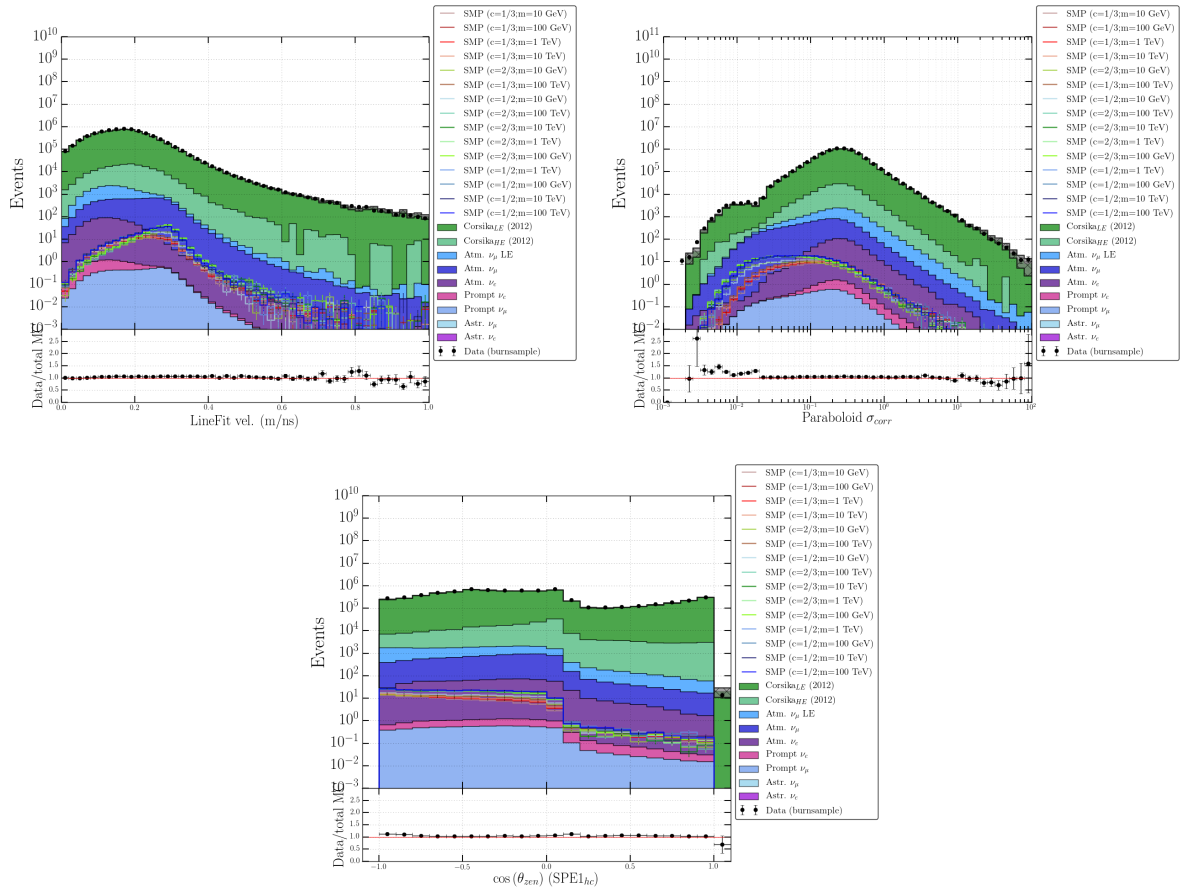


Figure 8.17: Blub

Table 8.4: My caption

Class	Variable	MRMR score	Importance	MRMR score	Variable
Commonvariables	ZMax	2	0.109	1	NewLength_150
	ZTravel	3	0.106	2	ZMax
	AvgDistToDom_150	9	0.048	3	ZTravel
	TrackSeparation_150	10	0.043	4	RunsAboveMean
	TrackDistribution_50	12	0.035	5	Mean_dEdX
	TrackSeparation_50	13	0.034	6	NewLength_all_z
	EmptyHits_100	16	0.027	7	LineFit_Velocity
	ZPattern	17	0.016	8	σ_{para}
Millipede	RunsAboveMean	4	0.105	9	AvgDistToDom_150
	Mean_dEdX	5	0.074	10	TrackSeparation_150
	TrackLength_60	11	0.039	11	TrackLength_60
New variables	NewLength_150	1	0.132	12	TrackDistribution_50
	NewLength_all_z	6	0.059	13	TrackSeparation_50
	SpeedRatio	14	0.033	14	SpeedRatio
Other variables	LineFit_Velocity	7	0.055	15	$\cos(\theta)_{\text{SPE}}$
	σ_{para}	8	0.051	16	EmptyHits_100
	$\cos(\theta)_{\text{SPE}}$	15	0.033	17	ZPattern

used for a limit computation.

8.4.1 BDT result

The parameters that were used for BDT training (see Section 7.6) are:

- Maximal depth: 2 (Fig. 7.8)
- Boosting β : 0.8 (Eq. 7.25)
- Number of trees: 400 (Section 7.6.3)
- Pruning factor: 35 (Section 7.6.4.1)

Training is done on 10% of the available burnsample as it showed to have a much better performance as opposed to training on background simulation due to the limited amount of CORSIKA simulation available. The other 90% of the burnsample is used for testing and is shown in the following plots. Testing on the MC datasets is also shown for the sake of completeness. Contribution of possible signal events, if they exist, in the data are minimal. Together with the very good data/MC agreement that is seen in the variables used, the training on data is a valid choice.

Also, it was chosen to select a (large) subsample of the signal to train the BDT to give the best possible results. One can see in the variable distributions in Figs. 8.10 and 8.16 that there are minimal contributions of events with negative ZTravel and/or negative NewLength values. Upgoing tracks should give positive values both and are therefore removed from the signal sample that is used to train the BDT*.

The result of one BDT can be seen in Fig. 8.18 and we can draw several conclusions:

- Data and MC show a very good agreement.
- The rate in background events is reduced with 4 to 5 orders of magnitude at the a BDT score around 0.25.
- At higher BDT scores, muons from low energetic muon neutrinos become a much more significant part of the total background than muons from air showers.
- The signal used to train the BDT is more concentrated at higher scores, as expected. The total signal sample and the subset used for training overlap at scores higher than 0.1.
- At the highest scores, where the signal dominates, it is clear that there is a lack of statistics in both CORSIKA simulations as the burn sample.

*Of course, the final signal rate is computed from the full signal sample.

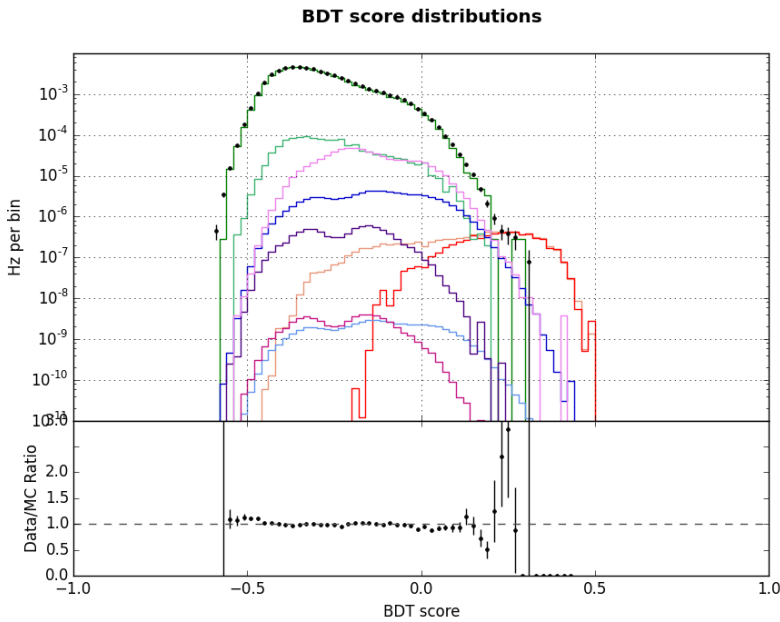


Figure 8.18: Blub

Additional checks can be found in Appendix G.

The limited amount of statistics in the tail of the CORSIKA datasets prove challenging. There is a need for an order of magnitude, at least, for more events, which is not feasible with the available resources. Other techniques, such as defining off-source or off-time regions [IeC {\textbullet}], are not available for this search as we have assumed an isotropic flux that is not time-dependent.

8.4.2 Pull-validation

Another way of dealing with limited statistics is by using re-sampling techniques. The method used here is called *Pull-Validation** (PV) and was used several times before in the IceCube collaboration [**Anna, Jan, atmospheric muons, ...**]. It is comparable to bootstrapping and cross-validation (see Appendix F), but uses much smaller training samples that lead to a larger variability that can be used as an estimator for the variability of the whole sample. As opposed to most bootstrapping and cross-validation methods, the resampling can be done without replacement[†] because the samples are much smaller.

As can be seen in Fig. 8.18, in the region of interest (at high BDT scores) there is a lack of statistics, mainly in data and atmospheric muon simulations. Because we want to compute an upper limit from this distribution, a cut on the BDT score at a value that is higher than for example 0.3 would not result in a trustworthy background estimation. We cannot know from the distribution how the tail evolves into higher BDT scores. Training the BDT on a slightly different training sample would result into a similar, but different BDT result. A subsequent cut implies a binary addition of an event to the final sensitivity: surviving the cut or not. By using slightly different training samples, one is able to give an estimate about the tail of the background distributions in function of the BDT score.

Let us assume we have N events making up a sample S . One BDT (Section 7.6) takes a subset S_1 and uses it as a training sample and using the remaining set for testing, S_2 .

$$k \cdot |S_1| = |S_2| \text{ with } S = S_1 \cup S_2 \text{ and } S_1 \cap S_2 = \emptyset, \quad (8.9)$$

*The term *pull* refers to the “pulling” of subsamples from a larger set, while *validation* refers to the method being used to estimate uncertainties.

[†]•

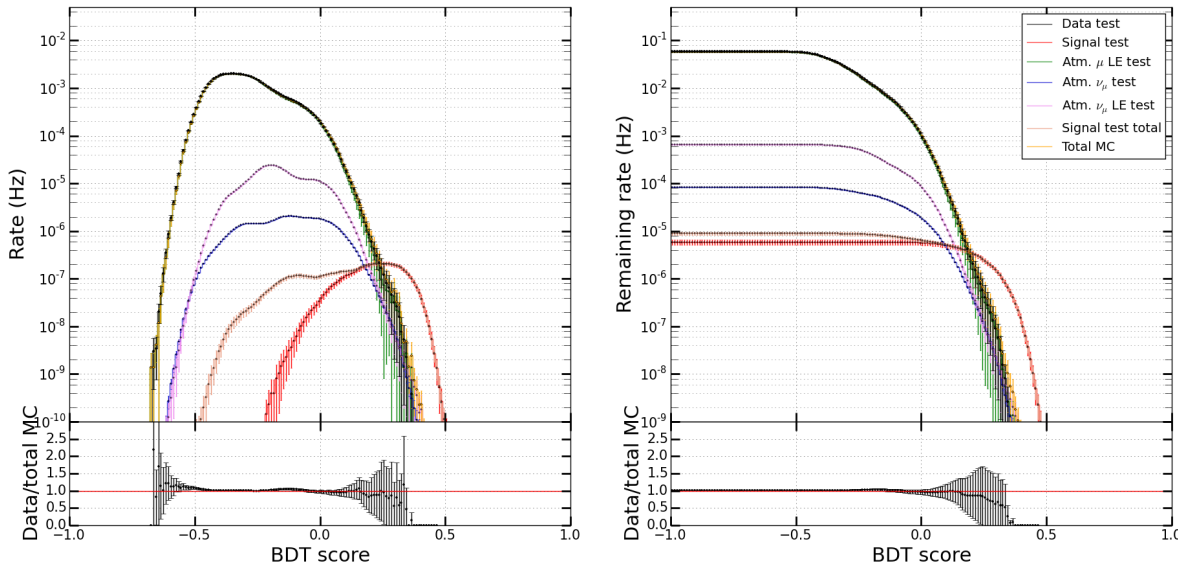


Figure 8.19: Result of the pull-validation method for an SMP with charge 1/2 and mass 100 GeV. Only the most prominent backgrounds are shown. *Left:* rate in function of the BDT score. *Right:* Cumulative rate to the right in function of the BDT score. The Y-axis shows the remaining rate of a dataset if were to cut at a certain BDT score. The weight of an event is given by Eq. 8.10.

where k refers to the order of missing events that is to be compensated. This factor cannot be made to large as the variability would diminish but cannot be made to large due to the limited size of S . Therefore, k is set at 10. Because S_2 is sizeably larger, the testing sample will extend further than the training sample S_1 as can be seen in Fig. G.1.

Pull-validation consists of repeating this procedure a number of time N_p . By combining the N_p distribution, we can gain additional information from an event by computing the Probability Density Function (PDF) of an event in function of the BDT score. A single event will have one BDT score attributed per iteration. By reprocessing this N_p times, by changing the training sample, the variation of an event in function of the BDT score becomes visible and can be used as an estimation of the rate in the tails.

Each event gets an appropriate weight, the *PV-weight* equal to

$$w_{PV} = \frac{\#\text{scores above cut threshold}}{N_p}. \quad (8.10)$$

The number of pull-validation iterations, N_p , should be high enough to extract as much information as possible, but low enough so that the subsamples, which are 10% of the total set chosen at random each time, are still adding information in the variability of the BDT performance. Too many iterations would induce correlation effects in the subsamples. Previous analyses indicated that $N_p = 200$ is a good enough to fulfill these requirements. The result for an SMP with charge 1/2 and mass 100 GeV is shown in Fig. 8.19 and shows the power of PV. Fig. ?? illustrates how one bin in this histogram is constructed.

8.4.3 Model Rejection Factor

The question remains where we should place a cut in the BDT score for an optimal signal discovery potential or upper limit computation. Since we do not know beforehand if the result will be a discovery or upper limit, the Feldman and Cousins method is used [Feldman:1997qc]. In this analysis, I want to compute the 90% confidence interval $\mu_{90} = (\mu_1, \mu_2)$, which is a function of the number of observed events, n_{obs} and of the number of expected background events, n_b

$$\mu_{90} (n_{\text{obs}}, n_b). \quad (8.11)$$

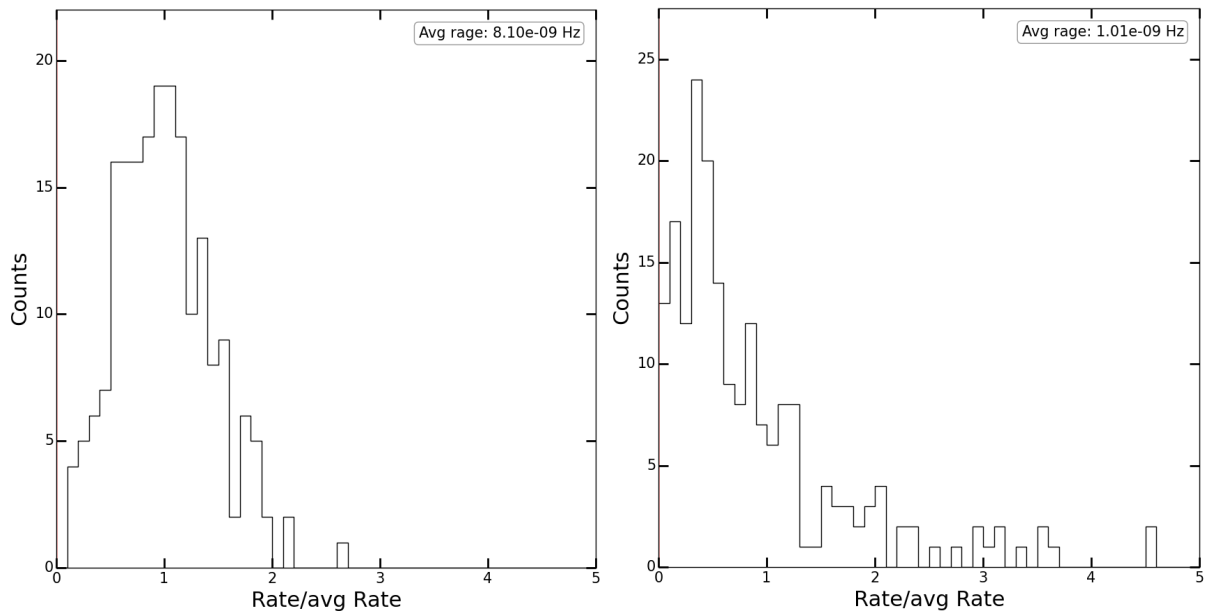


Figure 8.20: Uncertainty distribution of atmospheric ν_μ background with a BDT score between 0.29 and 0.3 (*left*) and with a BDT score between 0.34 and 0.35 (*right*). Between a BDT score, a sampleset has a certain expected rate that will change slightly when the BDT is trained with a different training sample. These rates (divided by the average rate) are shown in the figure. We can see that lower scores mean more statistics and have a Gaussian-like distribution. For higher scores, the distribution resembles a log-normal or Poisson. The average rate is computed and used in the pull-validation histogram.

If we assume that the expected amount of signal events is n_s , then the 90% confidence upper limit on the signal flux is

$$\Phi(E, \theta)_{90\%} = \Phi(E, \theta) \frac{\mu_{90}(n_{\text{obs}}, n_b)}{n_s}. \quad (8.12)$$

It is important to mention that n_s and Φ scale linearly, making the UL *independent* of the assumed absolute flux. Unfortunately an UL can only be computed once the number of observed events is known. The best *expected* UL could be computed by assuming that the number of observed events, is expected to be almost equal to the expected number of events from the MC background. Setting n_{obs} equal to n_b is however not a good approach for analyses that have small sample sets at the final level*.

A better way is to assume that the number of observed events is the mean of a Poisson distribution and we compute the *average upper limit* by summing over all the expected upper limits, weighted by their Poisson probability of occurring [Hill:2002nv]

$$\begin{aligned} \bar{\mu}_{90}(n_b) &= \sum_{n_{\text{obs}}=0}^{\infty} \mu_{90}(n_{\text{obs}}, n_b) \cdot \text{Poiss}(n_{\text{obs}}, n_b) \\ &= \sum_{n_{\text{obs}}=0}^{\infty} \mu_{90}(n_{\text{obs}}, n_b) \cdot \frac{(n_b)^{n_{\text{obs}}}}{(n_{\text{obs}})!} \exp(-n_b) \end{aligned} \quad (8.13)$$

The *Model Rejection Factor* (MRF) is defined as

$$\text{MRF}(n_b, n_s) = \frac{\bar{\mu}_{90}(n_b)}{n_s}. \quad (8.14)$$

*Say one expects 2.5 background events with a 1σ error of 2.1. If after unblinding one finds 0, 1, 2, 3, 4 or 5 events in data this would be considered as consistent with the expected background. The 90% Feldman-Cousins UL are however drastically different: $\mu_{90}(0, 2.5) = 1.18$, $\mu_{90}(5, 2.5) = 7.49$. Which is more than a factor of 6 difference!

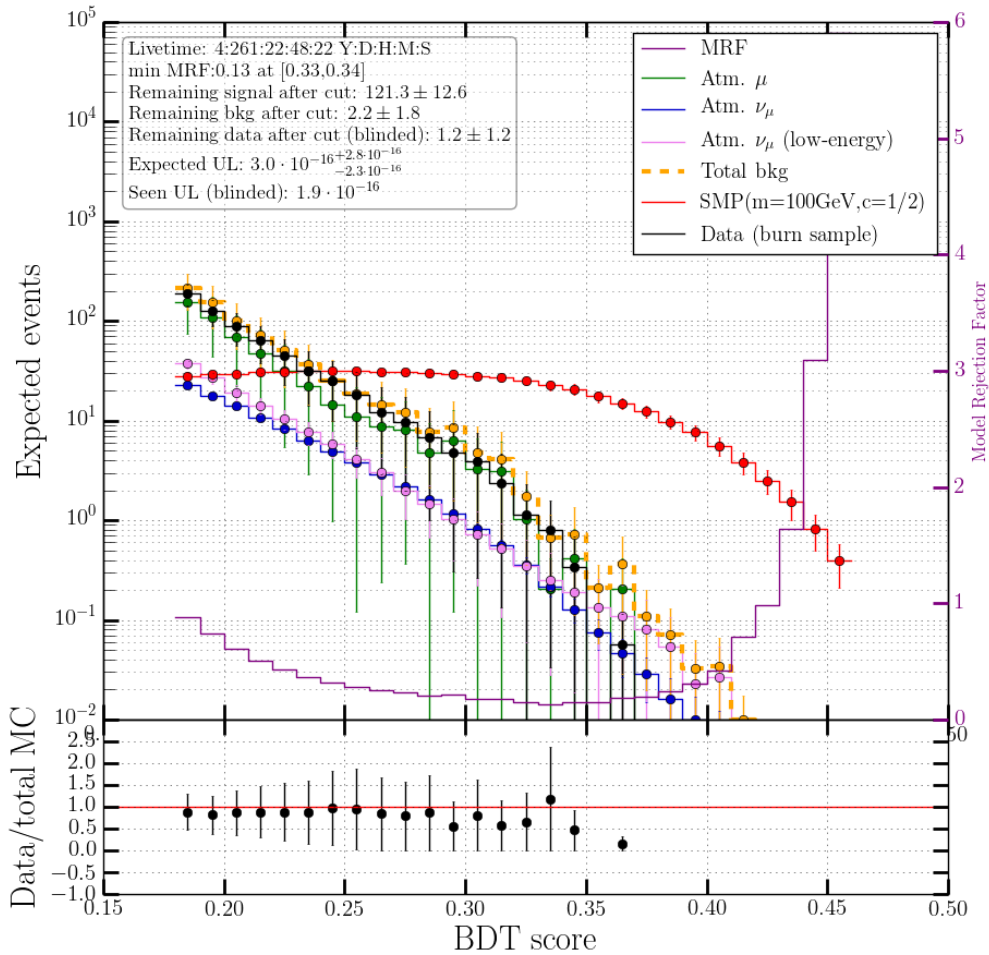


Figure 8.21: Zoomed in version of Fig. 8.19, focused on higher BDT scores, again for an SMP with charge 1/2 and mass 100 GeV. Only the most prominent backgrounds are shown. After pull-validation, there are enough statistics for a proper MRF computation (purple). Only statistical uncertainties are shown here. The small offset of data from MC is a common feature in PV and is accounted for in the systematic uncertainties.

Comparing this with Eq. 8.12, we can see that minimizing this factor corresponds to the strongest possible constraint on the expected signal flux. Because in each bin in Fig. 8.19 both the number of expected signal events and background events are known, the MRF can be computed in function of the BDT score. This is shown in Fig. 8.21 for one signal point.

The MRF gives a numerical indication at an optimal trade-off of expected signal and background events. At very high scores, there are less background events expected, but also less signal event while at lower scores both have higher expectancies.

The BDT score where the MRF is minimized is chosen as the final cut; this is the cut that will give the most stringent upper limit or best value for an observation. The results can be found in Tab. 8.5.

8.4.4 Systematic Uncertainties

There are four types of uncertainties that are assumed in the result of this analysis, which are listed below

1. **Statistical:** Limited statistics in the final event sample in both the expected signal and

Table 8.5: Expected amount signal and background events for 5 years of data (see Section ??), errors are statistical only. The signal is normalized to a flux of $10^{-14}\text{cm}^{-2}\text{s}^{-1}\text{sr}^{-1}$. The optimal BDT cut value from the MRF minimization is shown together with the expected upper limit and the statistical error.

Mass	Charge	Remaining signal events per 1723 days	Remaining background events per 1723 days	$\bar{\mu}_{90} (\text{cm}^{-2}\text{s}^{-1}\text{sr}^{-1})$	BDT cut value
10 GeV	1/2	73.2 ± 7.7	2.2 ± 1.6	$5.0 \cdot 10^{-16}^{+2.9 \cdot 10^{-16}}_{-3.8 \cdot 10^{-16}}$	0.32
100 GeV	1/2	121.3 ± 12.6	2.2 ± 1.8	$3.0 \cdot 10^{-16}^{+2.8 \cdot 10^{-16}}_{-2.3 \cdot 10^{-16}}$	0.33
1 TeV	1/2	90.7 ± 9.6	0.8 ± 0.6	$1.9 \cdot 10^{-16}^{+2.5 \cdot 10^{-16}}_{-1.8 \cdot 10^{-17}}$	0.35
10 TeV	1/2	127.8 ± 11.0	1.8 ± 1.1	$2.1 \cdot 10^{-16}^{+1.4 \cdot 10^{-16}}_{-1.2 \cdot 10^{-16}}$	0.34
100 TeV	1/2	107.7 ± 9.7	2.2 ± 1.3	$3.4 \cdot 10^{-16}^{+1.9 \cdot 10^{-16}}_{-2.6 \cdot 10^{-16}}$	0.34
10 GeV	1/3	45.3 ± 5.2	2.2 ± 1.9	$8.2 \cdot 10^{-16}^{+7.7 \cdot 10^{-16}}_{-6.2 \cdot 10^{-16}}$	0.32
100 GeV	1/3	60.5 ± 4.1	2.4 ± 1.9	$5.9 \cdot 10^{-16}^{+5.1 \cdot 10^{-16}}_{-4.5 \cdot 10^{-16}}$	0.35
1 TeV	1/3	64.0 ± 5.6	3.1 ± 2.7	$6.7 \cdot 10^{-16}^{+5.0 \cdot 10^{-16}}_{-5.4 \cdot 10^{-16}}$	0.32
10 TeV	1/3	57.6 ± 4.9	1.2 ± 1.0	$5.5 \cdot 10^{-16}^{+3.4 \cdot 10^{-16}}_{-3.1 \cdot 10^{-16}}$	0.34
100 TeV	1/3	79.7 ± 5.9	2.2 ± 1.5	$4.6 \cdot 10^{-16}^{+2.4 \cdot 10^{-16}}_{-3.5 \cdot 10^{-16}}$	0.34
10 GeV	2/3	40.4 ± 4.5	9.6 ± 3.7	$1.4 \cdot 10^{-15}^{+1.5 \cdot 10^{-15}}_{-1.0 \cdot 10^{-15}}$	0.29
100 GeV	2/3	71.5 ± 7.5	5.0 ± 1.4	$5.1 \cdot 10^{-16}^{+5.1 \cdot 10^{-16}}_{-1.5 \cdot 10^{-16}}$	0.3
1 TeV	2/3	79.3 ± 7.7	7.2 ± 2.1	$6.7 \cdot 10^{-16}^{+4.6 \cdot 10^{-16}}_{-3.1 \cdot 10^{-16}}$	0.3
10 TeV	2/3	74.4 ± 7.9	7.9 ± 2.2	$6.3 \cdot 10^{-16}^{+6.7 \cdot 10^{-16}}_{-3.1 \cdot 10^{-16}}$	0.29
100 TeV	2/3	59.0 ± 6.0	5.7 ± 1.6	$7.4 \cdot 10^{-16}^{+5.6 \cdot 10^{-16}}_{-2.7 \cdot 10^{-16}}$	0.3

background events lead to uncertainties. We assume that the variancy of this number follows a Poisson distribution where the statistical uncertainty of a rate is defined as the square root of the rate. The statistical uncertainties can be seen in Tab. 8.5.

2. Detector: Detector simulations assume certain properties of the optical modules and the ice (explained in Chapter 5), which can differ from true values or are over-simplistic. Therefore, the following detector uncertainties are assumed:

- DOM efficiency +10%
- DOM efficiency -10%
- Ice absorption +10%
- Ice scattering +10%
- Ice absorption and scattering -7.1%

Because of the limited statistics in the systematic background sample sets, these detector uncertainties are investigated before the BDT training at Level 4. The specialized datasets that were used for this are given in Tab. 6.3. The effects on the signal were investigated after BDT cuts of 0.3 for charge 2/3 particles and 0.32 for charge 1/3 and 1/2 particles. There were no significant differences found for different masses and are therefore not specified. Results are shown in Tab. 8.6.

3. Flux: The models that were used in flux normalizations are not set in stone. Therefore variations to the flux were assumed to determine the possible discrepancies.

- *SMP flux*: As there is no clear production model or clear possible origin of these anomalous charged particles, the signal flux is assumed to range between E^{-1} and E^{-3} .
- *Atmospheric μ flux*: We look at the difference between the GaisserH3a [94] and GaisserH4a [188] models.
- *Atmospheric ν_μ flux*: We look at the difference between the Bartol [189] and Honda2006 [125] models.

Similar to the detector uncertainties, the effects were computed at Level 4 for background

Table 8.6: Results from the detector and flux uncertainties

	Atm. μ	Atm. ν_μ	SMP (charge 1/3)	SMP (charge 1/2)	SMP (charge 2/3)
DOM eff. +10%	30.9%	2.9%	7.6%	5.2%	3.6%
DOM eff. -10%	26.7%	29.4%	3.5%	16.7%	0.8%
Absorption +10%	23.9%	2.2%	22.7%	18.5%	38.3%
Scattering +10%	3.6%	2.9%	19.3%	3%	3.4%
Abs./Scat -7.1%	17.7%	5.8%	18.7%	6.4%	12.1%
Flux	0.35%	15.28%	1.7%	3%	11.8%
Total	50.7%	33.9%	36.2%	26.6%	42.5%

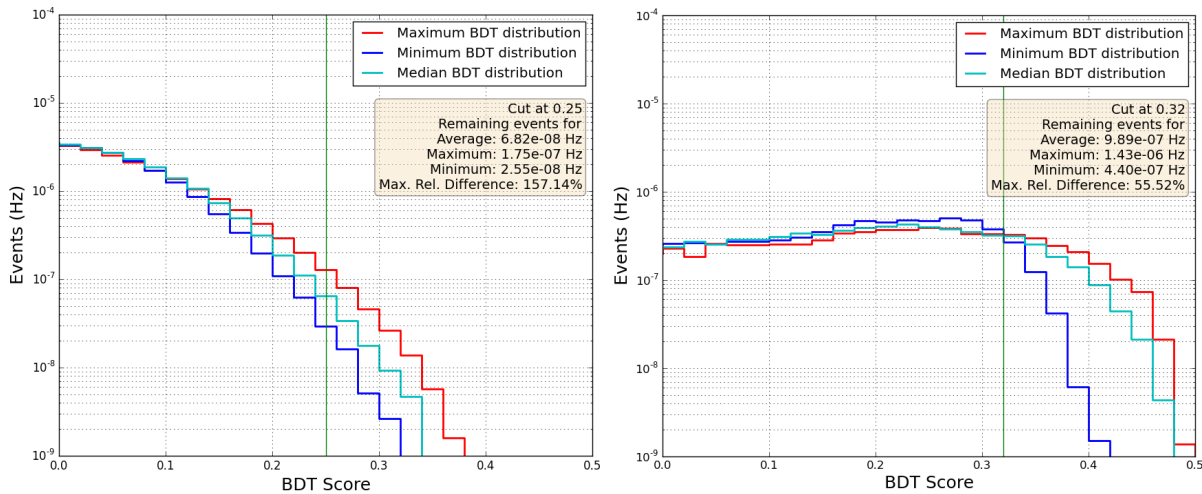


Figure 8.22: *Left:* Illustration how the pull-validation systematic error is computed. Here, the maximum rate, the median and minimum rates from 200 BDT score distributions are shown. *Right:* Similar comparison of BDT score distributions for an SMP with a charge 1/2 and mass 100 GeV.

datasets and at BDT cuts of 0.32, 0.32 and 0.3 for particles with charges 1/2, 1/3 and 2/3 respectively. Results are shown in Tab. 8.6.

4. **Pull-validation:** As explained in Section ??, only one BDT is used for the final event rate. Pull-validation offers us a way to get more statistics but choosing one BDT for the full data sample and comparing the data rate to the mean of a fluctuating pool of expected background events give rise to a large uncertainty. It was found that this uncertainty is highly dominating, but was chosen conservatively.

For each mass point I have looked at the minimal and maximal offsets between the 200 BDT outputs. As the signal distributions again had enough statistics at higher BDT scores, cuts at values of 0.32, 0.32 and 0.3 for particles with charges 1/2, 1/3 and 2/3 were chosen respectively. Background distributions showed unrealistic large fluctuations in the tails due to very low statistics and single events with high or low weights. Therefore the BDT cuts were lowered to 0.25 for the backgrounds. The largest discrepancy between the average and the minimum and maximum is set as the uncertainty as a conservative choice. An example is shown in Fig. 8.22. The results can be found in Tab. 8.7.

The final systematic uncertainty is obtained by summing the individual uncertainties in quadrature.

Implementing the uncertainties in the upper limit

Using Eq. 8.12, we are able to determine an upper limit in the scenario where we cannot claim detection. Because there are large uncertainties in both the background and signal rates, these

Table 8.7: Results from the pull-validation uncertainties

Mass	Charge	Atm. μ	Atm. ν_μ	SMP
10 GeV	1/2	66.4%	216.1%	59.8%
100 GeV	1/2	136.3%	157.1%	55.5%
1 TeV	1/2	159.8%	136.3%	42.1%
10 TeV	1/2	211.6%	73.7%	36.7%
100 TeV	1/2	218.4%	135.4%	52.5%
10 GeV	1/3	142%	176.7	39.6%
100 GeV	1/3	174.8%	225.6%	32.9%
1 TeV	1/3	108.3%	167%	40.9%
10 TeV	1/3	190.3%	150%	40.8%
100 TeV	1/3	223.6%	96.8%	35.6%
10 GeV	2/3	63.8%	103.6%	54.8%
100 GeV	2/3	58.7%	88.9%	52.5%
1 TeV	2/3	65.4%	72.5%	61.9%
10 TeV	2/3	10%	104.2%	72.1%
100 TeV	2/3	51.5%	83.4%	43.6%

uncertainties are included in the computation of the limit*. Gaussian distributions with large uncertainties overlap with negative rates, which are non physical, therefore we assume that the uncertainties follow a truncated normal distribution

$$\Phi(n_{\text{obs}})_{90\%} = \Phi \cdot \frac{\sum_{n'_{\text{bkg}}}^{\infty} [\mu_{90}(n_{\text{obs}}, n'_{\text{bkg}}) \cdot P_{\text{unc}}(n'_{\text{bkg}} | n_{\text{bkg}}, \sigma_{n_{\text{bkg}}})]}{\sum_{n'_{\text{s}}=0}^{\infty} P_{\text{unc}}(n'_{\text{s}} | n_{\text{s}}, \sigma_{n_{\text{s}}})}, \quad (8.15)$$

where

$$P_{\text{unc}}(n | \lambda, \sigma) = \int_{-\lambda}^{\infty} \frac{(\lambda + x)^n e^{-\lambda - x}}{n!} \cdot w(x, \sigma) dx, \quad (8.16)$$

with $w(x, \sigma)$ a normal distribution with mean 0 and variance σ^2 . An example of two distributions for both the signal and background are shown in Fig. 8.23.

8.5 Results

8.5.1 Unblinding

This analysis was presented to the collaboration after internal review and accepted for *data unblinding*[†]. As explained in Section 6.5, only 10% of the data was used in setting up the analysis. Expected rates, e.g. in Tab. 8.5, are normalized to the total livetime of the full dataset. The total livetime for the different years is equal to

- around 333.1 days of livetime for IC86-1,
- around 324.5 days of livetime for IC86-2,
- around 345.5 days of livetime for IC86-3,
- around 357.3 days of livetime for IC86-4,
- around 362.6 days of livetime for IC86-5,

resulting in a total livetime of around 1723 days.

*The *observed* limit will be weighted with an uncertainty probability. Additionally we will also show systematical uncertainty bands as can be seen in Fig. ???

[†]By only looking at part of the data, the analyzer “blinds” himself to not (sub-)consciously tweak the analysis [Roodman:2003rw]. After approval, the analyzer can “unblind” and look at the full data, which serves as an objective way to look at the data and provides for consistency check with the expected and seen rates.

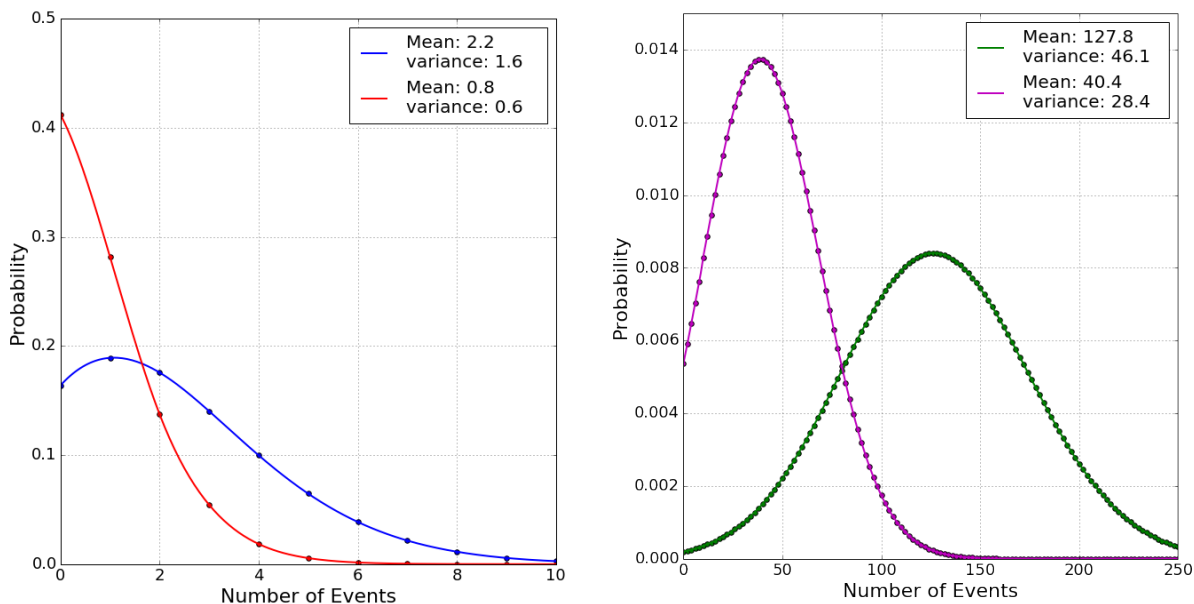


Figure 8.23: *Left:* Illustration of probability density function using Eq. 8.16 of two expected background rates with their variance. *Right:* Similar PDFs for two expected signal rates.

The cuts in the BDT score for each signal point were fixed by computing the most stringent upper limit with the model rejection factor with pull-validation. The full dataset is run through one BDT as an average of multiple BDTs could result in a systematic offset that is non-physical and would result in data events that contribute with a factor < 1 , which is prone to lead to confusion. Therefore, one BDT out of 200 was chosen at random for each signal point.

Before unblinding, a procedure was set depending on the outcome

- If the number of seen data events are consistent with the expected background rate, an upper limit on the SMP flux is set as described in Section 8.4.3.
- If there is a consistent overfluctuation of the data compared to the expected background, a more in-depth analysis on these events should be performed before signal discovery can be claimed.

8.5.2 Limits

After unblinding, the number of data events for all signal points were consistent with the expected background, which can be seen in Tab. 8.8. The upper limits were computed with Eq. 8.15. Event views of the types of these events can be found in Appendix H.

The resulting upper limits are shown in Fig. 8.24 and 8.25 and compared to the experiments that were discussed in Chapter 2. Previous experiments that were used for comparison did not have a mass dependency in the analysis and are therefore shown as straight lines. The limits from this analysis were computed with Eq. 8.15 and are more stringent than any other experiment that was done up to now. Also shown are the upper limits for the individual charges with the large systematical error bands.

There is an apparent optimum for discriminating SMPs from backgrounds in the IceCube experiment at a charge of 1/2. Particles with a higher charge (such as 2/3) resemble physical muons a lot more, while particles with a lower charge have a lot lower probability in producing enough light to trigger the detector.

<https://arxiv.org/pdf/1310.1284.pdf>

Table 8.8: Final results of the upper limit computations. Signal is the expected rate from a $10^{-14} \text{ cm}^{-2} \text{s}^{-1} \text{sr}^{-1}$ and background and signal are normalized to the total livetime of the full dataset.

Mass	Charge	Remaining signal events per 1723 days	Remaining background events per 1723 days	Seen events in data	$\bar{\mu}_{90} (\text{cm}^{-2} \text{s}^{-1} \text{sr}^{-1})$	$\mu_{90} (\text{cm}^{-2} \text{s}^{-1} \text{sr}^{-1})$
10 GeV	1/2	73.2 ± 48.5	$2.2^{+3.5}_{-2.2}$	0	$5.0 \cdot 10^{-16}^{+4.15 \cdot 10^{-15}}_{-4.35 \cdot 10^{-16}}$	$1.4 \cdot 10^{-16}$
100 GeV	1/2	121.3 ± 75.7	$2.2^{+4.4}_{-2.2}$	0	$3.0 \cdot 10^{-16}^{+2.45 \cdot 10^{-15}}_{-2.61 \cdot 10^{-16}}$	$8.1 \cdot 10^{-17}$
1 TeV	1/2	90.7 ± 46.1	$0.8^{+1.3}_{-0.8}$	0	$1.9 \cdot 10^{-16}^{+1.14 \cdot 10^{-15}}_{-1.13 \cdot 10^{-16}}$	$1.6 \cdot 10^{-16}$
10 TeV	1/2	127.8 ± 59.0	$1.8^{+3.0}_{-1.8}$	2	$2.1 \cdot 10^{-16}^{+1.24 \cdot 10^{-15}}_{-1.79 \cdot 10^{-16}}$	$2.5 \cdot 10^{-16}$
100 TeV	1/2	107.7 ± 64.2	$2.2^{+4.4}_{-2.2}$	0	$3.4 \cdot 10^{-16}^{+2.54 \cdot 10^{-15}}_{-2.96 \cdot 10^{-16}}$	$9.1 \cdot 10^{-17}$
10 GeV	1/3	45.3 ± 24.9	$2.2^{+4.6}_{-2.2}$	6	$8.2 \cdot 10^{-16}^{+5.31 \cdot 10^{-15}}_{-7.20 \cdot 10^{-16}}$	$1.5 \cdot 10^{-15}$
100 GeV	1/3	60.5 ± 29.9	$2.4^{+4.7}_{-2.4}$	5	$5.9 \cdot 10^{-16}^{+3.50 \cdot 10^{-15}}_{-5.22 \cdot 10^{-16}}$	$4.3 \cdot 10^{-16}$
1 TeV	1/3	64.0 ± 35.4	$3.1^{+6.5}_{-3.1}$	4	$6.7 \cdot 10^{-16}^{+5.07 \cdot 10^{-15}}_{-5.95 \cdot 10^{-16}}$	$5.8 \cdot 10^{-16}$
10 TeV	1/3	57.6 ± 31.8	$1.2^{+2.4}_{-1.2}$	5	$5.5 \cdot 10^{-16}^{+2.78 \cdot 10^{-15}}_{-4.78 \cdot 10^{-16}}$	$1.3 \cdot 10^{-15}$
100 TeV	1/3	79.7 ± 40.9	$2.2^{+4.3}_{-2.2}$	6	$4.6 \cdot 10^{-16}^{+2.77 \cdot 10^{-15}}_{-3.93 \cdot 10^{-16}}$	$8.9 \cdot 10^{-16}$
10 GeV	2/3	40.4 ± 28.4	$9.6^{+14.4}_{-9.6}$	9	$1.4 \cdot 10^{-15}^{+2.40 \cdot 10^{-14}}_{-1.29 \cdot 10^{-16}}$	$1.2 \cdot 10^{-15}$
100 GeV	2/3	71.5 ± 48.8	$5.0^{+6.4}_{-5.0}$	2	$5.1 \cdot 10^{-16}^{+7.17 \cdot 10^{-15}}_{-4.40 \cdot 10^{-16}}$	$2.7 \cdot 10^{-16}$
1 TeV	2/3	79.3 ± 60.0	$7.2^{+9.4}_{-7.2}$	9	$6.7 \cdot 10^{-16}^{+1.18 \cdot 10^{-14}}_{-6.11 \cdot 10^{-16}}$	$7.7 \cdot 10^{-16}$
10 TeV	2/3	74.4 ± 62.7	$7.9^{+10.3}_{-7.9}$	5	$6.3 \cdot 10^{-16}^{+2.10 \cdot 10^{-14}}_{-5.82 \cdot 10^{-16}}$	$3.9 \cdot 10^{-16}$
100 TeV	2/3	59.0 ± 36.4	$5.7^{+7.3}_{-5.7}$	1	$7.4 \cdot 10^{-16}^{+7.91 \cdot 10^{-15}}_{-6.73 \cdot 10^{-16}}$	$2.2 \cdot 10^{-16}$

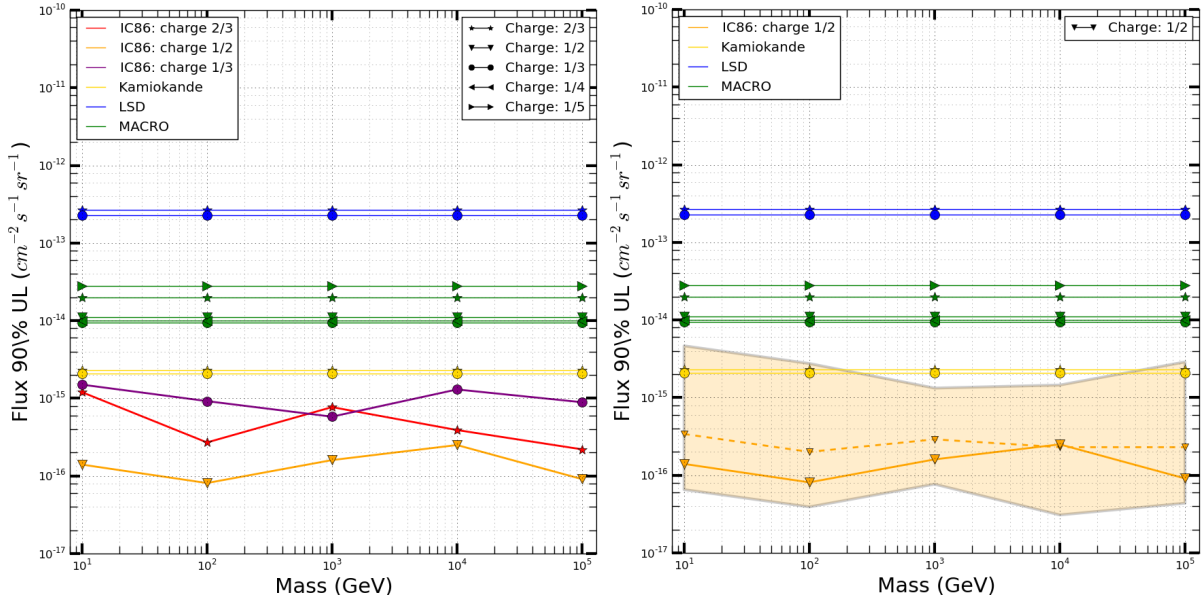


Figure 8.24: *Left:* Final upper limits for SMPs with three different charges in function of the mass. *Right:* Comparison of other experiments to the upper limit obtained for SMPs with a charge 1/2 including the systematic error bands. The observed limit is shown with a solid line and the expected limit is shown with a dashed line.

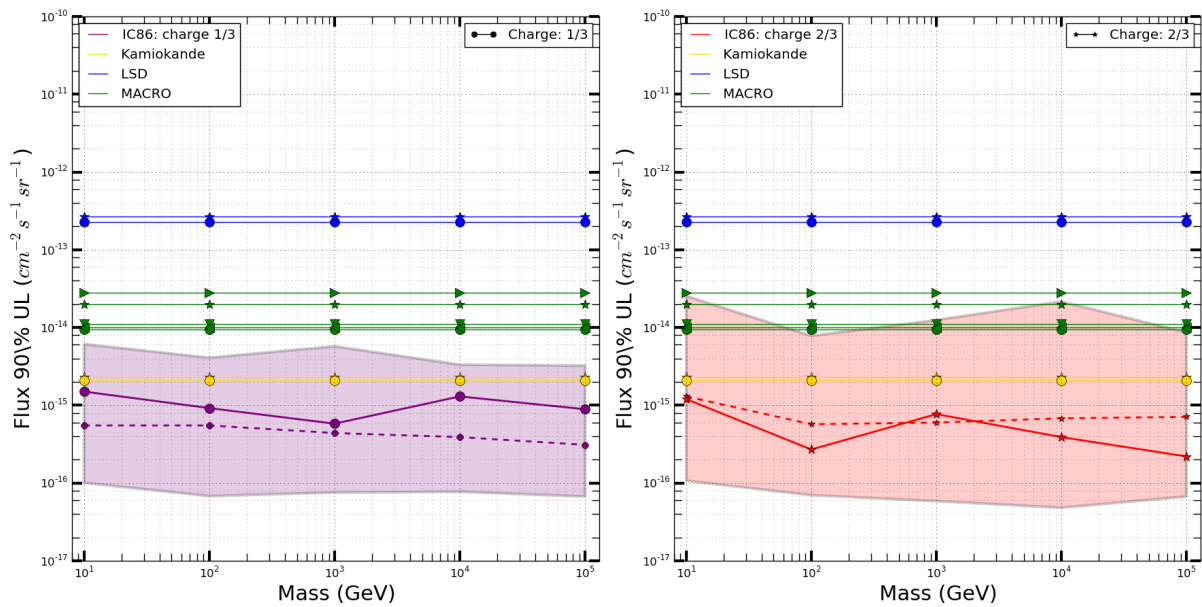


Figure 8.25: Comparison of other experiments to the upper limit obtained for SMPs including the systematic error bands. The observed limit is shown with a solid line and the expected limit is shown with a dashed line. *Left:* SMPs with charge 1/3. *Right:* SMPs with charge 2/3.



9. Summary and Conclusion

Ook verschillende mogelijkheden die je verschillende toepassingen zouden geven.

Vergelijken met andere experimenten, zeggen dat het appels met peren vgl is en ook wrm je zo weinig efficient bent met IC ondanks veel groter

The burn sample data and MC backgrounds in function of the BDT score shown an excellent agreement in Fig. 8.19 and Fig. ??, even at higher scores where the signal is expected to dominate.

Possible improvements: filter! Trigger! a speed cut... If multiple COGs, connection of both should be within time window.

Other machine learning techniques.

Energy estimators (although probably wrong)

Additions

Appendices 149

A Gauge symmetries 151

B Planck's law 153

B.1 Electromagnetic waves in a cubical cavity

C Statistics 155

D Distributions 157

D.1 Spherical random numbers

D.2 Power law distributions

D.3 Angular distributions

D.4 Weighting

E AdaBoost: simple example 163

F Resampling Methods 165

F.1 Bootstrapping

F.2 Cross-validation

G Additional BDT Checks 167

H Data Events at Final Level 169

10 Some useful things for LaTeX 173

10.1 Definitions

10.2 Remarks

10.3 Corollaries

10.4 Propositions

10.5 Examples

10.6 Exercises

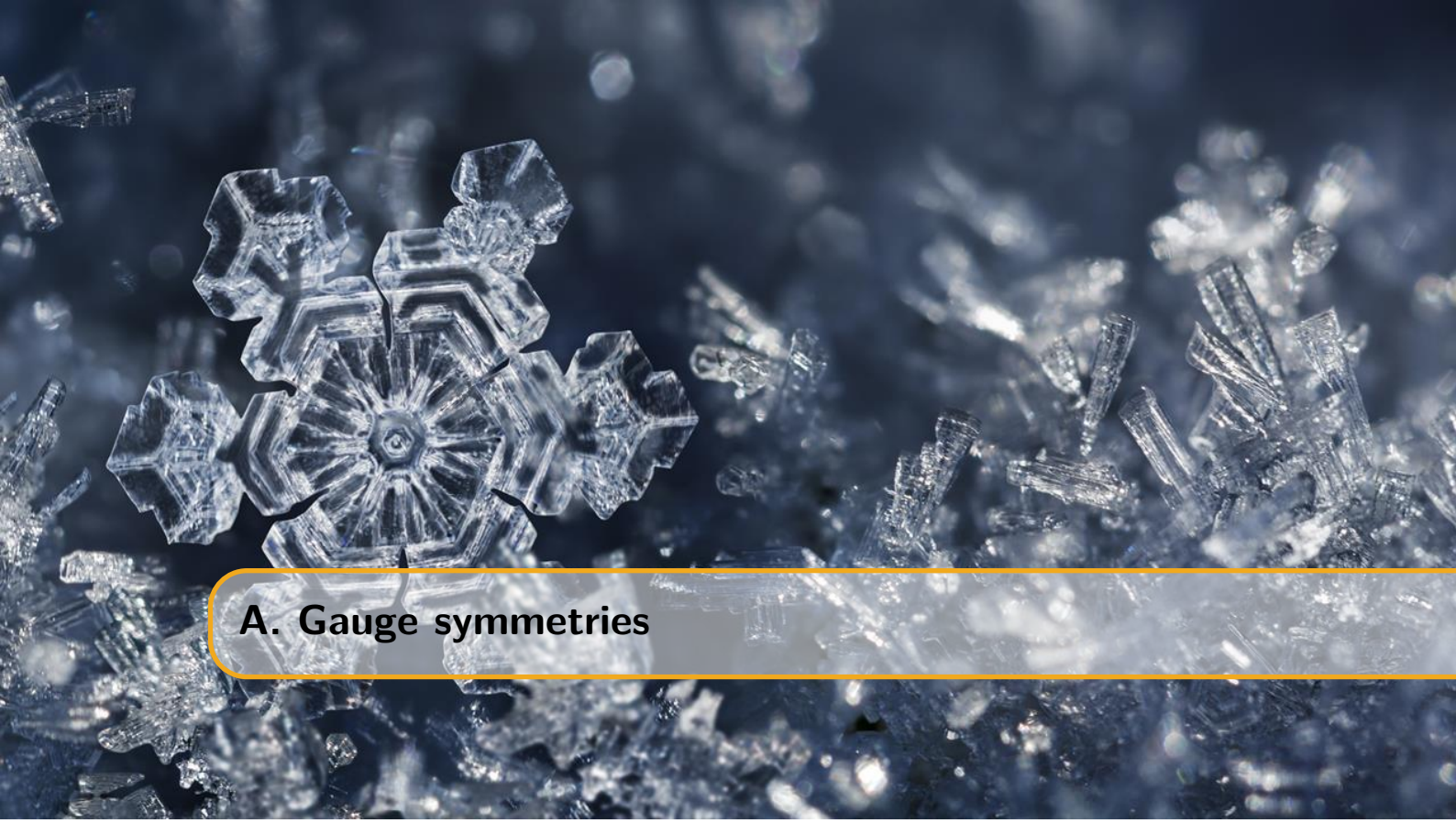
10.7 Problems

10.8 Vocabulary

Bibliography 175

Index 189

Appendices



A. Gauge symmetries

NOG NIET GEDAAN

The difference between global and local symmetries are not straightforward for everybody. In this appendix I try to give a better view of the matter.

Imagine that at each point in space and time there is a circle attached to it. If one shifts all circles of all points with a fixed angle the underlying physics hasn't changed. If we look at the whole in a different angle, nothing seems to be changed as everything holds the same relative orientation. This is a global symmetry. For local symmetries we instead shift each circle through a different angle, but an angle that changes smoothly from point to point and in a way that we can say how that angle is varying between different nearby regions. Then it will turn out that we can describe that rotation angle by means of a so-called gauge field, which just lets us transport the charged scalar field from one point in space time to another, taking account of how the rotation angle of the circle is changing. A gauge is a kind of coordinate system that is varying depending on the location with respect to some underlying space. In physics we are almost always concerned with space-time as the underlying space, and we are typically interested in theories that are invariant with respect to the choice of gauge or coordinate system.

Dan wat uitleg vanuit je QFT boek en de dingen hieronder: Je wilt je derivative anders doen werken in je theory onder een transformatie, maar daarvoor heb je een veld nodig. M.a.w.: dankzij een veld heb je lokale ijktransformatie mogelijk!

B. Planck's law

bron: <http://hyperphysics.phy-astr.gsu.edu/hbase/quantum/rayj.html>

B.1 Electromagnetic waves in a cubical cavity

Suppose we have EM waves in a cavity at equilibrium with its surroundings. These waves must satisfy the wave equation in three dimensions:

$$\frac{\partial^2 \Psi}{\partial x^2} + \frac{\partial^2 \Psi}{\partial y^2} + \frac{\partial^2 \Psi}{\partial z^2} = \frac{1}{c^2} \frac{\partial^2 \Psi}{\partial t^2}. \quad (\text{B.1})$$

The solution must give zero amplitude at the walls. A non-zero value would mean energy is dissipated through the walls which is in contradiction to our equilibrium assumption. A general solution takes the form of

$$\Psi(x, y, z, t) = \Psi_0 \sin k_1 x \sin k_2 y \sin k_3 z \sin k_4 t, \quad (\text{B.2})$$

which, after requiring $k_n L = n\pi$ with $n = 0, 1, 2, \dots$ and $k_4 \frac{\lambda}{2c} = \pi$, leads to

$$\Psi(x, y, z, t) = \Psi_0 \sin \left(\frac{n_1 \pi x}{L} \right) \sin \left(\frac{n_2 \pi y}{L} \right) \sin \left(\frac{n_3 \pi z}{L} \right) \sin \left(\frac{2\pi c t}{\lambda} \right). \quad (\text{B.3})$$

From the wave equation it is easy to find that

$$n^2 = n_1^2 + n_2^2 + n_3^2 = \frac{4L^2}{\lambda^2}, \quad (\text{B.4})$$

which span up a sphere in “n-space” with a volume of $\frac{1}{8} \frac{4}{3} \pi n^{3/2}$, where the first term originates from the positive nature of $n_{1,2,3}$. Because there are two possible polarizations of the waves one has to multiply with an additional factor 2. The number of modes per unit wavelength is equal to

$$\frac{dN}{d\lambda} \times \frac{1}{L^3} = \frac{d}{d\lambda} \left[\frac{8\pi L^3}{3\lambda^3} \right] \times \frac{1}{L^3} = - \left[\frac{8\pi}{\lambda^4} \right]. \quad (\text{B.5})$$

B.1.1 Classical approach

Following the principle of equipartition of energy, each standing wave mode will have an average energy kT with k the Boltzmann constant and T the temperature in Kelvin. The energy density is then:

$$\frac{du}{d\lambda} = -kT \frac{8\pi}{\lambda^4}. \quad (\text{B.6})$$

In function of frequency $\nu = \frac{c}{\lambda}$:

$$\frac{du}{d\nu} = -\frac{c}{\lambda^2} \frac{du}{d\lambda} = \frac{8\pi k T \nu^2}{c^3}, \quad (\text{B.7})$$

also known as the Rayleigh-Jeans law*. Problem: divergence

B.1.2 Quantum approach

The energy levels from a quantized harmonic oscillator are equal to

$$E_r = h\nu \left(r + \frac{1}{2} \right) = \frac{hc}{\lambda} \left(r + \frac{1}{2} \right) \quad \text{with } r = 0, 1, 2, \dots \quad (\text{B.8})$$

Implementing eq. B.4

$$E = \left(r + \frac{1}{2} \right) \frac{hc}{2L} \sqrt{n_1^2 + n_2^2 + n_3^2} \quad (\text{B.9})$$

According to statistical physics the average energy is now not equal to kT but follows a probability distribution

$$p(\nu, r) = \frac{e^{-r h \nu}}{\sum_{r=0}^{\infty} e^{-r h \nu}}, \quad (\text{B.10})$$

where we reference to the ground state of the oscillator: $E'_r = E_r - E_0$.

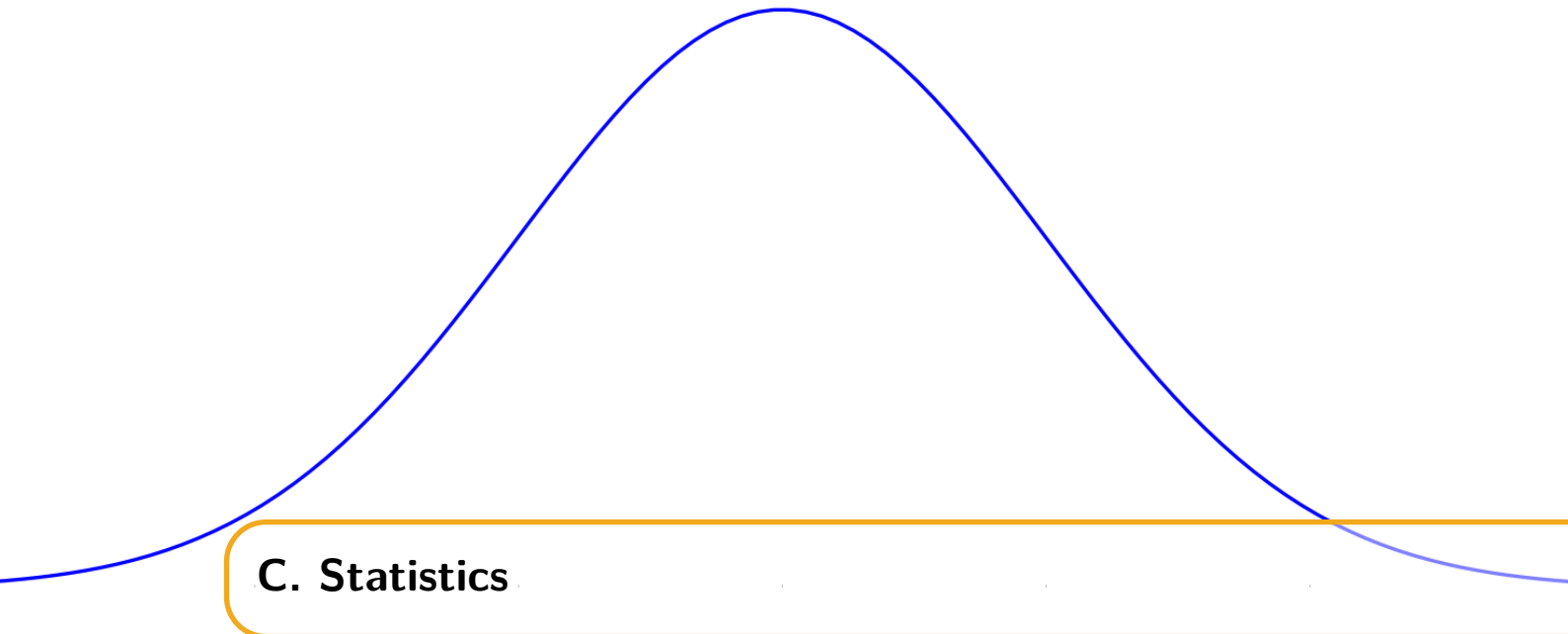
The average energy is now:

$$\begin{aligned} \langle E(\nu) \rangle &= \sum_{r=0}^{\infty} E(\nu, r) \cdot p(\nu, r) = \frac{\sum_{r=0}^{\infty} r h \nu e^{-r h \nu}}{\sum_{r=0}^{\infty} e^{-r h \nu}} \\ &= \frac{h \nu}{e^{h \nu / k T} - 1} \end{aligned} \quad (\text{B.11})$$

Substituting this for kT in eq. B.7 we find Planck's equation:

$$\frac{du}{d\nu} = \frac{8\pi h \nu^3}{c^3} \frac{h \nu}{e^{h \nu / k T} - 1} \quad (\text{B.12})$$

*This is often quoted per unit of steradian, which results in $\frac{2kT\nu^2}{c^3}$



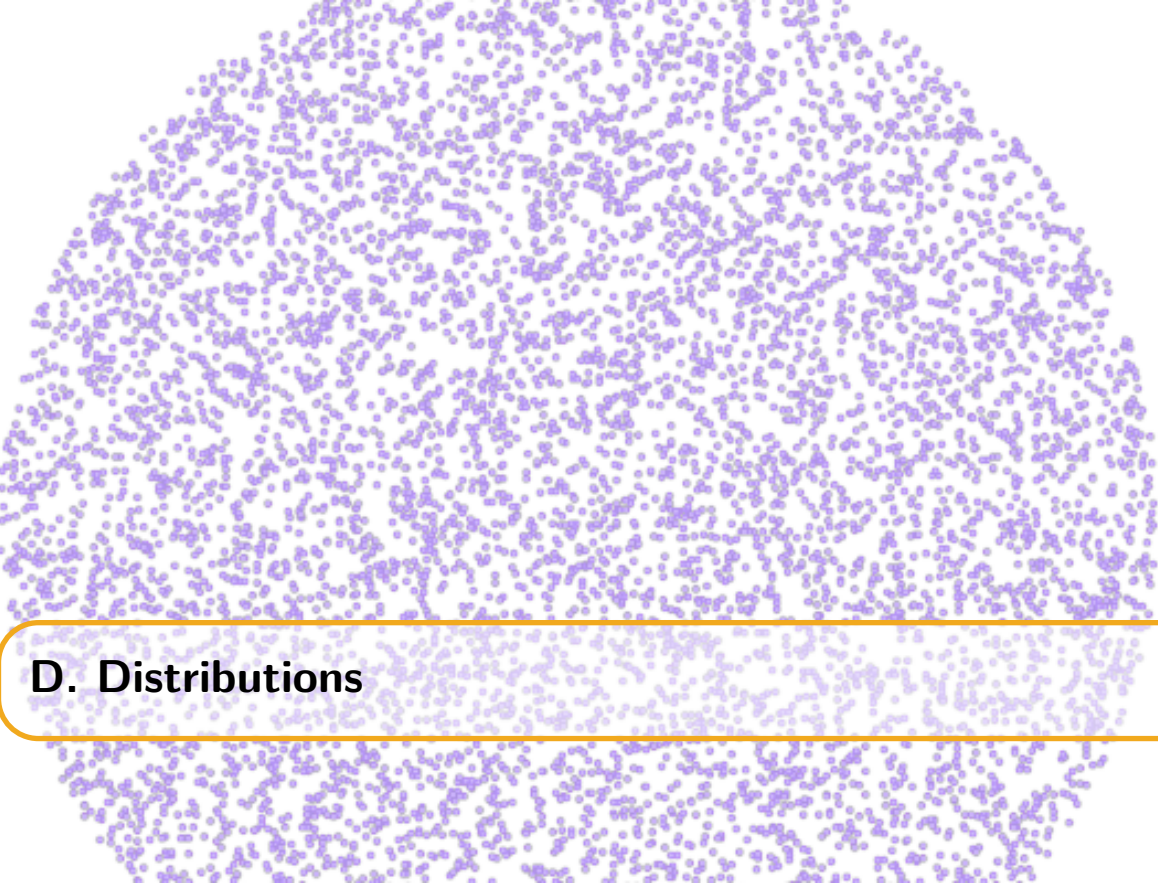
A word that is often mentioned in this work is “statistics”. It refers to the statistical error of a counting experiment, i.e. the Poissonian error. The Poisson distribution is a discrete probability of a certain number of n events occurring in a fixed time interval. The Poisson probability function is given by

$$P(n) = \frac{\lambda^n e^{-\lambda}}{n!}, \quad (\text{C.1})$$

where λ is the expected number of events and also equal to the variance. An experiment that counted N events therefore has a statistical error of

$$\sigma = \sqrt{N} \quad (\text{C.2})$$

In other words: higher statistics denotes a lower statistical error.



D. Distributions

D.1 Spherical random numbers

Most random number generators provide uniform distributions between the range $[0, 1]$. Assume we want to make a uniform distribution along a sphere with angles ϕ and θ and radius r , in spherical coordinates. Random numbers between $[0, \pi]$, $[0, 2\pi]$ and $[0, R]$ (the ranges of the coordinates) would not give a uniform distribution as illustrated in Fig. D.1 (left).

The differential surface area, dA , is equal to $dA(d\phi, d\theta) = r^2 \sin(\phi) d\phi d\theta$. If we want the distribution $f(v)$ to be constant for a uniform distribution, then $f(v) = \frac{1}{4\pi}$ since $\int \int_S f(v) dA = 1$ and $\int \int_S dA = 4\pi$. We want the distribution in function of the angles, so

$$f(v)dA = \frac{1}{4\pi} dA = f(r)f(\phi, \theta)d\phi d\theta. \quad (\text{D.1})$$

Since we know the expression for dA , we find that

$$f(\phi, \theta) = \frac{1}{4\pi} \sin(\phi), \quad (\text{D.2})$$

and separating the angles:

$$f(\theta) = \int_0^\pi f(\phi, \theta) d\phi = \frac{1}{2\pi}, \quad (\text{D.3})$$

$$f(\phi) = \int_0^{2\pi} f(\phi, \theta) d\theta = \frac{\sin(\phi)}{2}, \quad (\text{D.4})$$

where it is clear that $f(\phi)$ scales with $\sin(\phi)$; there are more points needed at the equator (this makes sense, as the surface at the equator is much larger!).

The question is now how one can get a sample to follow the distribution of $f(\phi)$. For this, we use the *inverse transform sampling* method where one makes use of the cumulative distribution function, $F(\phi)$, which increases monotonically

$$F(\phi) = \int_0^\phi f(\phi') d\phi' = \frac{1}{2} (1 - \cos(\phi)). \quad (\text{D.5})$$

The method shows that if u is a random variable drawn from a uniform distribution, we have to find the inverse function of F ,

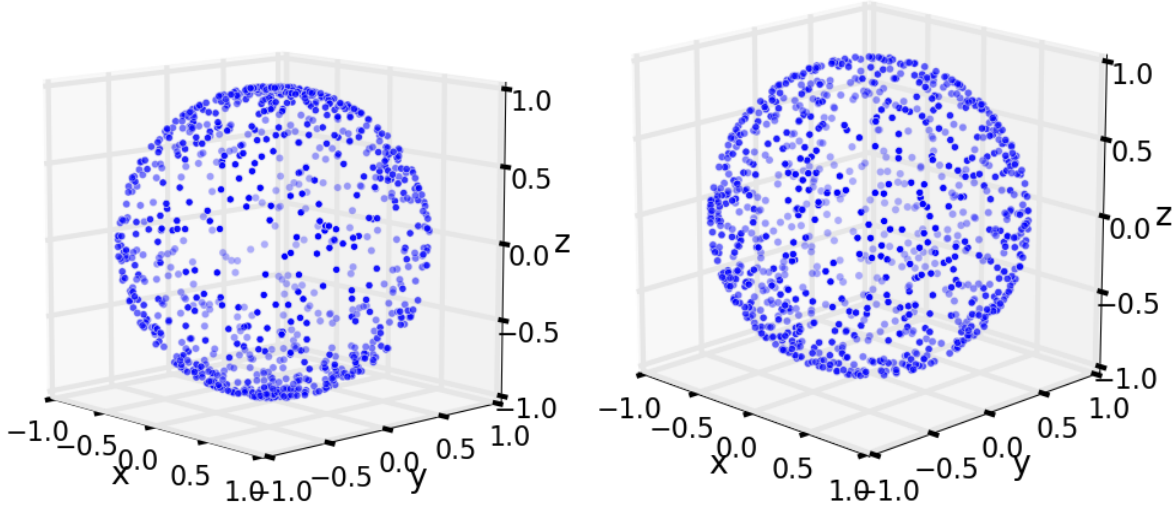


Figure D.1: *Left:* Illustration of a uniform sampling in angles ϕ and θ that doesn't give a uniform spherical distribution. *Right:* Illustration of a good spherical distribution.

$$F(F^{-1}(u)) = u \quad (\text{D.6})$$

$$\frac{1}{2} (1 - \cos(F^{-1}(u))) = u \quad (\text{D.7})$$

$$F^{-1}(u) = \arccos(1 - 2u). \quad (\text{D.8})$$

In other words: if u is a random variable drawn from a uniform distribution, then $\phi = \arccos(1 - 2u)$ follows a distribution necessary for a uniform spherical distribution. Similarly, $\theta = \frac{1}{2\pi}u$.

D.2 Power law distributions

Analogous to what was written in the previous section, one can produce a power law distribution from random numbers using the inverse transform sampling method:

$$\begin{aligned} f(E) &= A \cdot E^{-\gamma} \quad (\text{powerlaw}) \\ F(E) &= \int_{E_{min}}^E A \cdot E^{-\gamma} dE = u \quad (\text{inverse sampling, } u \text{ random number } [0,1]) \\ &= A \left[\frac{E^{-\gamma+1}}{-\gamma + 1} \right]_{E_{min}}^E \\ &= \frac{A}{-\gamma + 1} (E^{-\gamma+1} - E_{min}^{-\gamma+1}) \end{aligned} \quad (\text{D.9})$$

Because we know that $F(F^{-1}(u)) = u$, we can find an expression for $F^{-1}(u)$:

$$\begin{aligned} u &= \frac{A}{-\gamma + 1} \left((F^{-1}(u))^{-\gamma+1} - E_{min}^{-\gamma+1} \right) \\ &\Rightarrow \end{aligned} \quad (\text{D.10})$$

$$F^{-1}(u) = \left(\left(\frac{-\gamma + 1}{A} \cdot u \right) + E_{min}^{-\gamma+1} \right)^{1/(-\gamma+1)}$$

To find A , we use the property of a CDF:

$$F(E_{max}) = 1 \Rightarrow A = \frac{-\gamma + 1}{E_{max}^{-\gamma+1} - E_{min}^{-\gamma+1}}, \quad (\text{D.11})$$

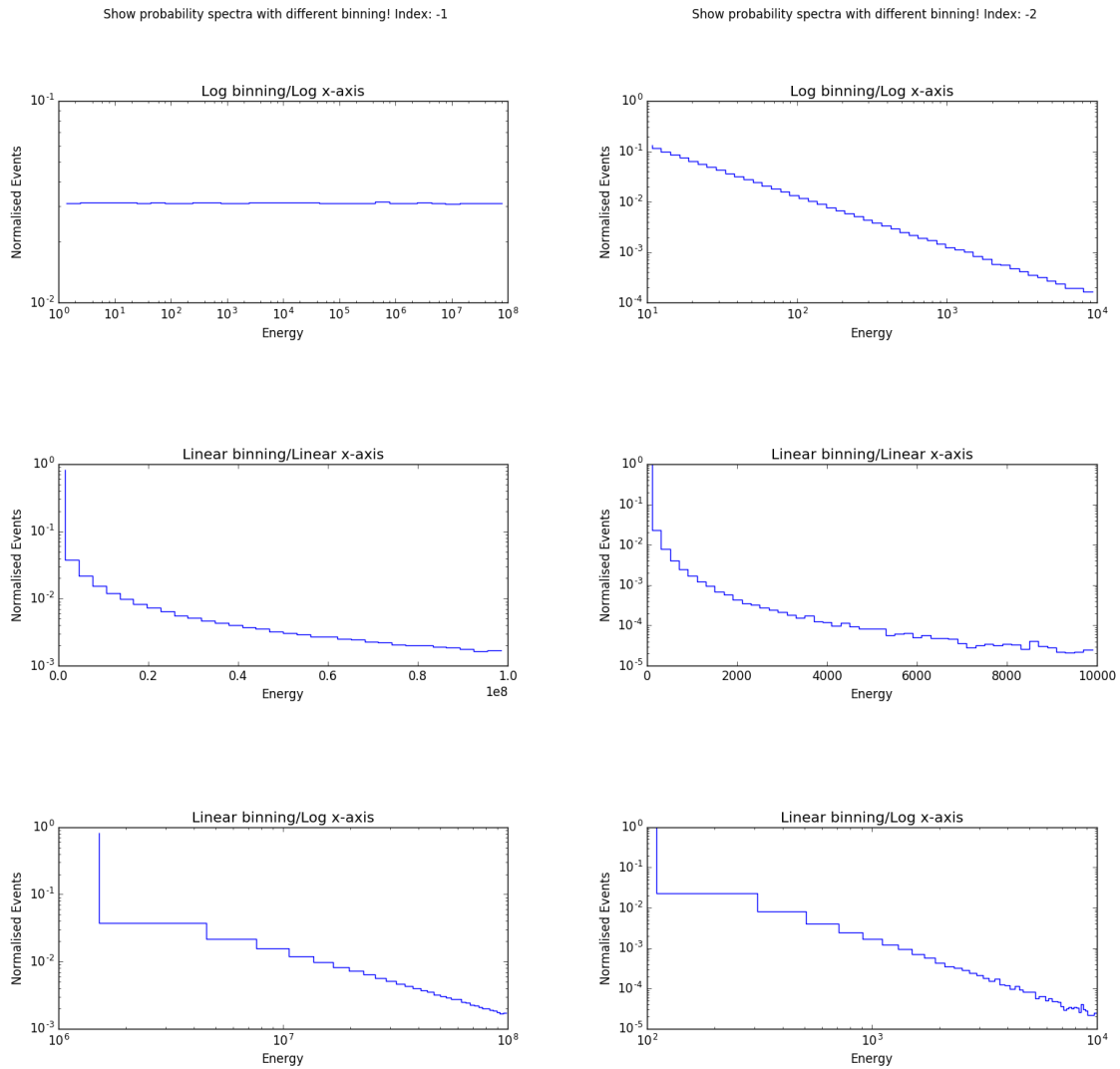


Figure D.2: *Left:* Histograms with different binnings showing the behavior of an energy spectrum with spectral index -1. *Right:* Histograms with different binnings showing the behavior of an energy spectrum with spectral index -2.

leading to

$$F^{-1}(u) = \left((1-u) \cdot E_{min}^{-\gamma+1} + u \cdot E_{max}^{-\gamma+1} \right)^{1/(-\gamma+1)}, \quad (\text{D.12})$$

which shows how one can draw a distribution in function of E following $f(E)$ with a uniform random number u .

For $\gamma = -1$, the computations are analogous and one can see that this will produce a uniform distribution in log space. This is shown in Fig. D.2.

$$\begin{aligned} E &= E_{min} \cdot 10^{u \cdot \log \frac{E_{max}}{E_{min}}} \\ &= 10^{u[\log E_{min}, \log E_{max}]} \end{aligned} \quad (\text{D.13})$$

In Fig. D.3 the signal reweighting is shown.

D.3 Angular distributions

As seen in Section D.1, the differential space angle $d\Omega$ is equal to

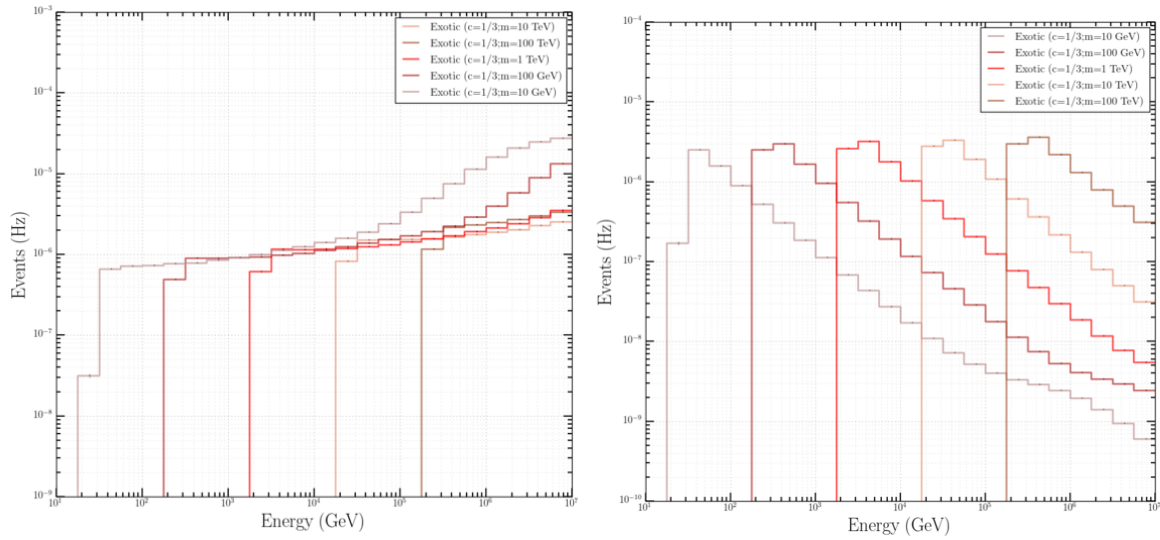


Figure D.3: *Left:* Spectrum of the signal before weighting following an E^{-1} spectrum. The rise in the rate in function of energy is due to the trigger efficiency that increases in function of energy. *Right:* Spectrum of the signal after reweighting to an energy spectrum of $E-2$.

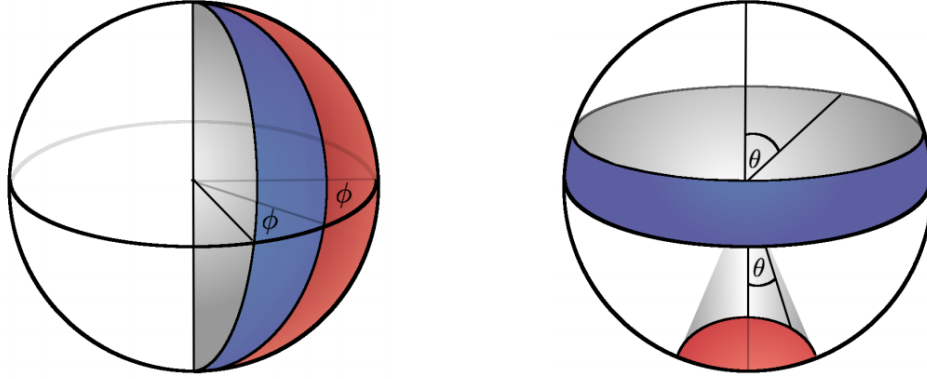


Figure D.4: Illustration of angle distributions in spherical coordinates. The blue and red surfaces are equal in size. The left figure clearly shows the surface to be proportional to the azimuth. The right figure shows how there is a non-trivial dependence on the zenith angle for equal partitions on the surface of a sphere.

$$d\Omega = \sin(\theta)d\theta d\phi. \quad (\text{D.14})$$

If one shows the distribution of ϕ and/or θ , then this is the same as showing partial integrations per bin. We find that

$$\Omega \propto \cos(\theta), \quad (\text{D.15})$$

or in other words: the space angle is proportional to the azimuth and the cosine of the zenith. An example is shown in Fig. D.4.

D.4 Weighting

A method that is often used in simulations is *weighting*. The simulated and expected differential flux of particles is often not the same, mainly due to two reasons:

- The flux has no uniform power law behavior. As can be seen in Fig. 3.2, there can be multiple “kinks” and changes in a spectrum. Instead of simulating the flux according to

one model, a general uniform flux is used and later reweighted to be able to fit to other models more easily.

- A steep power law indicates very few events at the highest energy bins. This means large CPU time would be necessary to simulate these events. As an example, let us assume two different fluxes

$$f_1 = A \cdot x^{-1}, \quad (\text{D.16})$$

$$f_2 = B \cdot x^{-2}, \quad (\text{D.17})$$

where $A = 10^3$ and $B = 10^4$, so the fluxes cross at a value of $x^{-1+2} = x = \frac{10^4}{10^3} = 10$. In the interval $x \in [10^3, 10^4]$, the number of events for f_1 is equal to 10^3 , whereas for f_2 this is equal to 9.

Simulating with harder spectra* leads to more statistics in high-energy bins.

The weights can be generally written down as

$$w = \frac{dN_{exp}}{dAd\Omega dEdt} \times \frac{dAd\Omega dE}{dN_{sim}}. \quad (\text{D.18})$$

A disadvantage of using weights is that certain events with a high weight are rare but can dominate or obscure the sample in the tails of certain distributions.

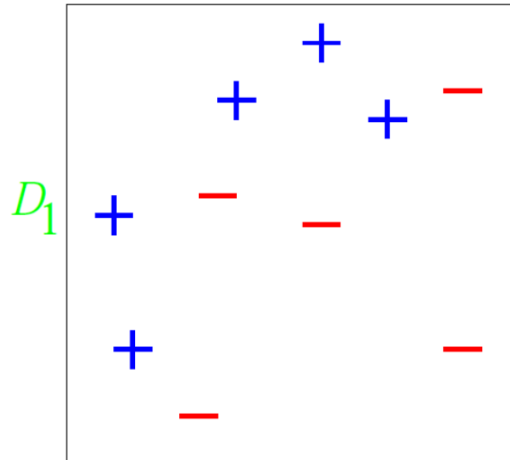
*Harder spectra equals to a lower gamma, since there will be more high-energy events.

E. AdaBoost: simple example

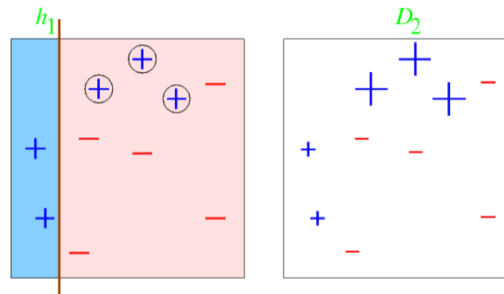
Consider a binary decision tree classification with 10 training examples. The illustrations below are 2D variable distributions.

We give each event an equal weight, making the weight distribution D_1 uniform. For this simple example, each of our classifiers will be an axis-parallel linear classifier (simple cut in one of the two variables).

Initial distribution

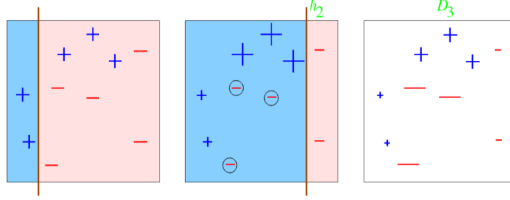


Round 1

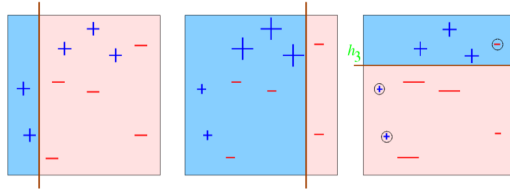


- Error rate of h_1 : $\epsilon_1 = 0.3$; weight of h_1 (see Eq. 7.25): $\alpha_1 = \frac{1}{2} \ln \left(\frac{1-\epsilon_1}{\epsilon_1} \right) = 0.42$

- An event that is misclassified gets a higher weight: weight multiplied with $\exp(\alpha_1)$
- An event that is correctly classified gets a lower weight: weight multiplied with $\exp(-\alpha_1)$

Round 2

- Error rate of h_1 : $\epsilon_1 = 0.21$; weight of h_2 (see Eq. 7.25): $\alpha_2 = \frac{1}{2} \ln \left(\frac{1-\epsilon_2}{\epsilon_2} \right) = 0.65$
- An event that is misclassified gets a higher weight: weight multiplied with $\exp(\alpha_2)$
- An event that is correctly classified gets a lower weight: weight multiplied with $\exp(-\alpha_2)$

Round 3

The error rate of h_1 : $\epsilon_1 = 0.21$; weight of h_2 (see Eq. 7.25): $\alpha_2 = \frac{1}{2} \ln \left(\frac{1-\epsilon_2}{\epsilon_2} \right) = 0.65$
Let us suppose to stop after this round, we now have a forest of 3 decision classifiers: h_1, h_2, h_3 .

Final step

The final classifier is a weighted linear combination of all the classifiers:

$$H_{\text{final}} = \text{sign} \left(0.42 \cdot h_1 + 0.65 \cdot h_2 + 0.92 \cdot h_3 \right)$$

= A 2x2 grid of points. The top-left cell is blue (+), top-right is red (-), bottom-left is blue (+), and bottom-right is red (-). This represents the weighted sum of the three classifiers from Round 3.

F. Resampling Methods

Resampling is a method used in statistical analyses and commonly refers to methods that extract information from a larger set by taking subsets and performing significance or validations tests. Two common examples are *bootstrapping* and *cross-validation* and are explained below.

F.1 Bootstrapping

The basic idea of bootstrapping is that we can draw conclusions from a certain sample in a larger, unknown, population by taking a subsample and performing inference about the sample from the subsample. The method assumes that the true probability distribution from a sample to a population can be reasonably estimated from an emperical probability distribution from a subsample to a sample.

Assume we have a total population P of size N_P and a measured sample N of size N_N , where

$$N_N < N_P \text{ and } N \subset P. \quad (\text{F.1})$$

From this sample, only one estimate of the mean can be computed. To get a sense of the variability we could assume a Gaussian or Poissonian probability, or what is done in this method: form a new subsample that is also of size N_N . This can only be done by *sampling with replacement* where the elements in the subsample can repeated. If N_N is sufficiently large, this will almost certainly result in subsamples that are different from the original sample. The mean can be computed from the new subsample and this process is repeated a large number of times (typically of the order of 1,000). The distribution of the means then indicates our confidence in the sample mean where a large variability assumes large uncertainties.

F.2 Cross-validation

Another example of a resampling method is cross-validation, sometimes called *rotation estimation* where one wants to estimate the predictive power of a model. From a sample, a subsample called the *training sample* is selected to train a model (e.g. a BDT). This model is then checked on another subsample called the *testing sample*. This allows to estimate how the model will generalize to another independent datasets. Training samples will often have a lower performance in parameter estimations from the testing sample than the training sample. In cross-validation one tries to get an estimate for this effect. An often uses cross-validation method is called *k-fold cross-validation*.

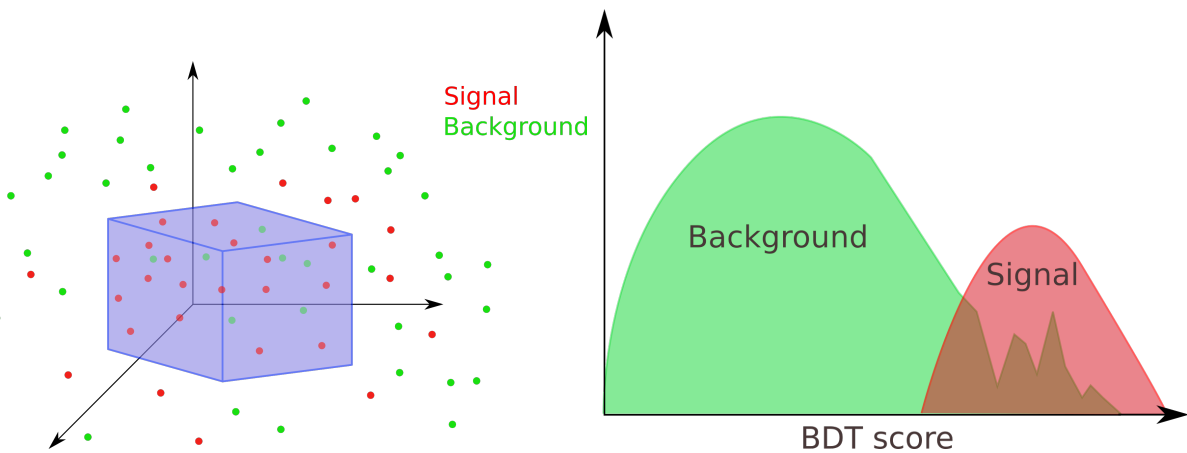


Figure F.1: Simplistic illustration of parameter space that originates from one branch in one BDT. The axis represent physical parameters that are used in the BDT. The blue box illustrates the cuts that are placed on the parameters. The BDT algorithm converts the survival probability of an event regarding these cuts into a score. Limited statistics for the background events are represented by a discontinuous tail.

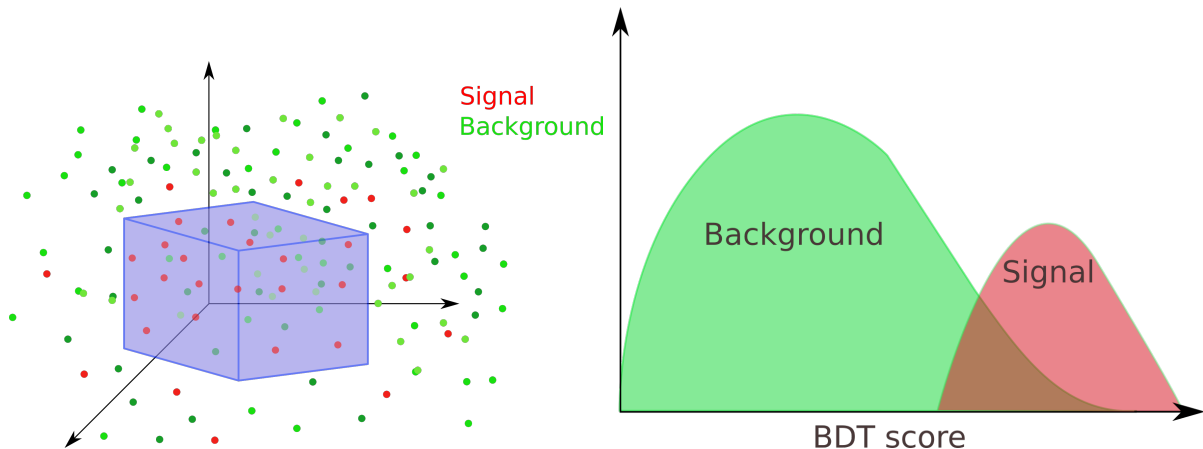


Figure F.2: Simplistic illustration of parameter space that originates from one branch in one BDT. Resampling the background (different green point) results in more statistics in the tail.

In this method, one iterates the procedure of selecting a training sample and a testing sample k times. If the total size of the samples set is N_N , the testing samples will have a size of N_N/k . As we have k iterations, the subsamples can be chosen without replacement and are unique each time. At each iteration, the training sample will have a size of $N_N - \frac{N_N}{k} = N_N \cdot \frac{k-1}{k}$. The k results can then be averaged to produce a single estimation.

Pull-validation is another example of a resampling method that is explained in more detail in Section 8.4.2. Illustratively it can be visualized as in Figs. F.1 and F.2.

G. Additional BDT Checks

As explained in Section 7.6, it is important to perform some checks to see if a BDT is performing normally. A first check is done to see if the distribution of the training and testing samples show significant differences. This is shown in Fig. G.1 and explained in more detail in Section 7.6.4.

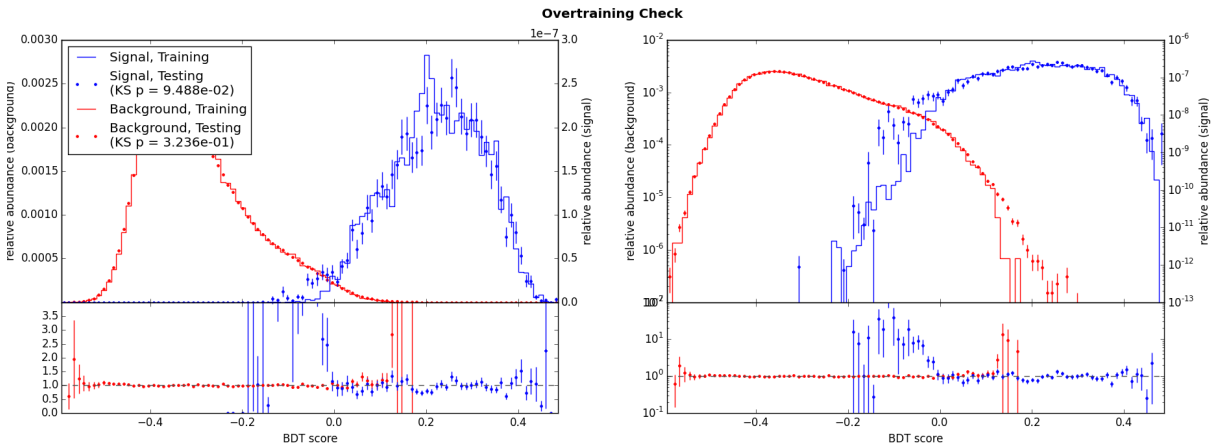


Figure G.1: No significant overtraining seems to be present in signal and background. The signal used here is an SMP of charge $\frac{1}{2}$ and mass 100 GeV.

The correlation between the 17 variables that were used in the BDT is shown in Fig. G.2. These variables were selected with the mRMR feature, which shows an excellent performance since there are no significant correlations in both signal and background visible.

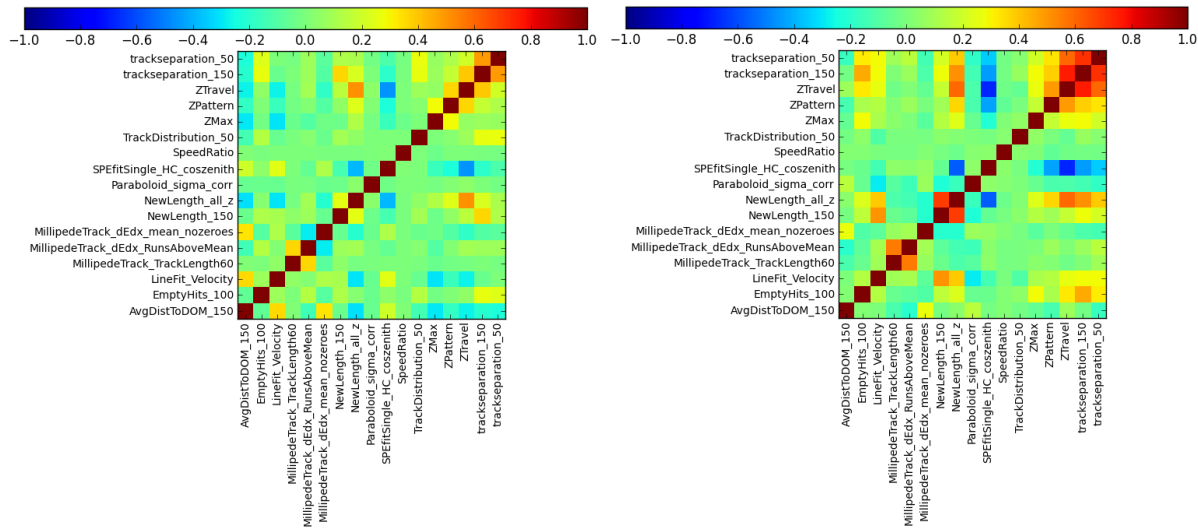


Figure G.2: Here we see the correlation between the variables that are used in the BDT. There is no significant correlation in *both* signal and background, making these variables appropriate to use.

H. Data Events at Final Level

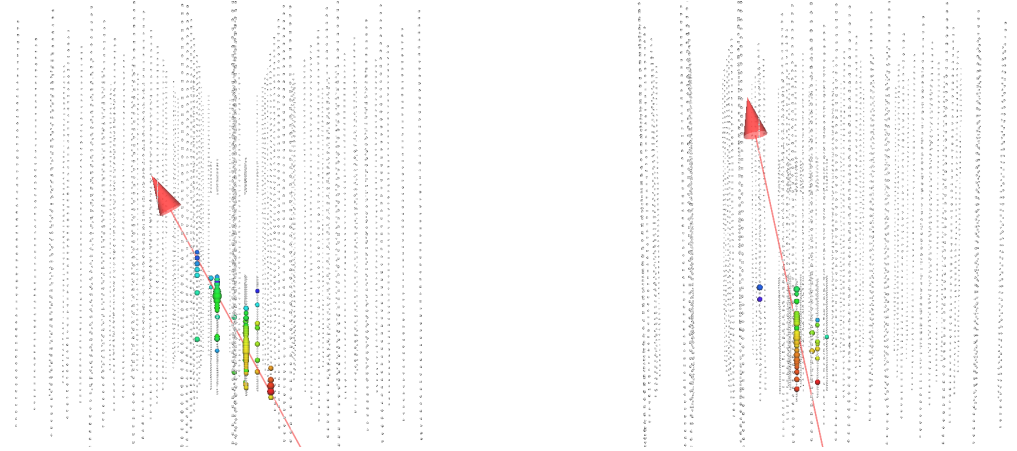


Figure H.1: Event viewers of an event that survive the SMP with mass 10 TeV and charge 1/2 selection. *Left (data)*: Short and bright up-going track corresponds to μ from an atmospheric ν_μ that stopped shortly after leaving DeepCore. *Right*: Simulated atmospheric ν_μ event that strongly resembles this data event.

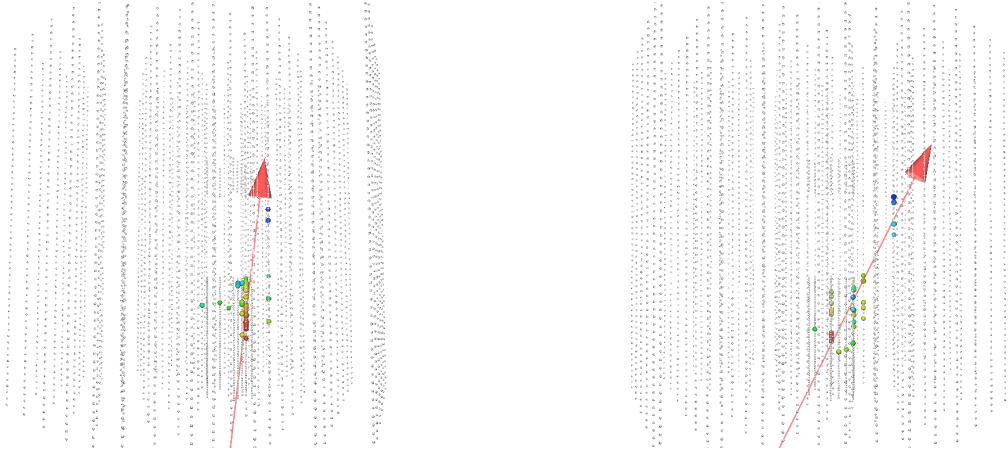


Figure H.2: Event viewers of an event that survive the SMP with mass 10 TeV and charge 1/2 selection. *Left (data)*: Corresponds to an up-going μ from atmospheric ν_μ that either starts or “corridors” in between strings and skims DeepCore. After leaving DeepCore it only passes close to one string, giving the two hits. *Right*: Simulated atmospheric ν_μ event that strongly resembles this data event.



Figure H.3: Event viewers of an event that survive the SMP with mass 10 GeV and charge 1/3 selection. *Left (data)*: Corresponds to a horizontal μ from atmospheric ν_μ that passes close to one string in IceCube and stops in DeepCore where more light is recorded. *Right*: Simulated atmospheric ν_μ event that strongly resembles this data event.

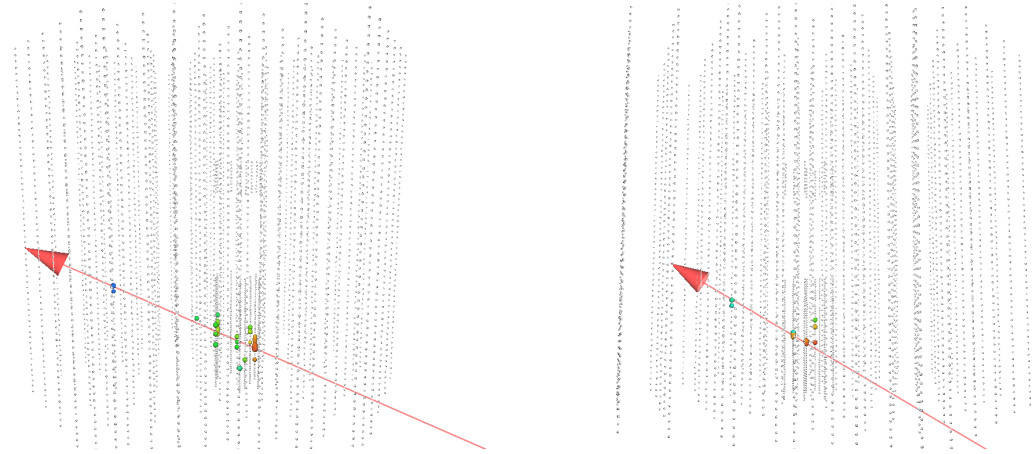


Figure H.4: *Left:* Typical SMP of 100 GeV and charge 1/2 that survives the final selection. *Right:* Typical SMP of 100 GeV and charge 1/3 that survives the final selection. Note that there is a lot less light produces compared to particles with higher charges.

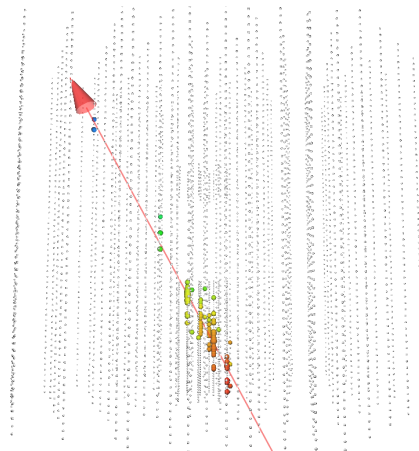


Figure H.5: Typical SMP of 100 GeV and charge 1/3 that survives the final selection. Note that there is a lot more light produces compared to particles with lower charges.

10. Some useful things for LaTeX

10.1 Definitions

This is an example of a definition. A definition could be mathematical or it could define a concept.

Definition 10.1.1 — Definition name. Given a vector space E , a norm on E is an application, denoted $\|\cdot\|$, E in $\mathbb{R}^+ = [0, +\infty[$ such that:

$$\|\mathbf{x}\| = 0 \Rightarrow \mathbf{x} = \mathbf{0} \quad (10.1)$$

$$\|\lambda\mathbf{x}\| = |\lambda| \cdot \|\mathbf{x}\| \quad (10.2)$$

$$\|\mathbf{x} + \mathbf{y}\| \leq \|\mathbf{x}\| + \|\mathbf{y}\| \quad (10.3)$$

10.2 Remarks

This is an example of a remark.



The concepts presented here are now in conventional employment in mathematics. Vector spaces are taken over the field $\mathbb{K} = \mathbb{R}$, however, established properties are easily extended to $\mathbb{K} = \mathbb{C}$.

10.3 Corollaries

This is an example of a corollary.

Corollary 10.3.1 — Corollary name. The concepts presented here are now in conventional employment in mathematics. Vector spaces are taken over the field $\mathbb{K} = \mathbb{R}$, however, established properties are easily extended to $\mathbb{K} = \mathbb{C}$.

10.4 Propositions

This is an example of propositions.

10.4.1 Several equations

Proposition 10.4.1 — Proposition name. It has the properties:

$$|||\mathbf{x}|| - ||\mathbf{y}||| \leq ||\mathbf{x} - \mathbf{y}|| \quad (10.4)$$

$$\left\| \sum_{i=1}^n \mathbf{x}_i \right\| \leq \sum_{i=1}^n \|\mathbf{x}_i\| \quad \text{where } n \text{ is a finite integer} \quad (10.5)$$

10.4.2 Single Line

Proposition 10.4.2 Let $f, g \in L^2(G)$; if $\forall \varphi \in \mathcal{D}(G)$, $(f, \varphi)_0 = (g, \varphi)_0$ then $f = g$.

10.5 Examples

This is an example of examples.

10.5.1 Equation and Text

■ **Example 10.1** Let $G = \{x \in \mathbb{R}^2 : |x| < 3\}$ and denoted by: $x^0 = (1, 1)$; consider the function:

$$f(x) = \begin{cases} e^{|x|} & \text{si } |x - x^0| \leq 1/2 \\ 0 & \text{si } |x - x^0| > 1/2 \end{cases} \quad (10.6)$$

The function f has bounded support, we can take $A = \{x \in \mathbb{R}^2 : |x - x^0| \leq 1/2 + \epsilon\}$ for all $\epsilon \in]0; 5/2 - \sqrt{2}[$. ■

10.5.2 Paragraph of Text

■ **Example 10.2 — Example name.** Nam dui ligula, fringilla a, euismod sodales, sollicitudin vel, wisi. Morbi auctor lorem non justo. Nam lacus libero, pretium at, lobortis vitae, ultricies et, tellus. Donec aliquet, tortor sed accumsan bibendum, erat ligula aliquet magna, vitae ornare odio metus a mi. Morbi ac orci et nisl hendrerit mollis. Suspendisse ut massa. Cras nec ante. Pellentesque a nulla. Cum sociis natoque penatibus et magnis dis parturient montes, nascetur ridiculus mus. Aliquam tincidunt urna. Nulla ullamcorper vestibulum turpis. Pellentesque cursus luctus mauris. ■

10.6 Exercises

This is an example of an exercise.

Exercise 10.1 This is a good place to ask a question to test learning progress or further cement ideas into students' minds. ■

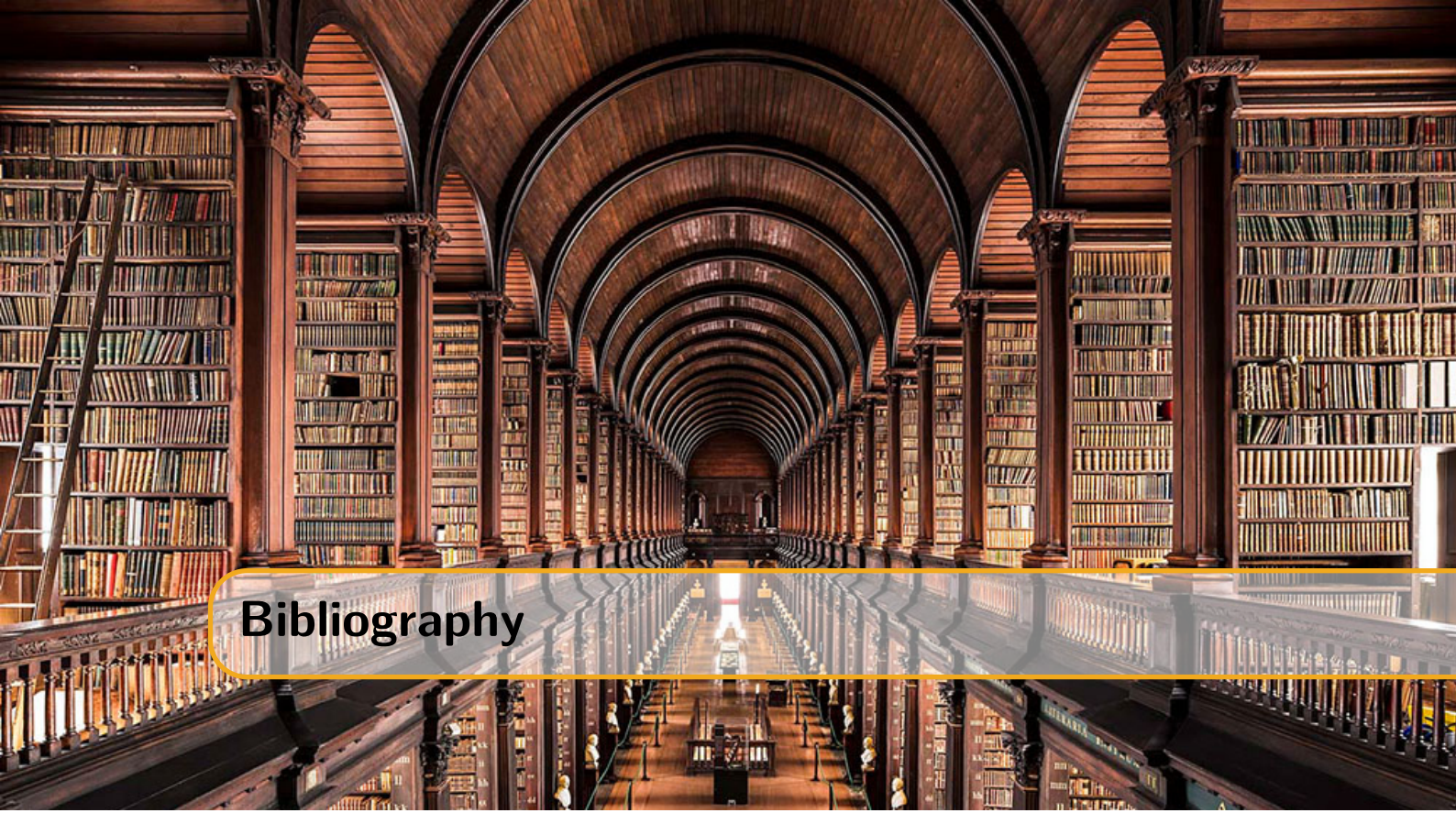
10.7 Problems

Problem 10.1 What is the average airspeed velocity of an unladen swallow?

10.8 Vocabulary

Define a word to improve a students' vocabulary.

Vocabulary 10.1 — Word. Definition of word.



Bibliography

- [1] B. Povh et al. *Particles and nuclei: An Introduction to the physical concepts*. 1995. DOI: 10.1007/3-540-36684-9 (cited on page 13).
- [2] Michael E. Peskin and Daniel V. Schroeder. *An Introduction to quantum field theory*. Reading, USA: Addison-Wesley, 1995. ISBN: 9780201503975, 0201503972. URL: <http://www.slac.stanford.edu/~mpeskin/QFT.html> (cited on page 13).
- [3] M. Tanabashi et al. “Review of Particle Physics”. In: *Phys. Rev. D* 98 (2018), page 030001 (cited on page 13).
- [4] Alessandro Bettini. *Introduction to elementary particle physics*. 2008. ISBN: 9780521880213. URL: <http://www.cambridge.org/catalogue/catalogue.asp?isbn=9780521880213> (cited on page 13).
- [5] CERN. URL: <https://home.cern/about/physics/standard-model> (cited on page 14).
- [6] Arthur B. McDonald. “Nobel Lecture: The Sudbury Neutrino Observatory: Observation of flavor change for solar neutrinos”. In: *Rev. Mod. Phys.* 88 (3 July 2016), page 030502. DOI: 10.1103/RevModPhys.88.030502. URL: <https://link.aps.org/doi/10.1103/RevModPhys.88.030502> (cited on page 15).
- [7] CMS. URL: <http://cms.web.cern.ch/news/jets-cms-and-determination-their-energy-scale> (cited on page 15).
- [8] A. Kircher. *Athanassii Kircherii... Magnes, sive De arte magnetica opus tripartitum...* sumptibus H. Scheus, 1641. URL: <https://books.google.be/books?id=1aZ3FcTAYdUC> (cited on page 16).
- [9] G. Farmelo. *The Strangest Man: The Hidden Life of Paul Dirac, Mystic of the Atom*. Basic Books, 2009. ISBN: 9780465019922. URL: <https://books.google.be/books?id=q sodmIGD0fMC> (cited on page 17).
- [10] F. Mandl and G. Shaw. *Quantum Field Theory*. Wiley, 2013. ISBN: 9781118716656. URL: <https://books.google.be/books?id=jTBzQfctvHAC> (cited on page 18).
- [11] Flip Tanedo. URL: <https://www.quantumdiaries.org/2012/02/14/why-do-we-expect-a-higgs-boson-part-ii-unitarization-of-vector-boson-scattering/> (cited on page 21).

- [12] S. L. Glashow, J. Iliopoulos, and L. Maiani. “Weak Interactions with Lepton-Hadron Symmetry”. In: *Phys. Rev.* D2 (1970), pages 1285–1292. DOI: 10.1103/PhysRevD.2.1285 (cited on page 25).
- [13] J. H. Christenson et al. “Evidence for the 2π Decay of the K20 Meson”. In: *Physical Review Letters* 13 (July 1964), pages 138–140. DOI: 10.1103/PhysRevLett.13.138 (cited on page 25).
- [14] Ziro Maki, Masami Nakagawa, and Shoichi Sakata. “Remarks on the Unified Model of Elementary Particles”. In: *Progress of Theoretical Physics* 28.5 (1962), pages 870–880. DOI: 10.1143/PTP.28.870. eprint: /oup/backfile/content_public/journal/ptp/28/5/10.1143/ptp.28.870/2/28-5-870.pdf. URL: <http://dx.doi.org/10.1143/PTP.28.870> (cited on page 25).
- [15] Unknown. *Young interference*. <https://www.shmoop.com/optics/young-double-slit.html>. [Online; accessed August 2018]. 2018 (cited on page 27).
- [16] Antoine Weis and Robert Wynands. “Three Demonstration Experiments on the Wave and Particle Nature of Light”. In: 1 (June 2003) (cited on pages 26, 27).
- [17] C. Davisson and L. H. Germer. “Diffraction of Electrons by a Crystal of Nickel”. In: *Phys. Rev.* 30 (1927), pages 705–740. DOI: 10.1103/PhysRev.30.705 (cited on page 26).
- [18] G P. Thomson and Reid AA. “Diffraction of Cathode Rays by a Thin Film”. In: 119 (Jan. 1927), pages 890–890 (cited on page 26).
- [19] Claus Jönsson. “Elektroneninterferenzen an mehreren künstlich hergestellten Feinspalten”. In: *Zeitschrift für Physik* 161.4 (Aug. 1961), pages 454–474. ISSN: 0044-3328. DOI: 10.1007/BF01342460. URL: <https://doi.org/10.1007/BF01342460> (cited on page 26).
- [20] P G Merli, G F Missiroli, and G Pozzi. “Electron interferometry with the Elmiskop 101 electron microscope”. In: *Journal of Physics E: Scientific Instruments* 7.9 (1974), page 729. URL: <http://stacks.iop.org/0022-3735/7/i=9/a=016> (cited on page 26).
- [21] C. D. Anderson. “The Positive Electron”. In: *Phys. Rev.* 43 (1933), pages 491–494. DOI: 10.1103/PhysRev.43.491 (cited on page 26).
- [22] Paul A. M. Dirac. “The quantum theory of the electron”. In: *Proc. Roy. Soc. Lond.* A117 (1928), pages 610–624. DOI: 10.1098/rspa.1928.0023 (cited on page 26).
- [23] C. M. G. Lattes et al. “PROCESSES INVOLVING CHARGED MESONS”. In: *Nature* 159 (1947). [,42(1947)], pages 694–697. DOI: 10.1038/159694a0 (cited on page 26).
- [24] S. H. Neddermeyer and C. D. Anderson. “Note on the Nature of Cosmic Ray Particles”. In: *Phys. Rev.* 51 (1937), pages 884–886. DOI: 10.1103/PhysRev.51.884 (cited on page 26).
- [25] S. W. Herb et al. “Observation of a Dimuon Resonance at 9.5-GeV in 400-GeV Proton-Nucleus Collisions”. In: *Phys. Rev. Lett.* 39 (1977), pages 252–255. DOI: 10.1103/PhysRevLett.39.252 (cited on page 27).
- [26] F. Abe et al. “Observation of top quark production in $\bar{p}p$ collisions”. In: *Phys. Rev. Lett.* 74 (1995), pages 2626–2631. DOI: 10.1103/PhysRevLett.74.2626. arXiv: [hep-ex/9503002](https://arxiv.org/abs/hep-ex/9503002) [hep-ex] (cited on page 27).
- [27] D. P. Barber et al. “Discovery of Three Jet Events and a Test of Quantum Chromodynamics at PETRA Energies”. In: *Phys. Rev. Lett.* 43 (1979), page 830. DOI: 10.1103/PhysRevLett.43.830 (cited on page 27).
- [28] S. Schael et al. “Precision electroweak measurements on the Z resonance”. In: *Phys. Rept.* 427 (2006), pages 257–454. DOI: 10.1016/j.physrep.2005.12.006. arXiv: [hep-ex/0509008](https://arxiv.org/abs/hep-ex/0509008) [hep-ex] (cited on page 27).
- [29] Sabine Riemann. “Precision electroweak physics at high energies”. In: *Rept. Prog. Phys.* 73 (2010), page 126201. DOI: 10.1088/0034-4885/73/12/126201 (cited on page 27).

- [30] Kenji Abe et al. “A High precision measurement of the left-right Z boson cross-section asymmetry”. In: *Phys. Rev. Lett.* 84 (2000), pages 5945–5949. DOI: 10.1103/PhysRevLett.84.5945. arXiv: hep-ex/0004026 [hep-ex] (cited on page 27).
- [31] Koya Abe et al. “First direct measurement of the parity violating coupling of the Z₀ to the s quark”. In: *Phys. Rev. Lett.* 85 (2000), pages 5059–5063. DOI: 10.1103/PhysRevLett.85.5059. arXiv: hep-ex/0006019 [hep-ex] (cited on page 27).
- [32] Koya Abe et al. “An Improved direct measurement of leptonic coupling asymmetries with polarized Z bosons”. In: *Phys. Rev. Lett.* 86 (2001), pages 1162–1166. DOI: 10.1103/PhysRevLett.86.1162. arXiv: hep-ex/0010015 [hep-ex] (cited on page 27).
- [33] K. Abe et al. “First measurement of the left-right charge asymmetry in hadronic Z boson decays and a new determination of sin**2 theta(W)(eff)”. In: *Phys. Rev. Lett.* 78 (1997), pages 17–21. DOI: 10.1103/PhysRevLett.78.17. arXiv: hep-ex/9609019 [hep-ex] (cited on page 27).
- [34] Timo Antero Aaltonen et al. “Combination of CDF and D0 W-Boson Mass Measurements”. In: *Phys. Rev.* D88.5 (2013), page 052018. DOI: 10.1103/PhysRevD.88.052018. arXiv: 1307.7627 [hep-ex] (cited on page 27).
- [35] “Combination of CDF and D0 Results on the Width of the W boson”. In: (2010). arXiv: 1003.2826 [hep-ex] (cited on page 27).
- [36] Morad Aaboud et al. “Measurement of the W-boson mass in pp collisions at $\sqrt{s} = 7$ TeV with the ATLAS detector”. In: *Eur. Phys. J.* C78.2 (2018), page 110. DOI: 10.1140/epjc/s10052-017-5475-4. arXiv: 1701.07240 [hep-ex] (cited on page 27).
- [37] ATLAS. URL: cds.cern.ch/record/2285809/files/ATLAS-CONF-2017-071.pdf (cited on page 27).
- [38] CMS. URL: cds.cern.ch/record/2235162/files/TOP-15-012-pas.pdf (cited on page 27).
- [39] CMS. URL: cds.cern.ch/record/2284594/files/TOP-17-007-pas.pdf (cited on page 27).
- [40] PDG. URL: <http://pdg.lbl.gov/2018/reviews/rpp2018-rev-standard-model.pdf> (cited on pages 28, 45, 46, 58, 61).
- [41] P. A. R. Ade et al. “Planck 2015 results. XIII. Cosmological parameters”. In: *Astron. Astrophys.* 594 (2016), A13. DOI: 10.1051/0004-6361/201525830. arXiv: 1502.01589 [astro-ph.CO] (cited on page 29).
- [42] Edvige Corbelli and Paolo Salucci. “The Extended Rotation Curve and the Dark Matter Halo of M33”. In: *Mon. Not. Roy. Astron. Soc.* 311 (2000), pages 441–447. DOI: 10.1046/j.1365-8711.2000.03075.x. arXiv: astro-ph/9909252 [astro-ph] (cited on page 29).
- [43] S. M. Faber and R. E. Jackson. “Velocity dispersions and mass to light ratios for elliptical galaxies”. In: *Astrophys. J.* 204 (1976), page 668. DOI: 10.1086/154215 (cited on page 29).
- [44] Steven W. Allen, August E. Evrard, and Adam B. Mantz. “Cosmological Parameters from Observations of Galaxy Clusters”. In: *Ann. Rev. Astron. Astrophys.* 49 (2011), pages 409–470. DOI: 10.1146/annurev-astro-081710-102514. arXiv: 1103.4829 [astro-ph.CO] (cited on page 29).
- [45] Priyamvada Natarajan et al. “Mapping substructure in the HST Frontier Fields cluster lenses and in cosmological simulations”. In: *Mon. Not. Roy. Astron. Soc.* 468.2 (2017), pages 1962–1980. DOI: 10.1093/mnras/stw3385. arXiv: 1702.04348 [astro-ph.GA] (cited on page 29).
- [46] Edwin Hubble. “A relation between distance and radial velocity among extra-galactic nebulae”. In: *Proc. Nat. Acad. Sci.* 15 (1929), pages 168–173. DOI: 10.1073/pnas.15.3.168 (cited on page 29).

- [47] John F. Donoghue. “The effective field theory treatment of quantum gravity”. In: *AIP Conf. Proc.* 1483 (2012), pages 73–94. DOI: 10.1063/1.4756964. arXiv: 1209.3511 [gr-qc] (cited on page 29).
- [48] J. L. Holzbauer. “The Muon g-2 Experiment Overview and Status”. In: *PoS NuFact2017* (2018), page 116. DOI: 10.22323/1.295.0116. arXiv: 1712.05980 [hep-ex] (cited on page 29).
- [49] Alexandre Deur, Stanley J. Brodsky, and Guy F. de Teramond. “The QCD Running Coupling”. In: *Prog. Part. Nucl. Phys.* 90 (2016), pages 1–74. DOI: 10.1016/j.ppnp.2016.04.003. arXiv: 1604.08082 [hep-ph] (cited on page 31).
- [50] nobel2004. URL: <https://www.nobelprize.org/prizes/physics/2004/popular-information/> (cited on page 32).
- [51] Xiao-Gang He, Girish C. Joshi, and B. H. McKellar. “The Quantization of the Electric Charge in Gauge Theories”. In: *Europhys. Lett.* 10 (1989), page 709. DOI: 10.1209/0295-5075/10/8/002 (cited on pages 32, 35).
- [52] Hong-Wei Yu. “SU(8) GUT MODELS WITH STABLE PROTON, N ANTI-N OSCILLATIONS, FRACTIONAL CHARGES AND LOW MASS MONOPOLES”. In: *Phys. Lett.* 142B (1984), pages 42–46. DOI: 10.1016/0370-2693(84)91132-8 (cited on pages 32, 36).
- [53] Stephen M. Barr, D. B. Reiss, and A. Zee. “Fractional Charges, Monopoles and Peculiar Photons”. In: *Phys. Rev. Lett.* 50 (1983), page 317. DOI: 10.1103/PhysRevLett.50.317 (cited on page 36).
- [54] P. H. Frampton and T. W. Kephart. “Fractionally Charged Particles as Evidence for Supersymmetry”. In: *Phys. Rev. Lett.* 49 (1982), page 1310. DOI: 10.1103/PhysRevLett.49.1310 (cited on page 36).
- [55] Katsuji Yamamoto. “Fractionally Charged Leptons in the SO(14) GUT”. In: *Phys. Lett.* 120B (1983), pages 157–160. DOI: 10.1016/0370-2693(83)90643-3 (cited on page 36).
- [56] Fang-xiao Dong et al. “Fractional Charges, Monopoles and Peculiar Photons in SO(18) GUT Models”. In: *Phys. Lett.* 129B (1983), pages 405–410. DOI: 10.1016/0370-2693(83)90129-6 (cited on page 36).
- [57] Xiang-Dong Jiang and Xian-Jian Zhou. “SO(10) X SO(8) MODEL WITH FRACTIONAL CHARGES, MONOPOLES AND PECULIAR PHOTONS. (IN CHINESE)”. In: *HEPNP* 9 (1985), pages 421–429 (cited on page 36).
- [58] Borut Bajc et al. “Threshold corrections to dimension-six proton decay operators in non-minimal SUSY SU (5) GUTs”. In: *Nucl. Phys.* B910 (2016), pages 1–22. DOI: 10.1016/j.nuclphysb.2016.06.017. arXiv: 1603.03568 [hep-ph] (cited on page 36).
- [59] H. Nishino et al. “Search for Proton Decay via $p \rightarrow e^+ \pi^0$ and $p \rightarrow \mu^+ \pi^0$ in a Large Water Cherenkov Detector”. In: *Phys. Rev. Lett.* 102 (2009), page 141801. DOI: 10.1103/PhysRevLett.102.141801. arXiv: 0903.0676 [hep-ex] (cited on page 36).
- [60] Xiao-Gang Wen and Edward Witten. “Electric and Magnetic Charges in Superstring Models”. In: *Nucl. Phys.* B261 (1985), pages 651–677. DOI: 10.1016/0550-3213(85)90592-9 (cited on page 36).
- [61] Ignatios Antoniadis and K. Benakli. “Fractionally charged particles and supersymmetry breaking in 4-D strings”. In: *Phys. Lett.* B295 (1992). [Erratum: *Phys. Lett.* B407,449(1997)], pages 219–224. DOI: 10.1016/S0370-2693(97)00755-7, 10.1016/0370-2693(92)91557-P. arXiv: hep-th/9209020 [hep-th] (cited on page 36).
- [62] Gregory G. Athanasiou et al. “Remarks on Wilson Lines, Modular Invariance and Possible String Relics in Calabi-yau Compactifications”. In: *Phys. Lett.* B214 (1988), pages 55–62. DOI: 10.1016/0370-2693(88)90451-0 (cited on page 36).
- [63] Bob Holdom. “Two U(1)’s and Epsilon Charge Shifts”. In: *Phys. Lett.* 166B (1986), pages 196–198. DOI: 10.1016/0370-2693(86)91377-8 (cited on page 36).

- [64] Eder Izaguirre and Itay Yavin. “New window to millicharged particles at the LHC”. In: *Phys. Rev.* D92.3 (2015), page 035014. DOI: 10.1103/PhysRevD.92.035014. arXiv: 1506.04760 [hep-ph] (cited on page 36).
- [65] David E. Brahm and Lawrence J. Hall. “U(1)-prime DARK MATTER”. In: *Phys. Rev.* D41 (1990), page 1067. DOI: 10.1103/PhysRevD.41.1067 (cited on page 36).
- [66] C. Boehm and Pierre Fayet. “Scalar dark matter candidates”. In: *Nucl. Phys.* B683 (2004), pages 219–263. DOI: 10.1016/j.nuclphysb.2004.01.015. arXiv: hep-ph/0305261 [hep-ph] (cited on page 36).
- [67] Maxim Pospelov, Adam Ritz, and Mikhail B. Voloshin. “Secluded WIMP Dark Matter”. In: *Phys. Lett.* B662 (2008), pages 53–61. DOI: 10.1016/j.physletb.2008.02.052. arXiv: 0711.4866 [hep-ph] (cited on page 36).
- [68] James D. Bjorken et al. “New Fixed-Target Experiments to Search for Dark Gauge Forces”. In: *Phys. Rev.* D80 (2009), page 075018. DOI: 10.1103/PhysRevD.80.075018. arXiv: 0906.0580 [hep-ph] (cited on page 36).
- [69] Gabriel Magill et al. “Millicharged particles in neutrino experiments”. In: (2018). arXiv: 1806.03310 [hep-ph] (cited on page 36).
- [70] R. Acciari et al. “Long-Baseline Neutrino Facility (LBNF) and Deep Underground Neutrino Experiment (DUNE)”. In: (2015). arXiv: 1512.06148 [physics.ins-det] (cited on page 36).
- [71] M. Anelli et al. “A facility to Search for Hidden Particles (SHiP) at the CERN SPS”. In: (2015). arXiv: 1504.04956 [physics.ins-det] (cited on page 36).
- [72] Marco Battaglieri et al. “US Cosmic Visions: New Ideas in Dark Matter 2017: Community Report”. In: (2017). arXiv: 1707.04591 [hep-ph] (cited on page 36).
- [73] S. I. Alvis et al. “First Limit on the Direct Detection of Lightly Ionizing Particles for Electric Charge as Low as e/1000 with the Majorana Demonstrator”. In: *Phys. Rev. Lett.* 120.21 (2018), page 211804. DOI: 10.1103/PhysRevLett.120.211804. arXiv: 1801.10145 [hep-ex] (cited on page 36).
- [74] L. Lyons. “Quark Search Experiments at Accelerators and in Cosmic Rays”. In: *Phys. Rept.* 129 (1985), page 225. DOI: 10.1016/0370-1573(85)90011-0 (cited on page 37).
- [75] J. J. Aubert et al. “A Search for Free Quarks in Deep Inelastic Muon Scattering”. In: *Phys. Lett.* 133B (1983), page 461. DOI: 10.1016/0370-2693(83)90828-6 (cited on page 37).
- [76] A. E. Bondar et al. “SEARCH FOR LIGHT PARTICLES WITH CHARGE 2/3 IN e+ e- ANNIHILATION”. In: *JETP Lett.* 40 (1984). [*Pisma Zh. Eksp. Teor. Fiz.* 40, 440 (1984)], pages 1265–1268 (cited on page 37).
- [77] H. Aihara et al. “Search for $q = 2/3e$ and $q = 1/3e$ particles produced in e^+e^- annihilations”. In: *Phys. Rev. Lett.* 52 (1984), page 2332. DOI: 10.1103/PhysRevLett.52.2332 (cited on page 37).
- [78] G. Abbiendi et al. “Search for stable and longlived massive charged particles in e+ e- collisions at $s^{**}(1/2) = 130\text{-GeV}$ to 209-GeV”. In: *Phys. Lett.* B572 (2003), pages 8–20. DOI: 10.1016/S0370-2693(03)00639-7. arXiv: hep-ex/0305031 [hep-ex] (cited on page 37).
- [79] P. Abreu et al. “Search for stable heavy charged particles in e+ e- collisions at $s^{**}(1/2) = 130\text{-GeV}$ to 136-GeV, 161-GeV and 172-GeV”. In: *Phys. Lett.* B396 (1997), pages 315–326. DOI: 10.1016/S0370-2693(97)00152-4 (cited on page 37).
- [80] R. Akers et al. “Search for heavy charged particles and for particles with anomalous charge in e^+e^- collisions at LEP”. In: *Z. Phys.* C67 (1995), pages 203–212. DOI: 10.1007/BF01571281 (cited on page 37).

- [81] D. Buskulic et al. “Search for particles with unexpected mass and charge in Z decays”. In: *Phys. Lett.* B303 (1993), pages 198–208. DOI: 10.1016/0370-2693(93)90066-Q (cited on page 37).
- [82] M. Banner et al. “A New Search for Relativistic Particles With Fractional Electric Charge at the CERN $p\bar{p}$ Collider”. In: *Phys. Lett.* 156B (1985), pages 129–133. DOI: 10.1016/0370-2693(85)91368-1 (cited on page 38).
- [83] F. Abe et al. “Limits on the production of massive stable charged particles”. In: *Phys. Rev.* D46 (1992), R1889–R1894. DOI: 10.1103/PhysRevD.46.R1889 (cited on page 38).
- [84] D. Acosta et al. “Search for long-lived charged massive particles in $\bar{p}p$ collisions at $\sqrt{s} = 1.8$ TeV”. In: *Phys. Rev. Lett.* 90 (2003), page 131801. DOI: 10.1103/PhysRevLett.90.131801. arXiv: hep-ex/0211064 [hep-ex] (cited on page 38).
- [85] Serguei Chatrchyan et al. “Search for fractionally charged particles in pp collisions at $\sqrt{s} = 7$ TeV”. In: *Phys. Rev.* D87.9 (2013), page 092008. DOI: 10.1103/PhysRevD.87.092008. arXiv: 1210.2311 [hep-ex] (cited on page 37).
- [86] M. Mori et al. “Search for fractionally charged particles in Kamiokande-II”. In: *Phys. Rev.* D43 (1991), pages 2843–2846. DOI: 10.1103/PhysRevD.43.2843 (cited on page 38).
- [87] M. Ambrosio et al. “Final search for lightly ionizing particles with the MACRO detector”. In: (2004). arXiv: hep-ex/0402006 [hep-ex] (cited on page 38).
- [88] Thomas K. Gaisser, Ralph Engel, and Elisa Resconi. *Cosmic Rays and Particle Physics*. Cambridge University Press, 2016. ISBN: 9780521016469, 9781316598917. URL: <http://www.cambridge.org/de/academic/subjects/physics/cosmology-relativity-and-gravitation/cosmic-rays-and-particle-physics-2nd-edition?format=HB> (cited on pages 41, 44, 49).
- [89] The Nobel Prize. URL: <https://www.nobelprize.org/prizes/physics/1936/ceremony-speech/> (cited on page 41).
- [90] R. A. Millikan and G. H. Cameron. “The Origin of the Cosmic Rays”. In: *Phys. Rev.* 32 (4 Oct. 1928), pages 533–557. DOI: 10.1103/PhysRev.32.533. URL: <https://link.aps.org/doi/10.1103/PhysRev.32.533> (cited on page 41).
- [91] J. Clay. *Penetrating radiation*. Volume 30. 1927, pages 1115–1127 (cited on page 41).
- [92] M.H. Israel et al. “Isotopic Composition of Cosmic Rays: Results from the Cosmic Ray Isotope Spectrometer on the ACE Spacecraft”. In: *Nuclear Physics A* 758 (2005). Nuclei in the Cosmos VIII, pages 201–208. ISSN: 0375-9474. DOI: <https://doi.org/10.1016/j.nuclphysa.2005.05.038>. URL: <http://www.sciencedirect.com/science/article/pii/S037594740500686X> (cited on page 42).
- [93] Pasquale Blasi. “The Origin of Galactic Cosmic Rays”. In: *Astron. Astrophys. Rev.* 21 (2013), page 70. DOI: 10.1007/s00159-013-0070-7. arXiv: 1311.7346 [astro-ph.HE] (cited on page 43).
- [94] Thomas K. Gaisser, Todor Stanev, and Serap Tilav. “Cosmic Ray Energy Spectrum from Measurements of Air Showers”. In: *Front. Phys.(Beijing)* 8 (2013), pages 748–758. DOI: 10.1007/s11467-013-0319-7. arXiv: 1303.3565 [astro-ph.HE] (cited on pages 44, 45, 94, 96, 139).
- [95] M A Malkov and L O’C Drury. “Nonlinear theory of diffusive acceleration of particles by shock waves”. In: *Reports on Progress in Physics* 64.4 (2001), page 429. URL: <http://stacks.iop.org/0034-4885/64/i=4/a=201> (cited on page 44).
- [96] “Detection of the Small Magellanic Cloud in gamma-rays with Fermi/LAT”. In: *Astron. Astrophys.* 523 (2010), A46. DOI: 10.1051/0004-6361/201014855. arXiv: 1008.2127 [astro-ph.HE] (cited on page 44).

- [97] W. D. Apel et al. “Kneelike structure in the spectrum of the heavy component of cosmic rays observed with KASCADE-Grande”. In: *Phys. Rev. Lett.* 107 (2011), page 171104. DOI: 10.1103/PhysRevLett.107.171104. arXiv: 1107.5885 [astro-ph.HE] (cited on page 45).
- [98] A. P. Garyaka et al. “All-particle primary energy spectrum in the 3–200 PeV energy range”. In: *J. Phys.* G35 (2008), page 115201. DOI: 10.1088/0954-3899/35/11/115201. arXiv: 0808.1421 [astro-ph] (cited on page 45).
- [99] Kenneth Greisen. “End to the cosmic ray spectrum?” In: *Phys. Rev. Lett.* 16 (1966), pages 748–750. DOI: 10.1103/PhysRevLett.16.748 (cited on page 45).
- [100] G. T. Zatsepin and V. A. Kuzmin. “Upper limit of the spectrum of cosmic rays”. In: *JETP Lett.* 4 (1966). [*Pisma Zh. Eksp. Teor. Fiz.* 4, 114 (1966)], pages 78–80 (cited on page 45).
- [101] J. Bellido et al. “Proceedings of Science”. In: *ICRC* 301 (506 2017) (cited on page 45).
- [102] Alexander Aab et al. “Observation of a Large-scale Anisotropy in the Arrival Directions of Cosmic Rays above 8×10^{18} eV”. In: *Science* 357.6537 (2017), pages 1266–1270. DOI: 10.1126/science.aan4338. arXiv: 1709.07321 [astro-ph.HE] (cited on page 46).
- [103] E. Waxman. “IceCube’s Neutrinos: The beginning of extra-Galactic neutrino astrophysics?” In: *Proceedings, 9th Rencontres du Vietnam: Windows on the Universe: Quy Nhon, Vietnam, August 11–17, 2013*. 2013, pages 161–168. arXiv: 1312.0558 [astro-ph.HE] (cited on page 46).
- [104] A. M. Hillas. “The Origin of Ultrahigh-Energy Cosmic Rays”. In: *Ann. Rev. Astron. Astrophys.* 22 (1984), pages 425–444. DOI: 10.1146/annurev.aa.22.090184.002233 (cited on page 47).
- [105] Pablo M. Bauleo and Julio Rodriguez Martino. “The dawn of the particle astronomy era in ultra-high-energy cosmic rays”. In: *Nature* 458N7240 (2009), pages 847–851. DOI: 10.1038/nature07948 (cited on page 48).
- [106] P. O. Lagage and C. J. Cesarsky. “The maximum energy of cosmic rays accelerated by supernova shocks”. In: *Astron. Astrophys.* 125 (1983), pages 249–257 (cited on page 51).
- [107] T. Stanev. *High Energy Cosmic Rays*. Springer Praxis Books. Springer Berlin Heidelberg, 2010. ISBN: 9783540851486. URL: <https://books.google.be/books?id=1y9YEYHAFBMC> (cited on page 51).
- [108] C. Megan Urry and Paolo Padovani. “Unified schemes for radio-loud active galactic nuclei”. In: *Publ. Astron. Soc. Pac.* 107 (1995), page 803. DOI: 10.1086/133630. arXiv: astro-ph/9506063 [astro-ph] (cited on page 51).
- [109] Robert Antonucci. “Unified models for active galactic nuclei and quasars”. In: *Ann. Rev. Astron. Astrophys.* 31 (1993), pages 473–521. DOI: 10.1146/annurev.aa.31.090193.002353 (cited on page 51).
- [110] Demosthenes Kazanas et al. “Toward a Unified AGN Structure”. In: (2012). arXiv: 1206.5022 [astro-ph.HE] (cited on page 51).
- [111] J. Abraham et al. “Correlation of the highest-energy cosmic rays with the positions of nearby active galactic nuclei”. In: *Astropart. Phys.* 29 (2008). [Erratum: *Astropart. Phys.* 30, 45 (2008)], pages 188–204. DOI: 10.1016/j.astropartphys.2008.06.004, 10.1016/j.astropartphys.2008.01.002. arXiv: 0712.2843 [astro-ph] (cited on page 51).
- [112] M. G. Aartsen et al. “Multimessenger observations of a flaring blazar coincident with high-energy neutrino IceCube-170922A”. In: *Science* 361.6398 (2018), eaat1378. DOI: 10.1126/science.aat1378. arXiv: 1807.08816 [astro-ph.HE] (cited on pages 52, 81).
- [113] Ray W. Klebesadel, Ian B. Strong, and Roy A. Olson. “Observations of Gamma-Ray Bursts of Cosmic Origin”. In: *Astrophys. J.* 182 (1973), pages L85–L88. DOI: 10.1086/181225 (cited on page 52).

- [114] C. A. Meegan et al. “Spatial distribution of gamma-ray bursts observed by BATSE”. In: *Nature* 355 (1992), pages 143–145. DOI: 10.1038/355143a0 (cited on page 52).
- [115] Tsvi Piran. “The physics of gamma-ray bursts”. In: *Rev. Mod. Phys.* 76 (2004), pages 1143–1210. DOI: 10.1103/RevModPhys.76.1143. arXiv: astro-ph/0405503 [astro-ph] (cited on page 52).
- [116] B. P. Abbott et al. “GW170817: Observation of Gravitational Waves from a Binary Neutron Star Inspiral”. In: *Phys. Rev. Lett.* 119.16 (2017), page 161101. DOI: 10.1103/PhysRevLett.119.161101. arXiv: 1710.05832 [gr-qc] (cited on page 52).
- [117] B. P. Abbott et al. “GW170814: A Three-Detector Observation of Gravitational Waves from a Binary Black Hole Coalescence”. In: *Phys. Rev. Lett.* 119.14 (2017), page 141101. DOI: 10.1103/PhysRevLett.119.141101. arXiv: 1709.09660 [gr-qc] (cited on page 52).
- [118] B.. P.. Abbott et al. “GW170608: Observation of a 19-solar-mass Binary Black Hole Coalescence”. In: *Astrophys. J.* 851.2 (2017), page L35. DOI: 10.3847/2041-8213/aa9f0c. arXiv: 1711.05578 [astro-ph.HE] (cited on page 52).
- [119] Benjamin P. Abbott et al. “GW170104: Observation of a 50-Solar-Mass Binary Black Hole Coalescence at Redshift 0.2”. In: *Phys. Rev. Lett.* 118.22 (2017). [Erratum: *Phys. Rev. Lett.* 121,no.12,129901(2018)], page 221101. DOI: 10.1103/PhysRevLett.118.221101, 10.1103/PhysRevLett.121.129901. arXiv: 1706.01812 [gr-qc] (cited on page 52).
- [120] B. P. Abbott et al. “GW151226: Observation of Gravitational Waves from a 22-Solar-Mass Binary Black Hole Coalescence”. In: *Phys. Rev. Lett.* 116.24 (2016), page 241103. DOI: 10.1103/PhysRevLett.116.241103. arXiv: 1606.04855 [gr-qc] (cited on page 52).
- [121] F. Acero. “Detection of Gamma Rays From a Starburst Galaxy”. In: *Science* 326 (2009), page 1080. DOI: 10.1126/science.1178826. arXiv: 0909.4651 [astro-ph.HE] (cited on page 53).
- [122] Niklas Karlsson. “Discovery of VHE Gamma-ray Emission from the Starburst Galaxy M82”. In: (2009). arXiv: 0912.3807 [astro-ph.HE] (cited on page 53).
- [123] Kohta Murase, Susumu Inoue, and Shigehiro Nagataki. “Cosmic Rays above the Second Knee from Clusters of Galaxies and Associated High-Energy Neutrino Emission”. In: *The Astrophysical Journal Letters* 689.2 (2008), page L105. URL: <http://stacks.iop.org/1538-4357/689/i=2/a=L105> (cited on page 53).
- [124] U. F. Katz and Ch. Spiering. “High-Energy Neutrino Astrophysics: Status and Perspectives”. In: *Prog. Part. Nucl. Phys.* 67 (2012), pages 651–704. DOI: 10.1016/j.ppnp.2011.12.001. arXiv: 1111.0507 [astro-ph.HE] (cited on page 54).
- [125] Morihiro Honda et al. “Calculation of atmospheric neutrino flux using the interaction model calibrated with atmospheric muon data”. In: *Phys. Rev. D* 75 (2007), page 043006. DOI: 10.1103/PhysRevD.75.043006. arXiv: astro-ph/0611418 [astro-ph] (cited on pages 54, 94–96, 139).
- [126] M. G. Aartsen et al. “The IceCube Neutrino Observatory - Contributions to ICRC 2017 Part II: Properties of the Atmospheric and Astrophysical Neutrino Flux”. In: (2017). arXiv: 1710.01191 [astro-ph.HE] (cited on pages 55, 81).
- [127] Kiyoshi Niu, Eiko Mikumo, and Yasuko Maeda. “A Possible Decay in Flight of a New Type Particle”. In: *Progress of Theoretical Physics* 46.5 (1971), pages 1644–1646. DOI: 10.1143/PTP.46.1644. eprint: /oup/backfile/content_public/journal/ptp/46/5/10.1143/ptp.46.1644/2/46-5-1644.pdf. URL: <http://dx.doi.org/10.1143/PTP.46.1644> (cited on page 54).
- [128] Rikard Enberg, Mary Hall Reno, and Ina Sarcevic. “Prompt neutrino fluxes from atmospheric charm”. In: *Phys. Rev. D* 78 (2008), page 043005. DOI: 10.1103/PhysRevD.78.043005. arXiv: 0806.0418 [hep-ph] (cited on pages 54, 94–96).

- [129] Linyan Wan et al. “Geoneutrinos at Jinping: Flux prediction and oscillation analysis”. In: *Phys. Rev.* D95.5 (2017), page 053001. DOI: 10.1103/PhysRevD.95.053001. arXiv: 1612.00133 [hep-ex] (cited on page 56).
- [130] Kate Scholberg. “Supernova Neutrino Detection”. In: *Ann. Rev. Nucl. Part. Sci.* 62 (2012), pages 81–103. DOI: 10.1146/annurev-nucl-102711-095006. arXiv: 1205.6003 [astro-ph.IM] (cited on page 56).
- [131] Lutz Kopke. “Supernova Neutrino Detection with IceCube”. In: *J. Phys. Conf. Ser.* 309 (2011), page 012029. DOI: 10.1088/1742-6596/309/1/012029. arXiv: 1106.6225 [astro-ph.HE] (cited on page 56).
- [132] C. Grupen. *Astroparticle physics*. 2005. ISBN: 9783540253129. URL: <http://www.springer.com/book/3-540-25312-2> (cited on page 57).
- [133] nobel1958. URL: <https://www.nobelprize.org/prizes/physics/1958/summary/> (cited on page 60).
- [134] “Design, Implementation and Test of a New Feature Extractor for the IceCube Neutrino Observatory”. In: (2010) (cited on page 62).
- [135] Dmitry Chirkin and Wolfgang Rhode. “Muon Monte Carlo: A High-precision tool for muon propagation through matter”. In: (2004). arXiv: hep-ph/0407075 [hep-ph] (cited on page 64).
- [136] AMANDA collaboration. URL: <http://amanda.uci.edu/> (cited on page 69).
- [137] E. Andres et al. “The AMANDA neutrino telescope: Principle of operation and first results”. In: *Astropart. Phys.* 13 (2000), pages 1–20. DOI: 10.1016/S0927-6505(99)00092-4. arXiv: astro-ph/9906203 [astro-ph] (cited on page 69).
- [138] J. Ahrens et al. “Observation of high-energy atmospheric neutrinos with the Antarctic Muon and Neutrino Detector Array”. In: *Phys. Rev.* D66 (2002), page 012005. DOI: 10.1103/PhysRevD.66.012005. arXiv: astro-ph/0205109 [astro-ph] (cited on page 69).
- [139] R. Abbasi et al. “The Design and Performance of IceCube DeepCore”. In: *Astropart. Phys.* 35 (2012), pages 615–624. DOI: 10.1016/j.astropartphys.2012.01.004. arXiv: 1109.6096 [astro-ph.IM] (cited on page 72).
- [140] M. G. Aartsen et al. “Measurement of South Pole ice transparency with the IceCube LED calibration system”. In: *Nucl. Instrum. Meth.* A711 (2013), pages 73–89. DOI: 10.1016/j.nima.2013.01.054. arXiv: 1301.5361 [astro-ph.IM] (cited on page 73).
- [141] M. Ackermann et al. “Optical properties of deep glacial ice at the South Pole”. In: *J. Geophys. Res. Atmos.* 111.D13 (2006), page D13203. DOI: 10.1029/2005JD006687 (cited on page 73).
- [142] Dmitry Chirkin. “Evidence of optical anisotropy of the South Pole ice”. In: *Proceedings, 33rd International Cosmic Ray Conference (ICRC2013): Rio de Janeiro, Brazil, July 2-9, 2013*, page 0580. URL: <http://www.cbpf.br/%7Eicrc2013/papers/icrc2013-0580.pdf> (cited on pages 73, 74).
- [143] M. G. Aartsen et al. “The IceCube Neutrino Observatory: Instrumentation and Online Systems”. In: *JINST* 12.03 (2017), P03012. DOI: 10.1088/1748-0221/12/03/P03012. arXiv: 1612.05093 [astro-ph.IM] (cited on pages 74–77).
- [144] R. Abbasi et al. “Calibration and Characterization of the IceCube Photomultiplier Tube”. In: *Nucl. Instrum. Meth.* A618 (2010), pages 139–152. DOI: 10.1016/j.nima.2010.03.102. arXiv: 1002.2442 [astro-ph.IM] (cited on pages 75, 99).
- [145] M. G. Aartsen et al. “The IceCube Neutrino Observatory - Contributions to ICRC 2017 Part IV: Searches for Beyond the Standard Model Physics”. In: (2017). arXiv: 1710.01197 [astro-ph.HE] (cited on page 80).

- [146] M. G. Aartsen et al. “Measurement of the multi-TeV neutrino cross section with IceCube using Earth absorption”. In: *Nature* 551 (2017), pages 596–600. DOI: 10.1038/nature24459. arXiv: 1711.08119 [hep-ex] (cited on page 81).
- [147] M. G. Aartsen et al. “Measurements using the inelasticity distribution of multi-TeV neutrino interactions in IceCube”. In: (2018). arXiv: 1808.07629 [hep-ex] (cited on page 81).
- [148] M. G. Aartsen et al. “Searches for Sterile Neutrinos with the IceCube Detector”. In: *Phys. Rev. Lett.* 117.7 (2016), page 071801. DOI: 10.1103/PhysRevLett.117.071801. arXiv: 1605.01990 [hep-ex] (cited on page 81).
- [149] Spencer R. Klein. “Astrophysical Neutrinos with IceCube”. In: *13th Conference on the Intersections of Particle and Nuclear Physics (CIPANP 2018) Palm Springs, California, USA, May 29-June 3, 2018*. 2018. arXiv: 1809.07873 [astro-ph.HE] (cited on page 81).
- [150] M. G. Aartsen et al. “A combined maximum-likelihood analysis of the high-energy astrophysical neutrino flux measured with IceCube”. In: *Astrophys. J.* 809.1 (2015), page 98. DOI: 10.1088/0004-637X/809/1/98. arXiv: 1507.03991 [astro-ph.HE] (cited on page 82).
- [151] M. G. Aartsen et al. “Measurement of Atmospheric Neutrino Oscillations at 6–56 GeV with IceCube DeepCore”. In: *Phys. Rev. Lett.* 120.7 (2018), page 071801. DOI: 10.1103/PhysRevLett.120.071801. arXiv: 1707.07081 [hep-ex] (cited on page 83).
- [152] Volker Baum. “Search for Low Energetic Neutrino Signals from Galactic Supernovae and Collisionally Heated Gamma-Ray Bursts with the IceCube Neutrino Observatory”. PhD thesis. Mainz U., Math. Comp. Sci., 2017. URL: https://publications.ub.uni-mainz.de/theses/frontdoor.php?source_opus=100001660&la=de (cited on page 82).
- [153] Thomas Kowarik, Timo Griesel, and Alexander Piesza. “Supernova Search with the AMANDA / IceCube Detectors”. In: (2009). arXiv: 0908.0441 [astro-ph.HE] (cited on page 82).
- [154] Don Colladay and V. Alan Kostelecky. “Lorentz violating extension of the standard model”. In: *Phys. Rev.* D58 (1998), page 116002. DOI: 10.1103/PhysRevD.58.116002. arXiv: hep-ph/9809521 [hep-ph] (cited on page 84).
- [155] M. G. Aartsen et al. “Neutrino Interferometry for High-Precision Tests of Lorentz Symmetry with IceCube”. In: *Nature Phys.* 14.9 (2018), pages 961–966. DOI: 10.1038/s41567-018-0172-2. arXiv: 1709.03434 [hep-ex] (cited on pages 83, 84).
- [156] R. Abbasi et al. “Search for a Lorentz-violating sidereal signal with atmospheric neutrinos in IceCube”. In: *Phys. Rev.* D82 (2010), page 112003. DOI: 10.1103/PhysRevD.82.112003. arXiv: 1010.4096 [astro-ph.HE] (cited on page 83).
- [157] M. G. Aartsen et al. “Search for Neutrinos from Dark Matter Self-Anihilations in the center of the Milky Way with 3 years of IceCube/DeepCore”. In: *Eur. Phys. J.* C77.9 (2017), page 627. DOI: 10.1140/epjc/s10052-017-5213-y. arXiv: 1705.08103 [hep-ex] (cited on page 83).
- [158] M. G. Aartsen et al. “Search for annihilating dark matter in the Sun with 3 years of IceCube data”. In: *Eur. Phys. J.* C77.3 (2017), page 146. DOI: 10.1140/epjc/s10052-017-4689-9. arXiv: 1612.05949 [astro-ph.HE] (cited on page 83).
- [159] R. Abbasi et al. “Limits on a muon flux from Kaluza-Klein dark matter annihilations in the Sun from the IceCube 22-string detector”. In: *Phys. Rev.* D81 (2010), page 057101. DOI: 10.1103/PhysRevD.81.057101. arXiv: 0910.4480 [astro-ph.CO] (cited on page 83).
- [160] M. G. Aartsen et al. “First search for dark matter annihilations in the Earth with the IceCube Detector”. In: *Eur. Phys. J.* C77.2 (2017), page 82. DOI: 10.1140/epjc/s10052-016-4582-y. arXiv: 1609.01492 [astro-ph.HE] (cited on page 83).

- [161] “Quantised singularities in the electromagnetic field,” in: *Proceedings of the Royal Society of London A: Mathematical, Physical and Engineering Sciences* 133.821 (1931), pages 60–72. ISSN: 0950-1207. DOI: 10.1098/rspa.1931.0130. eprint: <http://rspa.royalsocietypublishing.org/content/133/821/60.full.pdf>. URL: <http://rspa.royalsocietypublishing.org/content/133/821/60> (cited on page 83).
- [162] G.’t Hooft. “Magnetic monopoles in unified gauge theories”. In: *Nuclear Physics B* 79.2 (1974), pages 276–284. ISSN: 0550-3213. DOI: [https://doi.org/10.1016/0550-3213\(74\)90486-6](https://doi.org/10.1016/0550-3213(74)90486-6). URL: <http://www.sciencedirect.com/science/article/pii/0550321374904866> (cited on page 84).
- [163] Alexander M. Polyakov. “Particle Spectrum in the Quantum Field Theory”. In: *JETP Lett.* 20 (1974). [,300(1974)], pages 194–195 (cited on page 84).
- [164] M. G. Aartsen et al. “Search for non-relativistic Magnetic Monopoles with IceCube”. In: *Eur. Phys. J.* C74.7 (2014), page 2938. DOI: 10.1140/epjc/s10052-014-2938-8. arXiv: 1402.3460 [astro-ph.CO] (cited on page 84).
- [165] Samridha Kunwar et al. “The IceTop Scintillator Upgrade”. In: *PoS ICRC2017* (2018), page 401. DOI: 10.22323/1.301.0401 (cited on page 85).
- [166] Alexander Aab et al. “The Pierre Auger Observatory Upgrade - Preliminary Design Report”. In: (2016). arXiv: 1604.03637 [astro-ph.IM] (cited on page 85).
- [167] Delia Tosi and Hershal Pandya. “Performance of IceTop as a veto for IceCube”. In: *PoS ICRC2017* (2018), page 967. DOI: 10.22323/1.301.0967 (cited on page 85).
- [168] Jan Auffenberg. “IceAct: Imaging Air Cherenkov Telescopes with SiPMs at the South Pole for IceCube-Gen2”. In: *PoS ICRC2017* (2018), page 1055. DOI: 10.22323/1.301.1055 (cited on page 85).
- [169] Satoshi Shimizu et al. “Overview and performance of the D-Egg optical sensor for IceCube-Gen2”. In: *PoS ICRC2017* (2018), page 1051. DOI: 10.22323/1.301.1051 (cited on page 86).
- [170] Lew Classen et al. “The mDOM - A multi-PMT digital optical module for the IceCube-Gen2 neutrino telescope”. In: *PoS ICRC2017* (2018), page 1047. DOI: 10.22323/1.301.1047 (cited on page 86).
- [171] M. Jeong and W. Kang. “A camera system for IceCube-Gen2”. In: *PoS ICRC2017* (2018), page 1040. DOI: 10.22323/1.301.1040 (cited on page 86).
- [172] Elisa Resconi, Kai Krings, and Kai Krings Martin Rongen. “The Precision Optical CAlibration Module for IceCube-Gen2: First Prototype”. In: *PoS ICRC2017* (2018), page 934. DOI: 10.22323/1.301.0934 (cited on page 87).
- [173] Erik Blaufuss, C. Kopper, and C. Haack. “The IceCube-Gen2 High Energy Array”. In: *PoS ICRC2015* (2016), page 1146. DOI: 10.22323/1.236.1146 (cited on page 87).
- [174] Markus Ahlers and Francis Halzen. “Pinpointing Extragalactic Neutrino Sources in Light of Recent IceCube Observations”. In: *Phys. Rev.* D90.4 (2014), page 043005. DOI: 10.1103/PhysRevD.90.043005. arXiv: 1406.2160 [astro-ph.HE] (cited on page 87).
- [175] Sebastian Euler, Javier Gonzalez, and Ben Roberts. “Simulation Studies for a Surface Veto Array to Identify Astrophysical Neutrinos at the South Pole”. In: *PoS ICRC2015* (2016), page 1070. DOI: 10.22323/1.236.1070 (cited on page 88).
- [176] Frank G. Schröder. “Radio detection of Cosmic-Ray Air Showers and High-Energy Neutrinos”. In: *Prog. Part. Nucl. Phys.* 93 (2017), pages 1–68. DOI: 10.1016/j.ppnp.2016.12.002. arXiv: 1607.08781 [astro-ph.IM] (cited on page 88).
- [177] P. Allison et al. “Performance of two Askaryan Radio Array stations and first results in the search for ultrahigh energy neutrinos”. In: *Phys. Rev.* D93.8 (2016), page 082003. DOI: 10.1103/PhysRevD.93.082003. arXiv: 1507.08991 [astro-ph.HE] (cited on page 88).

- [178] Christian Glaser. “ARIANNA: Measurement of cosmic rays with a radio neutrino detector in Antarctica”. In: *Acoustic and Radio EeV Neutrino Detection Activities (ARENA 2018) Catania, Italy, June 12-15, 2018*. 2018. arXiv: 1811.10661 [astro-ph.IM] (cited on page 88).
- [179] D Schultz. “IceProd 2: A Next Generation Data Analysis Framework for the IceCube Neutrino Observatory”. In: *Journal of Physics: Conference Series* 664.6 (2015), page 062056. URL: <http://stacks.iop.org/1742-6596/664/i=6/a=062056> (cited on page 93).
- [180] Ralph Engel et al. “Towards the next generation of CORSIKA: A framework for the simulation of particle cascades in astroparticle physics”. In: (2018). arXiv: 1808.08226 [astro-ph.IM] (cited on page 93).
- [181] Giuseppe Battistoni et al. “Overview of the FLUKA code”. In: *Annals Nucl. Energy* 82 (2015), pages 10–18. DOI: 10.1016/j.anucene.2014.11.007 (cited on page 94).
- [182] Askhat Gazizov and Marek P. Kowalski. “ANIS: High energy neutrino generator for neutrino telescopes”. In: *Comput. Phys. Commun.* 172 (2005), pages 203–213. DOI: 10.1016/j.cpc.2005.03.113. arXiv: astro-ph/0406439 [astro-ph] (cited on page 94).
- [183] M. G. Aartsen et al. “Observation of High-Energy Astrophysical Neutrinos in Three Years of IceCube Data”. In: *Phys. Rev. Lett.* 113 (2014), page 101101. DOI: 10.1103/PhysRevLett.113.101101. arXiv: 1405.5303 [astro-ph.HE] (cited on pages 95, 96).
- [184] C. Andreopoulos et al. “The GENIE Neutrino Monte Carlo Generator”. In: *Nucl. Instrum. Meth.* A614 (2010), pages 87–104. DOI: 10.1016/j.nima.2009.12.009. arXiv: 0905.2517 [hep-ph] (cited on page 95).
- [185] Costas Andreopoulos et al. “The GENIE Neutrino Monte Carlo Generator: Physics and User Manual”. In: (2015). arXiv: 1510.05494 [hep-ph] (cited on page 95).
- [186] M. Honda et al. “Atmospheric neutrino flux calculation using the NRLMSISE-00 atmospheric model”. In: *Phys. Rev. D* 92.2 (2015), page 023004. DOI: 10.1103/PhysRevD.92.023004. arXiv: 1502.03916 [astro-ph.HE] (cited on pages 95, 96).
- [187] Joerg R. Hoerandel. “On the knee in the energy spectrum of cosmic rays”. In: *Astropart. Phys.* 19 (2003), pages 193–220. DOI: 10.1016/S0927-6505(02)00198-6. arXiv: astro-ph/0210453 [astro-ph] (cited on page 96).
- [188] Thomas K. Gaisser. “Spectrum of cosmic-ray nucleons, kaon production, and the atmospheric muon charge ratio”. In: *Astropart. Phys.* 35 (2012), pages 801–806. DOI: 10.1016/j.astropartphys.2012.02.010. arXiv: 1111.6675 [astro-ph.HE] (cited on pages 96, 139).
- [189] G. D. Barr et al. “Three-dimensional calculation of atmospheric neutrinos”. In: *Phys. Rev. D* 70 (2 July 2004), page 023006. DOI: 10.1103/PhysRevD.70.023006. URL: <https://link.aps.org/doi/10.1103/PhysRevD.70.023006> (cited on pages 96, 139).
- [190] Mario Dunsch et al. “Recent Improvements for the Lepton Propagator PROPOSAL”. In: (2018). arXiv: 1809.07740 [hep-ph] (cited on page 98).
- [191] Dmitry Chirkin. “Study of South Pole ice transparency with IceCube flashers”. In: *Proceedings, 32nd International Cosmic Ray Conference (ICRC 2011): Beijing, China, August 11-18, 2011*. Volume 4, page 161. DOI: 10.7529/ICRC2011/V04/0333 (cited on page 99).
- [192] Johan Lundberg et al. “Light tracking for glaciers and oceans: Scattering and absorption in heterogeneous media with Photonics”. In: *Nucl. Instrum. Meth.* A581 (2007), pages 619–631. DOI: 10.1016/j.nima.2007.07.143. arXiv: astro-ph/0702108 [ASTRO-PH] (cited on page 99).
- [193] K. J. Ma et al. “Time and Amplitude of Afterpulse Measured with a Large Size Photomultiplier Tube”. In: *Nucl. Instrum. Meth.* A629 (2011), pages 93–100. DOI: 10.1016/j.nima.2010.11.095. arXiv: 0911.5336 [physics.ins-det] (cited on page 99).

- [194] IceCube collaboration. URL: https://wiki.icecube.wisc.edu/index.php/Pass2_Region_Processing (cited on page 100).
- [195] J. Ahrens et al. “Muon track reconstruction and data selection techniques in AMANDA”. In: *Nucl. Instrum. Meth.* A524 (2004), pages 169–194. DOI: 10.1016/j.nima.2004.01.065. arXiv: astro-ph/0407044 [astro-ph] (cited on pages 104–106).
- [196] M. G. Aartsen et al. “Improvement in Fast Particle Track Reconstruction with Robust Statistics”. In: *Nucl. Instrum. Meth.* A736 (2014), pages 143–149. DOI: 10.1016/j.nima.2013.10.074. arXiv: 1308.5501 [astro-ph.IM] (cited on page 105).
- [197] IceCube collaboration. URL: https://internal-apps.icecube.wisc.edu/reports/data/icecube/2014/04/001/icecube_201404001_v1.pdf (cited on page 107).
- [198] Stef Verpoest. URL: https://lib.ugent.be/fulltxt/RUG01/002/479/620/RUG01-002479620_2018_0001_AC.pdf (cited on page 107).
- [199] Till Neunhoffer. “Estimating the angular resolution of tracks in neutrino telescopes based on a likelihood analysis”. In: *Astropart. Phys.* 25 (2006), pages 220–225. DOI: 10.1016/j.astropartphys.2006.01.002. arXiv: astro-ph/0403367 [astro-ph] (cited on page 108).
- [200] URL: https://wiki.icecube.wisc.edu/index.php/SLC_hit_cleaning (cited on page 109).
- [201] URL: <https://www.dissertations.se/dissertation/fef1f8e4ba/> (cited on pages 110, 111).
- [202] Yoav Freund and Robert E Schapire. “A Decision-Theoretic Generalization of On-Line Learning and an Application to Boosting”. In: *Journal of Computer and System Sciences* 55.1 (1997), pages 119–139. ISSN: 0022-0000. DOI: <https://doi.org/10.1006/jcss.1997.1504>. URL: <http://www.sciencedirect.com/science/article/pii/S00220009791504X> (cited on page 114).
- [203] S. Fink C. Böser and S. Röcker. *Introduction to boosted decision trees: A multivariate approach to classification problems*. Presented at the KSETA Doctoral Workshop, Berlin, Germany. July 2014 (cited on page 115).
- [204] Hanchuan Peng, Fuhui Long, and C. Ding. “Feature selection based on mutual information criteria of max-dependency, max-relevance, and min-redundancy”. In: *IEEE Transactions on Pattern Analysis and Machine Intelligence* 27.8 (Aug. 2005), pages 1226–1238. ISSN: 0162-8828. DOI: 10.1109/TPAMI.2005.159 (cited on page 116).
- [205] IceCube collaboration. URL: <https://docushare.icecube.wisc.edu/dsweb/Get/Document-56551/VEFproposal.pdf> (cited on page 119).
- [206] IceCube collaboration. URL: https://docushare.icecube.wisc.edu/dsweb/Get/Document-59303/lowup_2012_proposal.pdf (cited on page 121).
- [207] IceCube collaboration. URL: <https://docushare.icecube.wisc.edu/dsweb/Get/Document-59728/onlinel2proposal2012.pdf> (cited on page 121).
- [208] IceCube collaboration. URL: <https://docushare.icecube.wisc.edu/dsweb/Get/Document-59397/DeepCoreFilterProposal.pdf> (cited on page 121).
- [209] IceCube collaboration. URL: https://wiki.icecube.wisc.edu/index.php/Effects_of_DOM_Mainboard_Release_443 (cited on page 123).
- [210] S. Verpoest. “Search for particles with fractional charges in IceCube based on anomalous energy loss”. Master’s thesis. UGent, 2018 (cited on page 126).
- [211] J. Künnen. “A Search for Dark Matter in the Center of the Earth with the IceCube Neutrino Detector”. Master’s thesis. VUB, 2015 (cited on page 131).



Index

B

burn sample 100

C

CLSim 99
coincident events 109
CoincSuite 111
Corollaries 159
CORSIKA 93

D

Definitions 159

E

Examples 160
 Equation and Text 160
 Paragraph of Text 160
Exercises 160

F

FLUKA 94

I

i3file 81
IceTray 91

L

Line-Fit 104

M

MMC 99
Monte Carlo 91

N

neutrino-generator 94

P

Paragraphs of Text 9
Photonics 99
PMT jitter 99
PPC 99
Problems 160
PROPOSAL 97
Propositions 159
 Several Equations 160
 Single Line 160

R

Remarks 159

S

seededRT 109
SPE 106
Steamshovel 101

T

TopologicalSplitter 109

V

Vocabulary 160